TESIS DE LA UNIVERSIDAD DE ZARAGOZA

2025 133

Cristina Pérez Martínez

Quantification of QT Interval Adaptation Time to Gradual Changes in Heart Rate and its Use for Cardiac Risk Stratification

Director/es
Laguna Lasaosa, Pablo
Pueyo Paules, Esther

ISSN 2254-7606

Prensas de la Universidad Universidad Zaragoza

Universidad de Zaragoza
Servicio de Publicaciones

ISSN 2254-7606

Universidad Zaragoza
1542

Tesis Doctoral

QUANTIFICATION OF QT INTERVAL ADAPTATION TIME TO GRADUAL CHANGES IN HEART RATE AND ITS USE FOR CARDIAC RISK STRATIFICATION

Autor

Cristina Pérez Martínez

Director/es

Laguna Lasaosa, Pablo
Pueyo Paules, Esther

UNIVERSIDAD DE ZARAGOZA
Escuela de Doctorado

2024

Universidad Zaragoza
1474

Instituto Universitario de Investigación en Ingeniería de Aragón
Universidad Zaragoza

Ph.D. Thesis

Quantification of QT Interval Adaptation Time to Gradual Changes in Heart Rate and its Use for Cardiac Risk Stratification

Cuantificación del tiempo de adaptación del intervalo QT ante cambios graduales en la frecuencia cardíaca y su uso para la estratificación del riesgo cardíaco

Autor

Cristina Pérez Martínez

Supervisors

Pablo Laguna Lasaosa

Esther Pueyo Paules

Instituto de Investigación en Ingeniería de Aragón
Universidad de Zaragoza

2024

Quantification of QT Interval Adaptation Time to Gradual Changes in Heart Rate and its Use for Cardiac Risk Stratification

Cristina Pérez Martínez, 2024
Quantification of QT Interval Adaptation Time to Gradual Changes in Heart Rate and its Use for Cardiac Risk Stratification

Date of current version: Tuesday 10th December, 2024

This Ph.D. thesis belongs to the inter-universitary Biomedical Engineering Ph.D. Program of the University of Zaragoza and Polytechnic University of Cataluña, and has been developed within the Biomedical Signal Interpretation and Computational Simulations (BSICoS) group of the Aragón Institute for Engineering Research (I3A), and the Department of Electronic Engineering and Communications at the University of Zaragoza (Zaragoza, Spain).

The research presented in this thesis was supported by a personal grant to Cristina Pérez Martínez by Gobierno de Aragón (Spain) (Ref: IIU/796/2019), by Ministerio de Ciencia, Innovación y Universidades (MICINN) under projects PID2019-104881RB-I00, PID2019-105674RB-I00, TED2021-130459B-I00, and PID2022-140556OB-I00 by H2020 European Research Council under project ERC-StG 638284, by CIBERBBN through Instituto de Salud Carlos III, and by Gobierno de Aragón (Ref: T39_23R BSICoS Group, and project LMP94_21). The computation was performed at the high performance computing platform of the NANBIOSIS ICTS (HPC Unit, U27). The research visit at Lund University was partly supported by Fundación Bancaria Ibercaja y Fundación CA de Estancias de Investigación (Ref: IT 3/22).

This thesis was printed thanks to the financial support of BSICoS Group at University of Zaragoza.

El corazón es agua
que se acaricia y canta.

El corazón es puerta
que se abre y se cierra.

El corazón es agua
que se remueve, arrolla,
se arremolina, mata.

Miguel Hernández

A la sonrisa de mis abuel@s.

ABSTRACT

The QT interval of the electrocardiogram (ECG) represents the time from the beginning of depolarization to the end of repolarization of the left and right ventricles, although it is generally considered as an overall measure of ventricular repolarization. The relation between the QT interval and the RR interval (inverse of heart rate) has been thoroughly investigated in the literature. A prolonged time for QT interval adaptation in response to changes in the RR interval has been related to high risk of ventricular arrhythmias and sudden cardiac death (SCD), which could be partially explained by the enhanced heterogeneity in the repolarization duration across the ventricles due to different cellular adaptation times.

In previous studies, the response of the QT interval to changes in the RR interval has been characterized by considering the QT interval time series as the output of a system whose input is the RR interval time series. The system has been modeled with two sequential, time-invariant blocks: one block represents the steady-state relation between the QT interval and the RR interval and is typically described by a nonlinear memoryless function; the other block represents the memory of the QT interval in response to RR interval changes and is described by a linear filter that allows quantifying the QT-RR hysteresis. This QT-RR model has been evaluated in different scenarios, with a particular focus on the QT response to abrupt RR changes commonly obtained from Holter recordings. However, these types of changes are not always present in ECG recordings. If the linear filter of the proposed model is assumed to be a first-order system, and consequently fully characterized by its time constant, it is known from control theory that the time constant can be evaluated as the delay between a linear ramp input signal and the delayed ramp output signal.

In this work, the dynamics of the relation between the QT and RR intervals extracted from ECG signals recorded during exercise stress testing (EST) are investigated. Thus, gradual RR interval changes from EST are considered as the

input to the system and, based on control theory and the expected response of a first-order linear system to a ramp function, an alternative method is proposed to estimate the QT adaptation time lag. The gradual RR interval changes are identified in both the exercise phase and the recovery phase of the EST. Usually, these two phases are preceded, or followed in the case of recovery, by a phase where the RR interval almost remains at a stationary basal state.

The QT adaptation time lag is here proposed to be quantified as the delay between the time series of the observed QT intervals and a memoryless QT series estimated from the observed RR intervals in the ECG. This delay is evaluated in the exercise and recovery phases, separately, by applying both Laplacian and Gaussian Maximum Likehood estimators. A hyperbolic regression model is chosen to estimate the memoryless QT series that characterizes the QT interval according to the observed RR interval values, since it is the model that leads to the best fit, in terms of mean squared error, out of the tested regression models. The parameters of the model are estimated for each patient individually. Three learning windows in the EST are selected to learn the model parameters in phases where the RR interval can be assumed to remain essentially stationary (i.e. the series do not present any low-frequency trend): one window in each of the two basal zones and another around the peak exercise. The last mentioned window, even questionable in terms of RR interval stationarity, is selected to cover the widest possible range of RR values so as to guarantee a better fit of the QT-RR dependency. To compensate for the lack of stationarity at the peak exercise window, three different choices of the window, and modification of the corresponding data values, are proposed: (1) the window is selected to be centered at the peak exercise, so that the dynamics of the heart rate during exercise are compensated with those of the recovery phase; (2) the window selection in (1) is complemented by a modification of the QT interval values inside the window based on a pre-estimated QT delay in exercise calculated from the first window definition; (3) on top of modifying the data as in (2), the window is replaced with another that only includes values corresponding to the exercise phase, where the data correction in (2) is meaningful.

The methods proposed in the Ph.D. thesis are first technically evaluated in datasets containing simulated ECGs with known QT-RR dependency and time lag. For this purpose, a simulation environment is generated that allows to: (a) set a user-defined QT adaptation time lag; (b) add simulated noise components with characteristics similar to those of the muscle noise present in exercise ECG stress testing and with different signal-to-noise ratios, so that the robustness of the methods against this contamination can be studied. The results show that the QT adaptation time lag is estimated more accurately

when the model parameter learning is performed using the window at peak exercise with modified data values and located only in the exercise phase.

Next, the clinical added value of the QT adaptation time lag estimated by the proposed procedure is evaluated in the exercise phase, in the recovery phase, and as the difference between these two. This evaluation allows to stratify patients with different risk of suffering coronary artery disease (CAD) and to predict SCD and overall mortality. The results show that the delay in the exercise phase increases as the risk of CAD increases, while the delay in the recovery phase decreases with the CAD risk. In addition, the recovery delay is longer in patients with SCD than in survivors and in patients who died due to any cause versus survivors.

Another technological challenge studied throughout this Ph.D. thesis is the delineation of the end of the T wave from very noisy exercise ECGs stress testing, where an overlap between the T wave and the P wave can occur as the heart rate increases during the exercise phase. This phenomenon, along with the increased presence of exercise-induced noise, complicates the delineation of the QT interval series. Therefore, different methods based on two lead space transformation techniques are proposed to improve the delineation of the T wave: (a) applying principal component analysis, which maximizes the signal variance; (b) applying periodic component analysis, which maximizes the signal beat periodicity. The emphasis of these characteristics are mostly reflected in the first transformed lead, so the T wave is delineated only in this one. The results of the delineation with these methods are compared with one of the most traditional multi-lead based methods, which consists of delineating each lead individually and applying a rule to obtain a single delineation mark. The delineation of the T wave end is evaluated in simulated ECG signals using a reference mark from the same signal with almost no noise, and in clinical recordings by using the inverse of the signal power of the high-pass filtered observed QT interval series as a surrogate of the delineation performance. In both simulated and clinical ECGs, the best results are obtained by delineating the first transformed lead after applying periodic component analysis, and then proposed as the choice for the rest of the work.

From the analysis of the clinical ECGs of CAD patients, the delay between the observed and the memoryless estimated QT series in the exercise phase is not constant, but it is reduced when approaching the peak exercise. In addition to the influence of heart rate on the QT interval, the autonomic nervous system could play a more general role in modulating the ventricular repolarization and its adaptation to heart rate. This autonomic modulation could occur both directly via the autonomic innervation of the ventricular myocardium

and indirectly via the effects on the heart rate. Based on previous studies of the literature, we hypothesize that an increase in the sympathetic activity as the peak exercise is approached, that is, an increase in the pre-stimulation levels of β-adrenoceptors when approaching the peak exercise, could explain the reduction in the QT interval adaptation time observed at the end of the exercise. To study the autonomic modulation of the QT adaptation time lag, the last chapter of this Ph.D. thesis proposes an *in silico* study to investigate the dynamics of the ventricular repolarization adaptation in response to β-adrenergic stimulation, at the cellular and tissue levels and at the ECG. The estimated QT adaptation time delays in response to the same RR interval changes as in clinical ECGs are quantified for different patterns of β-adrenergic stimulation and are compared with those obtained in the clinical recordings. It is concluded that a time-varying β-adrenergic stimulation pattern better reproduces the QT adaptation characteristics observed from the analysis of clinical ECGs.

Keywords: QT-RR modeling; QT adaptation time lag; electrocardiogram; simulated ECGs; T wave end delineation; periodic component analysis; exercise stress testing; coronary artery disease; sudden cardiac death.

RESUMEN Y CONCLUSIONES

El intervalo QT del electrocardiograma (ECG) representa el tiempo desde el inicio de la despolarización hasta el final de la repolarización de ambos ventrículos, izquierdo y derecho, aunque generalmente se considera como una medida global de la repolarización ventricular. Se ha relacionado un tiempo prolongado de adaptación del intervalo QT en respuesta a cambios en el intervalo RR con un alto riesgo de arritmias ventriculares y muerte súbita cardíaca (SCD), lo que podría explicarse parcialmente por la mayor heterogeneidad en la duración de la repolarización entre los ventrículos debido a diferentes tiempos de adaptación celular.

En estudios previos, se ha caracterizado la respuesta del intervalo QT a los cambios en el intervalo RR considerando la serie temporal del intervalo QT como la salida de un sistema cuya entrada es la serie temporal de los intervalos RR. Este sistema se modela con dos bloques secuenciales e invariantes en el tiempo: un bloque que representa la relación en estado estacionario entre el intervalo QT y el intervalo RR y se describe mediante una función típicamente no lineal y sin memoria; y el otro bloque representa la memoria del intervalo QT en respuesta a cambios en el intervalo RR y se describe mediante un filtro lineal que permite cuantificar la histéresis QT-RR. Este modelo QT-RR ha sido evaluado en diferentes escenarios, con un enfoque particular en la respuesta del QT a cambios abruptos en el RR, típicamente obtenidos de registros Holter. Sin embargo, estos tipos de cambios no siempre están presentes en los registros de ECG. Si se asume que el filtro lineal del modelo propuesto es un sistema de primer orden, este queda unívocamente caracterizado por su constante de tiempo, la cual, a partir de la teoría de control, puede medirse como el retardo entre una señal de entrada al sistema tipo rampa lineal y la señal también tipo rampa lineal retardada que se genera a la salida.

En este trabajo, se investigan las dinámicas de la relación entre los intervalos QT y RR extraídos de señales de ECG registradas durante pruebas de esfuerzo

(EST). Así, se consideran los cambios graduales en el intervalo RR durante la EST como la entrada al sistema y, con la base del modelo antes mencionado, se propone un método alternativo para estimar el tiempo de adaptación del intervalo QT. Los cambios graduales en el intervalo RR se identifican tanto en la fase de ejercicio como en la fase de recuperación de la EST. Normalmente, estas dos fases están precedidas, o seguidas en el caso de la recuperación, por una fase donde el intervalo RR permanece en un estado basal esencialmente estacionario.

Se propone cuantificar el tiempo de adaptación del intervalo QT como el retardo entre la serie temporal de los intervalos QT observados y una serie QT sin memoria estimada a partir de los intervalos RR observados en el ECG registrado durante una EST. Este retardo se evalúa en las fases de ejercicio y recuperación, por separado, aplicando tanto estimadores Laplacianos como Gaussianos de Máxima Verosimilitud. Se elige un modelo de regresión hiperbólico para estimar la serie QT sin memoria que caracteriza el intervalo QT según los valores observados del intervalo RR, ya que es el modelo que conduce al mejor ajuste en términos de error cuadrático medio entre los modelos de regresión probados. Los parámetros del modelo se estiman individualmente para cada paciente. Se definen tres ventanas de aprendizaje para estimar los parámetros del modelo en fases donde se puede suponer que el intervalo RR permanece prácticamente estacionario, es decir, sin experimentar ningún cambio en su tendencia: una ventana en cada una de las dos zonas basales y otra alrededor del pico de ejercicio. La última ventana mencionada, aunque cuestionable en términos de estacionariedad del intervalo RR, se selecciona para cubrir el mayor rango posible de valores de RR, garantizando así un mejor ajuste de la dependencia QT-RR. Para tener en cuenta la falta de estacionariedad en la ventana del pico de ejercicio, se proponen tres elecciones diferentes de la ventana y los valores de datos QT de ellas extraídos: (1) la ventana se centra en el pico de ejercicio, de modo que las dinámicas de la frecuencia cardíaca durante el ejercicio se compensen con las de la fase de recuperación; (2) sobre la misma ventana en (1) se modifican los valores de QT que se extraen de la ventana basándose en un retardo estimado en el ejercicio, haciendo uso de la primera elección de ventana en (1); (3) además de modificar los valores de QT como en la definición de la ventana (2), la posición de la ventana se cambia para incluir solo valores correspondientes a la fase de ejercicio donde la corrección de los datos es significativa, acabando justo en el pico de ejercicio.

Los métodos propuestos en esta tesis doctoral se evalúan primero técnicamente en conjuntos de datos que contienen señales ECG simuladas con dependencia QT-RR y retardo conocidos. Para este propósito, se ha generado un entorno de simulación que permite: (a) establecer un tiempo de adaptación

del intervalo QT definido por el usuario y (b) añadir componentes de ruido simulado con características similares a las del ruido muscular presente en las pruebas de esfuerzo y con diferentes relaciones señal-ruido, de modo que se pueda estudiar la robustez de los métodos frente a esta contaminación. Los resultados muestran que el tiempo de adaptación del intervalo QT se estima con mayor precisión cuando el cálculo de los parámetros del modelo se realiza utilizando la ventana con los datos de QT modificados y situada solo en la fase de ejercicio, es decir, con la ventana mencionada en la definición (3).

A continuación, se evalúa la capacidad clínica del parámetro tiempo de adaptación del intervalo QT estimado mediante el procedimiento propuesto en la fase de ejercicio, en la fase de recuperación, y como la diferencia entre estas dos. Esta evaluación permite estratificar a los pacientes con diferentes riesgos de sufrir enfermedad arterial coronaria (CAD) y predecir SCD o muerte por cualquier causa. Los resultados muestran que el retraso medido en la fase de ejercicio aumenta a medida que aumenta el riesgo de CAD, mientras que el retraso en la recuperación disminuye con el riesgo. Además, el retardo estimado en la recuperación es mayor en pacientes que han sufrido SCD que en aquellos que no. También el retardo en la recuperación es mayor en los pacientes fallecidos por cualquier tipo de causa que en los supervivientes.

Otro desafío estudiado a lo largo de esta tesis doctoral es la delineación del final de la onda T en pruebas de esfuerzo con ECG muy ruidosas, donde puede ocurrir una superposición entre la onda T y la onda P a medida que aumenta la frecuencia cardíaca durante la fase de ejercicio. Este fenómeno, junto con la mayor presencia de ruido inducido por el ejercicio, complica la delineación de las series de intervalos QT. Por lo tanto, se proponen diferentes métodos basados en dos técnicas de transformación espacial para mejorar la delineación de la onda T: (a) aplicando análisis de componentes principales, que maximiza la varianza de la señal; (b) aplicando análisis de componentes periódicos, que maximiza la periodicidad de los latidos de la señal. La mayor parte de estas características maximizadas se reflejan en la primera derivación transformada, por lo que la onda T se delinea solo en esta. Los resultados de la delineación con estos métodos se comparan con uno de los métodos basados en múltiples derivaciones, que consiste en delinear cada derivación individualmente y aplicar una regla para obtener una única marca final de delineación. La delineación del final de la onda T se evalúa en señales de ECG simuladas utilizando una marca de referencia medida sobre la misma señal cuando está contaminada con casi nada de ruido, y en registros clínicos utilizando la inversa de la potencia de la señal de intervalos QT observados, después de aplicarle un filtro paso alto, se usa como un sustituto de la calidad de la delineación. Tanto en los ECG

simulados como en los clínicos, se obtienen los mejores resultados cuando se delinea el final de la onda T con la primera derivación transformada después de aplicar el análisis de componentes periódicos, y por tanto es la técnica que se usa en los estudios clńicos.

A partir del análisis de los ECG clínicos de pacientes con CAD, se observa que el retraso entre la serie QT observada y la serie de QT sin memoria estimada no es constante, sino que se reduce en la zona de ejercicio a medida que se acerca el pico de éste. Además de la influencia de la frecuencia cardíaca en el intervalo QT, el sistema nervioso autónomo juega un papel en la modulación de la repolarización ventricular y su adaptación a la frecuencia cardíaca. Dicha modulación autonómica ocurre tanto directamente a través de la inervación autonóma del miocardio ventricular como indirectamente a través de los efectos sobre la frecuencia cardíaca. Basándonos en estudios previos, planteamos la hipótesis de que un aumento en la actividad simpática a medida que se acerca el pico de ejercicio, es decir, un aumento en los niveles de pre-estimulación de los β-adrenoceptores al acercarse al pico de ejercicio, podría explicar la reducción en el tiempo de adaptación del intervalo QT observado al final del ejercicio. Para estudiar la modulación autonómica del tiempo de adaptación del QT, el último capítulo de esta tesis doctoral propone un estudio *in silico* para investigar las dinámicas de la adaptación de la repolarización ventricular en respuesta a la estimulación β-adrenérgica, a nivel celular y tisular, así como en el ECG. Se estiman los tiempos de adaptación del intervalo QT en respuesta a los mismos cambios en el intervalo RR que en los ECG clínicos para diferentes patrones de estimulación β-adrenérgica y se comparan con los obtenidos en los registros clínicos. Se concluye que un patrón de estimulación β-adrenérgica variante en el tiempo reproduce mejor las características de adaptación del intervalo QT observadas en el análisis de los ECG clínicos.

Palabras clave: modelado QT-RR; tiempo de adaptación del intervalo QT; electrocardiograma; ECG simulada; delineació onda T; análisis de las componentes principales; prueba de esfuerzo; enfermedad de las arterias coronarias; muerte súbita cardiaca.

ACKNOWLEDGEMENTS

Antes de poner fin a esta etapa de montaña, me gustaría dedicarle unas palabras a las personas que han formado parte de este camino.

En primer lugar, a mis directores de tesis, Pablo y Esther, así como a Juan Pablo y Leif. Gracias por dejarme aprender a vuestro lado. Me siento privilegiada de haber podido adquirir conocimientos de grandes investigadores y, sobre todo, de grandes personas como vosotras. Esto también se refleja en el gran grupo que es BSICoS, y bendita suerte la mía de haber podido formar parte (o gracias a Carlos por acogerme para hacer el TFM). De este grupo me llevo una de las mejores etapas de mi vida, vivida sobre todo en el laboratorio 3.07: Carmen, Estela, con simplemente mencionaros creo que sabéis lo importantes que habéis sido en esta etapa. Diego y Pablo Armañac, nunca olvidéis lo grandes que sois y la pasión que le tenéis a este mundillo. Me llevo las risas, el buen ambiente y las miradas cómplices de estos años. Saúl, Rodrigo, a todos a los que he visto convertiros en doctores y a todas las personas que, bien de estancia o por trabajos universitarios, han disfrutado de este laboratorio, espero haberos transmitido la buena energía que habéis compartido, permitiendo vaciles varios :) También me gustaría dedicar unas palabras al resto de predocs con los que he compartido esta etapa. Gracias por fomentar las actividades sociales fuera de la universidad y por llevar más allá esa inquietud de "la vida después del doctorado".

Si acabas de llegar a este grupo de investigación, no te pierdas la hora del café. Es el ambiente donde más rápido vas a aprender, donde vas a conocer a tus compañer@s y donde tienes aseguradas unas risas cuando necesites un respiro en tu investigación; y esto es gracias sobre todo a seniors y a postdocs, que pueden ser "unos pesados" con el tema del running, que te animan a "hacer las cosas con miedo" o incluso pueden pedirte embutido de tu tierra.

A 500 km tengo a las personas que terminan de llenarme el corazón cada vez que las veo: mi familia y mis amistades. A mis amigos de siempre, Ismael,

Fran, Miguel Ángel y Fernando. Sacáis tiempo de donde no lo hay para seguir compartiendo momentos juntos y haciéndome ver que siempre estaréis. Espero que me dejéis un hueco en el pueblo para seguir compartiendo grandes vivencias juntos. También dedicarle unas palabras a esas amistades del instituto con las que he compartido las vivencias de esta etapa. Cómo no, a mi Pu**pandi, Alejandro, Irene, Arturo, Juangra y Marta. Os habéis llegado a hacer kilómetros e incluso superado miedos cuando más lo necesitaba. Aún alucino con vosotr@s. *Con permiso compañeros*, gracias chicas por contar entre nosotras para lo que sea. En este apartado de amistades no puedo olvidarme de vosotras, Lucía y Mercedes, por haber sido mi primera familia en vuestra tierra.

Para poner fin a esto y dejaros disfrutar de esta tesis, gracias mamá por hacernos ver que se puede hacer de tu hobby tu profesión, gracias papá por hacernos sacar el ingenio diariamente, y gracias a mis hermanas, Miriam y Ángela, por demostrarme que cuando una tiene pasión por conseguir algo, se consigue, aunque haya que intentarlo varias veces. Por último, a ti, Fer, gracias por convertir los momentos malos en buenos, y los buenos en extraordinarios.

CONTENTS

LIST OF ACRONYMS

ANS autonomic nervous system . . . 3
AF atrial fibrillation . . . 15
AP action potential . . . 4
APD action potential duration . . . 21
APDR action potential duration restitution . . . 20
AR autoregressive . . . 65
AV atrioventricular . . . 3
CAD Coronary artery disease . . . 14
COR Coronary angiography . . . 16
COR-LR low-risk COR . . . 99
COR-MR mild-risk COR . . . 99
COR-HR high-risk COR . . . 99
CVD cardiovascular disease . . . 1
CVDeath cardiovascular death . . . 100
DM2 type 2 diabetes . . . 99
ECG electrocardiogram . . . 6
ECG-LR low-risk ECG . . . 99
EST exercise stress testing . . . 12
HF high-frequency . . . 57
HRV heart rate variability . . . 8
Hyp hyperbolic . . . 40
$\mathcal{HZR}$ hazard ratio . . . 101

Iso isoproterenol . . . 142
ICD implantable cardioverter defibrillator . . . 18
IQR interquartile range . . . 100
Lin linear . . . 40
Log logarithmic . . . 40
LQTS long QT syndrome . . . 23
ML maximum likelihood . . . 42
MLE maximum likelihood estimator . . . 44
MLeads multi-lead wavelet-based delineation . . . 38
MN muscle noise . . . 56
Par parabolic . . . 40
PCA principal component analysis . . . 34
PDE partial differential equation . . . 142
pECG pseudo-ECG . . . 141
PDF probability distribution function . . . 43
QT_c corrected QT . . . 8
QTV QT variability . . . 19
RMS root mean square . . . 38
SA sinoatrial . . . 3
SCA sudden cardiac arrest . . . 15
SCD Sudden cardiac death . . . 8
SNR signal-to-noise ratio . . . 34
SR sinus rhythm . . . 57
SXscore SYNTAX score . . . 24
SXscore-LR low-risk SXscore . . . 100
SXscore-MR mild-risk SXscore . . . 100
SXscore-HR high-risk SXscore . . . 100
TL1 first transformed lead . . . 36
TWA T wave alternans . . . 20
VCG vectorcardiogram . . . 10

CHAPTER 1

INTRODUCTION

1.1 Motivation

The number of deaths attributable to cardiovascular disease (CVD) around the world is projected to rise from an estimated 18.9 million in 2020 to more than 22.2 million in 2030 and 32.3 million in 2050 according to the World Heart Federation. CVD is one of the leading causes of death worldwide, accounting for over 32% of all global deaths, and Europe is not exempt from this alarming trend. The *European Research Area Network on Cardiovascular*

Diseases recognized the need for prevention strategies. In 2019, the Strategic Research Agenda for CVD was published, underscoring the importance of early disease detection using predictive markers. CVD encompasses a wide range of conditions affecting the heart and blood vessels, whose unpredictability can lead to sudden and unexpected deaths. The economic and social consequences of CVD are significant. The cost of CVD to the European Union economy is currently 210 billion euros annually. These statistics justify any effort to implement cost-effective, accessible strategies that reduce the incidence of CVD.

1.2 The Heart

1.2.1 Anatomy

The heart is the central and vital organ of the cardiovascular system. It is responsible for pumping blood into the pulmonary circulation (from the right side of the heart) and the systemic circulation (from the left side of the heart) in order to deliver oxygen and nutrients to metabolically active tissue. Anatomically, the structure of the human heart is characterized by several key components, which are represented in Fig. 1.1:

Chambers and valves: the heart consists of four chambers, with the left and right atria located above the left and right ventricles, and four valves to manage the proper direction of blood flow during the heart's contractions. The right atria receive oxygen-poor blood, which flows into the right ventricle through the tricuspid valve. Then, the right ventricle pumps the blood into the pulmonary system through the pulmonary valve. The oxygenated blood returns to the heart, entering the left atrium and passing through the mitral valve to reach the left ventricle. Finally, the blood is injected into the systemic circulation through the aortic valve.

Cardiac muscle: The myocardium consists of specialized muscle cells called cardiomyocytes and other cell types including fibroblasts and endothelial cells. The cardiomyocytes along the ventricular wall can have different properties depending on their location in the subendocardium (inner region), midmyocardium (middle region), and subepicardium (outer region). The cardiomyocytes contract and relax rhythmically, which allows propelling the blood to the circulatory system. A double-layered membrane called the pericardium surrounds the heart. This layer acts as a protective sac and helps to lubricate the heart to prevent friction with surrounding tissues.

Electrical conduction system: The effective pumping of the heart is ultimately

dependent on its electrical conduction system, which coordinates its rhythmic contractions. The cardiac conduction system includes the sinoatrial (SA) node, atrioventricular (AV) node, bundle of His, and Purkinje fibers. The SA node, which acts as a self-depolarizing pacemaker located in the right atrium, initiates the cardiac cycle. Its autonomous function is modulated by the autonomic nervous system (ANS), with the sympathetic activation accelerating the heart rate, and the parasympathetic activation decelerating it. The electrical signal travels from the SA node through the atria, is delayed briefly at the AV node, and later travels through the bundle of His, which subdivides into two bundle branches, and, finally, through the Purkinje fibers to ensure an effective heart function. This specialized electrical conduction system allows for the synchronous contraction and relaxation cycles of the left and right parts of the heart and the sequential contraction and relaxation of the atria and ventricles. These two movements, commonly known as systole and diastole, are critical in maintaining an efficient heart performance. A schematic of the electrical conduction system of the heart is represented in Fig. 1.2.

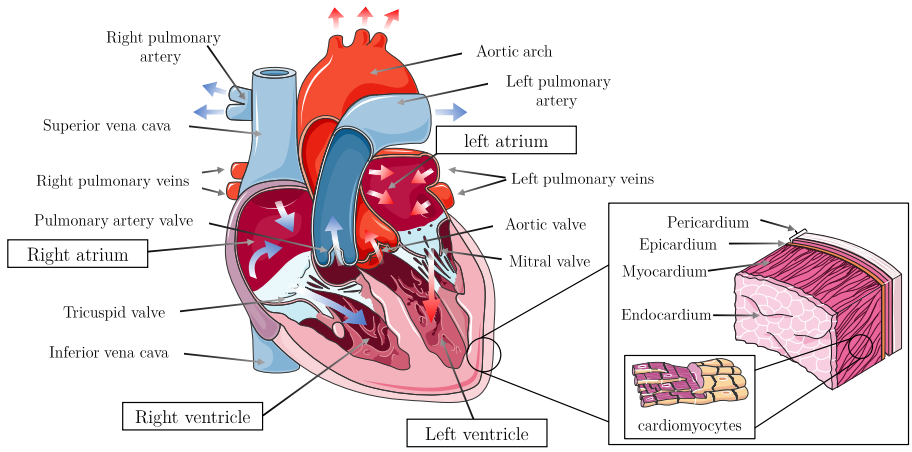

Figure 1.1: Schematic of the structural anatomy of the heart and the blood flow in the frontal plane. Adapted from `https://smart.servier.com/`.

1.2.2 Electrophysiology

The cardiomyocytes are enclosed by a semipermeable membrane composed of a lipid bilayer with various proteins, including ion channels, transporters, receptors, and enzymes. This membrane serves as a barrier separating the

intracellular and extracellular spaces of the muscle cell. The voltage difference between the intracellular and extracellular regions of the myocyte is known as the membrane potential, which is typically negative at rest, representing the electrical inactivity of the cell. The resting membrane potential is in the range -65 to -80 mV for atrial myocytes and -90 to -80 mV for ventricular myocytes.

The electrophysiology of the myocardium is a complex process that involves various ions, including calcium (Ca^{2+}), chloride (Cl^{-}), sodium (Na^{+}), and potassium (K^{+}). These ions are more abundant in the extracellular space, except for K^{+}, which is more abundant in the intracellular space. The movement of these ions through the ion channels located in the membrane of the cardiac cells is a passive procedure controlled by two main forces: the electrical gradient, which reflects the difference in potential between the interior and the exterior of the cell, and the chemical gradient, related to the difference in the ion concentration between the intracellular and extracellular spaces. In contrast, pumps and exchangers actively move ions against their gradients, requiring energy derived from ATP hydrolysis or based on the electrochemical gradients. These ion movements are influenced by factors such as changes in ion concentrations inside and outside the cell, alterations in membrane potential, and the presence of specific ligands.

The cardiac cellular action potential (AP) describes the dynamic changes in the membrane potential and the ionic flow of a cell. The AP consists of a depolarization phase (activation) followed by a repolarization one (recovery), divided into five distinct phases (labeled as phases 0 to 4). A diagram showing a cardiac AP and the corresponding ion flow is shown in Fig. 1.2.

Phase 0 - Rapid depolarization: This phase is characterized by a rapid increase in the membrane potential associated with the opening of the fast inward Na^{+} channels. This fast sodium current I_{Na} into the cell produces a rapid positive membrane potential.

Phase 1 - Early repolarization: This phase is characterized by a transient repolarization. The fast Na^{+} channels become inactivated and an outward K^{+} current I_{to} is produced. The result is a reduction in the membrane potential to 0 V, which is represented as a "notch" in the AP morphology.

Phase 2 - Plateau: The membrane potential is maintained close to 0 V by a balance between the inward movement of Ca^{2+} through the L-type Ca^{2+} channels (I_{CaL} current), and the outward movement of K^{+} through slow delayed rectifier potassium channels (I_{Ks} current). This equilibrium is crucial to ensure the heart's contraction and efficient blood pumping. The concentration of Ca^{2+} ions in the cytosol increases due to the movement of Ca^{2+} from the interstitial

fluid and from the sarcoplasmic reticulum, ultimately triggering the heart's contraction. Therefore, the electrical activation of the cardiomyocytes leads to their mechanical contraction through the above described excitation-contraction coupling process. The strength of the contraction is directly related to the myocyte's Ca^{2+} transient. Analogously, cardiac relaxation and ventricular refilling are associated with a decline in the cytosolic Ca^{2+} concentration.

Phase 3 - Rapid repolarization: In this phase, the membrane potential returns to the resting membrane potential. This change is fundamentally produced by the rapid delayed rectifier K^+ current I_{Kr} and the inwardly rectifying K^+ current I_{K1}. The L-type Ca^{2+} channels become closed.

Phase 4 - Slow diastolic depolarization or rest: In this phase, the membrane potential is stable (for atrial and ventricular myocytes) or presents a slow depolarization (for cells with spontaneous activity). The cell is prepared for the next AP cycle. The Na^+/K^+ ATPase pump plays a crucial role in maintaining this state by actively transporting Na^+ ions out of the cell and K^+ ions into the cell.

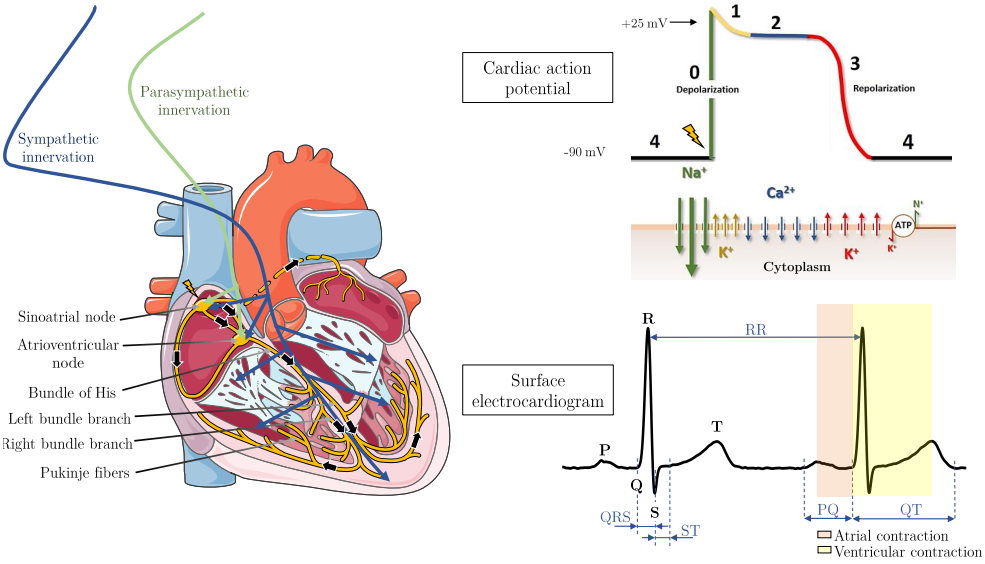

Figure 1.2: Left: schematic of the electrical conduction in the heart, from the SA node to the Purkinje fibers. Autonomic nervous system innervation by the sympathetic and parasympathetic nerves is shown too. Top right: schematic of a ventricular cell AP and the ion flow involved in each AP phase. Bottom right: schematic of two consecutive beats from an ECG lead with their characteristic waves and intervals. Adapted from `https://smart.servier.com/` and `https://studmed.uio.no/elaring/fag/hjertesykdommer/en/ecg/`.

1.2.3 Autonomic nervous system

The ANS regulates cardiac functions such as the heart rate, atrial and ventricular refractoriness, conduction, contractility, and blood flow. The ANS has two branches: the sympathetic and the parasympathetic systems. The sympathetic branch controls the human body's reaction to situations of emergency and during exercise (known as the "fight-or-flight" response). The parasympathetic branch regulates restful conditions and facilitates the functions of the internal organs, such as digestion [1].

The periodicity of the SA node discharge is controlled by a balance between both autonomic limbs. Sympathetic stimulation increases heart rate and myocardial contractility, while the parasympathetic nervous system exerts antagonistic effects on the regulation of heart function, reducing the heart rate and the AV nodal conduction, and causing vasorelaxation. The cardiac ANS plays an essential role in cardiac arrhythmogenesis, with certain autonomically-mediated alterations in cardiac electrical activity being able to generate cardiac arrhythmias.

The parasympathetic nerves release acetylcholine, while the sympathetic nerves release norepinephrine. These neurotransmitters modulate the ion flows described previously and mediate the AP propagation through the atria, the conduction system, and the ventricles of the heart. For example, in ventricular myocytes, the activation of the sympathetic system leads to the release of norepinephrine, which binds to β-adrenergic receptors and stimulated them. This activates signaling pathways that cause the phosphorylation of cellular substrates like the I_{CaL}, the I_{Ks} and others [2], which altogether modulate the AP characteristics.

1.3 Electrocardiogram

The cardiac cycle relies on the recruitment of the AP of all cardiomyocytes. The electrical activity of these cells triggers their mechanical contraction. The electrical activity of the heart can be easily recorded on the surface of the chest wall by placing a set of electrodes via an electrocardiogram (ECG). The ECG is a cost-effective and noninvasive tool used for clinical diagnosis that provides valuable information on the health of the heart [3]. The voltage difference measured between a pair of electrodes is known as a lead. The magnitude of the electrical signal generated by the depolarizing muscle is directly proportional to the corresponding muscle mass.

1.3.1 Waveforms

The cardiac cycle, known as heartbeat, is described in the ECG by a series of waves whose morphology and timing convey information. Their well-recognized pattern and nomenclature are presented in Fig. 1.2. Each heartbeat in the ECG is normally composed of a P wave, a QRS complex, and a T wave. The amplitude of a wave is measured with respect to the ECG baseline level, commonly defined as the isoelectric line.

The P wave reflects the depolarization of the right and left atria. The duration of the P wave is typically less than 120 ms, which reflects slow cell-to-cell propagation of the electrical activity in the atria. Its amplitude is usually less than 300 μV, with a positive polarity and monophasic morphology in most leads. From the end of the P wave to the onset of the QRS complex, the electrical activity is absent, reflecting an isoelectric time window with slow propagation of the electrical activity through the AV node.

The QRS complex is generated from the summation of the right and left ventricular AP during their electrical depolarization before mechanical contraction. The QRS complex has three deflections: the first negative deflection is denoted as the Q wave, the first positive ones is called the R wave, and the following negative deflection is denoted as the S wave. The normal heartbeat lasts for about 70-110 ms. Its amplitude is the largest one of all the ECG waveforms, sometimes reaching 2-3 mV. This higher amplitude of the QRS complex with respect to the P wave reflects a greater myocardial mass of the ventricles when compared to the atria and a much more rapid spread of the electrical depolarization due to the high speed of the ventricular conduction system. The repolarization of the atria is hidden within the QRS complex.

After the QRS complex, there is a brief time interval in which no net current is flowing because the cells are all at nearly the same potential of phase 2 and, thus, the ECG amplitude returns to the isoelectric line. This time interval is known as the ST segment. This segment starts at the end of the S wave (the J point) and proceeds almost horizontally until it curves into the T wave, which corresponds to the onset of ventricular repolarization. Changes in the ST segment, such as elevation, depression, or steepness, often indicate the presence of some underlying cardiac conditions.

Lastly, the T wave represents the repolarization of the ventricles. The T wave is longer in duration but lower in peak magnitude than the QRS complex. The repolarization normally occurs in the ventricular muscle between 250 to 350 ms after depolarization. The temporal location of the T wave in the ECG heartbeat strongly depends on heart rate and tends to become narrower and closer to

the QRS complex at higher rates. This rate dependence does not apply to the P wave or the QRS complex [3]. The normal T wave has a smooth morphology and a single positive peak in most leads. The T wave is sometimes followed by another slow wave, the U wave, whose origin is unclear. Some studies have suggested the presence of after-potentials on some cardiac APs as a possible explanation for the genesis of the U wave [4, 5].

The ECG contains other commonly measured time intervals. In this thesis, the RR and QT intervals are of particular interest.

The RR interval represents the time elapsed between two successive R waves of the QRS complex, and its inverse is the heart rate. The RR interval is a function of the intrinsic properties of the SA node as well as ANS influences. This interval is used to characterize abnormal heart rhythms, known as arrhythmias, as well as to study heart rate variability (HRV). During rest, sleep, or emotional tranquility, heart beats at a rate of about 60-75 beats per minute [1]. Arrhythmias can occur when the electrical impulses become irregular, too fast (tachycardia) or too slow (bradycardia). The electrical and mechanical efficiency and performance of the heart are significantly influenced by factors such as family history, personal health history, and lifestyle choices.

The QT interval represents the total duration of ventricular depolarization and repolarization, measured from the onset of the QRS complex to the end of the T wave. The QT duration is inversely related to the heart rate, i.e., the QT interval increases at slower heart rates and decreases at higher heart rates. At high heart rates, the P wave may merge with the T wave, causing the T wave endpoint and P wave onset to become indistinct. As a result, eventually it may become difficult to determine the T wave endpoint. In a resting state, the normal QT interval is less than 400 to 440 ms, with women typically having a slightly longer QT interval than men. However, to determine whether the QT interval is within normal limits, it is necessary to adjust for the heart rate, and it is referred to as the corrected QT ($\mathrm{QT_c}$) interval. Prolongation of the QT interval has been observed in various cardiac disorders associated with a higher risk of ventricular arrhythmias and Sudden cardiac death (SCD). The $\mathrm{QT_c}$ duration has traditionally been calculated using the Bazett's formula:

$$\mathrm{QT}_c = \frac{\mathrm{QT}}{\sqrt{\mathrm{RR}}}, \tag{1.1}$$

where RR is expressed in seconds. This form of correction constitutes a particular case of correction based on a parabolic relation between the QT and RR interval, see Sec.2.5. The Bazzet's formula has been shown to lead to undercorrection at slower heart rates and overcorrection at faster heart rates in some studies.

Other formulas, such as the Fridericia's formula, have been suggested to be better suited [6]. To obtain even more precise QT_c interval measurements, other studies have suggested to use formulas personalized for each subject, since the QT-RR dependency can be subject-dependent [7].

Finally, the PQ interval of the ECG represents the distance between the onset of the P wave and the onset of the QRS complex. In other words, it is the time interval from the onset of atrial depolarization to the onset of ventricular depolarization which includes the delay at the AV node. The length of the PQ interval is slightly dependent on heart rate, with normal ranges between 120 and 200 ms.

Alterations in the magnitude, duration and/or orientation of any PQRST component may reflect physiological and/or pathological changes in cardiac structure, function or neural control.

1.3.2 Leads

The ECG is typically recorded with a multiple-lead configuration and presents different characteristics depending on the location of the recording electrodes. Each lead represents the movement of the electrical waves through the heart projected on a different axis, thus offering a specific spatial perspective of the heart's electrical activity. If a lead is set up in such a way that the depolarizing current moves towards that lead while the repolarizing current moves away from that lead, depolarization and repolarization waves with positive and negative polarity with regards to the isoelectric line are produced, respectively [3].

There are two main lead types: unipolar or bipolar leads. A so-called unipolar lead reflects the voltage variation of a single electrode and is measured with respect to a reference (commonly called the central terminal) whose voltage remains almost constant throughout the cardiac cycle. A bipolar lead reflects the voltage difference between two electrodes.

The number of electrodes attached to the body surface depends on the clinical information that is of interest. The two lead systems that have received the most attention are the standard 12-lead ECG and the orthogonal lead system, which are described in the following.

Standard 12-lead ECG: A standard 12-lead ECG is recorded by placing 10 electrodes on the body surface. It contains a combination of three different lead configurations: bipolar limb leads, augmented unipolar limb leads and unipolar precordial leads. The first two configurations examine the heart in a frontal plane while the last one does that from the transverse plane perspective.

The three bipolar limb leads are denoted I, II, and III and are obtained by measuring the voltage difference between the left arm, the right arm, and the left leg. These three electrode positions can be viewed as the corners of a triangle ("Einthoven's triangle") with the heart at its center (see the left representation of Fig. 1.3). The augmented unipolar leads (aVF, aVL, and aVR) use the same electrodes as the bipolar limb leads, but are defined as the voltage differences between one corner of the triangle and the average of the remaining two corners (see the central representation of Fig. 1.3). The six precordial leads, by convention labeled from V1 to V6, are unipolar leads positioned on the front and the left side of the chest, whose central terminal, named "Wilson central terminal", is defined as the average of the voltages measured on the right and left arms, and the left leg (see the right representation of Fig. 1.3). Leads V1 and V2 face the surface of the right ventricle, V3 and V4 face the anterior wall of the left ventricle, and V5 and V6 face the lateral wall of the left ventricle [3].

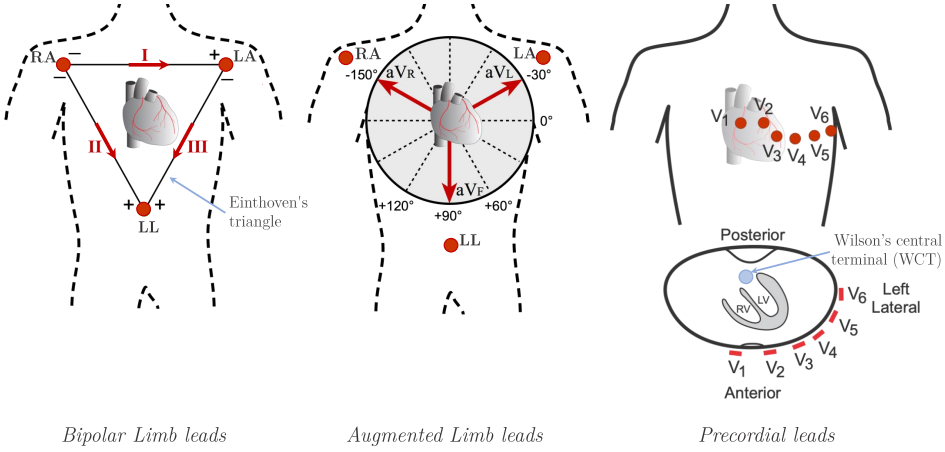

Figure 1.3: Electrode placement to obtain the bipolar (left panel), augmented (middle panel) and precordial (right panel) leads. Adapted from `https://cvphysiology.com/`.

Orthogonal ECG leads: An orthogonal lead system reflects the electrical activity as a three-dimensional loop together with its projection onto the XY-, XZ-, and YZ-planes. The loop is traced out by the tip of the vector that describes the dominant direction of the electrical wavefront during the cardiac cycle, so this particular type of recording is referred to as a vectorcardiogram (VCG). The most widely used orthogonal lead system, known as the Frank lead system [8], is obtained as linear combinations of 7 electrodes positioned on the chest, back, neck, and left foot. The resulting leads X, Y and Z view the heart from the left side, from below, and from the front.

The 12-lead ECG is the most widely used lead system in the clinical routine, since this lead system offers information on waveform morphology and well-established criteria for its interpretation have been defined, while the VCG provides a time-varying description of how the magnitude and direction of the dominant vector change [3]. Mathematical transformations have been proposed to bridge both lead configurations. For example, the inverse Dower matrix [9] and the more advanced Kors matrix [10] relate the standard and orthogonal lead configurations, improving the understanding of cardiac activity, and therefore the diagnostic potential of ECGs.

It is important to realize that the polarity, amplitude, and morphology of the individual ECG waves are significantly influenced by the position of the electrodes on the body and by their location in relation to the heart. This aspect is crucial for interpreting ECG data and assisting clinicians in diagnosing certain heart conditions by analyzing specific leads. For instance, this could be considered when assessing if there are damaged areas in the cardiac muscle, irregular blood flow, or any abnormal patterns of electrical activity that may increase the likelihood of arrhythmias. In this regard, the integration of biomedical signal processing can improve the diagnostic capabilities by extracting relevant clinical information from ECGs using signal processing techniques. This can aid clinicians when taking diagnostic decisions, customized to individual cases and informed by the processed results.

1.3.3 Noises and interferences

An acquired ECG is normally contaminated by noises from both technical and biological origin. The presence of noise complicates the accurate analysis of the ECG signal, potentially leading to errors in the automated algorithms and the clinical diagnoses. Among the different noises and artifacts encountered in the ECG, below is a list of some of the most common sources of noncardiac noise [3, 11].

Baseline wander is a low-frequency activity in the ECG that interferes with the signal analysis, leading to inaccurate clinical interpretations due to the not well-defined isoelectric line. Often induced by exercise, baseline wander can result from a variety of noise sources, including respiration, body movements, and poor electrode contact. Its magnitude may exceed the amplitude of the QRS complex, and its spectral content ranges typically between 0.05 and 1 Hz, although it may contain higher frequencies during strenuous exercise as the breathing rate increases.

Electrode motion artifacts are primarily caused by skin stretching, altering

the skin's impedance around the electrode. This low-frequency noise represents a significant challenge due to the considerable spectral overlap with the PQRST complex (1 to 10 Hz). In the ECG, these artifacts are manifested as high-amplitude waveforms, which are sometimes mistaken for QRS complexes. Its presence is more problematic in ambulatory ECG monitoring, where they represent the main source of falsely detected heartbeats.

Powerline interference comes from improper grounding of ECG equipment and interference from nearby equipment. The exposure to those electromagnetic fields introduces frequency noise of around 50-60 Hz.

Electromyographic noise, or muscle noise, results from the electrical activity of skeletal muscles during contraction, commonly observed in ECGs during ambulatory monitoring or exercise stress testing (EST). Intermittent or more stationary in nature, their frequency components can considerably overlap with those of the QRS complex and also extent into higher frequencies with a bandwidth between 20 and 1000 Hz. Thus, removal of muscle artifacts without introducing distortion is quite challenging.

Respiratory activity influences ECG measurements through heart rate and beat morphology. Chest movements, changes in heart position, and alterations in lung conductivity lead to beat-to-beat variations in morphology during a respiratory cycle, modifying the morphology of the dominant direction of the electrical wave propagation vector. Although variations in QRS amplitude represent an undesirable signal characteristic, it may be exploited for estimation of the respiratory frequency.

To minimize the effects of the above described noises and interferences, robustly ECG acquisition systems are designed to try to mitigate the introduction of noise through various devices and resistances. Also, the deployment of high-quality electrodes can prevent voltage drops across the electrode-electrolyte interface.

1.3.4 ECG recordings

Nowadays, the most common ECG recordings in clinical applications are resting ECG, ambulatory ECG monitoring, and EST, being indispensable tools to facilitate accurate diagnosis, risk stratification, and personalized patient cardiovascular care. While ambulatory monitoring is designed to capture daily cardiac electrical activity and transient abnormalities, EST evaluates the heart under controlled physical stress. These types of ECG recordings are briefly described in the following [3].

Resting ECG is one of the most widely used diagnostic tests in the clinical routine. The standard 12-lead ECG is recorded for 10 s in conditions that are favorable from a signal quality perspective since the patient is at rest in the supine position. The brief recording time limits the significance of the test to heart problems of a permanent nature [3].

Ambulatory ECG monitoring, also called Holter monitoring, is a continuous recording of the electrical activity of the heart over an extended period, typically ranging from 24 to 48 hours. This method uses a portable device equipped with multiple leads, typically two or three, attached to the patient while performing his/her routine activities [12]. This noninvasive, continuous monitoring is useful for diagnosing various cardiac conditions, including arrhythmias, syncope, unexplained chest pain, and transient or infrequent cardiac problems that could be missed during traditional physical examinations or resting ECGs. This registry is also used to assess patients on antiarrhythmic drugs or patients at high risk of SCD after myocardial infarction. In some devices, there is the so called *event button*, which can be pressed by the patient whenever a symptom occurs to facilitate linking symptoms to arrhythmic events. Once the patient has returned the device to the hospital, the recorded ECG is analyzed by a physician. The extended duration and large data generated by Holter recordings usually requires the application of signal processing techniques for efficient analysis and interpretation. Moreover, these signals are susceptible to external noise, such as electrical interference and movement artifacts [3].

Exercise ECG stress testing is a common procedure used to evaluate the heart's ability to cope with increased myocardial oxygen demand. The test is typically performed on a treadmill or cycle ergometer and involves gradually increasing exercise workload, speed and/or slope, while monitoring the 12-lead ECG. The recovery period post-exercise is also recorded because it can help to determine if the ECG returns to its basal state before exercise. There are different stress testing protocols. Most protocols include a resting phase, an exercise phase, and a recovery phase [13, 14]. The two most widely used methods are maximal or submaximal exercise tests. In these two methods, the patient attains his/her highest or 85%-90% of his/her theoretical highest heart rate, which is calculated based on the age and physical condition [13]. The test concludes when the patient reaches a predefined maximum heart rate, experiences fatigue or symptoms such as chest pain and shortness of breath, or when abnormal ECG changes appear. The general response to exercise is evaluated based on maximum workload, maximum heart rate, ECG changes, blood pressure, and respiratory rate. Signal processing techniques, especially during high workloads, are crucial for accurate measurements of the heart's

electrical activity due to baseline wander and muscle noise affecting the quality of the signal. The stress test aids in assessing whether the blood supply to the heart's coronary arteries is sufficient to cover the increased demand for oxygen during exercise. It can help diagnose angina pectoris and identify patients who may have experienced undiagnosed episodes of silent ischemia. The test can also reveal abnormalities in patients with severe Coronary artery disease (CAD) who may present normal resting ECGs. For a detailed clinical interpretation of EST, please refer to [13].

1.4 Coronary Artery Disease

CVD comprises a number of heart and blood vessel diseases, including CAD (which can lead to myocardial infarction, also called heart attack), elevated blood pressure (hypertension), and cerebrovascular disease (including stroke). Currently, the prevalence of CVDs is increasing due to several factors such as the obesity epidemic, high blood pressure, and a significant increase in type 2 diabetes. The most important modifiable risk factors associated with CVDs are smoking, stress, sleep quality, physical inactivity, unhealthy diet and alcohol. Ethnic background, age, gender and family history of CVD are nonmodifiable risk factors that can also exert influence.

1.4.1 Concept

CAD, also called coronary heart disease, is the most common type of heart disease. It occurs when fatty plaque, which is an accumulation of cholesterol and other substances, builds up in the walls of the heart's arteries, a condition known as *atherosclerosis*. This narrowing of one or more coronary arteries results in a reduction or block of blood flow to the cardiac muscle, causing a deficiency of oxygen-rich blood in the myocardium and reducing the elasticity of the vessel wall. These alterations may cause chest pain, myocardial ischemia, or a heart attack. Over time, CAD can also lead to heart failure and arrhythmias due to the induced mechanical and electrical heart alterations [15–19]. Sometimes, the plaque can break or rupture and the body attempts to repair it by forming a blood clot over it, named *thrombus*. The blood clot can completely block blood flow and cause a heart attack.

Some people may not experience symptoms until they are on the verge of a serious cardiac event. However, a common symptom of CAD is chest pain known as *angina*. It occurs when the heart needs more blood and oxygen than

the amount it is getting, for example during exercise or stressful situations, because the demand for oxygen becomes greater than the supply of oxygen due to narrowed coronary arteries. Additional symptoms may be palpitations, shortness of breath, and weakness. Other symptoms of CAD may be experienced, particularly for women, elderly, and/or with diabetes.

1.4.2 Cardiac arrhythmogenesis and sudden cardiac death

An irregular generation or propagation of the electrical pulse can develop into an arrhythmia, which, depending on its location, is classified as supraventicular or ventricular. Supraventricular arrhythmias occur in structures above the ventricles, mainly the atria, and some examples are supraventricular tachycardia or paroxysmal supraventricular tachycardia, atrial fibrillation (AF), atrial flutter, and supraventricular premature contractions. Ventricular arrhythmias occur in the ventricles, as its name implies, and include ventricular tachycardia, ventricular fibrillation, and premature ventricular contractions.

Arrhythmias can be congenital or can be generated due to some of the above mentioned risk factors. The presence of symptoms depends on the severity, frequency, duration, and type of arrhythmia. The most commonly used test to diagnose an arrhythmia is Holter monitoring. Often, the first step to treat an arrhythmia is the administration of antiarrhythmic drugs, for example, digitalis, $\beta-$blockers, and calcium channel blockers. Other treatments including transcatheter interventions, implantable devices, and surgery are required in severe cases.

SCD is defined as unexpected, nontraumatic death occurring within 1 hour of the onset of an abrupt change in clinical status and loss of consciousness or, if unwitnessed, within 24 h of last being seen alive. By definition, a patient with SCD does not survive. When the patient survives, the event is termed aborted SCD or sudden cardiac arrest (SCA) [3, 20].

Although unexpectedness is a key feature of SCD definition, much of the progress that has been made to date in profiling risk of SCD has been based on clinical markers, which primarily identify the extent of disease either at a myocardial or a vascular level [21, 22]. For example, the initiation and progression of disease in the coronary arteries, followed by the development of myocardial scarring/fibrosis, transition of vascular lesions, initiation of acute coronary syndromes and, finally, acute arrhythmogenesis is a typical cascade of pathophysiology that leads to SCD [2]. Indicators such as myocardial scarring revealed by cardiac magnetic resonance imaging and left ventricular volumes are emerging as markers of potential interest [23, 24].

CAD is the most common underlying substrate of SCD, which is frequently due to ventricular arrhythmias, from ventricular tachycardia to ventricular fibrillation [25]. Ventricular fibrillation is a condition characterized by uncoordinated electrical impulses due to the division of the cardiac impulse along multiple pathways, which causes rapid and ineffective ventricular contractions. Enhanced repolarization heterogeneity can contribute to increase the risk for SCD. Today, SCD remains a significant public health problem and accounts for 15-20% deaths in Western societies [26].

1.4.3 Diagnosis and treatment

Apart from the family medical history, some of the tests used to diagnose CAD, and determine the location and severity of the coronary occlusion before treating it, include:

- A resting standard 12-lead ECG recording to identify an abnormal heartbeat or damage to the heart muscle.
- EST to evaluate the heart in a stress situation, which may be complemented with nuclear imaging. According to *2019 ESC Guidelines for the diagnosis and management of chronic coronary syndromes* [27], EST may be considered in case of suspected CAD. Diagnostic imaging tests may be used to clarify the diagnosis of obstructive CAD. ST-segment changes evaluated from the ECG can add to other clinical indices like exercise tolerance, arrhythmias or blood pressure response.
- Echocardiogram to assess mechanical heart function. It can show the blood flow through the heart's chambers and valves and the vessels. The evaluation of ventricular function and the presence of regional wall motion abnormalities is used in the diagnosis of acute coronary syndrome, while wall thickening is preferred to locate infarcted myocardium [28].
- Coronary angiography (COR) to test the circulation through the coronary arteries. In this procedure, a special dye or contrast medium is injected through a small tube (catheter) to evaluate the diameter of the lumen (stenosis). Although this technology identifies structural changes in coronary arteries with an acceptable degree of accuracy, its value is limited by the fact that identification of the structural abnormality does not reveal the vulnerability of plaques or specific markers of arrhythmic risk. Repeated exposure to radiation over time is also considered a limitation of this as a screening approach [2].

The degree of stenosis is reported as the estimated percentage of lumen reduction of the most severely narrowed segment compared to the adjacent angiographically normal vessel segment, seen in the x-ray projection where the stenosis is more severe. In some cases, the area stenosis may be greater than the diameter stenosis, as the lumen is assumed to be circular, whereas the lumen is usually eccentric. In general, four categories of lesion severity can be assigned:

1. Low, narrowing <50%.
2. Mild or moderate, stenosis between 50% and 75%.
3. High or severe, stenosis between 75% and 95%.
4. Total occlusion.

The treatment of CAD usually begins with lifestyle changes and/or medications that help the heart work more efficiently and increase the blood flow to the heart muscle. Nevertheless, an interventional procedure may be required if symptoms are not controlled or the artery narrowing is too large. Interventional procedures include the following:

- *Balloon agioplasty*: a small balloon is inflated within the narrowed portion of a blocked artery, pushing the plaque against the artery walls and increasing the blood flow to the heart.
- *Percutaneous coronary intervention*: this technique, formerly known as angioplasty with a metallic mesh tube (stent), is delivered on an angioplasty balloon to the narrowed portion of an artery to permanently support the artery walls and increase the blood flow. The stent can be coated with medication to prevent an overgrowth of the artery lining that can occur as a reaction to stent implantation.
- *Bioresorbable vascular scaffold*: a nonmetallic mesh tube that is delivered on an angioplasty balloon to treat a narrowed artery, similar to a stent, but it slowly dissolves once the blocked artery can function naturally again and can stay open on its own. This is the latest advance in CAD therapy.
- *Coronary bypass surgery*: this intervention uses a healthy blood vessel taken from the chest, leg, or arm to redirect the flow of blood around the area of blockage.

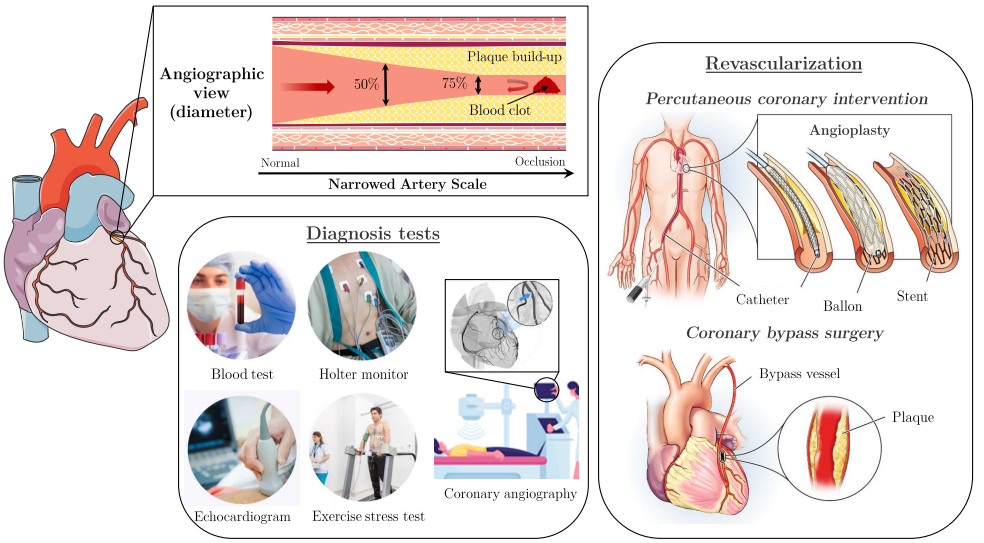

Figure 1.4: Infographic about coronary obstruction, the current diagnostic tests and risk assessment, and the most common treatments for a severe obstruction.

The principal CAD concepts explained in this section are summarized in Fig. 1.4.

The most common and severe complications of CAD are myocardial infarction, which occurs when the heart muscle does not receive an adequate amount of oxygen and the damaged tissue dies, and SCD. To prevent the occurrence of SCD, implantable cardioverter defibrillators (ICDs) are implanted to treat arrhythmias. ICDs improve survival in CAD patients with symptomatic heart failure and left ventricular ejection fraction less than 30% to 35%. Unfortunately, more than 70% of SCDs due to CAD occur in individuals with left ventricular ejection fraction greater than 35% who do not qualify for ICDs [29]. The primary prevention ICD implantation is indeed associated with lower mortality in CAD, as well as in other pathologies like dilated cardiomyopathy, with its benefits being less clear in patients with nonischemic heart failure [30]. In any case, ICDs are invasive and expensive devices. Thus, developing less expensive and noninvasive tools to aid in risk assessment in the context of CAD is of great social and technological interest. In this regard, the ECG is a cheap and noninvasive technology, widely used in the diagnosis, prognosis and treatment of CAD, myocardial infarction and arrhythmias [3, 31].

1.4.4 Risk assessment from the ECG

Despite the availability of direct imaging modalities, such as echocardiography, nuclear scanning, computerized tomography, and magnetic resonance imaging, the ECG remains the most commonly used cardiovascular diagnostic tool due to its wide availability, low cost, and rapid interpretation [32, 33].

Over the last years, several ECG-derived markers have been proposed to assess CAD severity and characterize the spatial and temporal heterogeneities of ventricular repolarization [31]. These markers may be essential to identify patients who are at risk for events that trigger fatal outcomes [34, 35] and may help to optimize the treatment [36, 37]. Some commonly cited markers in the literature are briefly presented below.

The most conventional ECG index for arrhythmic risk prediction is the QT interval duration [38]. Since the duration of the QT interval is largely dependent on the corresponding heart rate, the QT_c interval has been used to standardize the measurements and the clinical capacity of the QT_c interval has been studied in different contexts. A variety of heart rate correction formulas to compute the QT_c interval has been proposed in the literature to compare QT measurements at different heart rates [39]. The QT_c interval has been shown to be longer in patients with obstructive coronary artery disease (COR shows more than 50% diameter stenosis) than in those without it, with such a prolongation increasing with the severity of the disease [40]. Also, prolongation of the QT interval or of the QT_c interval has been recognized in some studies as a marker of arrhythmic risk [35, 41]. In particular, a longer QT_c interval has been observed in SCD patients with CAD than in CAD patients with no history of SCD [42].

QT variability (QTV) refers to beat-to-beat temporal variability of the QT interval due to direct and indirect effects of the ANS activity, that is, the ANS action on the ventricular myocardium and on the SA node, respectively [43]. QTV can be quantified in the time or the frequency domains and it is usually adjusted by HRV. Increased beat-to-beat repolarization variability has been associated with enhanced risk of developing arrhythmic events in post-myocardial infarction patients [44, 45]. Other forms of measuring QT instability in the z-domain have been proposed in the literature and shown to be related to the generation of arrhythmias [46].

QT dynamics is another important phenomenon that accounts for the relation between the RR and QT intervals, both transiently and at steady state. The QT-RR adaptation time lag, measured in response to transient RR changes using different theoretical models, has been identified as a marker of arrhythmic

risk [47, 48]. As the phenomenon of QT adaptation is the central part of this thesis, a detailed description of this concept is presented in Section 1.5. Another marker of QT dynamics is the slope of the linear regression between QT and RR intervals, which has been increasingly used since the incorporation of the algorithm for its measurement into commercial Holter software [49]. The slope marker quantifies the steepness of the QT dependence on heart rate under stationary conditions corresponding to a range of stable heart rates, in contrast to the phenomenon of QT rate adaptation, which is measured in response to transient changes in heart rate. Higher QT-RR slopes have been suggested to indicate decreased vagal tone and increased sympathetic activity, which has been associated with higher arrhythmic risk [49]. Pathak *et al.* evaluated the QT dynamics from 24-hour Holter recordings of chronic heart failure patients and reported that an increased QT-RR slope was a strong predictor of SCD [50]. Other studies have investigated QT dynamics from the recovery phase of EST. An abnormally long QT interval at a cycle length of 500 ms, calculated using a linear regression of the QT-RR relation during early recovery from a treadmill EST, showed the capacity to predict all-cause mortality (without distinguishing arrhythmic or cardiac death from other mechanisms due to the lack of available clinical follow-up information) [51].

Other ECG risk markers include those quantifying T wave characteristics. Large values of the T wave amplitude have been related to the location of the acute occlusion of a coronary artery and large T wave width has been associated with enhanced ventricular repolarization dispersion [52–54]. Nevertheless, amplitude changes may occur due to other medical conditions (hyperventilation, increased intracranial pressure, stroke, drugs, etc.) or may even be normal based on the age or gender of the patient. The T peak-to-T end (T_{pe}) interval has been postulated as a measurement of ventricular repolarization. A marker derived from the relation between the T_{pe} and the RR intervals has been proposed as an indirect ECG surrogate of the action potential duration restitution (APDR) dispersion [55], which quantifies the properties of the ventricular repolarization dispersion at different heart rates. An increase in APDR dispersion has been associated with the occurrence of malignant ventricular arrhythmias [56]. T wave alternans (TWA) is another marker derived from the T wave, which consists of a periodic beat-to-beat alternating change, i.e. the ABABAB pattern, in amplitude, duration or morphology of the ST segment and/or the T wave [31,57]. An increase in heart rate is commonly required to trigger TWA, so controlled tests are usually used, such as EST. It is commonly considered that TWA should be present at a heart rate above 110-115 bpm. Higher magnitudes of TWA have been shown to be associated with ventricular arrythmogenesis under

different conditions [58], and the presence of TWA has been widely validated as a marker of SCD risk [31]. Recently, T wave time and amplitude variability quantified by time-warping-derived metrics have been defined as other markers for identifying cardiac abnormalities in cohorts of patients with chronic heart failure [59] as well as a SCD predictor index [60].

Finally, ST elevation is usually associated with transmural myocardial ischemia due to an acute occlusion of a coronary artery [32], while ST depression is mainly a marker of subendocardial ischemia [2]. However, persistent ST segment deviation may be indicative of other conditions (aneurysm, secondary repolarization changes) [61]. Changes in the ST segment can be influenced by the affected artery. Some studies have suggested that ST elevation in lead aVR can be a useful clinical tool to identify patients at increased risk for severe CAD [33], although there is some controversy about this association, particularly when ST segment changes are computed from EST [62].

1.5 QT-RR adaptation and hysteresis

As described previously, the QT interval duration is influenced by changes in the heart rate. The QT adaptation to a change in heart rate has been shown to present two phases: a fast initial phase lasting for around 30-60 s, followed by a 2-minute slow phase [63, 64]. The first phase has been suggested to be mainly related to the $I_{Ca\text{-}L}$ and the I_{Ks} currents, while the second phase has been suggested to be driven by intracellular sodium concentration Na_i dynamics [31, 65]. The adaptation of the ventricular repolarization duration has been described both for the QT interval of the surface ECG and for the action potential duration (APD) at the cellular, tissue and whole-organ levels [63, 65–71]. These fast and slow adaptations of the QT interval in response to heart rate changes have been modeled in a study by Cabasson *et al.* [72]. The modeling of the fast adaption phase is based on the electrical restitution curve that relates the cellular APD and the preceding diastolic interval. The modeling of the slow adaptation phase, which explains the QT-RR hysteresis, is supported by experimental studies and allows to obtain a slow step response similar to the one described for the APD [63]. The separate modeling of both the fast and the slow adaptation phases considers low-complexity autoregressive processes.

The time lag of the QT interval accommodation to heart rate changes is in correspondence to the so called QT-RR hysteresis, which is characterized by longer QT intervals at a given RR interval while heart rates increase during

exercise, and shorter QT intervals at the same RR interval while heart rates decrease during recovery, creating a "hysteresis loop". The QT-RR hysteresis was proposed to be quantified to improve the reliability of the QT_c interval measurement. Currently, different studies propose the quantification of the individual QT-RR hysteresis as a risk marker additional to the conventionally measured QT_c. Different methods for evaluating the magnitude of the QT-RR hysteresis have been proposed. Gravel *et al.* reviewed some published methods to quantify the hysteresis of the repolarization duration [73]. Some of the most commonly employed methods for quantification of the QT-RR adaptation or hysteresis are described in the following: [1]

- In some studies, the time course of QT adaptation following a provoked and sustained heart rate change, induced by atrial and/or ventricular pacing, has been characterized by computing the time to reach 90% of the total QT variation and by quantifying the adaptation time constant after fitting an exponential function [64, 74–76].

- In other studies, the QT-RR hysteresis has been computed by comparing the QT response at similar RR interval values during sequential heart rate acceleration and deceleration. A first approach has been to measure the difference of QT intervals (ΔQT) at the same RR interval during heart rate increases/decreases, typically based on data from exercise tests [77–79]. The result is, however, highly dependent on the reference RR interval chosen to calculate ΔQT. A second approach has been to measure the area between the QT/RR curves obtained separately during increasing and decreasing rates [80–82]. Several methods for quantifying this area have been suggested. Various stress protocols, curve fitting techniques, reference RR range, and reference timing of measurement have been proposed, which hampers the comparison of the results from different studies.

- Yet other studies have characterized the QT-RR adaptation by using models that relate the QT and RR intervals, from which various memory parameters describing the QT time lag after RR changes can be estimated. This methodology is the most extended one. It allows to separately quantify the QT-RR adaptation and the steady-state QT-RR relation. This methodology can be applied to a wide range of clinical and experimental settings, as no requirement on the type of RR changes is imposed [47,83–85].

[1] For further details on hysteresis quantification until 2017, see [73].

Graphical diagrams of some of the methods used to quantify the QT-RR adaptation or hysteresis described previously are shown in Fig. 1.5.

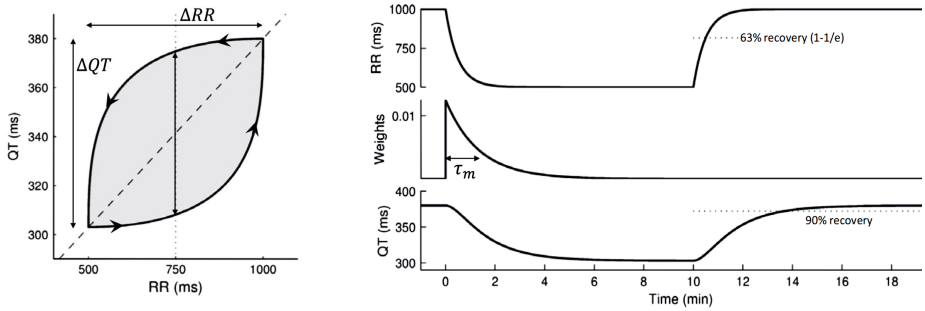

Figure 1.5: (a) QT-RR loop during exercise and recovery. The arrows indicate the temporal evolution and the dashed line corresponds to the static QT/RR curve. (b) On the top, the RR interval time course follows two exponential curves corresponding to the exercise and recovery phases. The QT interval time course is represented on the bottom panel. The QT interval achieves a stable state after the RR interval does. The linear filter weights that describe the influence of the previous RR intervals on the repolarization index (i.e. the QT interval) are represented in the middle panel. The effective RR interval is calculated as a linear combination of preceding RR intervals with the coefficients of such a combination being the represented exponentially decaying weights, which have an associated time constant τ_m. Adapted from [73].

From a clinical point of view, the QT-RR hysteresis index has been evaluated in different scenarios. A rise in this index has been associated with severe arrhythmias, shown to be a predictor of long QT syndrome (LQTS) phenotypes and genotypes, and proposed as a marker of exercise-induced ischemia in patients with suspected CAD [37]. The mechanism explaining such clinical findings is likely not to be unique but may possibly be explained by both the electrophysiological characteristics of ventricular cells and the influence of cardiac autonomic modulation on ventricular repolarization [78]. Specifically regarding the LQTS syndrome, it is caused by genetic mutations that result in malfunction of cardiac ion channels and an increased risk of syncope and SCD [37]. The most common types of LQTS are LQTS type 1 and LQTS type 2, which are mainly related to a decrease in the I_{Ks} current and a decrease in the I_{Kr} current, respectively [86]. Alterations in the QT-RR hysteresis in patients with LQTS have been shown to depend on the LQTS type [37]. Wong *et al.* showed that the QT-RR hysteresis was more pronounced in patients with LQTS type 2 compared with LQTS type 1 and LQTS-negative patients [87].

A variety of studies have evaluated the correlation between CAD and a

hysteresis index based on the QT-RR loop area during gradual heart rate acceleration and deceleration controlled by pacing or during EST [37]. The hysteresis index has been compared with the SYNTAX score (SXscore), results from angiography or the Duke treadmill score and the role of the ANS in determining its values has been investigated [81, 82]. Clinically, it has been shown that the QT-RR hysteresis improves the diagnostic value of the EST for CAD significantly when combined with other conventional criteria and it is associated with the severity of CAD [82].

In other works, the QT interval adaptation to sudden heart rate changes has been shown to provide information on the risk of arrhythmic complications and SCD [88]. In particular, an increase in the QT rate adaptation time in survivors of acute myocardial infarction has been associated with a higher probability of dying from an arrhythmic cause [47, 48]. Other studies have measured the rate adaptation of the QT interval after sudden heart rate changes due to conversion of AF and have postulated that delayed QT adaptation could be a potential risk factor for proarrhythmia [89, 90]. In other studies conducted in guinea-pig hearts, the rate adaptation of the APD and the QT interval in response to rapid cardiac pacing has been shown to be prolonged by arrhythmogenic interventions, such as quinidine, procainamide, and hypokalemia, but not by a clinically safe antiarrhythmic agent like lidocaine [71]. The analysis of both *in vivo* electrograms from patients and *in silico* simulations has allowed to show that the heterogeneity in the slow phase of APD adaptation could be an important component of arrhythmogenesis [69]. In another study with patients undergoing an electrophysiological study, a close relation between the rate adaptation of APD and the rate adaption of the effective refractory period has been shown, which has led to postulate that the repolarization adaptation can have a large impact on arrhythmia inducibility and should be accounted for in the design of stimulation protocols for electrophysiological studies [66]. To shed more light on the cell and tissue mechanisms underlying the QT-RR adaptation phenomenon and the relation with arrhythmic risk, experimental, clinical and simulated electrophysiological methods have been used and potential foundations have been described [37, 46, 65, 91, 92].

Other aspects that have been investigated include the effect of quantifying the adaptation speed in terms of absolute time or number of cardiac cycles and the influence of sex and gender on the QT-RR hysteresis [84, 85]. The full potential of the QT-RR hysteresis as an adjunct tool to conventional clinical indices to improve the prediction of cardiac risk is yet to be determined.

Another interesting aspect regarding QT-RR hysteresis is the comparison of the QT-RR hysteresis when it is calculated from ECGs recorded in different

settings, including a tilt test, EST and a 24-hour Holter. This was investigated in [84] using different exponential QT-RR hysteresis models, whose associated time constant parameter was estimated in two conditions separately, which corresponded to heart rate acceleration and deceleration during tilt test, exercise and recovery during EST, and day and night in 24-h Holter. During EST, the time constant was significantly longer during recovery regardless of the model, while the significance between the two time constant estimates depended on the model when analyzing ECGs from a tilt test or a 24-hour Holter.

In summary, optimizing the accuracy and refined interpretation of exercise ECG stress testing by including other exercise variables may improve the diagnostic accuracy in low-to-intermediate probability patients with CAD, helping in the prediction of SCD, and reduce the financial burden and medical resources.

1.6 Objectives and outline of the thesis

This Ph.D. dissertation is focused on the computation of the QT adaptation time in response to gradual heart rate changes. Most articles in the literature measure this adaptation time when abrupt heart rate changes are observed. The novel methods proposed in this Ph.D. can help to evaluate the accommodation of the repolarization duration in clinical practice by analyzing exercise ECGs stress testing that offer a more controllable scenario than Holter ECG recordings. In addition, the markers derived from the proposed analysis can serve to noninvasively stratify patients according to their level of coronary occlusion and to predict their risk for SCD.

The content of this Ph.D. thesis is organized into six chapters, describing the methodology developed to quantify the QT adaptation time and evaluating the proposed markers for separating patients according to their level of coronary occlusion and for stratifying patients according to their risk of SCD.

- **Chapter 2:** This chapter describes the methodology developed to estimate the QT adaptation time using information from exercise ECG stress testing. Two main objectives are distinguished: (1) to assess different lead space reduction techniques for robust computation of the T wave end; (2) to develop a method to compute the QT adaptation time, proposing three different markers related to such QT adaptation time in response to a ramp-like heart rate change. Additionally, this chapter points out that the QT adaptation time lag can be estimated not only in response to linear

exercise/recovery heart rate changes along the exercise ECG stress testing, but also in response to heart rate trends with low-frequency changes. The performance of the proposed algorithm to estimate the QT adaptation time lag is compared with other approaches of the literature.

- **Chapter 3:** This chapter describes our novel contributions to improving the simulator for paroxysmal AF proposed in [93], providing a new, more general ECG simulator that is suitable to evaluate the QT adaptation time lag estimation here proposed.

  The following publications are based on the results described in this chapter:

  - L. Bachi, H. Halvaei, **C. Pérez** *et al.*, "ECG Modeling for Simulation of Arrhythmias in Time-Varying Conditions," in IEEE Transactions on Biomedical Engineering, vol. 70, no. 12, pp. 3449-3460, 2023, doi: 10.1109/TBME.2023.3288701.
  - **C. Pérez**, E. Pueyo, J. P. Martínez, L. Sörnmo and P. Laguna, "Simulación de señales ECG incluyendo dinámica del intervalo PQ con el ritmo cardiaco y ruido muscle variante en el tiempo," XLI Congreso Anual de la Sociedad Española de Ingeniería Biomédica (CASEIB), Valladolid, Spain, 2022, pp. 436-439.

- **Chapter 4:** This chapter describes different simulated datasets generated using the simulator described in Chapter 3. In particular, simulated ECG datasets that are similar to those recorded from EST are produced. The generated datasets are used to assess the methods described in Chapter 2, which are related to: (1) the T wave end delineation from exercise ECG stress testing using different lead space reduction techniques; (2) the estimation of the QT adaptation time; (3) the study of the influence of the heart rate trend along the exercise ECG stress testing in the estimation of the QT adaptation time lags.

  The following publications are based on the results described in this chapter:

  - **C. Pérez**, E. Pueyo, J. P. Martínez, J. Viik, L. Sörnmo and P. Laguna, "Performance Evaluation of QT-RR Adaptation Time Lag Estimation in Exercise Stress Testing ," in IEEE Transactions on Biomedical Engineering, vol. 71, no. 11, pp. 3170-3180, 2024, doi: 10.1109/TBME.2024.3410008.

  - S. Romagnoli, **C. Pérez**, L. Burattini, E. Pueyo, M. Morettini, A. Sbrollini, J.P. Martínez, P. Laguna, "Model-based Estimators of QT Series Time Delay in Following Heart-Rate Changes," Annu Int Conf IEEE Eng Med Biol Soc., Sidney, Astralia, 2023, pp. 1-4, doi: 10.1109/EMBC40787.2023.10340130.
  - **C. Pérez**, E. Pueyo, J. P. Martínez, L. Sörnmo and P. Laguna, "Evaluation of a QT Adaptation Time Estimator for ECG Exercise Stress Test in Controlled Simulation," 2023 Computing in Cardiology, Atlanta, USA, 2023, pp. 1-4, doi: 10.22489/CinC.2023.235.
  - **C. Pérez**, E. Pueyo, J. P. Martínez, L. Sörnmo and P. Laguna, "Estimadores del retardo entre las series de QT y RR en registros ECG de prueba de esfuerzo: evaluación en simulación," XLI Congreso Anual de la Sociedad Española de Ingeniería Biomédica (CASEIB), Cartagena, Spain, 2023, pp. 606-609.

- **Chapter 5:** The clinical power of the proposed markers are evaluated in this chapter. Firstly, the QT adaptation time lag is estimated in exercise and recovery phases, separately, using exercise ECG stress testing of patients with different likelihood of suffering CAD. The discriminative capacity of the proposed markers is assessed. Additionally, the predictive capacity of the proposed markers is also evaluated using a second clinical database, in which the purpose is to risk stratify CAD patients according to their risk of suffering SCD or die due to any cause of mortality. Finally, the estimated values of the QT adaptation time are compared with those reported in previous studies that assessed the QT response to abrupt heart rate changes.

  The following publications are based on the results described in this chapter:

  - **C. Pérez**, E. Pueyo, J. P. Martínez, J. Viik and P. Laguna, "QT interval time lag in response to heart rate changes during stress test for coronary artery disease diagnosis, "Biomedical Signal Processing and Control, 2023, vol. 86, p. 105056, doi: 10.1016/j.bspc.2023.10505.
  - **C. Pérez**, E. Pueyo, J. P. Martínez, J. Viik and P. Laguna, "Characterization of impaired repolarization by quantification of the QT delay in response to heart rate changes from stress test recordings," 2020 11th Conference of the European Study Group on Cardiovascular Oscillations (ESGCO), Pisa, Italy, 2020, pp. 1-2, doi: 10.1109/ESGCO49734.2020.9158186.

  - **C. Pérez**, E. Pueyo, J. P. Martínez, J. Viik and P. Laguna, "Characterization of Impaired Ventricular Repolarization by Quantification of QT Delayed Response to Heart Rate Changes in Stress Test," 2020 Computing in Cardiology, Rimini, Italy, 2020, pp. 1-4, doi: 10.22489/CinC.2020.194.
  - **C. Pérez**, E. Pueyo, J. P. Martínez, J. Viik and P. Laguna, "Retardo entre QT y RR en registros de prueba de esfuerzo como indicador de la heterogeneidad de la repolarización ventricular," XXXVIII Congreso Anual de la Sociedad Española de Ingeniería Biomédica (CASEIB), Virtual, 2020, pp. 6-9.
  - **C. Pérez**, E. Pueyo, J. P. Martínez, J. Viik and P. Laguna, "Characterization of impaired repolarization by quantification of the QT delay in response to heart rate changes from stress test recordings," 45th Annual Conference of International Society for Computerized Electrocardiology (ISCE), Virtual, 2021.
  - Young Investigator Award for the best oral presentation. "Characterization of Impaired Ventricular Repolarization by Quantification of QT Delay after Heart Rate Changes in Stress Test," 17th STAFF/MALT Symposium, Sirolo, Italy, 2021.
  - **C. Pérez**, A. Martín-Yebra, J. Viik, J. P. Martínez, E. Pueyo and P. Laguna, "Eigenvector-based spatial ECG filtering improves QT delineation in stress test recordings," 2021 55th Asilomar Conference on Signals, Systems, and Computers, Pacific Grove, CA, USA, 2021, pp. 261-264, doi: 10.1109/IEEECONF53345.2021.9723261.

- **Chapter 6:** The methodology presented in Chapter 2 allowed to identify a phenomenon that is produced around the peak exercise. The work of this chapter is focused on investigating the role of β-adrenergic stimulation in the QT adaptation rate. Biophysically-detailed cell models coupling mathematical formulations of human ventricular electrophysiology and β-adrenergic signaling are used and pseudo-ECG signals are computed from modeled transmural ventricular tissue fibers. The main conclusion is that time-varying β-adrenergic stimulation patterns, rather constant β-adrenergic stimulation, better explain the QT adaptation phenomenon measured from CAD patients undergoing EST.

  The following publications are based on the results described in this chapter:

  - **C. Pérez**, R. Cebollada, K.A. Mountris, J.P. Martínez, P. Laguna,

E. Pueyo, "The role of β-adrenergic stimulation in QT interval adaptation to heart rate during stress test," PLoS One, 2023, vol. 18, no 1, p. e0280901, doi: 10.1371/journal.pone.0280901.

– R. Cebollada, **C. Pérez**, K. A. Mountris, J. P. Martínez, P. Laguna and E. Pueyo, "Mechanisms Underlying QT interval Adaptation Behind Heart Rate During Stress Test," 2021 Computing in Cardiology (CinC), Brno, Czech Republic, 2021, pp. 1-4, doi: 10.23919/CinC53138.2021.9662880

- **Chapter 7:** This chapter contains the main achievements, conclusions and limitations of this Ph.D. thesis as well as discussions about future work directions.

Matlab® software is employed for signal processing and result representation, while R© software is used for statistical analysis.

CHAPTER 2

QT-RR ADAPTATION TIME LAG ESTIMATES IN EXERCISE ECG STRESS TESTING

2.1 Motivation

Two distinct processes can be disguised in the dynamics of the QT-RR relation: the steady-state QT-RR dependency, which describes how the steady-state QT interval varies for a range of physiological RR intervals, and the QT-RR adaptation, which describes the accommodation of the QT interval to attain its steady-state following a sustained variation in the RR interval [37]. The adaptation of the QT interval to RR changes has been characterized by two

distinct phases and is, thus, the result of a combination of a fast and a slow adaptation phases [74]. Some studies have proposed to model these two phases separately using autoregressive processes [72] to individually characterize them. Although addressing the separate modeling of the two phases of QT interval dynamics allows to better account for the physiological phases observed at the cellular level (see Sec. 1.5), the estimation is more challenging and many clinical studies in the literature have focused on a global delay characterization, as will be performed in this thesis.

In previous studies, the QT-RR relation has been described by a system composed of two blocks. The first block is defined by a finite impulse response filter and the second block represents a memoryless transformation. In some of the studies the filter impulse response and the memoryless transformation vary along time while in other studies they are constant along time. In any case, a QT adaptation time lag is calculated from the impulse response of the filter, [47, 64, 75, 83]. This phenomenon occurs on top of the beat-to-beat QT interval variability, which is commonly quantified under stationary conditions and thus can provide complementary information to the QT adaptation phenomenon [94]. As described in Sec.1.5, previous works have highlighted the importance of determining normal and abnormal ranges of QT adaptation time lag in response to sudden changes in heart rate as a possible way to characterize the risk of cardiac arrhythmias and SCD [88]. In particular, an increase in the QT rate adaptation time in survivors of acute myocardial infarction has been associated with a higher probability of dying from an arrhythmic cause [47, 48]. Other studies have measured the rate adaptation of the QT interval after sudden heart rate changes due to conversion of AF and have postulated that a delayed QT adaptation could be a potential risk factor for proarrhythmia [89, 90]. The presence and availability of abrupt heart rate changes, e.g. in the form of step-like changes, in Holter recordings, may not always be guaranteed. Although such type of changes are not required by most of the above cited works, having smooth changes might hamper the adaptation lag estimation in some occasions. Also, the distribution of abrupt heart rate changes in a Holter recording can be very variable from subject to subject.

Theoretically, the time constant T of a first-order system in response to a step input is measured as the time where the corresponding exponential output reaches 63.2% of its final value (see Fig. 2.1a). It can be noted that the ramp-response of the same first-order system is characterized by another ramp delayed by a lag of the same value as the time constant of the step response (see Fig. 2.1b). Therefore, the time constant of the same first-order system can be measured using either a step-like or a ramp-like input [95].

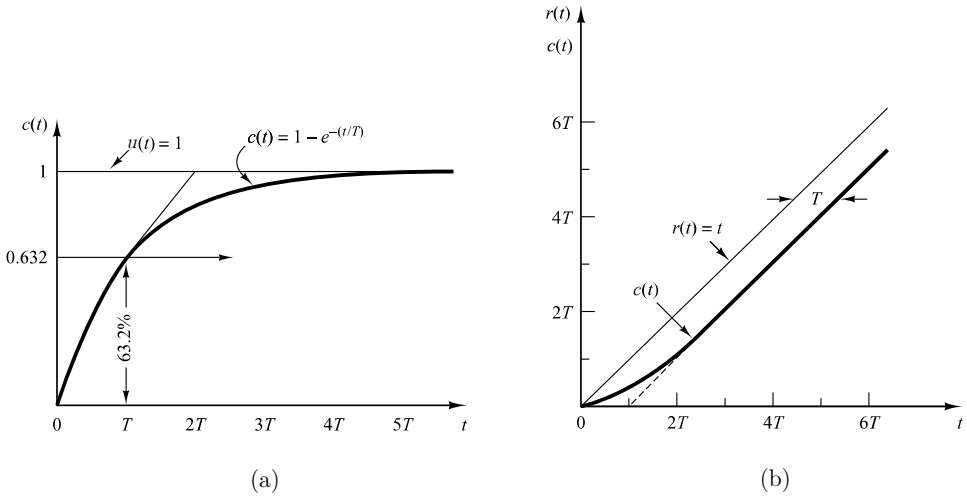

Figure 2.1: The response $c(t)$ of a first-order system when the input is (a) a unit-step $u(t)$ and (b) a ramp $r(t)$. The time constant T of the system can be measured using any of these inputs. Adapted from [95].

During EST, heart rate changes are also observed. The adaptation time of the QT interval to heart rate changes may be alternatively estimated in this type exercise tests. Heart rate changes are easily induced by exercise and a wide range of change is produced, thus offering the opportunity to assess the dynamics of the QT interval in response to gradual changes in heart rate [51,80]. These heart rate changes follow a trend comparable to a ramp. Thus, developing robust individualized methods to estimate the QT adaptation time lag from exercise ECG stress testing is the main contribution of this thesis. This chapter describes the methodology to perform such an estimation.

We suggest expressing the QT-RR relation by using the same two separate blocks proposed by Pueyo *et al.* [47, 83] and focus on the linear block to characterize the QT adaptation time lag. We define a methodology to compute the QT adaptation time lag as the delay between the observed QT intervals and the QT intervals derived from the observed RR intervals. This estimated delay should provide clinical information equivalent to that provided by the time constant of the QT response to a step-like heart rate change.

The procedure proposed here requires measuring the QT interval from exercise ECG stress testing, where the influence of noise, artifacts, and even the eventual overlap of the T wave and the P wave at very high heart rates complicate the delineation of the T wave end. Recent studies investigating

exercise ECGs stress testing incorporate manual delineation to compute the T wave end, which implies that the number of patients is necessarily reduced [96], or do not study the dynamics of the QT interval at high heart rates [81, 97]. Therefore, we also study and propose different automated procedures in this work to improve the T wave end delineation during exercise.

2.2 ECG pre-processing

The ECG is subject to filtering prior to applying any other processing. First, the influence of high-frequency noise is attenuated by forward–backward filtering using a sixth-order Butterworth, lowpass filter (cut-off frequency at 50 Hz) to avoid ECG distortion. Afterwards, baseline wander is attenuated by applying a third-order Butterworth highpass filter (cut-off frequency at 0.5 Hz).

Areas with large amplitude due to the presence of artifacts (i.e. electrode movements) are detected by defining a threshold based on the median-envelope of the signal. The samples contained in a 100-ms window around a sample whose value is higher than the defined threshold are replaced by 0 mV value.

Finally, a cubic spline interpolation [98] is applied to further improve the attenuation of the baseline wander. The isoelectric level for each beat is estimated as the averaged value of the filtered ECG in a 20-ms window starting 80 ms before the QRS fiducial point taken as the R point of the QRS complex.

Detection of ectopic beats is also implemented [99] as these beats are usually present during the recovery phase in EST.

2.3 Enhancement of T wave end delineation

The T wave end delineation is critical in the analysis of the QT interval. In recent studies [90], wavelet-based delineation [100] is preceded by lead space reduction to improve the performance. The lead space reduction is defined by either principal component analysis (PCA) [101] or generalized periodic component analysis (GπCA$_P$) [102], with the latter exploiting the fact that the T wave is 1-to-P-beat periodic [90]. Using the most significant, transformed lead, a robust delineation performance is reported for Holter recordings.

These two ECG lead space reduction techniques are applied separately to the 8 independent standard leads (V1–V6, I, II) of an ECG signal. In this way, new transformed leads are generated, which have higher signal-to-noise ratio (SNR). The delineation of the waves and the extraction of ECG features are more

accurate when the transformed leads are considered. This is particularly relevant in the usually very noisy exercise ECGs stress testing.

The spatial lead transformation is computed by applying a transformation matrix $\mathbf{\Psi}^T$ to the original leads:

$$\mathbf{w}(n) = \mathbf{\Psi}^T \mathbf{x}(n). \tag{2.1}$$

where the columns of $\mathbf{x}(n)$ contain the information of each of the L leads of the filtered ECG at sample n:

$$\mathbf{x}(n) = \begin{bmatrix} x_1(n) & x_2(n) & \dots & x_L(n) \end{bmatrix}^T,$$

and $\mathbf{w}(n)$ contains the corresponding transformed leads:

$$\mathbf{w}(n) = \begin{bmatrix} w_1(n) & w_2(n) & \dots & w_L(n) \end{bmatrix}^T.$$

To calculate the transformation matrix $\mathbf{\Psi}$, a time window learning period is selected, where excerpts from each beat are piled in the matrix $\mathbb{X}_q$. Specifically, the beat signal excerpts corresponding to the T waves from the K beats are contained in the selected window. The T wave excerpt for each k-th beat is taken from sample $n_{\text{QRS}}(k) + (25 + 1.2\text{RR}_m^{1/2})F_s/1000$ to sample $n_{\text{QRS}}(k) + (300 + 1.2\text{RR}_m^{1/2})F_s/1000$, where $n_{\text{QRS}}(k)$ is the QRS complex fiducial point [103], and RR_m is the median RR interval value (in miliseconds) in the learning window. For the k-th beat, the T wave of the l-th lead has a length of N samples and is expressed in vector notation as:

$$\mathbf{x}_{k,l} = \begin{bmatrix} x_{k,l}(1) & x_{k,l}(2) & \cdots & x_{k,l}(N) \end{bmatrix}^T. \tag{2.2}$$

The T waves from all L leads of the k-th beat are put together into matrix $\mathbf{X}_k$:

$$\mathbf{X}_k = \begin{bmatrix} \mathbf{x}_{k,1} & \mathbf{x}_{k,2} & \cdots & \mathbf{x}_{k,L} \end{bmatrix}^T, \tag{2.3}$$

where each column contains the n-th samples from the k-th beat T waves in all the L leads, resulting in a $L \times N$ matrix.

Finally, the $(L \times (NK))$ matrix $\mathbb{X}_q$ is constructed by concatenating the $\mathbf{X}_k$ matrix from all K beats:

$$\mathbb{X}_q = \begin{bmatrix} \mathbf{X}_1 & \mathbf{X}_2 & \cdots & \mathbf{X}_K \end{bmatrix} \tag{2.4}$$

The PCA technique yields transformed leads guided by a maximum-variance concentration criterion. The orthogonal transformation matrix, now $\mathbf{\Psi} \equiv \mathbf{\Psi}_{\text{PCA}}$,

is the eigenvector decomposition matrix of the 8×8 interlead ECG autocorrelation matrix $\mathbf{R}_{\mathbb{X}_q}$,

$$\mathbf{R}_{\mathbb{X}_q}\mathbf{\Psi}_{\text{PCA}} = \mathbf{\Psi}_{\text{PCA}}\mathbf{\Lambda}, \tag{2.5}$$

with $\mathbf{R}_{\mathbb{X}_q}$ estimated from the learning data matrix as

$$\hat{\mathbf{R}}_{\mathbb{X}_q} = \frac{1}{KN}\mathbb{X}_q\mathbb{X}_q{}^T, \tag{2.6}$$

and $\mathbf{\Lambda}$ being a diagonal matrix containing the eigenvalues of $\mathbf{R}_{\mathbb{X}_q}$ sorted in descending order. The columns of $\mathbf{\Psi}_{\text{PCA}}$ contain the corresponding eigenvectors.

The GπCA$_P$ technique is alternatively used to maximize a given beat periodicity in the transformed lead, rather than to maximize the variance as in the case of PCA. In [104], this GπCA$_P$ transformation is proposed to emphasize the beat-to-beat periodicity in the transformed lead, making use of the beat-to-beat coherence observed in the ECG signal. In highly noisy recordings with low SNR, like exercise ECG stress testing, the first transformed lead (TL1) of PCA can emphasize noise when it is dominant or comparable in energy (variance) to the true (noiseless) ECG signal.

In this study, we hypothesize that the periodicity maximization criterion used by GπCA$_P$ could better filter out noise, even in cases of low SNR, provided that it does not have the beat periodicity of the signal. The transformation matrix, now $\mathbf{\Psi} \equiv \mathbf{\Psi}_{\text{G}\pi\text{CA}_P}$, is derived as the generalized eigenvector matrix of a matrix pair, ordered in ascending order of eigenvalue magnitude [104]. Specifically, the generalized eigenvector problem,

$$\mathbf{R}^P_{\Delta\mathbb{X}_{p,q}}\mathbf{\Psi}_{\text{G}\pi\text{CA}} = \mathbf{R}_{\mathbb{X}_q}\mathbf{\Psi}_{\text{G}\pi\text{CA}}\mathbf{\Lambda}, \tag{2.7}$$

including the matrix pair $\left(\mathbf{R}^P_{\Delta\mathbb{X}_{p,q}}, \mathbf{R}_{\mathbb{X}_q}\right)$ [90], is solved. The spatial correlation of the nonperiodic residual, $\mathbf{R}^P_{\Delta\mathbb{X}}$, is estimated as:

$$R^P_{\Delta\mathbb{X}_{p,q}} = \frac{1}{PKN}\sum_{p=1}^{P}\Delta\mathbb{X}_{p,q}\Delta\mathbb{X}^T_{p,q}, \tag{2.8}$$

with

$$\Delta\mathbb{X}_{p,q} = \mathbb{X}_{p,q} - \mathbb{X}_q. \tag{2.9}$$

The matrix $\mathbb{X}_{p,q}$ is $\mathbb{X}_q$ shifted p beats forward.

The selection of the signal excerpt where to learn the transformation matrix may be relevant for the study. The eigenvector accounts for a kind of smoothed

version of the different T wave morphologies contained in the learning window, aiming to generate a transformed lead better suited for T wave delineation. Nevertheless, the large dynamics of the heart rate in EST could generate doubts about the stability and suitability of this smoothed eigenvector as the best suited when derived from the entire recordings. For this reason, we propose exploring two strategies: unique learning of the transformation matrix in a selected learning window; and relearning of the transformation matrix every 150 s. The latter is introduced to better account for the long-term T wave changes (not beat-to-beat), which are the ones relevant to estimate the QT adaptation time lag from the QT and RR time series.

Depending on the selected strategy for learning the matrix $\mathbf{\Psi}$, six variants of the two lead space reduction techniques are proposed:

- $\mathbf{G\pi CA}_1$: the transformation is learned in each window of 150 s, recalculating the $\mathbf{\Psi}$ matrix in each window, for $P = 1$.
- $\mathbf{G\pi CA}_3$: the transformation is learned in each window of 150 s, recalculating the $\mathbf{\Psi}$ matrix in each window, for $P = 3$.
- $\mathbf{G\pi CA}_{1,o}$: the $\mathbf{\Psi}$ matrix is estimated once using the first 150 s at the beginning of the signal, and then the same transformation $\mathbf{\Psi}$ is applied to the rest of signal, with $P = 1$.
- $\mathbf{G\pi CA}_{3,o}$: The $\mathbf{\Psi}$ matrix is estimated once using the first 150 s at the beginning of the signal, and then applied to the complete signal, with $P = 3$.
- **PCA**: The PCA technique is applied with the $\mathbf{\Psi}$ matrix being reestimated in each window of 150 s.
- $\mathbf{PCA}_o$: The PCA technique is applied with the $\mathbf{\Psi}$ matrix being estimated once using the first 150 s at the beginning of the signal, and then applied to the complete signal.

2.3.1 Evaluation of T wave end delineation

To evaluate the performance of the different methods proposed to compute the T wave end, two different cases are considered:

First, the case of real clinical ECG recordings, where the variability of the raw QT interval series $d_{\mathrm{QT}}(k)$ (see Sec.2.4 for series definition) interpolated at a rate of 4 Hz, resulting in the QT interval series $d^r_{\mathrm{QT}}(n)$, is estimated as the power

$\mathcal{P}_{\mathrm{QTV}}$ of the 0.04 Hz high-pass filtered interval series, separately in exercise and recovery phases. Under the assumption that delineation errors are uncorrelated to the (method-invariant) physiological variability of the QT interval, the power of the filtered series $\mathcal{P}_{\mathrm{QTV}}$ includes both the natural variability of QT interval (common for all methods) and the power of the delineation errors. Therefore, $\mathcal{P}_{\mathrm{QTV}}$ is considered a surrogate for the delineation performance when a reference mark is not available. The lower $\mathcal{P}_{\mathrm{QTV}}$, the better the performance.

For the second case with simulated added noise to each ECG contained in a simulated dataset, the performance is quantified by the root mean square (RMS) error, denoted as ϵ_θ, between the T wave ends determined from a noisy and a reference beat, denoted as θ_k and θ_k^r, respectively, where k denotes the k-th beat out of the K total beats.

$$\epsilon_\theta = \sqrt{\frac{1}{K}\sum_{k=1}^{K}(\theta_k - \theta_k^r)^2} \tag{2.10}$$

The reference beat is defined in the same way as the noisy beat except that the SNR is very high (using the definition in (4.2), the SNR is set to 40 dB). A totally noise-free reference beat is not used to avoid that matrices manipulation leads to deal with a singular transformation matrix.

2.4 RR and QT series

The starting point of the QT-RR adaptation time lag estimation is the beat-to-beat RR and QT interval series, denoted as $d_{\mathrm{RR}}(k)$ and $d_{\mathrm{QT}}(k)$, respectively, with k being the beat index. To obtain these series, the multi-lead wavelet-based delineation (MLeads) method [100] is used to determine a lead-independent R wave position, $n_{\mathrm{QRS}}(k)$, leading to the RR series defined by

$$d_{\mathrm{RR}}(k) = n_{\mathrm{QRS}}(k) - n_{\mathrm{QRS}}(k-1), \tag{2.11}$$

and the QRS complex onset $n_{\mathrm{QRSo}}(k)$. This technique is applied over the delineation marks of the 8 independent standard leads to assign unique marks $n_{\mathrm{QRS}}(k)$ and $n_{\mathrm{QRSo}}(k)$ for each k-th beat. For the identification of the T wave end mark $n_{\mathrm{Te}}(k)$, the single-lead delineation method applied over the TL1, offering the best performance from Sec. 2.3, is used. Therefore, the QT time series is defined as

$$d_{\mathrm{QT}}(k) = n_{\mathrm{Te}}(k) - n_{\mathrm{QRSo}}(k), \tag{2.12}$$

for each k-th beat.

An example of a clinical ECG with the delineation marks $n_{\mathrm{QRS}}(k)$, $n_{\mathrm{QRSo}}(k)$ and $n_{\mathrm{Te}}(k)$ of the single-lead and multi-lead methodologies, SLead and MLeads, respectively, is shown in Fig. 2.2.

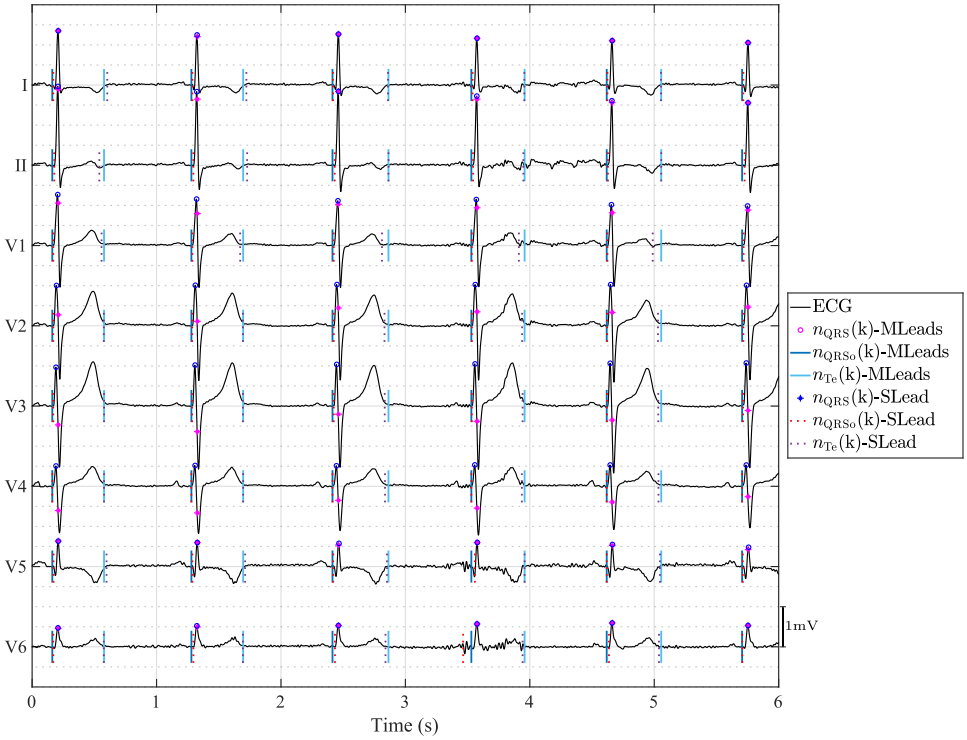

Figure 2.2: Independent standard 8-lead clinical ECG where both the single-lead and multi-lead delineation, SLead and MLeads, respectively, of R $n_{\mathrm{QRS}}(k)$, QRS onset Q$n_{\mathrm{QRSo}}(k)$ and T wave end $n_{\mathrm{Te}}(k)$ points are marked.

Outlier values of both $d_{\mathrm{RR}}(k)$ and $d_{\mathrm{QT}}(k)$ series, identified as those deviating by more than $\pm 10\%$ or $\pm 5\%$, respectively, from the running median of each series computed over 40 consecutive beats, are replaced with the corresponding median value. Subsequently, missing points are interpolated using a piecewise cubic Hermite polynomial. In most cases, these missed points are close to the peak exercise and no long time intervals are observed without any QT measure. Using piecewise cubic Hermite polynomial avoids overshoots and a larger oscillation if the data are not smooth. This process helps to emphasize the series trends and facilitate the estimation of the QT adaptation time lag. Finally, using interpolation, the $d_{\mathrm{RR}}(k)$ and $d_{\mathrm{QT}}(k)$ are resampled at a rate of 4 Hz, resulting

in the uniformly sampled series $d_{\mathrm{RR}}(n)$ and $d_{\mathrm{QT}}(n)$ measured in seconds, where n is the uniform sample index. The 4 Hz resampling rate is selected to be higher than the frequency content of the QT and RR series, which is under 2 Hz, while still being sufficiently low to ensure computational efficiency.

2.5 QT-RR modeling

The process to estimate the QT adaptation time lag can be divided in two blocks, see Fig. 2.3. The first block accounts for the calculation of an instantaneous series $d^i_{\mathrm{QT}}(n)$, related to $d_{\mathrm{RR}}(n)$ through a memoryless transformation (corresponding to the memoryless, usually nonlinear, QT-RR dependence at steady-state), and the second block represents the QT adaptation time lag estimation, which considers the observed QT interval series $d_{\mathrm{QT}}(n)$ and the instantaneous series $d^i_{\mathrm{QT}}(n)$ series (related by a linear system).

The series $d^i_{\mathrm{QT}}(n)$ represents the QT interval that would correspond to an RR interval in the series $d_{\mathrm{RR}}(n)$ if the conditions were stationary. For this reason, it can be called the expected instantaneous (memoryless) heart rate-dependent QT interval.

The instantaneous series $d^i_{\mathrm{QT}}(n)$ is obtained from the RR series $d_{\mathrm{RR}}(n)$ by a differentiable function $g_f\left(d_{\mathrm{RR}}(n);\alpha,\beta\right)$ whose values are determined by the two scalar parameters α and β. The series $d^i_{\mathrm{QT}}(n)$ keeps the same temporal variation as $d_{\mathrm{RR}}(n)$, but its values are comparable to those of the $d_{\mathrm{QT}}(n)$ series. Taking this into account, it can be seen that, in the model displayed in Fig. 2.3, the delay between $d_{\mathrm{QT}}(n)$ and $d^i_{\mathrm{QT}}(n)$ determines the QT adaptation time lag τ.

Focusing on the computation of the instantaneous series $d^i_{\mathrm{QT}}(n)$, the transformation $g_f\left(d_{\mathrm{RR}}(n);\alpha,\beta\right)$ accounts for the QT-RR relation under stationary conditions, understanding "stationary" here in the broader sense as "nonchanging trend". The four regression models considered to compute $d^i_{\mathrm{QT}}(n)$ are parabolic (Par) ($f\equiv$Par), linear (Lin) ($f\equiv$Lin), hyperbolic (Hyp) ($f\equiv$Hyp) and logarithmic (Log) ($f\equiv$Log):

$$\text{Parabolic log/log}\,(Par)\quad d^i_{\mathrm{QT}}(n)=g_f\left(d_{\mathrm{RR}}(n);\alpha,\beta\right)=\beta(d_{\mathrm{RR}}(n))^{\alpha} \tag{2.13}$$

$$\text{Linear}\,(Lin)\quad d^i_{\mathrm{QT}}(n)=g_f\left(d_{\mathrm{RR}}(n);\alpha,\beta\right)=\beta+\alpha\, d_{\mathrm{RR}}(n) \tag{2.14}$$

$$\text{Hyperbolic}\,(Hyp)\quad d^i_{\mathrm{QT}}(n)=g_f\left(d_{\mathrm{RR}}(n);\alpha,\beta\right)=\beta+\frac{\alpha}{d_{\mathrm{RR}}(n)} \tag{2.15}$$

$$\text{Logarithmic}\,(Log)\quad d^i_{\mathrm{QT}}(n)=g_f\left(d_{\mathrm{RR}}(n);\alpha,\beta\right)=\beta+\alpha\,\ln(d_{\mathrm{RR}}(n)) \tag{2.16}$$

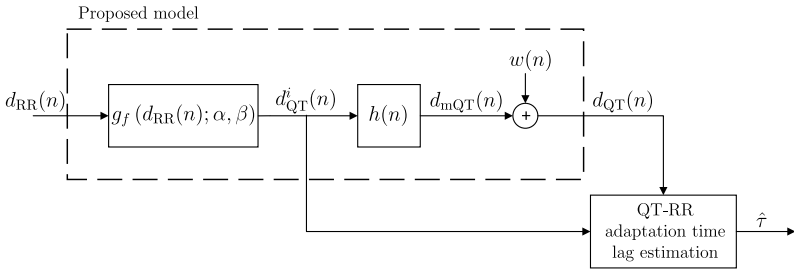

Figure 2.3: The proposed model relating the observed RR series $d_{\mathrm{RR}}(n)$ to the observed QT series $d_{\mathrm{QT}}(n)$. The output of the memoryless transformation $g_f\left(d_{\mathrm{RR}}(n);\alpha,\beta\right)$ is an instantaneous QT series $d^i_{\mathrm{QT}}(n)$, which results in the modeled QT series $d_{\mathrm{mQT}}(n)$ when it is filtered by a linear, time-invariant, first-order filter $h(n)$. The observed $d_{\mathrm{QT}}(n)$ is modeled as the sum of $d_{\mathrm{mQT}}(n)$ and noise $w(n)$. The QT-RR adaptation time lag τ is estimated as the delay between $d^i_{\mathrm{QT}}(n)$ and $d_{\mathrm{QT}}(n)$.

Using the least square technique, the values of the model parameters α and β are estimated for each tested regression model. Patient-specific values of these two model parameters are obtained using the data pairs $[d_{\mathrm{QT}}(n), d_{\mathrm{RR}}(n)]$ contained in three disjoint learning windows along the EST.

The positions of the three learning windows are the following (the notation for each window is within parenthesis): the first 40 s of rest before exercise (W_b), 20 s centered around peak exercise (W_e), and the last 40 s of late recovery (W_{lr}). Thus, for each ECG, α and β are estimated using the data pairs of the three concatenated windows. Together, the concatenated windows $W_b \cup W_e \cup W_{lr}$ should contain a wide range of RR intervals to produce a more reliable least squares fit. The exercise window is replicated twice to have the three regions equally weighted in the estimation. Examples of $d_{\mathrm{RR}}(n)$ and $d_{\mathrm{QT}}(n)$ series from a clinical ECG are represented in Fig. 2.5(a) together with the learning window positions.

Initially, the data pairs of these three windows are assumed to be stationary. This assumption is reasonable only for the resting and the recovery windows, but not for the exercise window, which is, however, included so as to account for the whole excursion of RR when evaluating the QT-RR dependency. The defined exercise window includes QT values from heart rate acceleration and deceleration phases, with opposite effects on the QT interval. Although we hypothesize that this window could compensate for the QT dynamics, making the mean QT-RR relation not far from that under stationary conditions, different definitions of this window are proposed in Sec. 2.7 to reduce the effect of nonstationarity.

To select the best model when clinical ECGs are evaluated, the patient-specific fitting of each regression model is compared by computing the RMS error using the unified data from the three learning windows, $W_b \cup W_e \cup W_{lr}$, in the 4 Hz interpolated series, with each of windows having a length of 40 s (or 20 s but twice):

$$\varepsilon_{\text{rms}} = \sqrt{\frac{1}{3 \times 40 \times 4} \sum_{n \in \{W_j\}} \left(d_{\text{QT}}(n) - d^i_{\text{QT}}(n) \right)^2}, \; j \in \{b, e, lr\}, \tag{2.17}$$

where j covers the three learning windows W_b, W_e or W_{lr}, allowing n to cover the samples of the three windows of 40 s sampled at 4 Hz.

2.5.1 Reverted QT-RR modeling

The estimation of the QT adaptation time lag can also be calculated as the delay between the observed RR intervals and an instantaneous series $d^i_{\text{RR}}(n)$ related to the observed QT intervals by the inverse linear filter of $h(n)$, which becomes $h(-n)$ for a pure delay as its impulse response. We hypothesize that this late option may offer better performance since the RR series has a greater range of variation than the QT series from which the delays can be computed. The corresponding model is shown in Fig. 2.4, where the instantaneous series $d^i_{\text{RR}}(n)$ is now delayed with respect to $d_{\text{RR}}(n)$. Note that a direct inversion of the model in Fig. 2.3 would have implied that the model in Fig. 2.4 had the linear and nonlinear blocks swapped. However, in Sec. 2.9 it is described that, for the QT and RR series measured during an EST, the swapping of the blocks is irrelevant to the final result and thus, the two blocks can be interchanged.

2.6 QT-RR adaptation time lag estimation

The QT adaptation time lag to gradual heart rate changes, τ, is estimated as the time lag between the time series $d^i_{\text{QT}}(n)$ and $d_{\text{QT}}(n)$. This estimation is performed separately in the exercise and recovery phases using the maximum likelihood (ML) technique. Both Gaussian and Laplacian estimators of τ, depending on the assumption on the noise statistic, are used [105, 106].

The estimation of the time delay τ between $d_{\text{QT}}(n)$ and $d^i_{\text{QT}}(n)$ during an episode of heart rate change can be formulated as a two-channel time delay estimation [3]. To derive the ML time delay estimator, the signal model of the

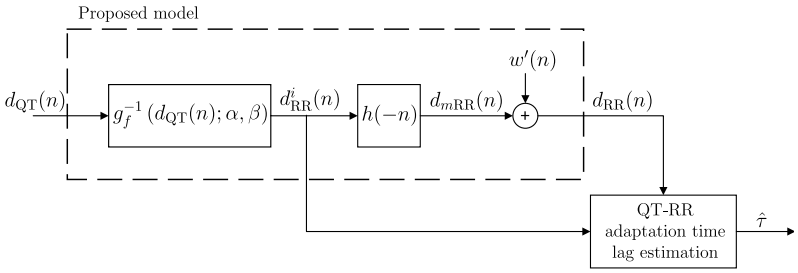

Figure 2.4: The proposed model relating the observed QT series $d_{\mathrm{QT}}(n)$ to the observed RR series $d_{\mathrm{RR}}(n)$. The output of the memoryless transformation $g_f^{-1}(d_{\mathrm{QT}}(n);\alpha,\beta)$ is an instantaneous RR series $d^i_{\mathrm{RR}}(n)$, which results in the modeled RR series $d_{\mathrm{mRR}}(n)$ when it is filtered by a linear, time-invariant, first-order filter $h(-n)$. The observed $d_{\mathrm{RR}}(n)$ is modeled as the sum of $d_{\mathrm{mRR}}(n)$ and noise $w'(n)$. The QT-RR adaptation time lag τ is, in this case, estimated as the delay between $d_{\mathrm{RR}}(n)$ and $d^i_{\mathrm{RR}}(n)$.

two series is described as:

$$\left.\begin{array}{l} y_1(n) = s(n) + v_1(n) \\ y_2(n) = s(n-\tau) + v_2(n) \end{array}\right\} n = 0, ..., N-1, \tag{2.18}$$

where $y_1(n)$ and $y_2(n)$ correspond to $d^i_{\mathrm{QT}}(n)$ and $d_{\mathrm{QT}}(n)$, respectively. The observed signal $y_1(n)$ is assumed to be composed of an unknown linear trend corresponding to the signal $s(n)$, representing the QT change trend, and additive stationary white noise $v_1(n)$ with variance σ_v^2 (modeled as Gaussian or Laplacian). The same assumption applies to the second channel, except that the QT trend is delayed by an unknown time τ. The QT trend $s(n)$ is assumed to have flat (constant) behavior at the initial and final extremes of the observation window, with a duration that guarantees that, although the series is delayed by τ, it still has the same flat value at its initial and final samples (step transition much shorter than the observation interval). The integer N is the length of the interval, which contains either the exercise or the recovery trend, where the estimation of τ is performed.

The ML time delay estimate of τ depends on the assumed distribution of the series. If $v_1(n)$ and $v_2(n)$ are assumed to be uncorrelated and with Gaussian probability distribution function (PDF), the PDF characterizing the observations $\mathbf{y}_i = \left[y_i(0) \cdots y_i(N-1)\right]^T \; i \in \{1, 2\}$, with $\mathbf{s} = \left[s(0) \cdots s(N-1)\right]^T$, results in

the following expression [3]:

$$p_v(\mathbf{y}_1, \mathbf{y}_2; \tau, \mathbf{s}) = \prod_{n=0}^{N-1} \frac{1}{2\pi\sigma_v^2} \exp\left[-\frac{\big(y_1(n)-s(n)\big)^2 + \big(y_2(n)-s(n-\tau)\big)^2}{2\sigma_v^2} \right]. \tag{2.19}$$

Taking the logarithm and grouping factors independent of τ and $\mathbf{s}$, the following is obtained:

$$\ln p_v(\mathbf{y}_1, \mathbf{y}_2; \tau, \mathbf{s}) = \text{Constant} + -\frac{1}{2\sigma_v^2} \sum_{n=0}^{N-1} \Big(\big(y_1(n)-s(n)\big)^2 + \big(y_2(n)-s(n-\tau)\big)^2 \Big). \tag{2.20}$$

Maximization of the log-likelihood function in (2.20) is performed by first differentiating with respect to $s(n)$ for a given τ,

$$\frac{\partial \ln p_v(\mathbf{y}_1, \mathbf{y}_2; \tau, \mathbf{s})}{\partial s(n)} = \frac{1}{\sigma_v^2} \big(y_1(n) + y_2(n+\tau) - 2s(n) \big), \tag{2.21}$$

which, when set to zero, results in the following estimator for $s(n)$:

$$\hat{s}(n; \tau) = \frac{y_1(n) + y_2(n+\tau)}{2}. \tag{2.22}$$

Inserting $\hat{s}(n; \tau)$ into the log-likelihood function in (2.20) and maximizing with respect to the other parameter τ leads to:

$$\hat{\tau} = \arg\min_{\tau} \left(\sum_{n=0}^{N-1} \big(y_1(n) - y_2(n+\tau)\big)^2 + \big(y_2(n) - y_1(n-\tau)\big)^2 \right) \tag{2.23}$$

Since the signal $s(n)$ is supposed to have constant value in intervals wider than τ at the observation window extremes, the estimator in (2.23) is just the least square estimate varying τ,

$$\hat{\tau}^{\mathrm{G}} = \arg\min_{\tau} \sum_{n=0}^{N-1} \big(y_1(n) - y_2(n+\tau)\big)^2. \tag{2.24}$$

The maximum likelihood estimator (MLE) $\hat{\tau}^{\mathrm{G}}$ is derived from Gaussian noise assumption. However, features derived from the ECG are better represented by Laplacian rather than Gaussian distributions, as is the case of the QRS angles [107] or the Karhunen-Loève transform coefficients for the T wave [108].

The QT interval is a measure based on the QRS onset and T wave end identifications that can be largely subject to outliers, thus suggesting the consideration of Laplacian models when estimating the delay between the QT series.

The derivation of the ML time delay estimation under Laplacian noise distribution departs from the same signal model described in (2.18), but now with Laplacian noise PDF. This results in the following expression for the PDF characterizing the observation signals [105, 106]:

$$p_v(\mathbf{y}_1, \mathbf{y}_2; \tau, \mathbf{s}) = \prod_{n=0}^{N-1} \frac{1}{2\sigma_v^2} \exp\left[-\frac{\sqrt{2}}{\sigma_v}(|y_1(n)-s(n)|+|y_2(n)-s(n-\tau)|)\right]. \tag{2.25}$$

Taking the logarithm and grouping factors independent of τ and $\mathbf{s}$, the following is obtained:

$$\ln p_v(\mathbf{y}_1, \mathbf{y}_2; \tau, \mathbf{s}) = \text{Constant} + -\frac{\sqrt{2}}{\sigma_v} \sum_{n=0}^{N-1} (|y_1(n)-s(n)|+|y_2(n)-s(n-\tau)|). \tag{2.26}$$

Maximization of the log-likelihood function in (2.26) is performed by first differentiating with respect to $s(n)$ for a given τ,

$$\begin{aligned} \frac{\partial \ln p_v(\mathbf{y}_1,\mathbf{y}_2;\tau,\mathbf{s})}{\partial s(n)} &= -\frac{\sqrt{2}}{\sigma_v}\left(\frac{y_1(n)-s(n)}{|y_1(n)-s(n)|}+\frac{y_2(n+\tau)-s(n)}{|y_2(n+\tau)-s(n)|}\right) \\ &= -\frac{\sqrt{2}}{\sigma_v}\left[\operatorname{sgn}(y_1(n)-s(n))+\operatorname{sgn}(y_2(n+\tau)-s(n))\right], \end{aligned} \tag{2.27}$$

which, when set to zero, results in the following estimator:

$$\hat{s}(n;\tau) = \operatorname{med}\{y_1(n), y_2(n+\tau)\} = \frac{y_1(n)+y_2(n+\tau)}{2}. \tag{2.28}$$

Inserting $\hat{s}(n;\tau)$ into the log-likelihood function in (2.26) and maximizing with respect to the other parameter τ leads to:

$$\hat{\tau} = \arg\min_{\tau} \sum_{n=0}^{N-1} \left(\frac{|y_1(n)-y_2(n+\tau)|}{2}+\frac{|y_2(n)-y_1(n-\tau)|}{2}\right). \tag{2.29}$$

Making use of the assumption that $s(n)$ has a constant value at the extremes of the observation interval for segments wider than τ, the MLE of τ for Laplacian noise can be written as:

$$\hat{\tau}^{\mathrm{L}} = \arg\min_{\tau} \sum_{n=0}^{N-1} |y_1(n) - y_2(n+\tau)|. \tag{2.30}$$

From all the above, it can be noted that the expressions for the estimators can be written in terms of the QT series. Also, grouping the expressions for the two estimates, they can be expressed as:

$$\tau_p = \arg \min_{-I \leqslant \tau \leqslant I} \sum_{n=n_{x,o}}^{n_{x,e}} |d^i_{\mathrm{QT}}(n) - d_{\mathrm{QT}}(n+\tau)|^p, \quad p = 1, 2, \tag{2.31}$$

where τ_1 and τ_2 relate to the Laplacian and Gaussian noises, respectively, and the delay τ is contained in the search range $[-I, I]$. It should be noted that neither $s(n)$ nor the statistical parameters need to be known to compute τ_p.

Thus, the MLEs are identical to minimizing either the least absolute error ($p = 1$, Laplacian) or the least squares error ($p = 2$, Gaussian) between $d^i_{\mathrm{QT}}(n)$ and $d_{\mathrm{QT}}(n + \tau)$. The limits $n_{x,o}$ and $n_{x,e}$ refer to the onset and end points of the selected exercise ($x \equiv e$) or recovery ($x \equiv r$) phase. Thus, four estimates $\tau_{p,x}$ are computed for each exercise ECG stress testing, being p the Laplacian or Gaussian estimator employed ($p = 1, 2$) and x the exercise or recovery phase selected ($x \in \{e, r\}$).

An automatic procedure is designed to determine the boundaries of the recovery and exercise ramps. The exercise onset $n_{e,o}$ (analogously, the recovery end $n_{r,e}$) is taken as the point that results in the minimum mean squared differences between $d^i_{\mathrm{QT}}(n)$ series and a piecewise linear approximation consisting of a plateau (incline, respectively, for $n_{r,e}$) until the candidate point followed by a subsequent incline (plateau, respectively, for $n_{r,e}$). In mathematical terms, the search for $n_{e,o}$ (or $n_{r,e}$) results from minimizing the following cost function [109]:

$$n_{e,o} = \arg \min_m (J(m)), \tag{2.32}$$

where

$$J(m) = \sum_{n=M_1}^{m-1} \left(d^i_{\mathrm{QT}}(n) - f_b(n)\right)^2 + \sum_{n=m}^{M_2} \left(d^i_{\mathrm{QT}}(n) - f_a(n)\right)^2. \tag{2.33}$$

The functions $f_b(n) = a_b + b_b n$ and $f_a(n) = a_a + b_a n$ are the best linear models fitted in the least squares sense of $d^i_{\mathrm{QT}}(n)$ series before and after the candidate sample point m, respectively, being $M_1 = 1$ and $M_2 = n_{pe} - 168$, with n_{pe} the sample corresponding to peak exercise value. For the determination of $n_{r,e}$, an analogous minimization is performed, but in this case $M_1 = n_{pe} + 72$ and M_2 is the last sample in $d^i_{\mathrm{QT}}(n)$.

The end of the exercise phase $n_{e,e}$ is defined as the first sample for which $d^i_{\mathrm{QT}}(n)$ shortened from $n_{e,o}$ by a percentage $100\gamma_e\%$ of the total reduction reached at the peak exercise:

$$n_{e,e}=\arg\min_{n}\left|\gamma_e\left(d^i_{\mathrm{QT}}(n_{e,o})–d^i_{\mathrm{QT}}(n_{pe})\right)-\left(d^i_{\mathrm{QT}}(n_{e,o})–d^i_{\mathrm{QT}}(n)\right)\right|. \tag{2.34}$$

Similarly, the onset of the recovery phase $n_{r,o}$ is identified as the first sample for which $d^i_{\mathrm{QT}}(n)$ increased by a percentage $100\gamma_r\%$ of the total increase reached at $n_{r,e}$:

$$n_{r,o}=\arg\min_{n}\left|(1–\gamma_r)\left(d^i_{\mathrm{QT}}(n_{r,e})–d^i_{\mathrm{QT}}(n_{pe})\right)-\left(d^i_{\mathrm{QT}}(n_{r,e})–d^i_{\mathrm{QT}}(n)\right)\right|. \tag{2.35}$$

With the estimated values of the exercise time lag $\tau_{p,e}$ and recovery time lag $\tau_{p,r}$, the difference between them is studied as an additional marker:

$$\Delta\tau_p=\tau_{p,r}-\tau_{p,e},\quad p=1,2. \tag{2.36}$$

Therefore, three ECG markers from exercise ECG stress testing are proposed in this Ph.D. dissertation: the QT adaptation time lag computed from the exercise and recovery phases, separately, and the difference between them.

An example of $d^i_{\mathrm{QT}}(n)$ and $d_{\mathrm{QT}}(n)$ series from a clinical ECG is shown in Fig. 2.5(b). The time points delimiting the different phases of the test and the estimated delays using the Gaussian estimator are illustrated. The same procedure but using $d_{\mathrm{RR}}(n)$ and $d^i_{\mathrm{RR}}(n)$ series to estimate the desired delays can be seen in Fig. 2.5(c).

In the case of simulated ECGs with controlled τ, see Chap. 3, the performance to estimate the QT adaptation time lag is quantified by the error ϵ_τ between the estimated time lag $\hat{\tau}_{p,x}$ and the true time lag $\tau_{p,x}$ imposed in the simulator:

$$\epsilon_\tau(p,x)=\hat{\tau}_{p,x}-\tau_{p,x},\quad p=1,2;\ x\in\{e,r\}. \tag{2.37}$$

2.7 Modification of the peak exercise window for model fitting

The estimation of the model parameters α and β is based on the assumption that the data pairs $[d_{\mathrm{QT}}(n),d_{\mathrm{RR}}(n)]$ are observed under stationary conditions in the three learning windows defined in Section 2.5. Since this assumption rarely holds for the data pairs in the window centered at the peak exercise, the proposal in this Ph.D. thesis is to replace $[d_{\mathrm{QT}}(n),d_{\mathrm{RR}}(n)]$ with $[d_{\mathrm{QT}}(n)-\Delta_{\mathrm{QT}},d_{\mathrm{RR}}(n)]$.

The decrement Δ_{QT} accounts for the additional shortening of $d_{\mathrm{QT}}(n)$, thus having QT interval values more similar to those that would have been obtained

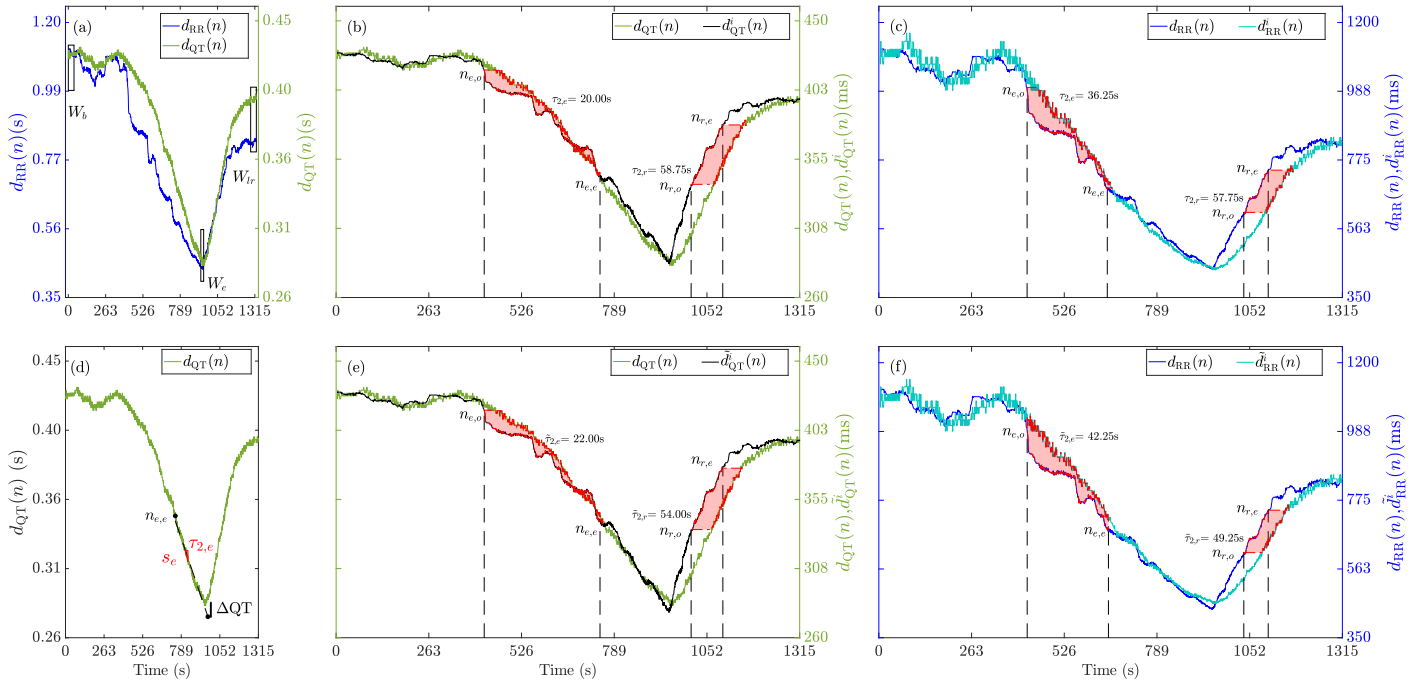

Figure 2.5: Example of the procedure for QT time lag estimation from an exercise ECG stress testing. (a) The time series $d_{\mathrm{RR}}(n)$ is shown together with the boxes defining the three windows, W_b, W_e and W_{lr}, used to estimate the values of the parameters α and β. The time series $d_{\mathrm{QT}}(n)$ is additionally shown. (b) The delimitation of the onset and end sample points in the exercise phase ($n_{e,o}$, $n_{e,e}$) and in the recovery phase ($n_{r,o}$, $n_{r,e}$) is presented. The corresponding QT lags obtained by minimizing the MSE criteria between $d_{\mathrm{QT}}(n)$ and $d^{i}_{\mathrm{QT}}(n-\tau)$ obtained using the Gaussian-based estimator are written for each of the two EST phases. (d) Graphical representation of the procedure proposed to obtain the value of ΔQT, which is used to modify $d_{\mathrm{QT}}(n)$ at the W$_e$ window in peak exercise using $\tau_{p,e}$ derived as in (b). (e) The corresponding exercise and recovery time lags obtained after regression estimation from the modification of the QT values in (d). The two processes for QT delay estimation shown in (a,b) and (c,d), respectively, are repeated but calculating the delay between $d_{\mathrm{RR}}(n)$ and $d^{i}_{\mathrm{RR}}(n)$, shown in panel (c), and the delay between $d_{\mathrm{RR}}(n)$ and $\tilde{d}^{i}_{\mathrm{RR}}(n)$, shown in panel (f).

provided that $d_{\mathrm{RR}}(n)$ had remained stationary long enough at the peak exercise until the time when the data pairs $[d_{\mathrm{QT}}(n), d_{\mathrm{RR}}(n)]$ would be stationary.

Firstly, the exercise time lag $\tau_{p,e}$ between $d_{\mathrm{QT}}(n)$ and $d^i_{\mathrm{QT}}(n)$ estimated considering the originally defined windows is used to compute the subtracting factor Δ_{QT}. Specifically, Δ_{QT} results from multiplying $\tau_{p,e}$ by the absolute value of the QT series slope s_e at the peak exercise: $\Delta_{\mathrm{QT}} = \tau_{p,e} \times s_e$. The value of s_e is calculated as the absolute value of the slope of the linear fit to the QT series from the selected end of the exercise area, $n_{e,e}$, defined in Sec. 2.6, to the point associated with the lowest $d_{\mathrm{QT}}(n)$ value. A graphic example of this process can be seen in Fig. 2.5(d).

Since the use of $[d_{\mathrm{QT}}(n) - \Delta_{\mathrm{QT}}, d_{\mathrm{RR}}(n)]$ data pairs from the exercise window, together with the data pairs from the stationary resting and recovery windows, yields other estimates of α and β, the modified instantaneous QT series is denoted as $\tilde{d}^i_{\mathrm{QT}}(n)$. The resulting $\tilde{d}^i_{\mathrm{QT}}(n)$ series and the corresponding $\tau_{p,e}$ and $\tau_{p,r}$ from an exercise ECG stress testing are shown in Fig. 2.5(e). This definition is also applied when $d_{\mathrm{RR}}(n)$ and $d^i_{\mathrm{RR}}(n)$ series are used to estimate the delays. An example of $\tilde{d}^i_{\mathrm{RR}}(n)$ is shown in Fig. 2.5(f).

To deal with the above assumption even further, the peak exercise window is redefined. In addition to modifying $d_{\mathrm{QT}}(n)$ with Δ_{QT}, the end of the exercise window W_e is aligned with the peak exercise time, denoted as $\check{W}_e$, so that only data pairs from exercise are used. For the modified and aligned window, the resulting instantaneous QT series is denoted as $\check{d}^i_{\mathrm{QT}}(n)$.

Thus, the following three definitions of instantaneous QT series are studied separately to render three different estimates of the QT adaptation time lags (the notation for the associated delay estimates are indicated in parentheses): $d^i_{\mathrm{QT}}(n)$ $(\tau_{p,x})$, $\tilde{d}^i_{\mathrm{QT}}(n)$ $(\tilde{\tau}_{p,x})$, and $\check{d}^i_{\mathrm{QT}}(n)$ $(\check{\tau}_{p,x})$. The block diagram in Fig. 2.6 shows the procedure to estimate α and β using the data pairs in the three concatenated windows $W_b \cup \left(W_e \text{ or } \check{W}_e\right) \cup W_{lr}$.

2.8 Conditions on RR and QT trends for time lag estimation

The output $d^i_{\mathrm{QT}}(n)$ of the memoryless transformation is fed to a linear, time-invariant, first-order filter $h(n)$, which is shown in Fig. 2.3. The impulse response is given by:

$$h(n) = \kappa e^{-n/\tau} u(n), \tag{2.38}$$

where τ is the memory time constant, expressed in samples, here considered as the QT adaptation time lag, κ is a constant whose value is chosen so that the

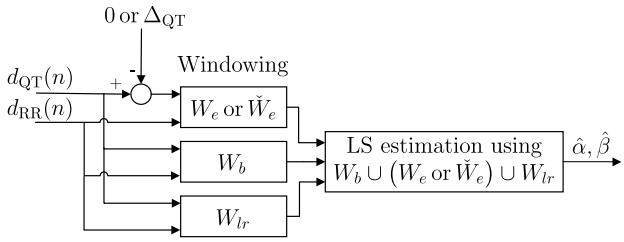

Figure 2.6: Estimation of α and β, defining the memoryless transformation $g\left(d_{\mathrm{RR}}(n); \alpha, \beta\right)$, which is based on $[d_{\mathrm{QT}}(n), d_{\mathrm{RR}}(n)]$ (or corresponding modifications) in the three concatenated learning windows. In the first case, the estimation uses the unmodified series $d_{\mathrm{QT}}(n)$ in the window W_e, with the instantaneous QT series being $d^i_{\mathrm{QT}}(n)$. In the second case, the estimation uses the series $d_{\mathrm{QT}}(n)$ in the window W_e but modified by subtracting Δ_{QT}, with the instantaneous QT series being $\tilde{d}^i_{\mathrm{QT}}(n)$. In the third case, the estimation uses the series $d_{\mathrm{QT}}(n)$ modified by subtracting Δ_{QT} in the window $\check{W}_e$, with the instantaneous QT series being $\check{d}^i_{\mathrm{QT}}(n)$. LS, least square.

filter has unitary gain and $u(n)$ is the unit step function. The output of the filter $h(n)$ is the modeled QT series $d_{\mathrm{mQT}}(n)$, which results in the time series $d_{\mathrm{QT}}(n)$ after adding the noise $w(n)$ accounting for modeling and delineation errors.

When $d_{\mathrm{RR}}(n)$ is better characterized by a low-frequency trend, denoted as $s(n)$, that does not exactly correspond to a linear trend, it can be shown that the first-order system $h(n)$ still behaves as a time-delay system provided that the spectral content of $s(n)$ is below a certain frequency.

The discrete-time Fourier transform of $h(n)$ in (2.38) has the following expression:

$$H(\omega) = \frac{\kappa}{1 - e^{-1/\tau} e^{-j\omega}}. \tag{2.39}$$

For healthy subjects, $\tau \approx 25$ s [83] and, accordingly, the system has a cut-off frequency $F_c = (2\pi\tau)^{-1} \approx 0.006$ Hz ($\omega_c \approx 0.01$), so the magnitude of the frequency response $H(\omega)$ can be approximated, for $\omega \ll 0.01$, by:

$$|H(\omega)| = \frac{\kappa}{\sqrt{1 - 2e^{-1/\tau}\cos(w) + e^{-2/\tau}}} \approx \frac{\kappa e^{1/\tau}}{e^{1/\tau} - 1}. \tag{2.40}$$

For $1/\tau \ll 1$, the phase of the frequency response, $\angle H(\omega)$, can be approximated by:

$$\angle H(\omega) = -\arctan\left(\frac{\sin(w)}{e^{1/\tau} - \cos(w)}\right) \approx -\frac{\omega}{e^{1/\tau} - 1} \approx -\omega\tau, \tag{2.41}$$

thus resulting in the following approximate expression for $H(\omega)$:

$$H(\omega) \approx \frac{\kappa e^{1/\tau}}{e^{1/\tau} - 1} e^{-j\omega\tau}, \tag{2.42}$$

which is a pure delay system for frequencies below F_c.

Therefore, in order to estimate τ by measuring the delay between $d_{\mathrm{QT}}(n)$ and $d^i_{\mathrm{QT}}(n)$, the trend $s(n)$ does not need to be a linear ramp, as assumed in (2.18), but it suffices that its frequency content is below F_c. The time series $d^i_{\mathrm{QT}}(n)$ and $d_{\mathrm{QT}}(n)$ can be still be modeled as in (2.18):

$$\left.\begin{aligned} d^i_{\mathrm{QT}}(n) &= s(n) + v^i(n), \\ d_{\mathrm{QT}}(n) &= s(n-\tau) + v(n), \end{aligned}\right\} n = 0, ..., N-1, \tag{2.43}$$

and the estimates derived in Sec. 2.6 remain as valid ML estimates. Both $v^i(n)$ and $v(n)$ account for short-term, beat-to-beat QT variability and delineation errors. The noise components $v^i(n)$ and $v(n)$ are statistically independent as $v(n)$ reflects uncertainty in determining the Q wave onset and T wave end, whereas $v^i(n)$ reflects uncertainty in determining the R wave position.

2.9 Interchangeability of QT-RR model blocks

In contrast to the original QT-RR model proposed in [83], illustrated in Fig. 2.7, $g_f\left(d_{\mathrm{RR}}(n); \alpha, \beta\right)$ is here placed before the first-order system $h(n)$, not after it (see Fig. 2.3). The two orderings are not mathematically equivalent since $g_f\left(d_{\mathrm{RR}}(n); \alpha, \beta\right)$ is typically nonlinear. In mathematical terms, the modeled

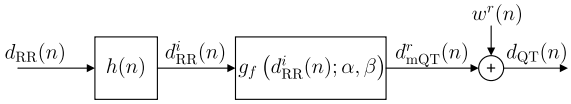

Figure 2.7: QT-RR model with a reversed block order, cf. Fig. 2.3. Note that the so-called reverted estimate of the QT series $d^r_{\mathrm{mQT}}(n)$ and the so-called reverted model of the delineation error $w^r(n)$ differ from their equivalent in Fig.2.3 , but the sum results in the observed $d_{\mathrm{QT}}(n)$ series in both cases, $d_{\mathrm{QT}}(n) = d^r_{\mathrm{mQT}}(n) + w^r(n)$.

QT series proposed in this Ph.D. thesis (Fig. 2.3) is given by:

$$d_{\mathrm{mQT}}(n) = \sum_{m=0}^{\infty} g_f(d_{\mathrm{RR}}(n-m))h(m). \tag{2.44}$$

In the following, the proposed model (Fig. 2.3) is shown to be approximately equal to the model with the reversed block order, for which the output of the second block is denoted as $d^r_{\mathrm{mQT}}(n)$. For convenience, $g_f(d_{\mathrm{RR}}(n);\alpha,\beta)$ is shortened to $g_f(d_{\mathrm{RR}}(n))$.

The starting point is to truncate the sum in (2.44) to include only up to the sample M of $h(n)$, with $M \approx 5\tau$, as the remaining samples have negligible significance. Thus,

$$d_{\mathrm{mQT}}(n) \approx \sum_{m=0}^{M} g_f(d_{\mathrm{RR}}(n-m))h(m). \tag{2.45}$$

Since $d_{\mathrm{RR}}(n-m)$ typically exhibits small changes around $d_{\mathrm{RR}}(n)$ in the interval $m \in [0, M]$, the first-order approximation of the Taylor series expansion of $g_f(d_{\mathrm{RR}}(n-m))$ around $d_{\mathrm{RR}}(n)$ becomes

$$d_{\mathrm{mQT}}(n) \approx \sum_{m=0}^{M} \left[g_f(d_{\mathrm{RR}}(n)) + g'_f(d_{\mathrm{RR}}(n))(d_{\mathrm{RR}}(n-m) - d_{\mathrm{RR}}(n))\right] h(m), \tag{2.46}$$

where $g'_f(d_{\mathrm{RR}}(n))$ denotes the first derivative. Assuming that $h(n)$ has unitary gain at zero frequency, the first-order approximation becomes:

$$d_{\mathrm{mQT}}(n) \approx g_f(d_{\mathrm{RR}}(n)) + g'_f(d_{\mathrm{RR}}(n))(d^i_{\mathrm{RR}}(n) - d_{\mathrm{RR}}(n)), \tag{2.47}$$

where $d^i_{\mathrm{RR}}(n) = \sum_{m=0}^{M} d_{\mathrm{RR}}(n-m)h(m)$. The series $d^i_{\mathrm{RR}}(n)$ can be interpreted as the expected memoryless RR interval series corresponding to the observed $d_{\mathrm{QT}}(n)$ under stationary conditions. By observing the equation (2.47), it becomes clear that this expression is a Taylor series approximation around $d_{\mathrm{RR}}(n)$ of the memoryless transformation that relates $d^i_{\mathrm{RR}}(n)$ to $d_{\mathrm{QT}}(n)$ and, thus,

$$\begin{aligned} d_{\mathrm{mQT}}(n) &\approx g_f(d^i_{\mathrm{RR}}(n)) = g_f\left(\sum_{m=0}^{M} d_{\mathrm{RR}}(n-m)h(m)\right) \\ &\approx g_f\left(\sum_{m=0}^{\infty} d_{\mathrm{RR}}(n-m)h(m)\right) = d^r_{\mathrm{mQT}}(n). \end{aligned} \tag{2.48}$$

The above result confirms the interchangeability of the model blocks in Fig. 2.3 under the described assumptions.

The input–output relation of the model in Fig. 2.3 is approximately equal to the original QT-RR model proposed in [83] if τ is small relative to the span

required for RR intervals to change significantly, showing that the block order is interchangeable. It is not clear which of the two orders is better to model the underlying physiological behavior. The order in Fig. 2.3 is better suited to estimate τ as it allows $d^i_{\mathrm{QT}}(n)$ to be paired with $d_{\mathrm{QT}}(n)$. The order in Fig. 2.7 is the one to use to pair $d^i_{\mathrm{RR}}(n)$ to $d_{\mathrm{RR}}(n)$, as commented on in Sec. 2.5.1.

CHAPTER 3

ECG SIMULATOR

3.1 Motivation

In Chapter 2, we have defined the methodology to estimate the QT adaptation time lag from the gradual heart rate changes that can be observed in EST. These gradual changes, rather than the sudden changes in Holter recordings, can always be observed during EST and therefore serve as a useful basis for time lag estimation.

Since a gold standard to determine the true time lag from real exercise ECG stress testing is lacking, the simulation of ECG signals is particularly well-suited to evaluate the performance of the proposed time lag estimation in the presence of QT dynamics with known and controllable properties.

ECG simulation has been shown to represent a powerful tool for evaluation and comparison of methods performance under controlled conditions. The simulated ECG signals can range from simple test signals to signals with complex characteristics, as for instance the signals generated by models to simulate maternal and fetal ECGs [110–112], TWA [113] and paroxysmal AF [93]. The cited simulators have in common that they are based on mathematical models of relevant physiological phenomena, while they do not pretend to model detailed biophysical mechanisms. Moreover, the purpose of these available ECG simulation tools is very specific.

Currently, Machine Learning tools are being increasingly used to extract specific aspects of ECGs, to group individuals based on their ECG signals or even to make diagnosis based on this signal. However, the models based on a black box usually neglect the physiological and mathematical aspects that may be behind cardiac changes [114]. Nonetheless, ECG signals generated by simulators can be additionally used to train neural networks, which can help overcome the issue of overfitting. This highlights the importance of simulating ECG signals based on realistic criteria.

Focusing on the exercise ECG stress testing, although there have been advances in simulating ECG signals similar to those measured during EST [115–117], there is a gap in the literature when it comes to including the relationship between the PR interval and the heart rate in a simulated environment. Some studies have shown that the length of the PR interval is not constant and has a certain dependence on heart rate [118, 119]. As a consequence, as heart rate increases, unless including proper modeling of this PR dependence with the heart rate, an overlap between the P wave and the T wave frequently occurs. Also, modeling muscle noise (MN) present in ECG signals is also a field that is poorly researched. Behar *et al.* [111] defined a model that modified the frequency spectrum over time slightly, but did not add any variation in power. Furthermore, defining time-varying conditions, that is, including temporal variations in the heart rate, noise and respiration, are required to properly model exercise ECG stress testing. The QT memory time lag in simulations was first introduced in the work by [90].

To adapt the currently available simulators to our simulation requirements for exercise ECG stress testing, the work of this Ph.D. thesis contributes to the improvement of the simulator proposed by [93], resulting in a recently proposed version which can model various cardiac conditions, including arrhythmias of atrial and ventricular origin, PQ and QT interval changes related to heart rate, and a known QT-RR adaptation time lag [120]. Moreover, this simulator offers statistical, time-varying modeling of MN, motion artifacts, and respiration,

which are components of particular significance when simulating ECGs recorded during exercise.

In this chapter, the contributions of this Ph.D. thesis to a new ECG simulator [120] are presented. Such contributions are necessary to generate simulated ECGs whose components are similar to those observed in EST.

3.2 Modeling the dynamics of sinus rhythm variability and its dependency with respiration

The RR intervals in sinus rhythm (SR) can be modeled as an associated HRV oscillating over a mean RR interval, which can also be time-varying.

Based on the McSharry *et al.* model [115] and the definition of SR in the ECG simulator of Petrenas *et al.* [93], the HRV power spectrum is assumed to be a bimodal power spectrum composed of a Gaussian, related to baroreflex regulation ("low-frequency component") and centered around a low frequency F_{LF}, and another Gaussian, related to parasympathetic stimulation ("high-frequency component") and centered around a time-varying high-frequency (HF) coincident with the respiratory frequency $F_{\mathrm{HF}}(t) = F_r(t)$. Here, the model is enhanced with respect to that in [93] to add the time-varying property. So, for $\Omega \geqslant 0$, the time-varying HRV power spectrum is defined by:

$$S_{\mathrm{RR}}(t,\Omega) = \frac{P_{\mathrm{LF}}(t)}{\sqrt{2\pi\sigma_{\mathrm{LF}}^2}} e^{-\frac{(\Omega-2\pi F_{\mathrm{LF}})^2}{2\sigma_{\mathrm{LF}}^2}} + \frac{P_{\mathrm{HF}}(t)}{\sqrt{2\pi\sigma_{\mathrm{HF}}^2}} e^{-\frac{(\Omega-2\pi F_r(t))^2}{2\sigma_{\mathrm{HF}}^2}}, \tag{3.1}$$

and, due to symmetry, $S_{\mathrm{RR}}(t,\Omega) = S_{\mathrm{RR}}(t,-\Omega)$. The powers $P_{\mathrm{LF}}(t)$ and $P_{\mathrm{HF}}(t)$ and the center frequency of the HF component $F_r(t)$ are time-varying, whereas the widths σ_{LF}^2 and σ_{HF}^2 and the center frequency F_{LF} are time-invariant.

An RR interval signal $d_{\mathrm{RR}}(t)$, whose properties are described by (3.1), is generated by linear filtering of white noise $v_{\mathrm{RR}}(t)$ so that the LF component is the output of the time-invariant filter $h_{\mathrm{LF}}(t)$ and the HF component is the output of the time-varying filter $h_{\mathrm{HF}}(t; F_r(t))$,

$$d_{\mathrm{RR}}(t) = \left(\sqrt{P_{\mathrm{LF}}(t)}h_{\mathrm{LF}}(t) + \sqrt{P_{\mathrm{HF}}(t)}h_{\mathrm{HF}}(t; F_r(t))\right) * v_{\mathrm{RR}}(t) + m_{\mathrm{RR}}(t), \tag{3.2}$$

where $m_{\mathrm{RR}}(t)$ represents the time-varying mean RR interval.

To derive the expression of the impulse responses of the filters, we start by recalling that the power spectrum of filtered white noise with variance $\sigma_{v,\mathrm{RR}}^2$

is given by the expression $S_{\mathrm{RR}}(t,\Omega) = |H(t,\Omega)|^2\sigma^2_{v,\mathrm{RR}}$, which implies that the frequency response of each of the filters is given by the square root of the power spectrum of a Gaussian. Applying the square root to each of the two terms in (3.1), it can be observed that terms of the following form appear:

$$H(\Omega) = e^{-\frac{|\Omega|}{\sigma}}. \tag{3.3}$$

Based on the Fourier transform pair $e^{-\upsilon|t|} \rightarrow \frac{2\upsilon}{\upsilon^2+\Omega^2}$ and the property that the transform of $F(t)$ is $2\pi f(-\Omega)$, where $F(\Omega)$ is the Fourier transform of $f(t)$, the impulse response $h(t)$, which is the inverse Fourier transform of the expression in (3.3), results in:

$$h(t) = \frac{1}{2\pi}\frac{\frac{2}{\sigma}}{\frac{1}{\sigma^2}+t^2}. \tag{3.4}$$

For the particular case where $\sigma^2 = 2\sigma^2_{\mathrm{LF}}$, the previous expression can be written as:

$$h(t) = \frac{1}{2\pi}\frac{\frac{\sqrt{2}}{\sigma_{\mathrm{LF}}}}{\frac{1}{2\sigma^2_{\mathrm{LF}}}+t^2}. \tag{3.5}$$

Introducing a shift in frequency to obtain $\Omega - \Omega_{\mathrm{LF}} = \Omega - 2\pi F_{\mathrm{LF}}$, knowing that the Fourier transform of $f(t)\cos(\Omega_0 t) \rightarrow \frac{1}{2}\left[F(\Omega-\Omega_0)+F(\Omega+\Omega_0)\right]$, and introducing the proper scaling factors in (3.1) and (3.2), the impulse response $h_{\mathrm{LF}}(t)$ becomes

$$h_{\mathrm{LF}}(t) = \frac{1}{\sqrt[4]{\pi^4 2\pi\sigma^2_{\mathrm{LF}}}}\frac{\frac{\sqrt{2}}{\sigma_{\mathrm{LF}}}}{\frac{1}{2\sigma^2_{\mathrm{LF}}}+t^2}\cos(2\pi F_{\mathrm{LF}}t). \tag{3.6}$$

Operating and applying the same transformation to the HF component, the two filter impulse responses are:

$$h_{\mathrm{LF}}(t) = \sqrt[4]{\frac{32}{\pi^5}}\frac{\sqrt{\sigma_{\mathrm{LF}}}}{1+2\sigma^2_{\mathrm{LF}}t^2}\cos(2\pi F_{\mathrm{LF}}t), \tag{3.7}$$

$$h_{\mathrm{HF}}(t;F_r(t)) = \sqrt[4]{\frac{32}{\pi^5}}\frac{\sqrt{\sigma_{\mathrm{HF}}}}{1+2\sigma^2_{\mathrm{HF}}t^2}\cos(2\pi F_r(t)t). \tag{3.8}$$

The discrete-time implementation is achieved by sampling each impulse response symmetrically around $t = 0$ until its envelope falls below 5% of its

peak value; the same sampling rate as that of $d_{\mathrm{RR}}(t)$ and $F_r(t)$ is used. Since the filters $h_{\mathrm{LF}}(t)$ and $h_{\mathrm{HF}}(t; F_r(t))$ are noncausal, each filter needs to be shifted by half its length to become causal.

Although the definition of a time-dependent frequency in the HF filter might be questioned, the implemented shift represents the nonstationarity of respiratory rate. Its inclusion accounts for the HRV frequency range dependent on respiratory rates, which is restrictive within a frequency band.

3.3 Modeling the influence of time-varying respiration on the ECG

Respiration is manifested in the ECG by relatively periodic changes in the electrical axis of the heart as well as changes in heart rate. So, asymmetric filling and emptying of the lungs produce rotation of the VCG loop and consequently variations in QRS morphology [121–123]. Since the respiratory frequency depends on the degree of physical effort, the assumption of a fixed respiratory frequency in [93] is generalized to become time-varying. Changes in heart rate due to respiration are modeled by a time-varying respiratory component of the HRV power spectrum, which has been already described in previous section.

To introduce this effect into the simulated ECG, the starting point is the respiratory interval tachogram, i.e. a series of successive respiration intervals $T_{r,0}, T_{r,1}, \ldots$, which can be transformed to a time-varying respiratory frequency $F_r(t)$ through the use of the inverse interval function [3].

The reference simulated, noise-free VCG signal $\mathbf{u}_{\mathrm{VCG}}(t)$ is transformed by rotation, defined by the product of three planar rotations around each of the X, Y, and Z axes,

$$\mathbf{x}(t) = \mathbf{Q}_{\mathrm{X}}(t)\mathbf{Q}_{\mathrm{Y}}(t)\mathbf{Q}_{\mathrm{Z}}(t)\mathbf{u}_{\mathrm{VCG}}(t), \tag{3.9}$$

where $\mathbf{u}_{\mathrm{VCG}}(t)$ is a 3×1 vector containing the values of the three orthogonal ECG lead at time t and the rotation matrices

$$\mathbf{Q}_{\mathrm{X}}(t) = \begin{bmatrix} 1 & 0 & 0 \\ 0 & \cos\varphi_{\mathrm{X}}(t) & \sin\varphi_{\mathrm{X}}(t) \\ 0 & -\sin\varphi_{\mathrm{X}}(t) & \cos\varphi_{\mathrm{X}}(t) \end{bmatrix}, \tag{3.10}$$

$$\mathbf{Q}_{\mathrm{Y}}(t) = \begin{bmatrix} \cos\varphi_{\mathrm{Y}}(t) & 0 & \sin\varphi_{\mathrm{Y}}(t) \\ 0 & 1 & 0 \\ -\sin\varphi_{\mathrm{Y}}(t) & 0 & \cos\varphi_{\mathrm{Y}}(t) \end{bmatrix}, \tag{3.11}$$

$$\mathbf{Q}_{\mathrm{Z}}(t) = \begin{bmatrix} \cos\varphi_{\mathrm{Z}}(t) & \sin\varphi_{Z}(t) & 0 \\ -\sin\varphi_{\mathrm{Z}}(t) & \cos\varphi_{\mathrm{Z}}(t) & 0 \\ 0 & 0 & 1 \end{bmatrix}, \tag{3.12}$$

are defined by the time-varying angle rotations on each respective axis: $\varphi_{\mathrm{X}}(t), \varphi_{\mathrm{Y}}(t)$, and $\varphi_{\mathrm{Z}}(t)$.

Introducing a template respiratory cycle $\phi(t)$, the angular variation is assumed to be proportional to the amount of air in the lungs, modeled as the product of two logistic functions accounting for inspiration and expiration [123, 124],

$$\phi(t; \delta_{\mathrm{in}}, \delta_{\mathrm{ex}}) = \frac{1}{1 + e^{-\gamma_{\mathrm{in}}(t-\delta_{\mathrm{in}})}} \frac{1}{1 + e^{\gamma_{\mathrm{ex}}(t-\delta_{\mathrm{ex}})}}, \tag{3.13}$$

where γ_{in} and γ_{ex} define the steepness of inspiration and expiration, respectively, and δ_{in} and δ_{ex} are positive-valued and uniformly distributed, defining the approximate duration of inspiration and expiration, respectively. The angular variation in each of the leads $o \in \{\mathrm{X}, \mathrm{Y}, \mathrm{Z}\}$ is modeled by

$$\varphi_o(t) = \xi_o \sum_{p=0}^{\infty} \alpha_{o,p} \phi\left(\frac{t - \sum_{q=0}^{p} T_{r,q}}{s_p}; \delta_{\mathrm{in},p}, \delta_{\mathrm{ex},p} \right), \tag{3.14}$$

where $\xi_o > 0$ is the maximum variation (expressed in degrees), $\alpha_{o,p}$ is a uniformly distributed amplitude, T_r is the duration of the template respiratory cycle, and $s_p = T_{r,p}/T_r$ is a scaling factor ensuring that the p:th cycle has the duration $T_{r,p}$.

As an example, for a linearly increasing $F_r(t)$ and a linearly decreasing $m_{\mathrm{RR}}(t)$, the angular function $\varphi_{\mathrm{X}}(t)$ and the RR interval signal $d_{\mathrm{RR}}(t)$ are illustrated in Figs. 3.1(a) and (b), respectively. The resulting simulated ECG is illustrated in Fig. 3.1(c).

For the particular cases of simulating an ECG similar to that obtained from EST, P_{LF}(t) and P_{HF}(t) are modulated by the results from [125]. This study analyzes both normalized median powers in five different intervals during maximal EST according to oxygen consumption: the basal phase (before starting the exercise phase), three intervals during the exercise phase (0-60%, 60-80% and 80-100%), and the recovery phase, named as I_b, I_{60}, I_{80}, I_{100} and I_r respectively. These are used to fit the intermediate values linearly along EST. Besides, the median values are randomly changed in each simulation using a standard deviation of 0.05.

Figure 3.2(a) represents an example of both m_{RR}(t) and Fr(t) pattern defined by the user to generate a final d_{RR}(t) (Fig. 3.2(c)), whose HRV is

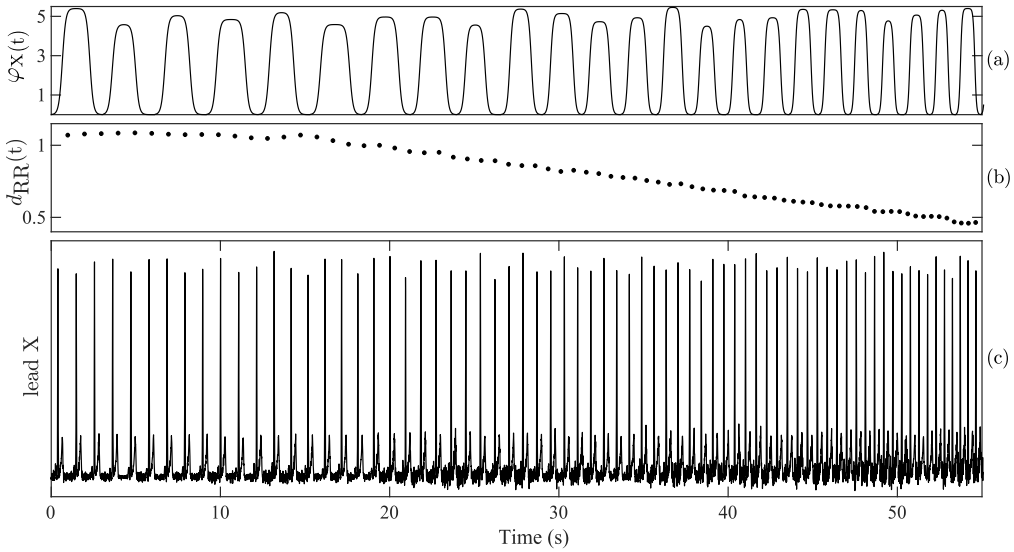

Figure 3.1: Time-varying respiratory frequency, linearly increasing from 0.2 to 0.5 Hz in a 60-s interval, influencing (a) the angular function $\varphi_X(t)$ (radians), partially describing the variation in the electrical axis, (b) the variation in RR intervals, visible at the end of the RR interval signal $d_{RR}(t)$ (expressed in seconds), and (c) the simulated ECG in lead X. The noise level gradually increases to mimic an exercise stress test.

calculated based on the time-varying $P_{LF}(t)$ and $P_{HF}(t)$ normalized powers presented in Fig. 3.2(b).

3.4 Modeling the influence of heart rate on the PQ interval

A model is proposed to account for the dependence of the PQ interval on heart rate. When simulating ECGs in time-varying conditions it is crucial to deal with this dependence, since the P wave tends to overlap with the T wave at high heart rates, e.g. during EST.

A simple nonlinear, memoryless model is introduced in this Ph.D. thesis to include the PQ interval dependence on heart rate at higher heart rates. The model builds on the physiological finding that the PR interval depends on heart rate at higher heart rates, while otherwise independent [118]. However, since the QR duration does not change significantly at higher heart rates [126], the dependence of the PQ interval $d_{PQ}(d_{RR}(k))$ on the preceding RR interval

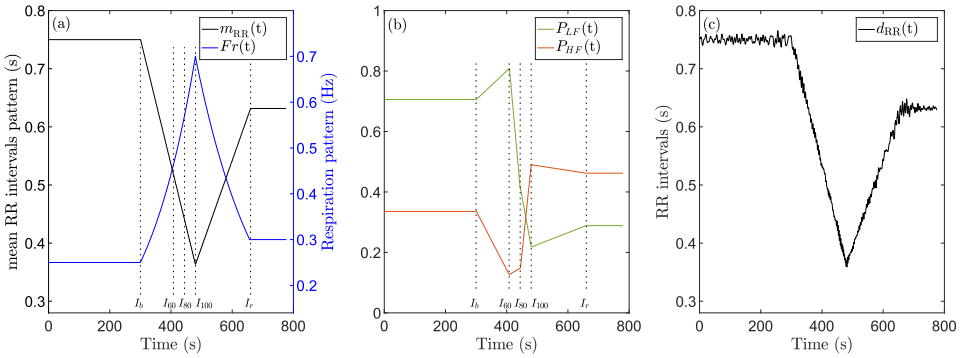

Figure 3.2: (a) Mean RR intervals $m_{\mathrm{RR}}(\mathrm{t})$ and time-varying respiratory frequency $Fr(\mathrm{t})$ whose patterns are similar to the ones observed from EST. (b) P_{LF} (t) and P_{HF} (t) powers modulated throughout the test according to the progression of RR intervals. (c) The resulting $d_{\mathrm{RR}}(\mathrm{t})$ series.

$d_{\mathrm{RR}}(k)$ of the k-th beat can be modeled by the following expression:

$$d_{\mathrm{PQ}}(d_{\mathrm{RR}}(k)) = \begin{cases} d_{\mathrm{PQ}_0} + \kappa_{\mathrm{PQ}}(d_{\mathrm{RR}}(k) - d_{\mathrm{RR,cp}}), & d_{\mathrm{RR}}(k) < d_{\mathrm{RR,cp}}; \\ d_{\mathrm{PQ}_0}, & d_{\mathrm{RR}}(k) \geqslant d_{\mathrm{RR,cp}}, \end{cases} \tag{3.15}$$

where d_{PQ_0} is the baseline PQ interval observed at lower heart rates, κ_{PQ} is the slope of the linear dependence, and $d_{\mathrm{RR,cp}}$ is the change point for the dependence. Thus, assuming that the P wave duration is independent of heart rate, the P wave onset is positioned $d_{\mathrm{PQ}}(d_{\mathrm{RR}}(k))$ seconds before QRS onset.

The values of the parameters d_{PQ_0}, κ_{PQ}, and $d_{\mathrm{RR,cp}}$ can be estimated by analyzing the dependence between PQ and RR intervals in subjects performing EST. Then, the range of RR intervals is divided into B_{RR} bins of equal width, and the median of the PQ intervals contained in each bin is computed, resulting in $d_{\mathrm{med}}(b) \equiv d_{\mathrm{PQ}}(d_{\mathrm{RR}}(b)), b = 1, \ldots, B_{\mathrm{RR}}$. The bin corresponding to the change point is estimated by minimizing the following least square error function with respect to b_0:

$$\begin{aligned} \varepsilon(b_0) = & \sum_{b=1}^{b_0} w(b)(d_{\mathrm{med}}(b) - d_{\mathrm{PQ}_0} - \kappa_{\mathrm{PQ}}(d_{\mathrm{RR}}(b) - d_{\mathrm{RR,cp}}))^2 \\ & + \sum_{b=b_0+1}^{B_{\mathrm{RR}}} w(b)(d_{\mathrm{med}}(b) - d_{\mathrm{PQ}_0})^2, \end{aligned} \tag{3.16}$$

thus yielding $\hat{d}_{\mathrm{RR,cp}} = d_{\mathrm{RR}}(\hat{b}_0)$. The weights $w(b)$ are taken as the number of subjects contributing to the b-th bin.

The estimation procedure is illustrated by analyzing ECGs recorded from patients with low risk of suffering CAD performing EST. The signals are selected from the database presented in Sec 5.2.1. The onset of the QRS complex is obtained by applying a single-lead plus rule wavelet [100] delineation to the 8 independent standard leads. The onset of the P wave is obtained by delineating the TL1 after applying spatial periodic component analysis to the 8 independent standard leads to improve the signal quality.

As hysteresis is observed when the PQ-RR relation is studied in the exercise and recovery phases independently [119], the values of the parameters in (3.15) are defined for decelerated heart rate using the information of the recovery part of EST. The estimated parameter values are shown in Table 3.1.

Table 3.1: Estimated values of the PQ interval model parameters in time-varying conditions for exercise and recovery phases, independently. The baseline PQ interval d_{PQ_0} is selected randomly an uniform distribution within the defined range using .

	d_{PQ_0}	$\hat{d}_{\mathrm{PQ}_0}$	$\hat{\kappa}_{\mathrm{PQ}}$	$\hat{d}_{\mathrm{RR,cp}}$
Exercise	$[140-160]$ ms	152 ms	0.358	520 ms
Recovery	$[130-150]$ ms	139 ms	0.470	430 ms

Figure 3.3(a) shows the median of all PQ intervals in each of the RR interval bins to which the function in (3.15) is fitted, for exercise and recovery phases separately. Figures 3.3(b)-(c) show simulated ECGs with and without the inclusion of the PQ–RR dependence, respectively. Without the PQ–RR dependence, P waves occur too far away from the QRS complex at high heart rates, thus not reflecting normal electrophysiological behavior.

Finally, the P wave is modeled as a linear combination of Hermite functions as in [93]. The duration of this wave can be considered time invariant and independent of heart rate. The duration of the P wave is set to be 120 ms.

3.5 Modeling the influence of heart rate on the QT interval

To simulate realistic ECGs that account for the QT interval adaptation to RR interval changes [47], an input–output model is introduced that makes it possible to simulate ECGs and use them to validate the methodology for QT lag estimation proposed in this Ph.D. thesis. This improvement in the ECG simulator is first implemented by Martín-Yebra *et al.* [90], with the QT interval

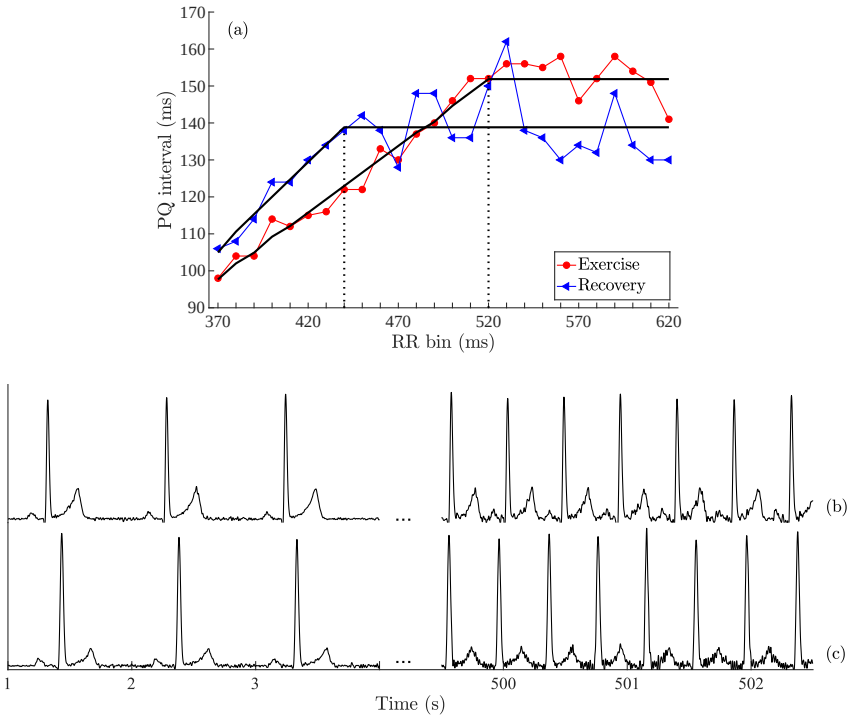

Figure 3.3: (a) The median of the PQ intervals contained in each RR interval bin for exercise (red curve) and recovery (blue curve), separately. The fitted functions are represented in black, and the values of $\hat{d}_{\mathrm{RR,cp}}$ are indicated by vertical dotted lines. (b) Simulated ECG with PQ–RR dependence modeled at low and high heart rates. (c) Simulated ECG without modeling the PQ–RR dependence, causing the P waves to be incorrectly hidden in the T waves at a high heart rate.

adaptation being composed of a fast, initial phase extending a few RR intervals and a subsequent slow phase lasting for several minutes [64].

Here, the input–output relation between the preceding RR intervals $d_{\mathrm{RR}}(n)$ and the QT interval $d_{\mathrm{QT}}(n)$ (Fig. 2.7) in the ECG simulator is defined by a finite impulse response filter, whose output is denoted $d^{i}_{\mathrm{RR}}(n)$, followed by a memoryless nonlinear function. The impulse response $h(n)$ is a truncated exponential,

$$h(n) = \frac{(1-\varrho)}{(1-\varrho^{N})}\varrho^{n}, \quad n = 0, \ldots, N-1, \tag{3.17}$$

whose length N corresponds to 300 s based on physiological considerations. The exponential decay ϱ ($0 < \varrho < 1$) is related to the time constant τ through $\varrho = e^{-\frac{1}{\tau}}$, where the value of τ can be defined by the user. Based on the

results in [47], the model output $d_{\mathrm{QT}}(n)$ is taken to be inversely related, with a hyperbolic relation, to $d^i_{\mathrm{RR}}(n)$,

$$d_{\mathrm{QT}}(n) = \beta + \frac{\alpha}{d^i_{\mathrm{RR}}(n)}, \tag{3.18}$$

where the values of α and β are defined according to the results obtained from the analysis of the clinical database defined in Sec. 5.2.1.

The QT interval of each k-th beat is then modified by resampling the T wave while maintaining the QRS duration so that the QT interval becomes equal to that indicated by the model. The model for QT–RR adaptation has proven useful not only in SR [47] but also in AF [90].

3.6 Modeling of time-varying muscle noise

Noise modeling is an essential part of any simulator aiming to generate realistic signals that can challenge the performance of a signal processing method. To account for time-varying spectral characteristics, time-varying autoregressive (AR) models driven by white Gaussian noise have been proposed for modeling of baseline wander [110] and MN [111]. In these studies, most of the model parameters are estimated from the PhysioNet MIT–BIH Noise Stress Test Database (NSTDB), resulting either in time-varying filter parameter estimates [110] or fixed filter parameter estimates made time-varying by letting the position of related pole pairs vary according to a random walk model [111].

The modeling of MN, commonly observed in EST, receives special attention. The filtered white noise approach serves as the starting point for MN modeling, but is altered in several respects to account for prominent characteristics such as a time-varying level of MN. Hence, the noise added to the noise-free simulated ECG is assumed to consist of MN $x_{\mathrm{MN}}(n)$. Baseline wander is less critical to model and therefore not considered here. It should be noted that each lead is corrupted by individual noise realizations, and, consequently, no interlead correlation is introduced in the simulated ECG. A diagram of MN modeling is shown in Fig. 3.4.

Muscle noise $x_{\mathrm{MN}}(n)$ is modeled as a nonstationary AR(p) process, defined by the following difference equation:

$$x_{\mathrm{MN}}(n) = a_{1,n}x_{\mathrm{MN}}(n-1) + \cdots + a_{p,n}x_{\mathrm{MN}}(n-p) + w(n), \tag{3.19}$$

where $w(n)$ is white, Gaussian noise with time-varying variance $\sigma^2_w(n)$ and p is the model order. The time-varying parameters $a_{1,n}, \ldots, a_{p,n}$ are estimated

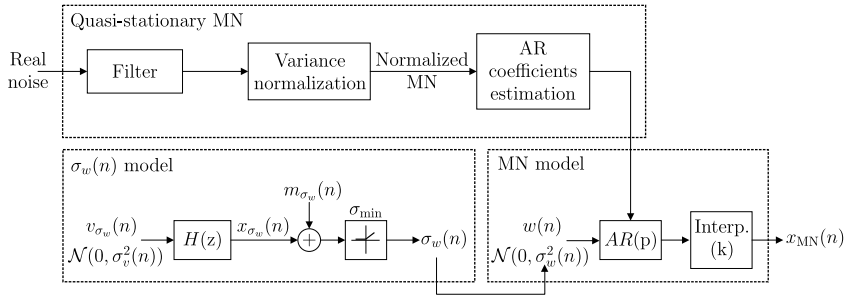

Figure 3.4: Muscle noise (MN) model with input information from a real MN signal.

using a two-step procedure. Firstly, the parameters of a stationary AR(p) model, i.e., $a_1, \ldots, a_p$, are estimated using a PQRST-cancelled, filtered and amplitude-normalized ECGs, recorded during EST [103]. Filtering is performed to ensure that the resulting signal closely approximates MN one. First, a 10-80 Hz bandpass filter is applied followed by a nonlinear 50 Hz notch filter to remove the 50 Hz contamination [3]. The normalization of the amplitude, achieved by means of the envelope of the canceled signal, is motivated by the large variation in the noise level. Since the spectral content of MN is confined to frequencies well below 100 Hz, parameter estimation is performed on signals sampled at a rate of 200 Hz to ensure a low-order AR model, taken to be $p = 4$. Hence, the sampling rate of the model output needs to be increased to the rate of the simulated ECG (1000 Hz). Secondly, the poles related to $\hat{a}_1, \ldots, \hat{a}_p$ are made time-varying using a simple random walk model [111].

Although the spectral properties of MN do not vary much over time, the noise level itself can vary considerably. These two characteristics are illustrated in Fig. 3.5. The following first-order model of how the standard deviation $\sigma_w(n)$ of $w(n)$ in (3.19) varies over time is proposed:

$$x_{\sigma_w}(n+1) = \nu x_{\sigma_w}(n) + v_{\sigma_w}(n), \tag{3.20}$$

$$\sigma_w(n) = \max(\sigma_{w,\min}, m_{\sigma_w}(n) + x_{\sigma_w}(n)), \tag{3.21}$$

where $v_{\sigma_w}(n)$ is white, Gaussian noise with variance σ_v^2; thus, the variance σ_x^2 of $x_{\sigma_w}(n)$ is $\sigma_x^2 = \sigma_v^2/(1-\nu^2)$. The initial value $x_{\sigma_w}(0)$ is set to 0 and the filter parameter ν is constrained to $[0, 1]$. The standard deviation $\sigma_w(n)$ is composed of $m_{\sigma_w}(n)$, defining the mean noise level of the simulated ECG, and $x_{\sigma_w}(n)$, defining its variation. While a constant mean noise level is used as default, i.e. $m_{\sigma_w}(n) \equiv m_{\sigma_w}$, other definitions are certainly possible, e.g. to let $m_{\sigma_w}(n)$ gradually increase over time to mimic the noise profile of EST. The half-wave

rectifier in (3.21) is introduced to ensure that $\sigma_w(n)$ exceeds a certain minimum level $\sigma_{w,\min}$.

Noise modeling is illustrated in Fig. 3.6 by simulated, single-lead ECGs paired with similar-looking real ECGs extracted from recordings made during EST, ambulatory monitoring, and handheld AF screening.

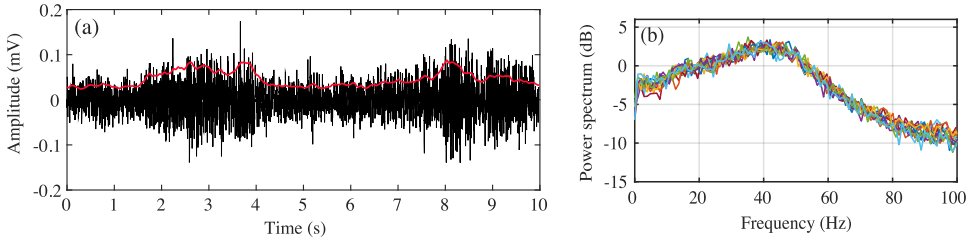

Figure 3.5: Typical examples of (a) time-varying muscle noise (the envelope is displayed in red), and (b) several superimposed muscle noise power spectra (logarithmic scale) displayed up to 100 Hz, computed in successive 1-min intervals. The analyzed signals were recorded during exercise stress testing [103].

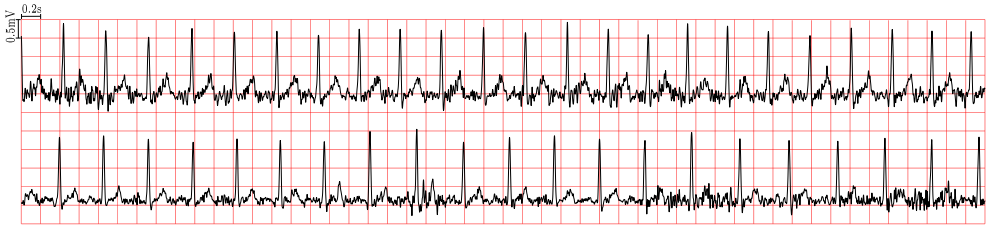

Figure 3.6: Single-lead, 10-s simulated ECG (top) and similar-looking real ECG (bottom) with muscle noise. The simulated ECG is generated according to equation (3.19).

CHAPTER 4

PERFORMANCE EVALUATION OF QT-RR ADAPTATION TIME LAG ESTIMATES IN EXERCISE ECG STRESS TESTING

4.1 Motivation

In Chapter 2, we defined a new methodology to estimate the QT adaptation time as the delay between the observed QT intervals and the QT intervals derived from the observed RR intervals using a memoryless transformation, assuming that the QT interval time series are corrupted with Gaussian or Laplacian noise. From the QT adaptation analysis, three markers were proposed: the delay measured in the exercise phase, the delay measured in the recovery phase and the difference between these two delays. Before assessing the clinical capacity of the proposed markers for CAD risk stratification, the validation of the developed methods is critical to ensure their reliability.

To address the challenges related to the validation of the methods described in Chapter 2, the open-access ECG simulator introduced in Chapter 3 is used here to generate simulated ECGs that mimic realistic RR and QT interval time series during EST, with a known time lag between them, with time-varying characteristics as in clinical exercise ECGs stress testing and with different noise levels.

The simulator provides a controlled environment where the performance of algorithms can be rigorously tested and validated. Here, different datasets with simulated ECGs are generated to: (1) study the performance of each lead space reduction technique proposed to delineate the T wave end using a reference mark; (2) evaluate the error between the estimated and the true QT time lag for several SNRs and different estimator structures; (3) demonstrate that the time lag estimation can be applied not only to linearly changing heart rate trends but also to trends having low-frequency components using simulated ECGs, mimicking EST heart rate trends; and (4) determine the potential advantages, in terms of estimation variance, when using RR series rather than QT series for QT time lag estimation.

Therefore, this chapter emphasizes the importance of simulated ECGs for the evaluation of both the delineation of the T wave and the estimation of the QT adaptation time lag using known values to allow characterizing the corresponding errors. These references for the evaluation, which are here obtained from simulated ECGs, are often not available when performing clinical validation, as manual marks annotated by clinicians for e.g. T wave delineation assessment are required and not always available or they may even be inaccessible, as in the case of the assessment of the QT adaptation time lag.

4.2 Simulated datasets

The following features provided by the ECG simulator described in Chapter 3 [120] are of particular relevance for simulating exercise ECGs stress testing: (a) user-defined heart rate trends; (b) inclusion of MN and motion artifacts with time-varying properties, commonly observed during exercise and recovery; (c) PQ interval being dependent on heart rate; and (d) full control of the QT adaptation time lag τ.

The simulations described in this chapter rely mostly on the default settings given in [120], including the hyperbolic, memoryless transformation,

$$g_f(d_{\mathrm{RR}}(n);\alpha,\beta) = \beta + \frac{\alpha}{d_{\mathrm{RR}}(n)}. \tag{4.1}$$

The modeling of RR intervals, MN, motion artifacts and respiratory rate are defined to account for pertinent characteristics of the four phases that together form an EST, i.e., rest (for notation reasons referred to as basal), exercise, early recovery and late recovery, whose respective endpoints are denoted as t_b, t_e, t_{er} and t_{lr}, see Fig. 4.1. The statistics of the duration of the exercise and early recovery phases are determined from 25 tests [103], while the basal and late recovery phases are set to 10 min.

Four different datasets are generated, each consisting of 400 simulated (500 in the case of the fourth dataset), standard 12-lead ECGs, sampled at a rate of 1000 Hz. Examples of ECGs from each of these datasets are shown in Fig. 4.1 and are described in the next subsections.

4.2.1 Simulated, typical exercise ECGs

This dataset, named $\mathcal{D}_t$, contains simulated ECGs defined by a template RR interval pattern mimicking typical EST trends. This template is defined by four phases: (1) constant mean RR interval during rest, $[0, t_b]$; (2) linearly decreasing trend of RR interval during exercise; $[t_b, t_e]$; (3) linearly increasing trend of RR interval during early recovery; $[t_e, t_{er}]$, and (4) constant mean RR interval during late recovery, $[t_{er}, t_{lr}]$. The values defining phase 1, phase 4 and the end of phase 2 of the RR template are obtained by computing the inter-patient mean of the intra-patient RR interval means at rest, recovery and exercise learning windows, respectively, using ECGs of 215 patients with low risk of CAD (see Table 5.1 for dataset details). The series $d_{\mathrm{RR}}(n)$ is obtained by adding variability to the RR interval template trend, using the model in [93] (see

Section 3.2 for more details). Figure 4.1(a) illustrates a template RR interval time series and a simulated $d_{\mathrm{RR}}(n)$ time series across the four phases.

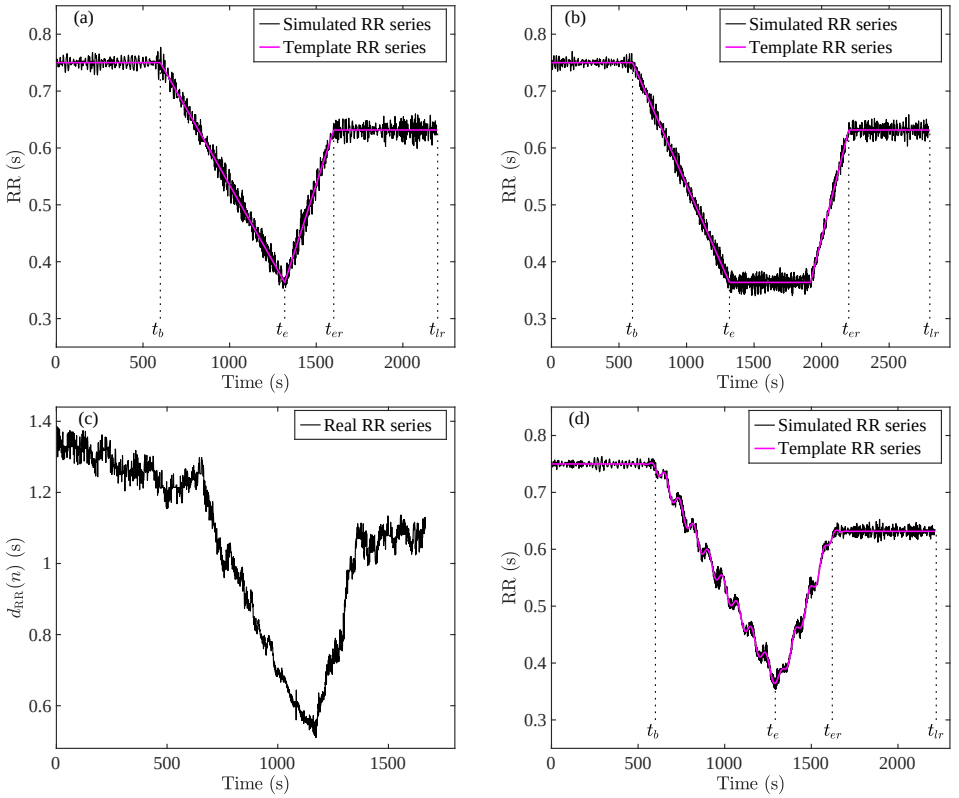

Figure 4.1: Template RR interval pattern and observed RR interval series $d_{\mathrm{RR}}(n)$ extracted from the four datasets: (a) $\mathcal{D}_t$, containing typical exercise ECGs with the four phases (rest: ending at t_b; exercise: ending at t_e; early recovery: ending at t_{er}; and late recovery: ending at t_{lr}); (b) $\mathcal{D}_{ee}$, containing exercise ECGs with extended exercise; (c) $\mathcal{D}_r$, containing exercise ECGs using real RR intervals; and (d) $\mathcal{D}_o$, containing typical exercise ECGs with oscillatory exercise|recovery trend.

A template pattern is also provided for the variance of MN, defined by the four phases: (1) constant; (2) linearly increasing to become four times higher at t_e than at t_b; (3) linearly decreasing until t_{er}; and (4) identical to the constant in phase 1. Together with the generated MN, motion artifacts are randomly included with an occurrence probability of 40% (see [120] for details).

The SNR at peak exercise is defined by

$$\mathrm{SNR} = 20 \log_{10} \left(\frac{A_{\mathrm{QRS}}}{\mathrm{RMS}_{\mathrm{noise}}} \right), \tag{4.2}$$

where A_{QRS} is the peak-to-peak amplitude of the ensemble-averaged QRS complex, determined in a 100-ms interval centered around the R-peak (see [90, 123] for details). The MN signal is rescaled so that its RMS value in a window of 60 s at peak exercise equals $\mathrm{RMS}_{\mathrm{noise}}$. All leads are assumed to have the same SNR. Simulated ECGs at different SNRs are exemplified in Fig. 4.2.

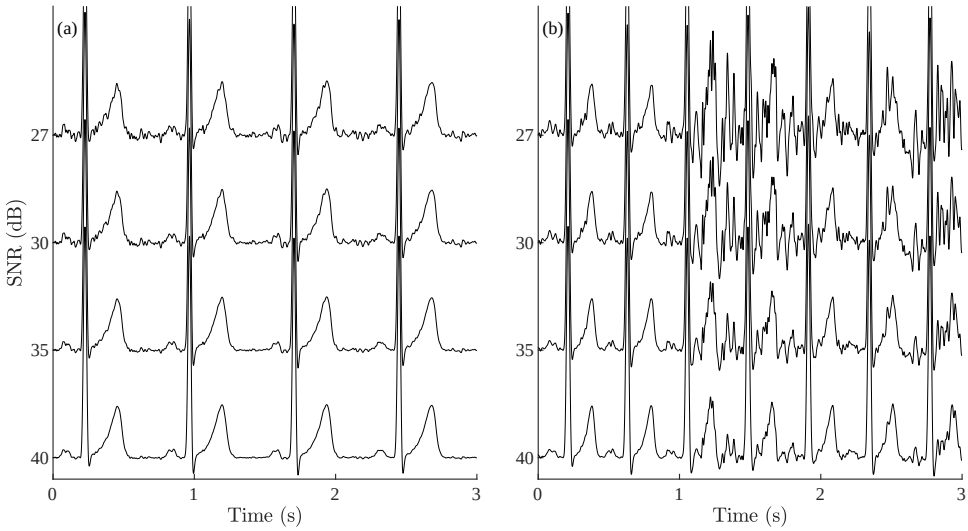

Figure 4.2: Simulated ECGs (lead V_4) with different SNRs at (a) low or (b) high heart rate.

The respiratory rate changes across the four phases according to a template pattern similar to the one defined for the MN variance [123]: (1) constant; (2) linearly increasing until t_e; (3) linearly decreasing until t_{er}; and (4) identical to the constant in phase 1. This respiratory rate modulates heart rate variability and QRS-T complex morphology [120].

The dataset $\mathcal{D}_t$ is obtained by simulating 25 ECGs for all combinations of τ and SNR values, with the following values being considered:

$$\tau_s = \{20, 30, 40, 50\} \text{ s}, \tag{4.3}$$

$$\mathrm{SNR}_s = \{27, 30, 35, 40\} \text{ dB}, \tag{4.4}$$

where the different SNRs correspond to the following RMS values: $\{45, 32, 18, 10\}$ μV. Thus, in total, $\mathcal{D}_t$ contains $25 \cdot 4 \cdot 4 = 400$ ECGs. The range of τ_s is based on the delay estimates obtained from the analysis of ECGs from low CAD risk patients contained in the database described in Sec. 5.2.1.

An example of the $d_{\mathrm{RR}}(n)$ series extracted for an ECG of this dataset is illustrated in Fig. 4.3(a), together with the windows that are used to estimate the values of the parameters α and β in (4.1). Figure 4.3(b) presents the corresponding $d^i_{\mathrm{QT}}(n)$ series, where the delay between this and the observed $d_{\mathrm{QT}}(n)$ series is clearly discernible, serving as an estimate of τ. The onset and end of the intervals used for time lag estimation during exercise and recovery are also depicted. The estimation of the parameter values that define the position of $n_{e,e}$ and $n_{r,o}$ points according to the methodology presented in Sec. 2.6 are described in Sec. 5.4.4. The methodology described in Fig. 2.4 is also evaluated, so the corresponding $d^i_{\mathrm{RR}}(n)$ series is shown in Fig. 4.3(b). In this case, the delay is estimated between the observed $d_{\mathrm{RR}}(n)$ and $d^i_{\mathrm{RR}}(n)$ series, where the larger range in the RR series transitions as compared to QT series transitions is evident.

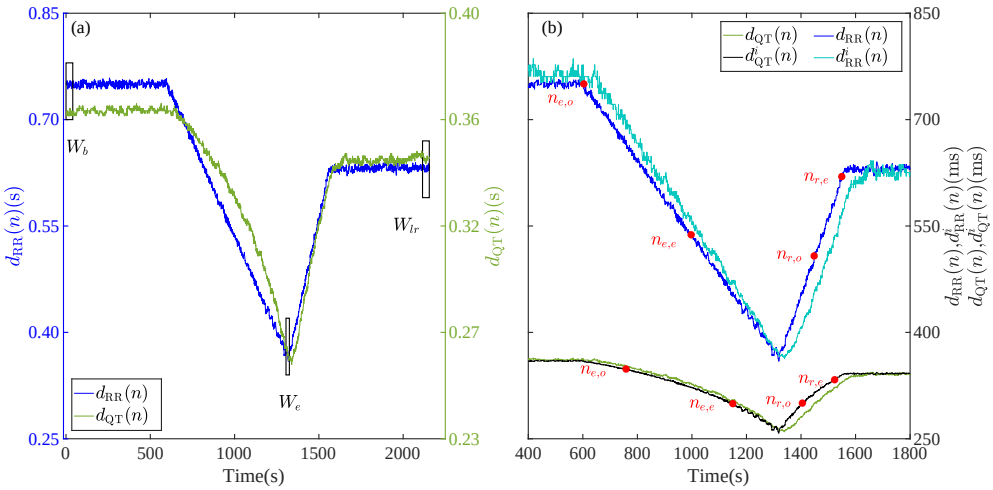

Figure 4.3: (a) An observed RR series $d_{\mathrm{RR}}(n)$ is presented together with the learning windows positioned at rest (W_b), exercise (W_e) and late recovery (W_{lr}), which are indicated by boxes. (b) An observed QT series $d_{\mathrm{QT}}(n)$ and the related instantaneous QT series $d^i_{\mathrm{QT}}(n)$ are shown, where the intervals for time lag estimation are delimited by $n_{e,o}$ and $n_{e,e}$ for exercise and $n_{r,o}$ and $n_{r,e}$ for recovery. An observed RR series $d_{\mathrm{RR}}(n)$ and the related instantaneous RR series $d^i_{\mathrm{RR}}(n)$ is also represented. The series $d_{\mathrm{RR}}(n)$ and $d_{\mathrm{QT}}(n)$ are obtained from a simulated, typical exercise ECG (see Sec. 4.2.1).

4.2.2 Simulated exercise ECGs with extended peak exercise

This dataset, named $\mathcal{D}_{ee}$, is generated in exactly the same way as $\mathcal{D}_t$, except that the peak exercise is extended for 10 min with constant mean RR interval, constant MN variance and constant respiratory rate (see Fig. 4.1(b)). Therefore, $\mathcal{D}_{ee}$ contains also 400 ECGs. When analyzing $\mathcal{D}_{ee}$, the end of the exercise learning window is aligned with the onset of early recovery. This position ensures that both the observed QT interval and the observed heart rate at peak exercise have become stationary and, consequently, α and β can be estimated from stationary data in the three learning windows.

Moreover, $\mathcal{D}_{ee}$ makes it possible to study the effect of nonstationarity in the exercise window W_e separately from the effect of selecting data pairs from only three windows during EST.

4.2.3 Simulated exercise ECGs using real RR intervals

This dataset, named $\mathcal{D}_r$, is generated using 25 different RR series from clinical exercise ECG stress testing [127], one of them displayed in Fig. 4.1(c). The use of real RR series as input to the simulator is motivated by the observation that RR trends during exercise and recovery can deviate considerably from a linear ramp, which makes the use of real RR series a valuable complement to simulated RR series when evaluating the performance of QT time lag estimation. Although the evaluation could have been based exclusively on simulated linear ramps, the use of real RR series is a means to validate the derivation in Section 2.8, showing that the estimate of τ is equally valid as long as the deviation of the trends from a linear ramp has frequency components of sufficiently low frequency. The same combination of SNR and τ_s values described in (4.2) and (4.3), respectively, are used to generate this dataset.

4.2.4 Simulated exercise ECGs with oscillatory heart rate trend

This dataset, named $\mathcal{D}_o$, contains simulated ECGs defined by a linear trend template of an RR interval pattern mimicking typical EST trends plus an added low-frequency oscillation of frequency F during both exercise and recovery. Simulated MN is added to ECGs with an SNR of 40 dB. This dataset is used to validate our hypothesis that the requirement of a linear heart rate trend can be relaxed to any change in the trend as long as its frequency content is below a certain frequency $F_c = 1/(2\pi\tau_s)$.

The dataset is obtained by simulating 25 ECGs for every combination of τ_s from (4.3) and oscillation frequency F, with values:

$$F \in \{0.002, 0.004, 0.006, 0.008, 0.01\} \text{ Hz}. \tag{4.5}$$

The range of F is below and slightly above the F_c imposed by τ_s.

The values of the parameters defining the mean duration of EST, heart rate and respiratory rate of the four simulated datasets are listed in Table 4.1.

Table 4.1: User-defined simulation parameters.

	Phase	$\mathcal{D}_t$	$\mathcal{D}_{ee}$	$\mathcal{D}_r$	$\mathcal{D}_o$
Mean duration of the exercise stress tests (min)	rest	10	10	5	10
	exercise	12	12	8	12
	extended peak exercise	–	10	–	–
	early recovery	5	5	3	5
	late recovery	10	10	4	10
Mean heart rate (beats per min)	rest	80	80	69	80
	peak exercise	165	165	139	165
	end of early recovery	95	95	81	95
Respiratory rate (breaths per min)	rest	15	15	–	15
	peak exercise	42	42	–	42
	end of early recovery	18	18	–	18

4.3 Results

4.3.1 T wave end delineation

The performance of the T wave end delineation is evaluated by the ϵ_θ error described in (2.10) for conditions closely resembling those of EST and using a T wave end reference. The results from the six delineation methods derived from different lead space reduction techniques and MLeads, all of them described in Sec. 2.3, are compared.

For the union of $\mathcal{D}_t$ and $\mathcal{D}_r$, the mean bias m_{ϵ_θ} and standard deviation σ_{ϵ_θ} of the delineation error ϵ_θ among records are presented in Fig. 4.4 for different types of lead space reduction and SNRs. The results show that the space reduction techniques GπCA$_\text{p}$ and PCA always offer better performance than

MLeads, with the lowest error being obtained for any GπCA$_{\mathrm{p}}$ method when the SNR decreases. The difference in m_{ϵ_θ} between these methods becomes smaller at higher SNRs. The statistically significant p-values are shown in the table included in Fig. 4.4. Although the lowest m_{ϵ_θ} is obtained for GπCA$_1$|GπCA$_3$, the GπCA$_{1,\mathrm{o}}$ technique is selected to compute the T wave end required to obtain QT series (see Sec. 2.5) since this shows similar results and avoids recomputing the transformation matrix. An additional reason for selecting this technique related to the variation of the T wave morphology due to the increase|decrease in heart rate along the EST will be commented on in Sec. 5.4.2. It should be noted that the statistical significance reported in the table depends on the number of simulations and, consequently, only comparisons in relative terms are meaningful.

4.3.2 Estimation of α and β

Table 4.2 presents the mean $m_{\hat{\alpha}}$ and the standard deviation $\sigma_{\hat{\alpha}}$ of $\hat{\alpha}$ and $\hat{\beta}$ for the three definitions of the instantaneous QT series given in Sec. 2.7, i.e. $d^i_{\mathrm{QT}}(n)$, $\tilde{d}^i_{\mathrm{QT}}(n)$, and $\check{d}^i_{\mathrm{QT}}(n)$. The parameters α and β have been assigned values identical to those used for the simulation in [120]. The main observation to be made from Table 4.2 is that $\hat{\alpha}$ and $\hat{\beta}$ are both biased since $m_{\hat{\alpha}}$ and $m_{\hat{\beta}}$ deviate considerably from their respective true values α and β. This observation applies to $\mathcal{D}_t$, $\mathcal{D}_r$ and $\mathcal{D}_{ee}$.

The origin of the bias can be understood from an experiment in which α and β are studied using a dataset of 25 simulated ECG (with SNR = 40 dB and $\tau = 40$ s) whose template RR series decreases step-wise from exercise onset to end, here taken to be 10 steps, each with a 5-min duration, as illustrated in Fig. 4.5. The last part of each step is then used as a learning window with stationary conditions, thereby providing denser sampling of data pairs when fitting $g_f(d_{\mathrm{RR}}(n); \alpha, \beta)$ than that provided by the typical template RR pattern from EST. The estimates of α and β resulting from using the data pairs of each step, denoted as $\hat{\alpha}_s$ and $\hat{\beta}_s$, are much closer to those obtained from $\mathcal{D}_t$, $\mathcal{D}_r$ and $\mathcal{D}_{ee}$ (see Table 4.2). This points to the origin of the bias being different to the fact that the analysis is restricted to the three learning intervals. The origin can be attributed to the automatic delineation system, whose criterion for identification of the T wave end applied to wider or narrower T waves, corresponding to lower or higher heart rates, presents a differential behavior. In particular, since such criterion uses a threshold based on the derivative, it generates an artificially different relation between the QT and RR intervals than that imposed in the simulator, which justifies the bias in the estimation of the

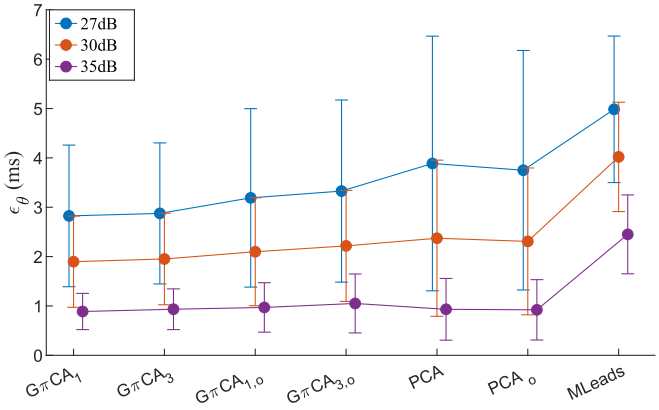

Significant p-values

	$G\pi CA_{1,o}$	$G\pi CA_{3,o}$	PCA	PCA_o	MLeads
SNR = 27 dB					
$G\pi CA_1$	0.026	0.003	<0.001	<0.001	<0.001
$G\pi CA_3$	-	0.006	<0.001	<0.001	<0.001
$G\pi CA_{1,o}$	-	-	0.002	0.009	<0.001
$G\pi CA_{3,o}$	-	-	0.013	-	<0.001
SNR = 30 dB					
$G\pi CA_1$	0.048	0.002	<0.001	<0.001	<0.001
$G\pi CA_3$	-	0.010	<0.001	<0.001	<0.001
$G\pi CA_{1,o}$	-	-	<0.001	<0.001	<0.001
$G\pi CA_{3,o}$	-	-	0.045	-	<0.001
SNR = 35 dB					
$G\pi CA_1$	-	0.001	-	-	<0.001
$G\pi CA_3$	-	0.023	-	-	<0.001
$G\pi CA_{1,o}$	-	-	-	-	<0.001
$G\pi CA_{3,o}$	-	-		0.030	<0.001

Figure 4.4: Top panel: mean and standard deviation of the T wave end delineation error ϵ_θ, $m_{\epsilon_\theta} \pm \sigma_{\epsilon_\theta}$ (ms), for different lead space reduction techniques and different SNRs. The results are based on $\mathcal{D}_t \cup \mathcal{D}_r$ and include all values of τ listed in (4.3), yielding a total of 600 ECGs. Bottom panel: table showing only the statistical significance p-values. The Mann-Whitney U test is applied for the comparisons between two techniques.

α and β values. Nevertheless, since this will apply to all records and situations, it is expected not to affect the potential of the method for characterization of clinical information and patient stratification.

4.3.3 QT-RR adaptation time lag estimation using $\mathcal{D}_t$ and $\mathcal{D}_r$

The estimation performance is investigated for the time lags and SNRs given in (4.3) and (4.4), respectively. The results are expressed in terms of mean bias m_{ϵ_τ} and standard deviation σ_{ϵ_τ} of the time lag error ϵ_τ, cf. (2.37), and presented for exercise and recovery, separately. Using $d^i_{\mathrm{QT}}(n)$, $\tilde{d}^i_{\mathrm{QT}}(n)$, and $\check{d}^i_{\mathrm{QT}}(n)$ in combination with the Laplacian noise assumption, the results obtained from $\mathcal{D}_t$

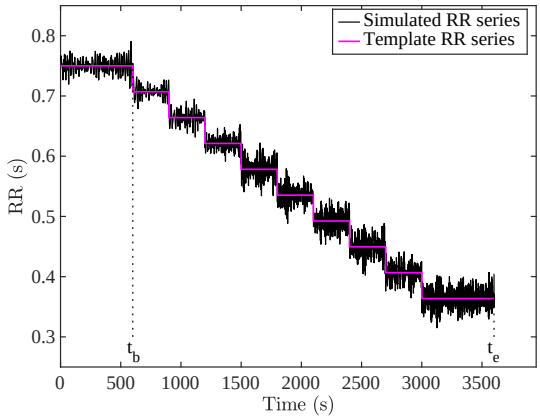

Figure 4.5: Template RR interval pattern and observed RR interval series $d_{\mathrm{RR}}(n)$ extracted from the datasets with decreasing RR intervals during exercise. $\mathrm{t_b} \equiv$ rest phase, $\mathrm{t_e} \equiv$ exercise phase.

Table 4.2: Mean $m_{\hat{\alpha}}$ and standard deviation $\sigma_{\hat{\alpha}}$ computed for different datasets and definitions of the instantaneous QT series.

Simulated value		α		β	
		-0.090		0.490	
Estimates obtained from dense sampling of $g_f(d_{\mathrm{RR}}(n); \alpha, \beta)$		$\hat{\alpha}_s$		$\hat{\beta}_s$	
		-0.078		0.461	
Dataset	Inst. QT series	$m_{\hat{\alpha}}$	$\sigma_{\hat{\alpha}}$	$m_{\hat{\beta}}$	$\sigma_{\hat{\beta}}$
$\mathcal{D}_{ee}$	$d^i_{\mathrm{QT}}(n)$	-0.078	0.005	0.459	0.012
$\mathcal{D}_t$	$d^i_{\mathrm{QT}}(n)$	-0.074	0.004	0.454	0.011
	$\tilde{d}^i_{\mathrm{QT}}(n)$	-0.078	0.004	0.461	0.010
	$\check{d}^i_{\mathrm{QT}}(n)$	-0.077	0.004	0.459	0.010
$\mathcal{D}_r$	$d^i_{\mathrm{QT}}(n)$	-0.074	0.005	0.456	0.012
	$\tilde{d}^i_{\mathrm{QT}}(n)$	-0.079	0.005	0.462	0.012
	$\check{d}^i_{\mathrm{QT}}(n)$	-0.078	0.005	0.461	0.012

and $\mathcal{D}_r$ are presented in Fig. 4.7. The reason for considering the results based on the Laplacian noise assumption rather than on the Gaussian one is provided at the end of this subsection. Using $d^i_{\mathrm{QT}}(n)$, $\tau_{1,e}$ is typically underestimated during exercise since m_{ϵ_τ} is negative, while $\tau_{1,r}$ is typically overestimated during recovery since m_{ϵ_τ} is positive. Moreover, m_{ϵ_τ} increases as τ becomes longer.

This tendency can be observed by analyzing the difference between the time

lag estimates obtained during recovery and exercise, i.e., $\Delta\hat{\tau}_1$, indicated as "Rec. minus Exe." in Fig. 4.7. The larger the time lag, the larger the bias. Since the time lag in the simulated ECGs is the same during exercise and recovery, a value of $\Delta\hat{\tau}_1$ closer to 0 indicates that the method offers a more accurate estimate. These observations apply to both $\mathcal{D}_t$ and $\mathcal{D}_r$, see Figs. 4.7(a)–(d) and (i)–(l), respectively.

Using $\tilde{d}^i_{\mathrm{QT}}(n)$ and $\check{d}^i_{\mathrm{QT}}(n)$, the under- and overestimation become less pronounced than for $d^i_{\mathrm{QT}}(n)$, where $\check{d}^i_{\mathrm{QT}}(n)$ is the better choice of the two. In addition, m_{ϵ_τ} is essentially independent of τ for $\tilde{d}^i_{\mathrm{QT}}(n)$ and $\check{d}^i_{\mathrm{QT}}(n)$. The estimate $\Delta\hat{\tau}_1$ is closer to 0 for $\check{d}^i_{\mathrm{QT}}(n)$ than for $\tilde{d}^i_{\mathrm{QT}}(n)$, confirming a more accurate estimation when using the modified and aligned learning window at exercise $\check{W}_e$. However, the improvement in m_{ϵ_τ} for $\tilde{d}^i_{\mathrm{QT}}(n)$ and $\check{d}^i_{\mathrm{QT}}(n)$ is traded for a larger σ_{ϵ_τ} during exercise, whereas σ_{ϵ_τ} differs only slightly between $d^i_{\mathrm{QT}}(n)$, $\tilde{d}^i_{\mathrm{QT}}(n)$ and $\check{d}^i_{\mathrm{QT}}(n)$ during recovery. Again, these observations apply to both $\mathcal{D}_t$ and $\mathcal{D}_r$, as shown in Figs. 4.7(e)–(h) and (m)–(p), respectively.

In general, m_{ϵ_τ} is not largely influenced by the SNR value when analyzing $\mathcal{D}_t$ and $\mathcal{D}_r$, whereas σ_{ϵ_τ} decreases for increasing SNR. Similar findings to the ones commented previously can be observed using the Gaussian assumption, see Fig. 4.8, which leads to results that are very similar to those of the Laplacian assumption (Fig. 4.7).

The results obtained from $\mathcal{D}_t$ and $\mathcal{D}_r$ are similar, thus supporting the derivation in Section 2.8, which shows that $s(n)$ does not have to be a linear ramp, but it can indeed be a trend whose spectral content is below a certain frequency.

The estimates of τ are also calculated between the observed RR series and $d^i_{\mathrm{RR}}(n)$, $\tilde{d}^i_{\mathrm{RR}}(n)$ and $\check{d}^i_{\mathrm{RR}}(n)$ separately, both for the Laplacian and the Gaussian noise assumption, presented in Fig. 4.9 and Fig. 4.10, respectively. Although a slightly lower m_{ϵ_τ} can be observed using the instantaneous RR series than using the instantaneous QT series, the tendency of the estimated values of τ are the same as those analyzed using the instantaneous QT series.

To study the statistical distribution of the observed QT intervals, the histogram of the difference $\Delta d_{\mathrm{QT}}(k) = d_{QT}(k) - \bar{d}_{QT}(k)$ is calculated, where $d_{QT}(k)$ is the QT interval of the k-th beat and $\bar{d}_{QT}(k)$ is the running median QT interval of five consecutive beats. Then, in the least square error sense, the best fit of the Laplacian and the Gaussian probability density functions to the histogram is determined, denoted as ϱ_L and ϱ_G, respectively. Using the simulated datasets $\mathcal{D}_t$ and $\mathcal{D}_r$, the least square error associated with the

Laplacian assumption is $\varrho_L = 0.0076$ a.u., while the error associated with the Gaussian assumption is $\varrho_G = 0.0099$ a.u., which justifies the use of the Laplacian assumption. The corresponding histogram is represented in Fig. 4.6.

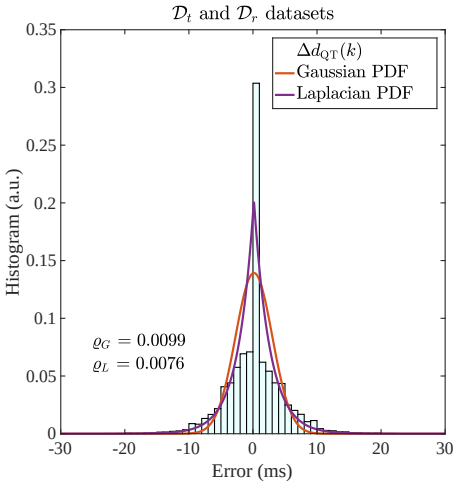

Figure 4.6: Histogram of $\Delta d_{\mathrm{QT}}(k)$ and best fitted Gaussian and Laplacian probability density functions (PDFs) for the simulated dataset $\mathcal{D}_t$. Fitting errors ϱ_G and ϱ_L are shown.

4.3.4 QT-RR adaptation time lag estimation using $\mathcal{D}_{ee}$

The peak exercise in $\mathcal{D}_{ee}$ is extended by 10 min to ensure that the QT and RR time series are stationary in the exercise window. Therefore, only $d^i_{\mathrm{QT}}(n)$ is relevant to use when analyzing this dataset, while $\tilde{d}^i_{\mathrm{QT}}(n)$ and $\check{d}^i_{\mathrm{QT}}(n)$ are not, as they aim to reduce the nonstationarity of the exercise window. By comparing the results obtained from $\mathcal{D}_{ee}$ with those from $\mathcal{D}_t$ and $\mathcal{D}_r$, the extent to which the estimation of τ is influenced by the nonstationarity is indicated.

The results from $\mathcal{D}_{ee}$ show that $\tau_{1,e}$ and $\tau_{1,r}$ are over- and underestimated, respectively, see Figs. 4.14(a)–(d), which stand in contrast to the results obtained from $\mathcal{D}_t$ and $\mathcal{D}_r$ where $\tau_{1,e}$ and $\tau_{1,r}$ are under- and overestimated, respectively, cf. Sec 4.3.3. This difference in time lag bias is unexpected since the data in the exercise window is stationary. This result is likely explained by the reduced RR interval range in this window compared to the exercise window of $\mathcal{D}_t$ or $\mathcal{D}_r$.

The importance of having a sufficiently wide RR interval range is illustrated in Fig. 4.11 where $[d_{\mathrm{QT}}(n), d_{\mathrm{RR}}(n)]$ are displayed for the three learning windows together with the fitted functions $g_f(d_{\mathrm{RR}}(n); \hat{\alpha}, \hat{\beta})$. Using $d^i_{\mathrm{QT}}(n)$ on $\mathcal{D}_t$ and

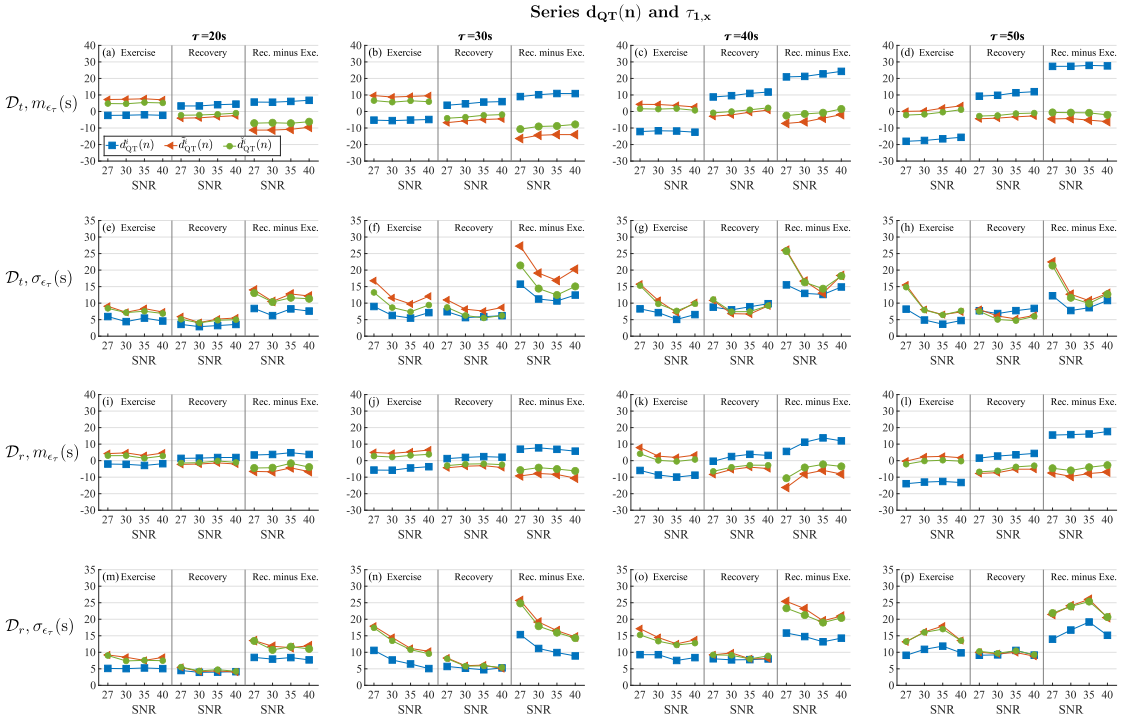

Figure 4.7: Mean m_{ϵ_τ} and standard deviation σ_{ϵ_τ} of the time lag error ϵ_τ in exercise, recovery and the difference between the two time lag estimates, computed for different values of τ (columns), SNRs (horizontal axis) and definitions of the instantaneous QT series. The results for $\mathcal{D}_t$ are shown in (a)–(d) and (e)–(h), respectively. Panels (i)–(l) and (m)–(p) show m_{ϵ_τ} and σ_{ϵ_τ} for $\mathcal{D}_r$. Errors computed with $d^i_{\mathrm{QT}}(n)$, $\tilde{d}^i_{\mathrm{QT}}(n)$ and $\check{d}^i_{\mathrm{QT}}(n)$ are represented in blue, orange and green colors, respectively. The results are based on the Laplacian noise assumption.

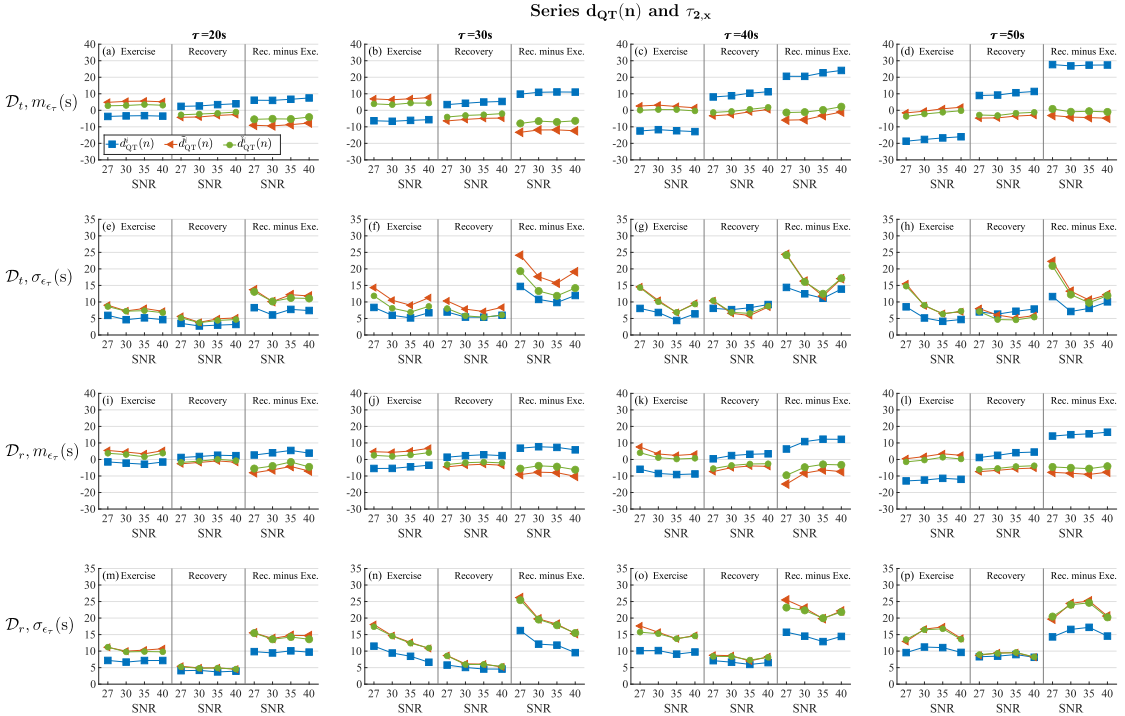

Figure 4.8: Mean m_{ϵ_τ} and standard deviation σ_{ϵ_τ} of the time lag error ϵ_τ in exercise, recovery and the difference between the two time lag estimates, computed for different values of τ (columns), SNRs (horizontal axis) and definitions of the instantaneous QT series. The results for $\mathcal{D}_t$ are shown in (a)–(d) and (e)–(h), respectively. Panels (i)–(l) and (m)–(p) show m_{ϵ_τ} and σ_{ϵ_τ} for $\mathcal{D}_r$. Errors computed with $d^i_{\mathrm{QT}}(n)$, $\breve{d}^i_{\mathrm{QT}}(n)$ and $\breve{d}^i_{\mathrm{QT}}(n)$ are represented in blue, orange and green colors, respectively. The results are based on the Gaussian noise assumption.

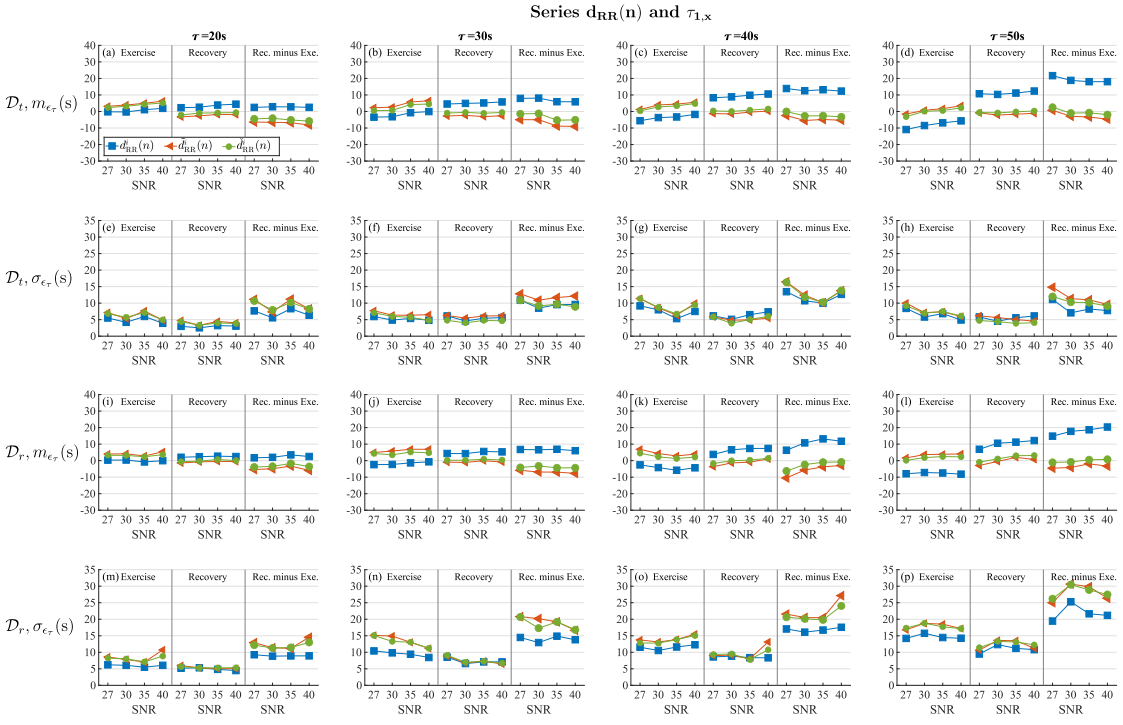

Figure 4.9: Mean m_{ϵ_τ} and standard deviation σ_{ϵ_τ} of the time lag error ϵ_τ in exercise, recovery and the difference between the two time lag estimates, computed for different values of τ (columns), SNRs (horizontal axis) and definitions of the instantaneous QT series. The results for $\mathcal{D}_t$ are shown in (a)–(d) and (e)–(h), respectively. Panels (i)–(l) and (m)–(p) show m_{ϵ_τ} and σ_{ϵ_τ} for $\mathcal{D}_r$. Errors computed with $d^i_{\mathrm{RR}}(n)$, $\tilde{d}^n_{\mathrm{RR}}(n)$ and $\check{d}^n_{\mathrm{RR}}(n)$ are represented in blue, orange and green colors, respectively. The results are based on the Laplacian noise assumption.

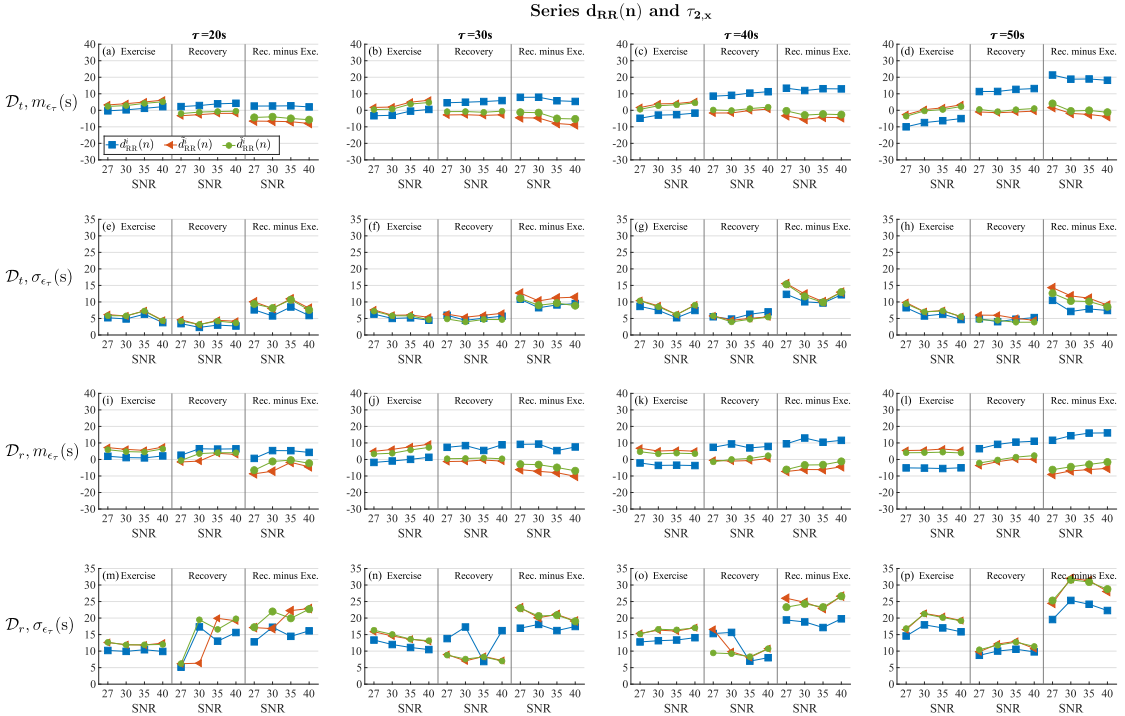

Figure 4.10: Mean m_{ϵ_τ} and standard deviation σ_{ϵ_τ} of the time lag error ϵ_τ in exercise, recovery and the difference between the two time lag estimates, computed for different values of τ (columns), SNRs (horizontal axis) and definitions of the instantaneous QT series. The results for $\mathcal{D}_t$ are shown in (a)–(d) and (e)–(h), respectively. Panels (i)–(l) and (m)–(p) show m_{ϵ_τ} and σ_{ϵ_τ} for $\mathcal{D}_r$. Errors computed with $d^i_{RR}(n)$, $\tilde{d}^i_{RR}(n)$ and $\check{d}^i_{RR}(n)$ are represented in blue, orange and green colors, respectively. The results are based on the Gaussian noise assumption.

$\mathcal{D}_{ee}$, the best fit is obtained for $\mathcal{D}_{ee}$. However, a still better fit is obtained when using $\check{d}^i_{\mathrm{QT}}(n)$ on $\mathcal{D}_t$. These observations corroborate the results in Sec. 4.3.3 and support the selection of $\check{d}^i_{\mathrm{QT}}(n)$. The performance achieved with $\check{d}^i_{\mathrm{QT}}(n)$ is explained by a better handling of the nonstationarity in the exercise window and a wider RR interval range of the three learning windows.

In line with the evaluation of the RR range, the estimated values of τ are also studied by computing the delay between $d_{\mathrm{RR}}(n)$ and $d^i_{\mathrm{RR}}(n)$ in combination with the Laplacian|Gaussian noise assumption. The results presented in Fig. 4.16|Fig. 4.17 show that these are similar to those obtained using $d_{\mathrm{QT}}(n)$ and $d^i_{\mathrm{QT}}(n)$.

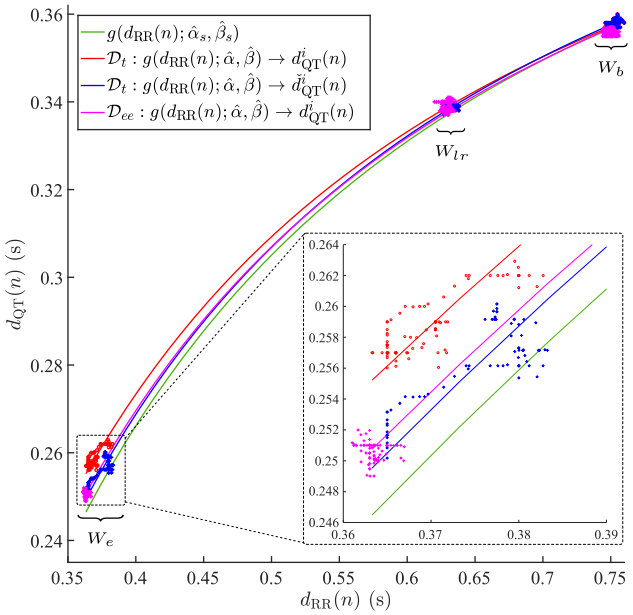

Figure 4.11: The two data pairs $[d_{\mathrm{QT}}(n), d_{\mathrm{RR}}(n)]$ and $[d_{\mathrm{QT}}(n) - \Delta_{\mathrm{QT}}, d_{\mathrm{RR}}(n)]$ of the three learning windows, the memoryless transformation $g(d_{\mathrm{RR}}(n);\hat{\alpha},\hat{\beta})$ with estimated parameters, and the reference $g(d_{\mathrm{RR}}(n);\hat{\alpha}_s,\hat{\beta}_s)$ described in Sec. 4.3.2. The three clusters of data pairs originate from the exercise W_e, the recovery W_{lr} and the resting W_b windows (left to right). The examples are taken from $\mathcal{D}_t$ and $\mathcal{D}_{ee}$. For the sake of clarity, the results for $\check{d}^i_{\mathrm{QT}}(n)$ are omitted.

4.3.5 QT-RR adaptation time lag estimation and its dependence on heart rate trend frequency content using $\mathcal{D}_o$

Examples of $d_{\mathrm{QT}}(n)$ and $d^i_{\mathrm{QT}}(n)$ for different values of τ and F are shown in Fig. 4.12. For the case of Fig. 4.12(d), where the frequency content of the ramps is higher than the cut-off frequency of the system, $F > F_c$, the effect of $h(n)$ results in a smoothed $d_{\mathrm{QT}}(n)$. In such cases, the model in (2.43) may seem inappropriate, since $s(n)$ is distorted, and even the evaluation in terms of the error when estimating τ remains to be conducted.

The mean error m_{ϵ_τ} and the standard deviation σ_{ϵ_τ} between the estimated $\hat{\tau}$ and the known simulated time lag τ are calculated separately for each pair (τ, F) during exercise and recovery and are represented in Fig. 4.13. The m_{ϵ_τ} value closest to zero, corresponding to $\tau_s = 20$ s, has the highest associated F_c cut-off frequency. For a fixed τ, m_{ϵ_τ} becomes larger, in absolute values, as F increases. When τ increases, the error m_{ϵ_τ} increases, in absolute values, for the same F, as it becomes closer to the decreasing F_c. This behavior is almost vanished for $F = 0.002$ Hz, since it is always lower than any F_c. Similar conclusions and arguments can be drawn for the analysis in terms of σ_{ϵ_τ}, as shown in the bottom panels of Fig. 4.13.

4.4 Discussion

4.4.1 T wave end delineation

To the best of our knowledge, this is the first simulation study evaluating the performance of the T wave end delineation for conditions closely resembling those of EST. The results in Fig. 4.4 show that any GπCA$_P$-based method yields significantly lower delineation errors ϵ_θ than any PCA-based method at a low SNR (27 dB), whereas the differences in performance at higher SNRs are negligible between both lead space reduction techniques. The MLeads delineation always shows the worst T wave end delineation performance. Thus, since the SNR is typically low during exercise, the GπCA-based techniques are better suited for delineation of exercise ECGs stress testing. Accordingly, the criterion based on the wave periodicity is concluded to be a more adequate criterion than the criterion based on variance to determine the best transformed lead for T wave end delineation.

Cabasson *et al.* [128] proposed a method to enhance the delineation of the T wave in EST that consisted in a batch processing mode of the improved

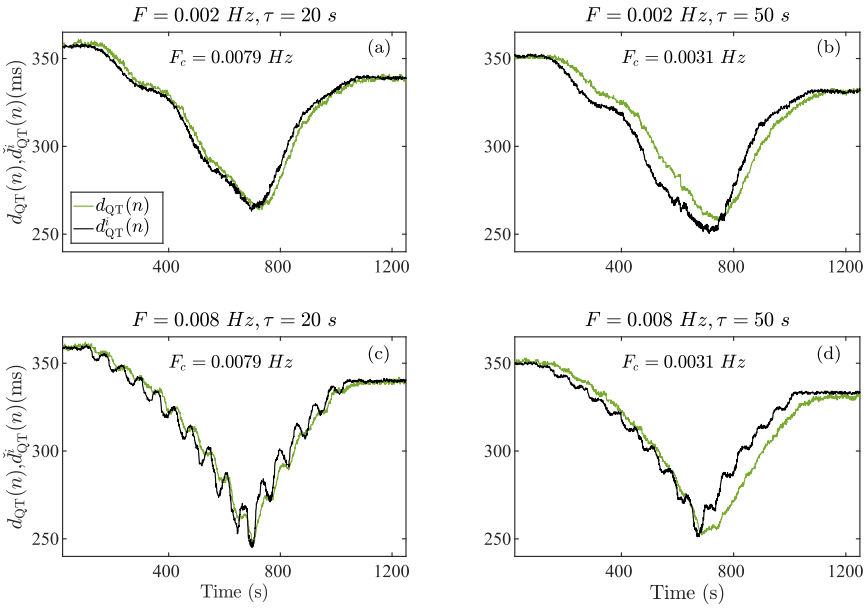

Figure 4.12: Examples of $d_{\mathrm{QT}}(n)$ and the instantaneous series $d^i_{\mathrm{QT}}(n)$ for different τ and F.

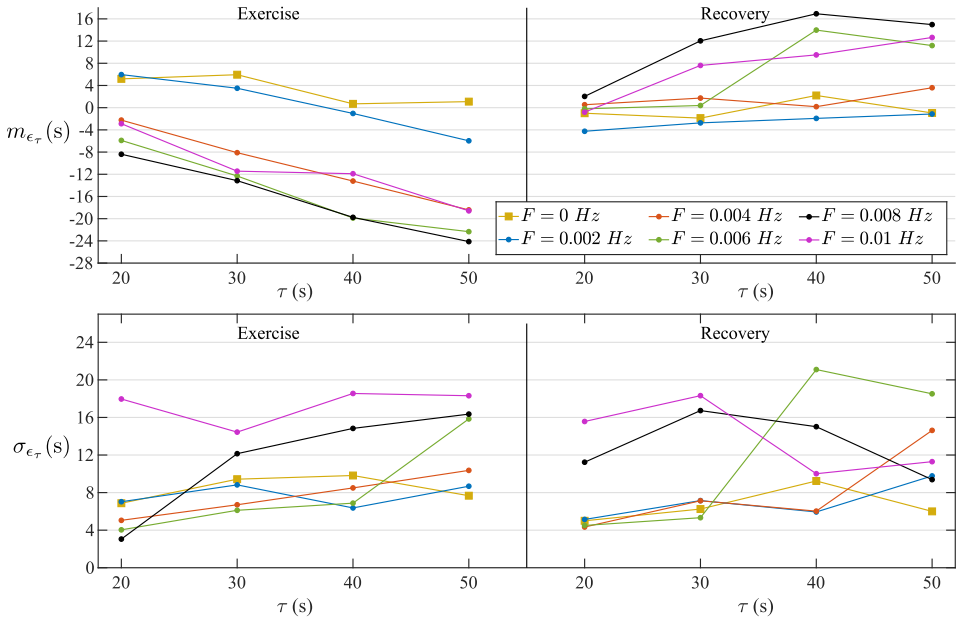

Figure 4.13: mean and standard deviation of error ϵ_τ, m_{ϵ_τ} and σ_{ϵ_τ}, respectively, for different τ and F pairs.

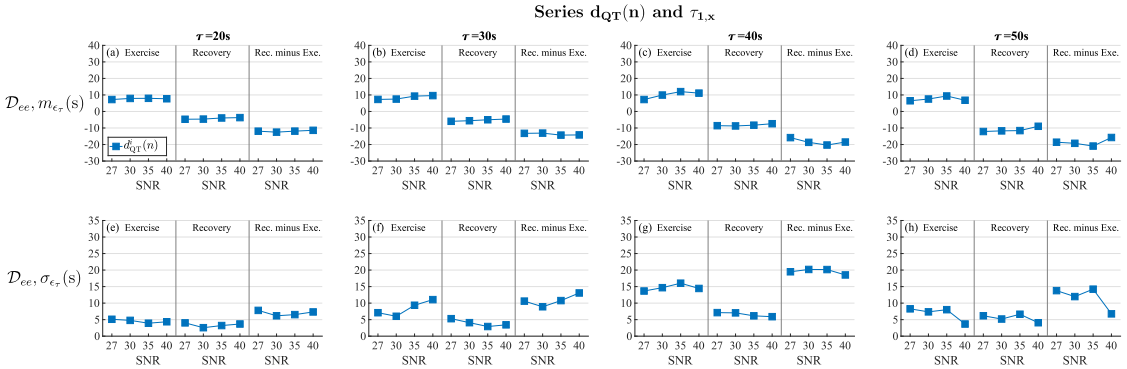

Figure 4.14: Mean m_{ϵ_τ} and standard deviation σ_{ϵ_τ} of the time lag error ϵ_τ for $\mathcal{D}_{ee}$ in exercise, recovery and the difference between the two time lag estimates, computed for different values of τ (columns) and SNRs (horizontal axis) are shown in (a)–(d) and (e)–(h), respectively. The results are based on $d^i_{\mathrm{QT}}(n)$ and the Laplacian noise assumption.

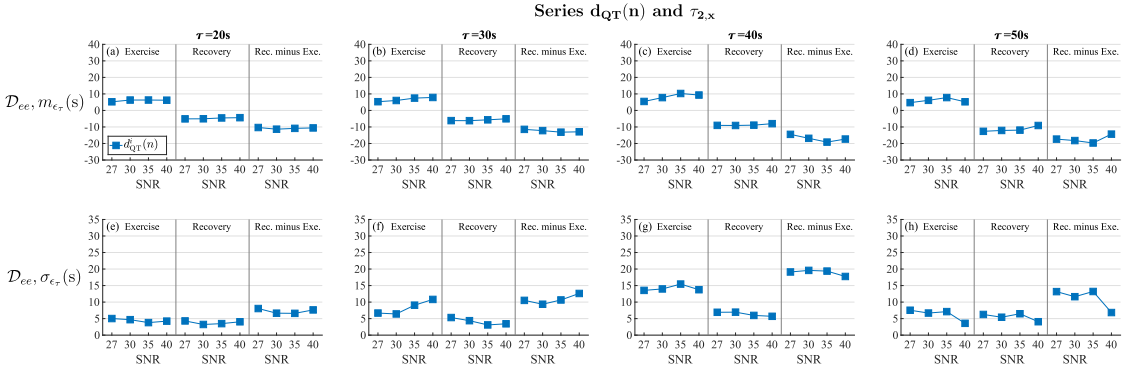

Figure 4.15: Mean m_{ϵ_τ} and standard deviation σ_{ϵ_τ} of the time lag error ϵ_τ for $\mathcal{D}_{ee}$ in exercise, recovery and the difference between the two time lag estimates, computed for different values of τ (columns) and SNRs (horizontal axis) are shown in (a)–(d) and (e)–(h), respectively. The results are based on $d^i_{\mathrm{QT}}(n)$ and the Gaussian noise assumption.

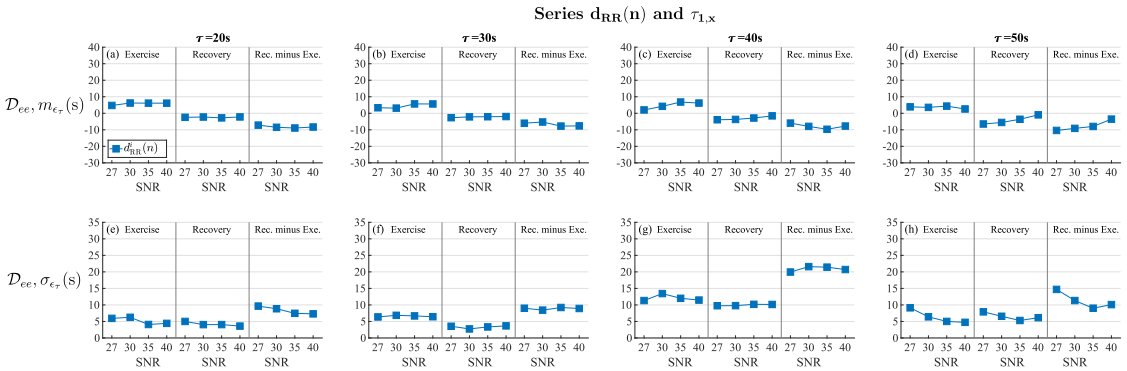

Figure 4.16: Mean m_{ϵ_τ} and standard deviation σ_{ϵ_τ} of the time lag error ϵ_τ for $\mathcal{D}_{ee}$ in exercise, recovery and the difference between the two time lag estimates, computed for different values of τ (columns) and SNRs (horizontal axis) are shown in (a)–(d) and (e)–(h), respectively. The results are based on $d^i_{\mathrm{RR}}(n)$ and the Laplacian noise assumption.

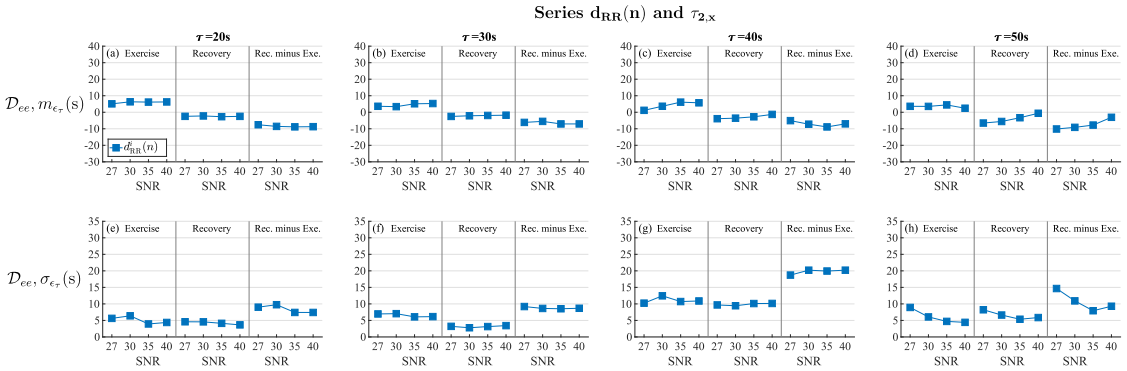

Figure 4.17: Mean m_{ϵ_τ} and standard deviation σ_{ϵ_τ} of the time lag error ϵ_τ for $\mathcal{D}_{ee}$ in exercise, recovery and the difference between the two time lag estimates, computed for different values of τ (columns) and SNRs (horizontal axis) are shown in (a)–(d) and (e)–(h), respectively. The results are based on $d^i_{\mathrm{RR}}(n)$ and the Gaussian noise assumption.

Woody's method previously proposed in another study. The method was evaluated using synthetic data presenting time-varying RT segment duration [72], with the RT segment defined from the R peak to the T wave peak. The method was reported to outperform other methods proposed in the literature. Nevertheless, estimating the QT interval rather than the RT interval should be better, whenever possible, since the T peak to T end interval may contain relevant information for risk assessment of arrhythmia risk.

Convolutional neural networks have recently been proposed for QT interval delineation [129–131], with performance results similar to those obtained with wavelet analysis [100]. Since the dynamic scenario of EST may prove a challenge to methods based on machine learning, further studies are warranted to more thoroughly characterize the performance of those methods.

4.4.2 Estimation of α and β

When identifying the nonlinear transformation in the model of the QT-RR relation shown in Fig. 4.11, the data pairs included in the exercise window are found to profoundly influence the estimation of the parameters α and β of such transformation and, consequently, the estimation of the QT adaptation time lag. This is substantiated by the results obtained from the dataset $\mathcal{D}_{ee}$ in this chapter, which show that $[d_{\mathrm{QT}}(n), d_{\mathrm{RR}}(n)]$ should be selected so that the QT interval achieves its actual stationary value corresponding to the stationary heart rate value to produce accurate estimates. Since the data pairs in the exercise window of $\mathcal{D}_t$ and $\mathcal{D}_r$ are nonstationary, data-dependent modification is necessary to obtain a better accuracy in the estimation of α and β.

An important point to highlight is the fact that the data pairs from the exercise window in $\mathcal{D}_t$ and $\mathcal{D}_r$ include a wider range of the RR intervals, i.e. from $\tilde{d}^i_{\mathrm{QT}}(n)$ or $\check{d}^i_{\mathrm{QT}}(n)$, than the pairs selected in a window with stationary data, i.e. in $\mathcal{D}_{ee}$ (see Fig. 4.11). The wider RR range leads to a better fit of $g_f(d_{\mathrm{RR}}(n); \alpha, \beta)$ in $\mathcal{D}_t$ and $\mathcal{D}_r$ with $\tilde{d}^i_{\mathrm{QT}}(n)$ or $\check{d}^i_{\mathrm{QT}}(n)$ as compared to that in $\mathcal{D}_{ee}$ with $d^i_{\mathrm{QT}}(n)$.

The discrepancy between α, β and $\hat{\alpha}_s$, $\hat{\beta}_s$, with the later being the estimated values obtained when the template RR series decreases step-wise from exercise onset to end, is likely to be a consequence of how the wavelet-based delineator handles the T waves at different heart rates, i.e. different T wave widths. The wavelet-based delineator makes use of time-invariant filters, which modify the width of the T waves, with these being narrower at high heart rates, since higher frequencies can be filtered out. Thus, the behavior of the delineator differs for

T waves at high and low heart rates. Therefore, $\hat{\alpha}_s$ and $\hat{\beta}_s$ represent better reference values than α and β to evaluate the performance, since differences in the estimated values can only be attributed to differential time lag estimation performance in data pair selection for computation of $d^i_{\mathrm{QT}}(n)$, $\tilde{d}^i_{\mathrm{QT}}(n)$ or $\check{d}^i_{\mathrm{QT}}(n)$ (see Table 4.2).

4.4.3 QT-RR adaptation time lag estimation

One of the main aims of this chapter is to evaluate whether the time delay between $d_{\mathrm{QT}}(n)$ and an instantaneous QT series, either given by $d^i_{\mathrm{QT}}(n)$, $\tilde{d}^i_{\mathrm{QT}}(n)$, or $\check{d}^i_{\mathrm{QT}}(n)$, can serve as a surrogate for estimating the QT-RR adaptation time lag. The results show that the data-dependent modification of the data pairs in the exercise window yields better performance than the unmodified data pairs, i.e., $\tilde{d}^i_{\mathrm{QT}}(n)$ and $\check{d}^i_{\mathrm{QT}}(n)$ yield better performance than $d^i_{\mathrm{QT}}(n)$. While the mean bias m_{ϵ_τ} becomes increasingly larger for $d^i_{\mathrm{QT}}(n)$ when τ increases from 20 to 50 s, m_{ϵ_τ} is essentially independent of τ for $\tilde{d}^i_{\mathrm{QT}}(n)$ and $\check{d}^i_{\mathrm{QT}}(n)$ (see Fig. 4.7). Moreover, when using $d^i_{\mathrm{QT}}(n)$ for large values of τ, a large overestimation during recovery and a large underestimation during exercise can be observed, which together potentiate $\Delta\hat{\tau}_p$, defined as the difference between $\hat{\tau}_{p,r}$ and $\hat{\tau}_{p,e}$, cf. (2.37). Consequently, $\Delta\hat{\tau}_p$ is not suitably characterized when using $d^i_{\mathrm{QT}}(n)$.

In terms of m_{ϵ_τ}, $\check{d}^i_{\mathrm{QT}}(n)$ offers better performance than $\tilde{d}^i_{\mathrm{QT}}(n)$, since m_{ϵ_τ} is somewhat closer to 0 for most values of τ and SNRs. As an example, the analysis of the exercise phase in the database $\mathcal{D}_t$ using $\tau = 50$ s and SNR = 40 dB results in $m_{\epsilon_\tau} = 3.43$ s and 1.09 s for $\tilde{d}^i_{\mathrm{QT}}(n)$ and $\check{d}^i_{\mathrm{QT}}(n)$, respectively (see Fig. 4.7(d)). The results in the recovery phase have about the same magnitude as those of exercise, but with reversed sign, -2.68 s and -0.95 s.

As noted in Sec. 4.3.3, the value of m_{ϵ_τ} observed during exercise for $\tilde{d}^i_{\mathrm{QT}}(n)$ and $\check{d}^i_{\mathrm{QT}}(n)$ is lower than that observed for $d^i_{\mathrm{QT}}(n)$, even if this is traded for a higher standard deviation σ_{ϵ_τ}. This result can be explained by the better learning achieved for data pairs in the exercise window, either only in the first half of the window when determining Δ_{QT} to compute $\tilde{d}^i_{\mathrm{QT}}(n)$ or entirely when aligning the window end to peak exercise before $\check{d}^i_{\mathrm{QT}}(n)$ is computed. It should be noted that the decrease in m_{ϵ_τ} is greater than the increase in σ_{ϵ_τ}.

The under- and overestimation in exercise and recovery delay estimates, respectively, and its dependency on τ are reduced when the delay is calculated between the observed RR series and $d^i_{\mathrm{RR}}(n)$. This bias reduction is observed in all the analyzed datasets (Fig. 4.9 and Fig. 4.10 for the results from the datasets $\mathcal{D}_t$ and $\mathcal{D}_r$, and Fig. 4.16 and Fig. 4.17 for the results from the dataset $\mathcal{D}_{ee}$).

The estimates using $\tilde{d}^{i}_{\mathrm{RR}}(n)$ or $\check{d}^{i}_{\mathrm{RR}}(n)$ are practically the same. The value of m_{ϵ_τ} is also lower when computing any of the instantaneous RR series than when using any of the instantaneous QT series. These results may be explained by the wider range of values and the more linear tendency of the RR series that the QT series (see Fig. 4.3(b)).

4.4.4 Conditions on heart rate and QT trend in time lag estimation

Out of the many parameters defining the simulator, the QT adaptation time lag and the SNR are deemed to be of primary interest to be investigated. When it comes to heart rate, which also plays a central role, the results obtained from simulated ECGs with a linearly increasing heart rate trend during exercise are almost identical to those obtained from simulated ECGs with a real heart rate measured during exercise, see Fig. 4.7. The same observation applies to a linearly decreasing heart rate trend during recovery. These results provide experimental evidence of the theoretical results derived in Section 2.8. The dataset $\mathcal{D}_o$ serves as a support for these results, showing that the requirement of a linear heart rate trend can be relaxed to any change in the trend as long as its frequency content is below a certain cut-off frequency F_c, which is related to the QT adaptation time lag τ. These low-frequency oscillations in real recordings could be a consequence of the step-like changes in the workload along the EST, rather than strictly linear changes. This can be corroborated by observing the RR series computed from clinical ECGs (Fig. 2.5(a)) in which the EST protocol in Sec. 5.2.1 only includes workload changes during the exercise phase, where these low-frequency oscillations are more easily visible.

4.4.5 Limitations

The work of this chapter assumes that τ remains constant for each individual, i.e., it does not vary with time during the exercise phase or the recovery phase of the EST. Some studies have shown that QT-RR adaptation may depend on the level of sympathetic activation [92], which will be studied in Chapter 6 of this Ph.D. thesis. Also, it could be the case that the relation between QT and RR varied during exercise and recovery. It is unclear whether the differences in QT adaptation are only due to differences in the adaptation time lag represented by $h(n)$ or are also due to differences in the QT-RR memoryless relation. Although the differences between exercise and recovery are accounted for by computing a time lag estimate for each phase, the changes in sympathetic activation during exercise, and recovery, suggest that further research is needed

to fully explore this aspect.

The noise added to simulated, noise-free ECGs is composed of MN and motion artifacts [120]; baseline wander is not part of the simulator as appropriate correction techniques are available today. While the MN model is specifically designed for EST, the motion artifact model is designed for ambulatory ECGs. Although the simulated motion artifacts resemble those observed during EST, the model could be improved to closely resemble the investigated scenario, e.g., by adjusting the artifact shape and occurrence probability pattern.

The GπCA$_P$ shows better performance in extracting the $n_{\mathrm{Te}}(k)$ points. To compute the $n_{\mathrm{QRSo}}(k)$ points, the MLeads over the 8 independent standard leads is shown to be preferred. This is a consequence of using only information from the ST-T complex to learn the transformation matrix, not so well adapted to the QRS complex. If required, a different transformation matrix could be learned for the QRS complex to improve the n_{QRSo} delineation.

4.5 Conclusions

Using simulated ECGs, the performance evaluation of the proposed method shows that the estimated QT-RR adaptation time lag agrees well with the true time lag. The original assumption of linear changes in heart rate trends is broadened to also apply to more realistic, low-frequency trends. In addition, the Laplacian-based estimator shows a better fitting of the QT interval statistical distribution than the Gaussian-based one.

CHAPTER 5

CLINICAL VALIDATION

5.1 Motivation

In Chapter 4, the methodology described in Chapter 2 was evaluated in simulated ECGs that mimic the typical EST trend, concluding that: (1) the lead space reduction GπCA$_P$ technique offers the more accurate T wave end delineation;

and (2) the QT adaptation time lag can be estimated as the delay between the observed QT intervals and the QT intervals derived from the observed RR intervals using a memoryless transformation. The best results are obtained when the information from the last part of the exercise phase is modified and then used to calculate the instantaneous QT series. In addition, the Laplacian estimator fits better to the QT interval statistical distribution.

The proposal in this chapter is, first, to evaluate the methodology that was tested in Chapter 4 but here from a clinical perspective. Specifically, the QT adaptation time lag is calculated from clinical ECGs of patients with different likelihood of suffering CAD. The statistical capacity of the proposed markers, i.e. $\tau_{p,e}$, $\tau_{p,r}$ and $\Delta\tau_p$, to separate the different CAD risk groups is studied for the proposed estimators and instantaneous QT series. The results are also compared to the QT lag estimated from abrupt heart rate changes, whose relation with arrhythmic risk has been reported in the literature. Additionally, the capacity of the proposed markers to predict SCD or any cause-mortality during clinical follow-up is assessed.

5.2 Databases

5.2.1 FINCAVAS

To evaluate the proposed time lag estimators, the clinical database FINCAVAS was analyzed, which consisted of 528 ECGs recorded from patients undergoing EST at Tampere University Hospital in Finland [127]. The objective of generating this database was to characterize patients at high risk of cardiovascular morbidity and mortality. For each patient, a continuous ECG was recorded at a sampling frequency of $F_s = 500$ Hz with CardioSoft exercise ECG system (Version 4.14, GE Healthcare, Freiburg, Germany) using the Mason-Likar modified 12-lead system. The exercise stress test was performed in a bicycle ergometer. The initial workload varied from 20 W to 30 W, with the load being increased stepwise by a fixed, patient-specific quantity in the range 10-30 W every minute (for females 10-20 W) based on physicians evaluation of the patient's condition. This patient-specific quantity is not annotated in the database. The workload was removed immediately after the peak exercise, which corresponds to the maximum theoretical heart rate ($\mathrm{HR_{max}}$) calculated as $\mathrm{HR_{max}} = 211 - 0.64\mathrm{v_{age}}$, where $\mathrm{v_{age}}$ is the age of the subject [132]. The study protocol was approved by the Ethical Committee of the Hospital District of Pirkanmaa, Finland. All patients gave informed consent before the interview and the acquisition of the

recordings, as stipulated in the Declaration of Helsinki. A total of 75 patients were discarded due to the presence of large artifacts, early finished test or frequent ectopic beats, which did not allow for the calculation of the QT interval series along the EST.

In the FINCAVAS database, patients were classified into four groups according to their likelihood of suffering CAD. The low-risk ECG (ECG-LR) group was identified based on the clinical history and the ECG interpretation. The remaining patients underwent COR within 180 days of EST to determine the percentage of luminal diameter narrowing in at least one major epicardial coronary artery or main branches, resulting in three groups: low-risk COR (COR-LR), mild-risk COR (COR-MR) and high-risk COR (COR-HR). These three groups included patients with an occlusion of less than 50%, between 50 and 75%, and 75% or more, respectively.

The ECG-LR, COR-LR, COR-MR and COR-HR groups contained 215, 59, 25 and 154 patients, respectively. Demographic variables and the average heart rate and QT interval values at baseline and during the exercise and recovery phases of the EST for each of the four groups are shown in Table 5.1.

The discriminative capacity of the three proposed markers $\tau_{p,e}$, $\tau_{p,r}$ and $\Delta\tau_p$ was assessed. This database was also used to compare the performance of different methods described in Sec. 2.3 to delineate the T wave end point, $n_{\mathrm{Te}}(k)$ and to study the regression models describing the nonlinear transformation introduced in Sec. 2.5.

5.2.2 ARTEMIS

A second clinical database [133], ARTEMIS, was used to evaluate the capacity of the proposed markers $\tau_{p,e}$, $\tau_{p,r}$ and $\Delta\tau_p$ for stratification of patients according to their risk of suffering SCD or any cause-mortality. The ARTEMIS database collected patients with CAD who had undergone coronary angiography at the Division of Cardiology at Oulu University Hospital, Oulu, Finland [133], with or without type 2 diabetes (DM2) (ClinicalTrials.gov identifier NCT1426685). Patients who met the criteria for prophylactic implantation of an ICD, including those with left ventricular ejection fraction <35%, were excluded from the study regardless of whether an ICD was implanted. The study was performed according to the Declaration of Helsinki and with the approval of the institutional ethics committee. All the subjects provided written informed consent. The study population comprised 1886 8-lead standard ECGs recorded during EST. Of these, 1472 recordings were analyzed, since ECGs with absence of rest phases, poor ECG or T wave quality and the presence of large areas with non-SR were

excluded from the analysis. The mean follow-up time was 8.9 years.

Patients were classified according to their CAD degree based on the SXscore, whose value was calculated by evaluating each coronary lesion with diameter stenosis $\geqslant$50% in vessels $\geqslant$1.5 mm. Patients in this database corresponded to patients from the COR-MR and COR-HR groups of the FINCAVAS database if only the results of the diameter stenosis were considered. The low-risk SXscore (SXscore-LR), mild-risk SXscore (SXscore-MR) and high-risk SXscore (SXscore-HR) groups correspond to a SYNTAX score of less than 23, between 23 and 33 and higher than 33, respectively [134]. The number of patients in each group was 1128, 136 and 93, respectively. SXscore values for 115 patients were not available.

The primary endpoint for this study was SCD or resuscitation from SCA, whichever occurred first. Secondary endpoints were cardiovascular death (CVDeath) (including SCD, aborted SCA, and death from a cardiovascular cause other than SCD, whichever occurred first), non-SCD, and all-cause mortality. The cause of death was defined by an endpoint committee based on death certificates, interviews with the closest relatives of victims and autopsy reports. A total of 49 patients (11 women) died from SCD and 63 patients (12 women) had any cause-mortality.

Demographic variables, the median heart rate and QT interval values at baseline and during the exercise and recovery phases of the EST for each SXscore groups are shown in Table 5.2.

5.3 Statistical analysis

All clinical data are presented as median value $\pm$ interquartile range (IQR). The QT adaptation time lag estimates are represented in box plot diagrams, in which both mean and median values are shown. Moreover, the QT adaptation time lag estimates are presented as mean value $\pm$ standard deviation to compare with other studies.

In multiple comparisons, the Kruskal-Wallis test was used to assess differences in continuous clinical and ECG variables. The Mann-Whitney U test was applied for the comparison of continuous variables between groups, that is, (1) when assessing the three proposed markers, i.e. $\tau_{p,e}$, $\tau_{p,r}$ and $\Delta\tau_p$ computed by the instantaneous QT series $d^i_{\mathrm{QT}}(n)$, $\tilde{d}^i_{\mathrm{QT}}(n)$ or $\check{d}^i_{\mathrm{QT}}(n)$; (2) when selecting the best method to compute T wave end for calculating the observed $d_{\mathrm{QT}}(n)$ series; and (3) in the selection of thresholds γ_e and γ_r for exercise and recovery ramp identification according to the expressions (2.34) and (2.35), respectively. The

Chi-square test was applied to assess differences in the categorical variable gender. A p-value $p < 0.05$ was considered statistically significant.

The Pearson correlation coefficient was calculated to analyze the relation between demographic indices and the proposed QT adaptation time lag markers. A t-test was used to study the differences between the two gender groups.

Also, a linear mixed model was built for each of the three proposed markers, following the equation:

$$\mathrm{z}_{ij} = (\lambda_0 + u_i) + \lambda_a \mathrm{v}_{a_{i,j}} + \lambda_b \mathrm{v}_{b_{i,j}} + \lambda_g \mathrm{v}_{g_{i,j}} + \epsilon_{ij} \tag{5.1}$$

where the subscripts i and j refer to the i-th risk-group and the j-th patient, respectively, z is one of the three proposed markers, $\mathrm{z} \in \{\tau_{p,e}, \tau_{p,r}, \Delta\tau_p\}$, λ are the fixed-effects regression coefficients (constant across risk groups), u_i is the *intercept* for each of the four risk groups, $\mathrm{v}_{a_{i,j}}$ is the age, $\mathrm{v}_{b_{i,j}}$ is the BMI, $\mathrm{v}_{g_{i,j}}$ is the gender and ϵ represents the residuals.

The Spearman correlation coefficient was computed to study the correlation between the proposed QT adaptation time lag markers and the degree of stenosis. As the exact degree of stenosis of each patient was unknown and only information on the range of stenosis for each risk group was available, a fixed degree of stenosis was defined for all patients in the same risk group, which corresponded to the mean value of the corresponding range. Thus, patients belonging to COR-LR (stenosis $< 50\%$), COR-MR (stenosis between 50 and 75%), and COR-HR groups (stenosis between 75 and 100%) were assigned with stenosis levels of 25%, 65.5%, and 87.5%, respectively.

Univariable and multivariable Cox regression analyses were performed to independently determine the predictive value of the risk markers for both endpoints in the ARTEMIS database. Only variables with an individual significant association with the endpoint in the univariable analysis were included to define the multivariable model. The C-index (ranging from 0 to 1) was used as score statistics to evaluate the model. A value close to 1 has the best ability to discriminate between patients with a higher and lower risk of events. A backward-stepwise regression analysis was performed to optimize the model and retain only the independent variables associated with the endpoint. Numeric covariables were standardized according to their median and IQR for both univariable and multivariable Cox regression analyses. For standardized variables, hazard ratio ($\mathcal{HZR}$) results presented in the tables along this chapter must be interpreted as the corresponding increase|decrease in the risk for events corresponding to an increment|decrement of one IQR in the (non-standardized) variable, with such hazard ratio denoted as$\mathcal{HZR}_{\mathrm{IQR}}$).

To facilitate clinical interpretation, the $\mathcal{HZR}$ of some variables can be presented along the text following this transformation:

$$\mathcal{HZR}_k = (\mathcal{HZR}_{\text{IQR}})^{\frac{k}{\text{IQR}}} \tag{5.2}$$

Therefore, the probability of suffering from an event can be directly related to an increase|decrease in k units of this specific variable $\mathcal{HZR}_k$.

5.4 Results

5.4.1 Clinical characteristics

Demographic information for each patient group together with median heart rate and QT intervals in resting, exercise and recovery windows W_j, $j \in \{b, e, lr\}$, HR_{W_j} and QT_{W_j}, respectively, are given in Table 5.1 and in Table 5.2 for FINCAVAS and ARTEMIS databases, respectively. The median (and IQR) of the age and the BMI and the proportion of males vs females are higher in the groups with higher CAD risk (or higher SXscore). The median heart rate at peak exercise, HR_{W_e}, decreased significantly with increasing CAD risk (or with increasing SXscore).

Table 5.1: Demographic information in patient groups from the FINVACAS database, including heart rate and QT interval median values ($\pm$ IQR), in windows W_j, $j \in \{b, e, lr\}$, HR_{W_j} and QT_{W_j}, respectively.

	ECG-LR	COR-LR	COR-MR	COR-HR	p-value
Clinical variables					
Gender [M|F]	134|81	34|25	16|9	122|32	0.002
Age (years)	49.0 ± 20.8	52.0 ± 12.8	60.0 ± 15.5	63.0 ± 14.0	< 0.001
BMI	25.5 ± 5.7	25.4 ± 6.9	27.8 ± 5.4	26.9 ± 4.8	< 0.001
ECG derived variables					
HR_{W_b} (bpm)	79.6 ± 19.8	74.6 ± 15.9	73.3 ± 13.5	64.2 ± 14.2	< 0.001
HR_{W_e} (bpm)	166.5 ± 22.1	153.9 ± 33.4	139.4 ± 29.2	116.2 ± 27.2	< 0.001
$\text{HR}_{W_{lr}}$ (bpm)	98.2 ± 20.6	88.3 ± 22.5	85.5 ± 19.2	72.8 ± 14.6	< 0.001
QT_{W_b} (ms)	366.7 ± 37.4	385.0 ± 41.4	382.4 ± 31.8	398.6 ± 42.11	< 0.001
QT_{W_e} (ms)	256.1 ± 26.6	273.7 ± 46.8	295.4 ± 33.0	315.5 ± 40.2	< 0.001
$\text{QT}_{W_{lr}}$ (ms)	345.0 ± 39.9	367.8 ± 48.3	373.9 ± 40.9	389.1 ± 34.2	< 0.001

Results are statistically significantly different ($p < 0.05$) between pairs of groups as follows: Gender: COR-HR with ECG-LR and COR-LR; BMI: ECG-LR with COR-HR; Age, HR_{W_b}, $\text{HR}_{W_{lr}}$, QT_{W_b}, QT_{W_e} and $\text{QT}_{W_{lr}}$: ECG-LR with COR-LR, COR-MR and COR-HR, and COR-HR with COR-LR and COR-MR. HR_{W_e}: all pairs of groups are statistically significant.

Table 5.2: Demographic information in patient groups from the ARTEMIS database including heart rate HR and QT interval median values (± interquartile range (IQR)), in windows W_j, $j \in \{b, e, lr\}$, HR_{W_j} and QT_{W_j}, respectively.

	SXscore-LR	SXscore-MR	SXscore-HR	None	p-value
Clinical variables					
Gender [M|F]	753|375	103|33	74|19	91|24	0.004
Age (years)	66.0 ± 11.0	68.0 ± 12.0	68.0 ± 11.0	69.0 ± 10.0	< 0.001
BMI	27.0 ± 5.0	27.0 ± 5.3	27.0 ± 4.0	28.0 ± 5.4	0.576
ECG derived variables					
HR_{W_b}(bpm)	59.6 ± 12.1	58.5 ± 9.6	61.0 ± 14.7	59.5 ± 11.0	0.113
HR_{W_e}(bpm)	126.1 ± 29.3	115.0 ± 26.9	114.8 ± 31.5	106.8 ± 25.2	< 0.001
$\mathrm{HR}_{W_{lr}}$(bpm)	75.5 ± 14.4	70.7 ± 14.4	73.01 ± 15.3	70.3 ± 13.2	< 0.001
QT_{W_b}(ms)	415.8 ± 41.0	421.9 ± 33.0	418.0 ± 46.0	423.1 ± 33.6	0.082
QT_{W_e}(ms)	303.7 ± 41.4	317.4 ± 42.0	320.7 ± 47.0	335.0 ± 45.8	< 0.001
$\mathrm{QT}_{W_{lr}}$(ms)	391.6 ± 38.6	400.0 ± 34.3	402.0 ± 44.0	408.0 ± 36.4	< 0.001

Results are statistically significantly different ($p < 0.05$) between pairs of groups as follows: SXscore-LR/SXscore-MR and SXscore-LR/SXscore-HR for age, HR_{W_e}, $\mathrm{HR}_{W_{lr}}$, QT_{W_e} and $\mathrm{QT}_{W_{lr}}$.

5.4.2 T wave end delineation

An example of the 8 standard leads of an ECG from the FINCAVAS database and the transformed leads of both lead space reduction techniques are shown in Fig. 5.1. It can be observed how the T wave in the TL1 of both $\mathrm{G}\pi\mathrm{CA}_{1,\mathrm{o}}$ and $\mathrm{PCA}_{\mathrm{o}}$, is emphasized, being more remarkable for $\mathrm{G}\pi\mathrm{CA}_{1,\mathrm{o}}$.

To compare the different transformed lead methods defined to improve the delineation of the T wave end, the power of the 0.04 Hz highpass filtered $d^r_{\mathrm{QT}}(n)$ series, $\mathcal{P}_{\mathrm{QTV}}$, was computed in exercise and recovery, separately, using the ECGs of the FINCAVAS database. The results are shown in Fig. 5.4. Median $\mathcal{P}_{\mathrm{QTV}}$ was lower for any lead space reduction technique than when the MLeads methodology was used to obtain the $n_{\mathrm{Te}}(k)$ points. Also, $\mathrm{G}\pi\mathrm{CA}_P$-based methods showed better results than PCA, both in exercise and recovery. Besides, these results showed that there are no significant differences among $\mathrm{G}\pi\mathrm{CA}_P$-based methods. Therefore, $\mathrm{G}\pi\mathrm{CA}_{1,\mathrm{o}}$ method was also selected for the analysis of the clinical data. These results are in agreement with those obtained in simulations in Sec. 4.3.1. An example of the T wave end delineation in an area near the peak exercise is shown in Fig. 5.3, where it can be observed that the T wave delineation is more robust using the $\mathrm{G}\pi\mathrm{CA}_{1,\mathrm{o}}$ method than the MLeads method.

Selecting a method that only requires calculating the transformation matrix once avoids introducing additional abrupt variations in the QT series, which

could occasionally appear due to significant transformation matrix changes when moving along consecutive windows. An example of this anomaly can be seen in Fig. 5.2(a) and Fig. 5.2(b), where the observed QT interval series $d_{\mathrm{QT}}(n)$ was computed using the seven evaluated methodologies. Moreover, a representation of TL1 from GπCA$_1$ and GπCA$_{1,\mathrm{o}}$ and their respective T wave end delineation marks are shown in Fig. 5.3, where an abrupt change in the morphology of the T wave is observed in GπCA$_1$ from 4 to 8 s.

5.4.3 QT-RR modeling

After delineating the T wave end using the TL1 of GπCA$_{1,\mathrm{o}}$ and computing the observed QT series $d_{\mathrm{QT}}(n)$, the instantaneous series $d^i_{\mathrm{QT}}(n)$ was calculated using the different regression models described in Sec. 2.5. The mean and standard deviation of the parameters α and β and the fitting error $\varepsilon_{\mathrm{rms}}$ for each regression model are shown in Table 5.3. The lowest $\varepsilon_{\mathrm{rms}}$ was obtained with the hyperbolic model, so in the following all instantaneous series $d^i_{\mathrm{QT}}(n)$, $\tilde{d}^i_{\mathrm{QT}}(n)$ and $\check{d}^i_{\mathrm{QT}}(n)$ are calculated with this model.

The statistical distribution of the QT intervals is again studied using the FINCAVAS database to corroborate the selection of the estimators introduced in (2.31). The histogram of the difference $\Delta d_{\mathrm{QT}}(k) = d_{QT}(k) - \bar{d}_{QT}(k)$ is computed, as defined in Sec. 4.3.3, and is shown in Fig. 5.5. The least square errors of fitting the Laplacian and the Gaussian probability density functions in the FINCAVAS database are 0.0029 and 0.0045 a.u., respectively. Thus, the Laplacian estimator is better suited for the τ delay estimation with any of the series $d^i_{\mathrm{QT}}(n)$, $\tilde{d}^i_{\mathrm{QT}}(n)$ and $\check{d}^i_{\mathrm{QT}}(n)$, as was also seen in the simulation results.

5.4.4 QT-RR adaptation time lag and its relation with coronary artery disease

FINCAVAS database

The time points that delimit the exercise and recovery phases are computed before calculating the QT adaptation time lag. Figure. 5.6 presents the time lags corresponding to the use of different thresholds γ_e to set the end of the exercise $n_{e,e}$ and γ_r to set the onset of the recovery $n_{r,o}$. These are computed for each of the four patient groups according to the CAD risk in the FINCAVAS database.

The optimal threshold values γ^*_e and γ^*_r are chosen as those that maximize the significance of the estimated τ in separating the different CAD risk groups.

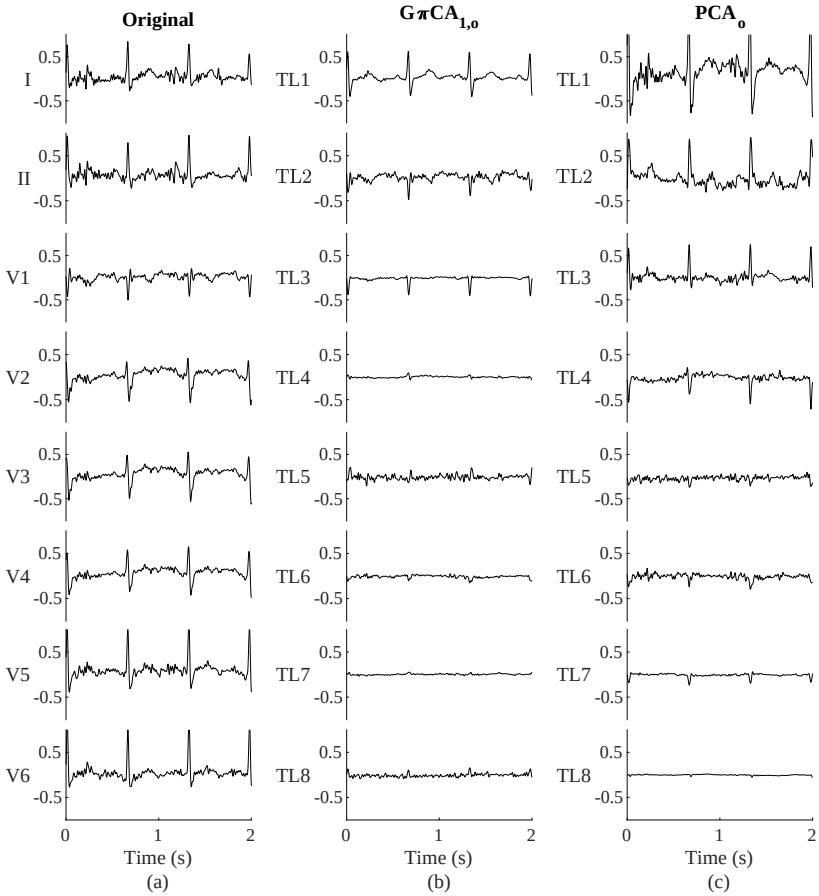

Figure 5.1: (a) Example of an ECG with 8 independent standard leads recorded during EST in mV, (b) the corresponding 8 transformed leads, in mV, obtained with $G\pi CA_{1,o}$ and (c) obtained with PCA_o, where the emphasized T waves at TL1 can be appreciated.

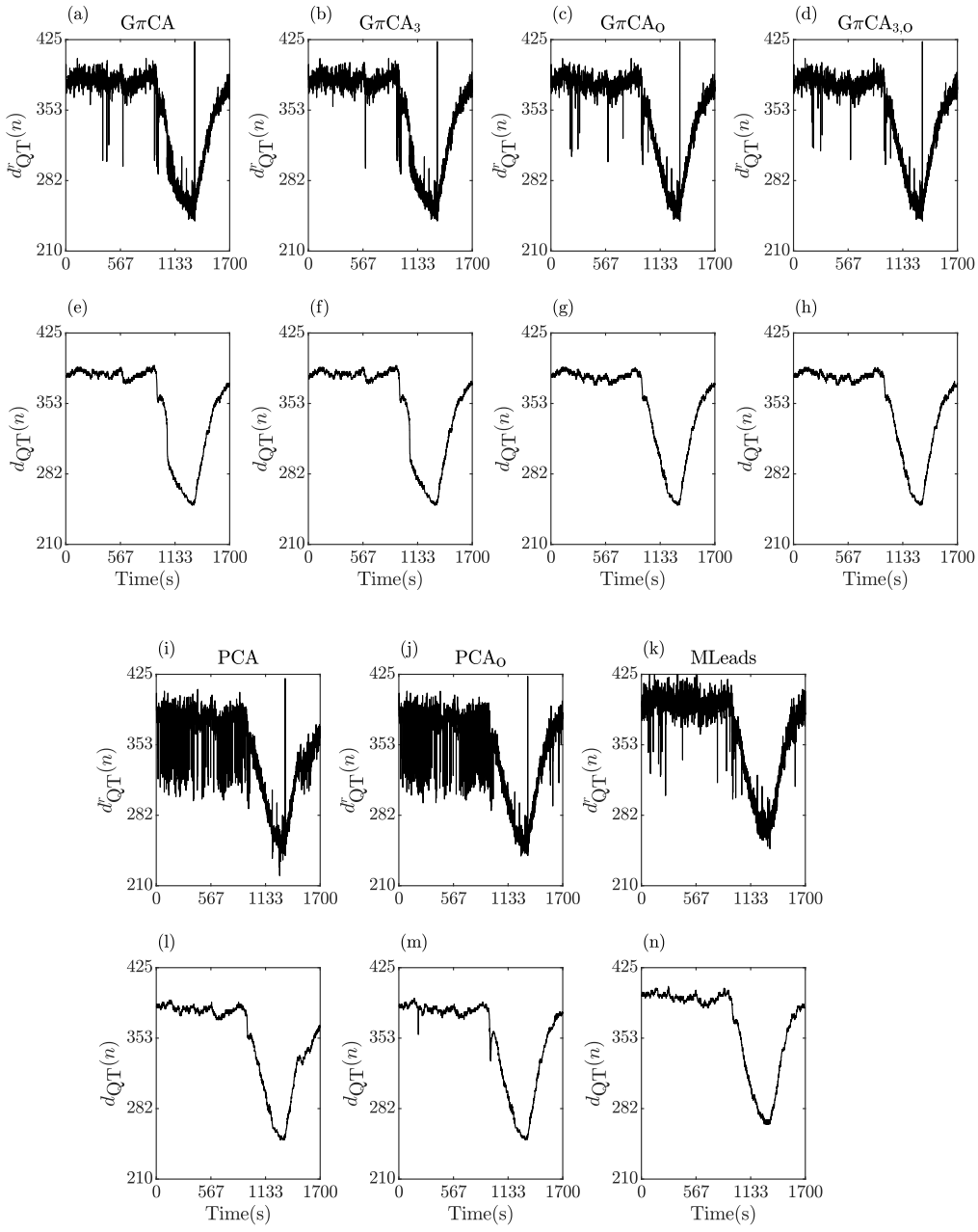

Figure 5.2: Examples of $d_{QT}(n)$ series calculated using all GπCA$_p$ methods, all PCA methods and the multi-lead strategy with the 8 independent standard leads. The first and third rows correspond to the $d^r_{QT}(n)$ series and the second and fourth rows to the $d_{QT}(n)$ after including the running median filter for outlier rejection.

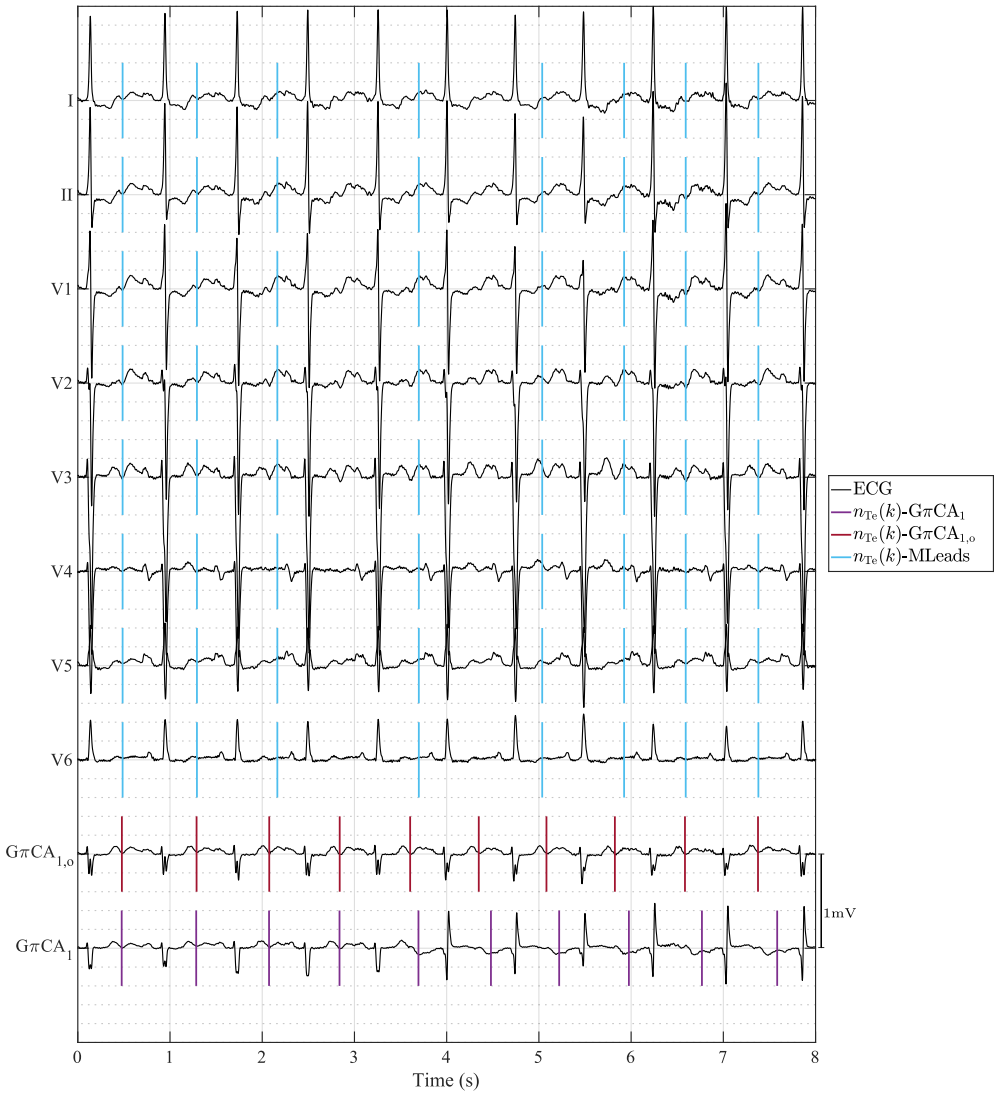

Figure 5.3: 8-lead clinical ECG with independent standard leads and the first transformed lead (TL1) for GπCA$_1$ and GπCA$_{1,o}$ methods. The T wave end point for each $k-$beat $n_{\mathrm{Te}}(k)$ delineating any TL1 or applying MLeads are marked in each lead.

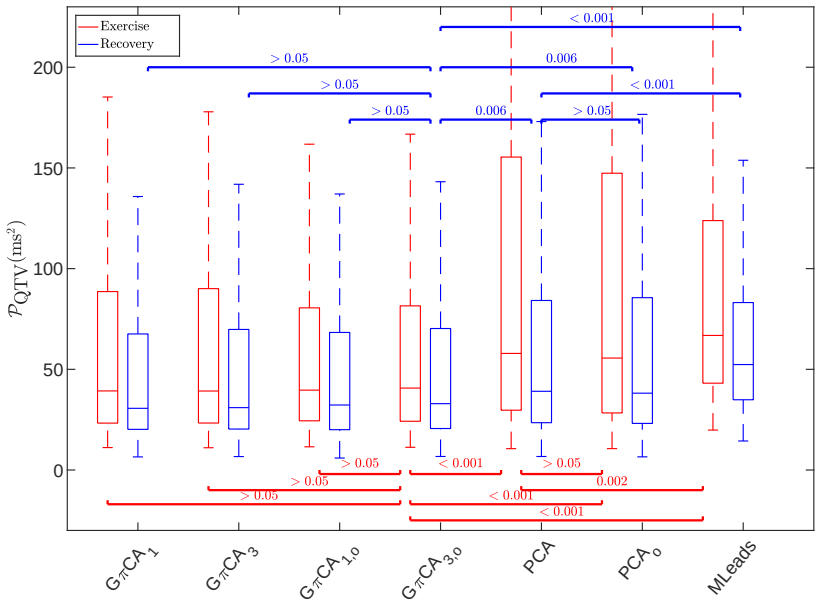

Figure 5.4: QT trend fitting error quantified by $\mathcal{P}_{\mathrm{QTV}}$ calculated both in the exercise and recovery phases, delineating T wave end from TL1 of each lead space reduction technique or applying a multi-lead delineation strategy using FINCAVAS database. Box plots are displayed to show the median values and the upper and lower whiskers, which are defined as 1.5 times the interquartile range (IQR).

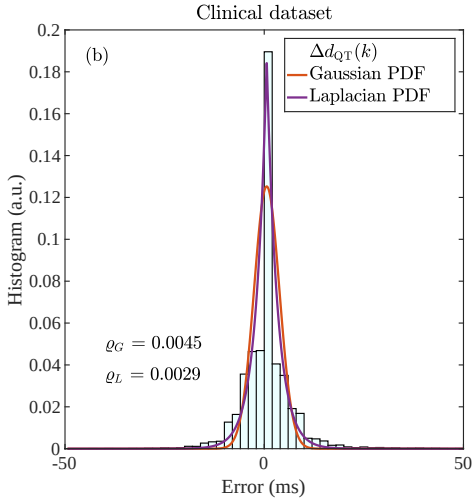

Figure 5.5: Histograms of $\Delta d_{\mathrm{QT}}(k)$ and best fit with Gaussian and Laplacian probability density functions (PDFs) in the FINCAVAS clinical dataset. The fitting errors ϱ_G and ϱ_G are written in the figure.

Table 5.3: Mean and standard deviation of the parameters α and β and the root mean square error ε_{rms}, in milliseconds, for different regression models. Each fitting is computed using all instantaneous QT series $d^i_{\text{QT}}(n)$, $\tilde{d}^i_{\text{QT}}(n)$ and $\check{d}^i_{\text{QT}}(n)$, which depend on how the peak exercise learning window W_e data is defined.

f	$d^i_{\text{QT}}(n) = g_f(d_{\text{RR}}(n); \alpha, \beta)$			ECG-LR	COR-LR	COR-MR	COR-HR
Parabolic log/log (Par)	$d^i_{\text{QT}}(n) = \beta(d_{\text{RR}}(n))^\alpha$	$d^i_{\text{QT}}(n)$	α	0.51 ± 0.08	0.48 ± 0.09	0.46 ± 0.09	0.41 ± 0.07
			β	0.43 ± 0.03	0.44 ± 0.03	0.43 ± 0.03	0.42 ± 0.02
			ε_{rms}	8.55 ± 4.66	9.61 ± 6.35	8.95 ± 4.76	6.95 ± 4.48
		$\tilde{d}^i_{\text{QT}}(n)$	$\tilde{\alpha}$	0.58 ± 0.09	0.55 ± 0.10	0.52 ± 0.09	0.50 ± 0.08
			$\tilde{\beta}$	0.45 ± 0.04	0.44 ± 0.03	0.44 ± 0.04	0.42 ± 0.02
			$\tilde{\varepsilon}_{\text{rms}}$	12.37 ± 5.84	13.16 ± 7.86	11.59 ± 5.05	10.71 ± 5.14
		$\check{d}^i_{\text{QT}}(n)$	$\check{\alpha}$	0.57 ± 0.09	0.54 ± 0.10	0.51 ± 0.09	0.49 ± 0.08
			$\check{\beta}$	0.44 ± 0.04	0.44 ± 0.03	0.44 ± 0.04	0.42 ± 0.02
			$\check{\varepsilon}_{\text{rms}}$	11.94 ± 5.78	12.72 ± 7.79	11.29 ± 4.96	10.52 ± 5.04
Linear (Lin)	$d^i_{\text{QT}}(n) = \beta + \alpha\ d_{\text{RR}}(n)$	$d^i_{\text{QT}}(n)$	α	0.30 ± 0.07	0.27 ± 0.07	0.25 ± 0.07	0.22 ± 0.05
			β	0.16 ± 0.03	0.18 ± 0.04	0.19 ± 0.04	0.21 ± 0.03
			ε_{rms}	10.27 ± 5.32	11.11 ± 7.00	10.27 ± 5.47	7.99 ± 5.21
		$\tilde{d}^i_{\text{QT}}(n)$	$\tilde{\alpha}$	0.33 ± 0.07	0.31 ± 0.07	0.29 ± 0.07	0.26 ± 0.05
			$\tilde{\beta}$	0.13 ± 0.03	0.14 ± 0.04	0.16 ± 0.03	0.17 ± 0.03
			$\tilde{\varepsilon}_{\text{rms}}$	14.22 ± 6.27	14.97 ± 7.99	13.16 ± 5.47	12.28 ± 5.73
		$\check{d}^i_{\text{QT}}(n)$	$\check{\alpha}$	0.33 ± 0.07	0.31 ± 0.07	0.28 ± 0.07	0.25 ± 0.05
			$\check{\beta}$	0.13 ± 0.03	0.15 ± 0.04	0.16 ± 0.03	0.18 ± 0.03
			$\check{\varepsilon}_{\text{rms}}$	13.79 ± 6.15	14.56 ± 7.95	12.88 ± 5.40	12.07 ± 5.61
Hyperbolic (Hyp)	$d^i_{\text{QT}}(n) = \beta + \frac{\alpha}{d_{\text{RR}}(n)}$	$d^i_{\text{QT}}(n)$	α	-0.08 ± 0.01	-0.09 ± 0.02	-0.09 ± 0.02	-0.10 ± 0.02
			β	0.48 ± 0.03	0.49 ± 0.04	0.50 ± 0.04	0.51 ± 0.04
			ε_{rms}	4.88 ± 2.71	6.00 ± 3.95	5.22 ± 2.63	4.91 ± 3.08
		$\tilde{d}^i_{\text{QT}}(n)$	$\tilde{\alpha}$	-0.08 ± 0.01	-0.09 ± 0.02	-0.10 ± 0.02	-0.11 ± 0.03
			$\tilde{\beta}$	0.48 ± 0.03	0.50 ± 0.05	0.51 ± 0.04	0.52 ± 0.04
			$\tilde{\varepsilon}_{\text{rms}}$	5.71 ± 2.66	7.05 ± 3.94	6.11 ± 2.49	6.38 ± 3.00
		$\check{d}^i_{\text{QT}}(n)$	$\check{\alpha}$	-0.08 ± 0.01	-0.09 ± 0.02	-0.10 ± 0.02	-0.11 ± 0.03
			$\check{\beta}$	0.48 ± 0.03	0.50 ± 0.04	0.51 ± 0.04	0.52 ± 0.04
			$\check{\varepsilon}_{\text{rms}}$	5.32 ± 2.30	7.27 ± 4.12	5.89 ± 2.45	6.07 ± 2.87
Logarithmic (Log)	$d^i_{\text{QT}}(n) = \beta + \alpha\ \ln(d_{\text{RR}}(n))$	$d^i_{\text{QT}}(n)$	α	0.16 ± 0.02	0.16 ± 0.03	0.15 ± 0.03	0.15 ± 0.02
			β	0.42 ± 0.02	0.42 ± 0.03	0.42 ± 0.03	0.42 ± 0.02
			ε_{rms}	6.71 ± 3.64	8.03 ± 5.46	7.56 ± 3.92	6.15 ± 3.88
		$\tilde{d}^i_{\text{QT}}(n)$	$\tilde{\alpha}$	0.17 ± 0.03	0.17 ± 0.03	0.17 ± 0.03	0.17 ± 0.03
			$\tilde{\beta}$	0.42 ± 0.02	0.43 ± 0.03	0.42 ± 0.03	0.42 ± 0.02
			$\tilde{\varepsilon}_{\text{rms}}$	8.98 ± 4.06	10.19 ± 5.93	9.27 ± 3.84	8.88 ± 4.03
		$\check{d}^i_{\text{QT}}(n)$	$\check{\alpha}$	0.17 ± 0.02	0.17 ± 0.03	0.17 ± 0.03	0.17 ± 0.03
			$\check{\beta}$	0.42 ± 0.02	0.43 ± 0.03	0.42 ± 0.03	0.42 ± 0.02
			$\check{\varepsilon}_{\text{rms}}$	8.65 ± 4.05	9.96 ± 6.01	9.28 ± 3.67	8.72 ± 3.97

$\gamma_e = 1$ and $\gamma_r = 0$ are equivalent to placing $n_{e,e}$ and $n_{r,o}$, respectively, at the peak exercise. To estimate the significance, the threshold values are first varied in the range [0.30, 1.00], for exercise, and in the range [0.00, 0.70], for recovery, in steps of 0.05, to calculate the corresponding delays, as illustrated in Fig. 5.6(a) and (b). Then, the p-value for the comparison between each pair of groups is calculated along the different thresholds, Fig. 5.6(c), and (d). Lastly, the mean p-value m_{pv} of the ones obtained for group pairs which result in significant differences in more than half of the considered thresholds is calculated in exercise $m_{pv,e}$ and recovery $m_{pv,r}$, respectively, Fig. 5.6(e), and (f). The selected thresholds γ_e^* and γ_r^* are the ones corresponding to the minimum of $m_{pv,e}$ and $m_{pv,r}$, for exercise and recovery, respectively.

The pairs of groups selected to calculate $m_{pv,e}$ are those found to be significantly different for at least half of the analyzed threshold values in the exercise phase (see Fig. 5.6(c)), with these being ECG-LR/COR-HR and COR-LR/COR-HR. In the recovery phase, the pairs of groups selected to calculate $m_{pv,r}$ are: ECG-LR/COR-HR, COR-LR/COR-HR, ECG-LR/COR-MR and COR-LR/COR-MR. It can be observed that the closer the ramp delimitation gets to the peak exercise (higher γ_e, lower γ_r), the lowest the significance. γ_e^* and γ_r^* are taken where $m_{pv,e}$ and $m_{pv,r}$ already converged to a stable minimum plateau, specifically in the extreme of these plateaus that provided the largest ramps, that is the largest γ_e and lowest γ_r within the plateau, so as to guarantee reliable τ estimates. After inspection of Fig. 5.6(e) and (f), the values of $\gamma_e^* = \gamma_r^* = 0.55$ are selected. The Laplacian estimator is used to estimate the time lags $\tau_{1,e}$ and $\tau_{1,r}$. The points that delimit both areas are exemplified in Fig. 2.5(b) and Fig. 2.5(d).

Once the areas for calculation of the time lags are defined, the discriminatory power to classify different levels of cardiac risk in CAD patients is evaluated for $\tau_{p,e}$, $\tau_{p,r}$ and $\Delta\tau_p$. These estimates are obtained using the hyperbolic regression model for the nonlinear transformation, each of the instantaneous QT series and either the Gaussian or Laplacian estimator.

The estimated QT adaptation time lags are shown in Fig. 5.7, where the top, middle and bottom rows contain the results using $d^i_{\mathrm{QT}}(n)$, $\tilde{d}^i_{\mathrm{QT}}(n)$ and $\check{d}^i_{\mathrm{QT}}(n)$ series, respectively. The mean exercise time lag $m_{\tau_{p,e}}$ increases with the CAD risk (Fig. 5.7(a)), while a reverted behavior is observed for the mean recovery time lag $m_{\tau_{p,r}}$ (Fig. 5.7(b)), with the time lag being reduced with increasing CAD risk. Given this asymmetric behavior, the difference in the adaptation time $\Delta\tau_p$ is found to be larger in the ECG-LR and COR-LR patient groups than in the COR-MR and COR-HR patient groups.

Statistically significant differences between each of the two low-risk groups and the COR-HR group, and the pair of groups ECG-LR/COR-MR are observed by analyzing the exercise time lag $\tau_{1,e}$ computed with the Laplacian estimator, while statistical significance is not reached when computing the exercise time lag $\tau_{2,e}$ with the Gaussian estimator. In the recovery, the two low-risk groups and the COR-HR group can be discriminated using $\tau_{p,r}$, $p = 1, 2$. Finally, statistically significant differences between the low-risk groups and the COR-HR group and the pair of groups ECG-LR/COR-MR are observed when $\Delta\tau_p$ is used.

The effect of modifying the exercise learning window and, therefore, the QT series at the peak exercise before regression parameter estimation causes an increase in the estimated exercise time lag and a decrease in the estimated recovery time lag. However, the tendency of the lag values with CAD risk is generally the same: the higher the CAD risk, the larger $m_{\tilde{\tau}_e}|m_{\check{\tau}_e}$ and the smaller $m_{\tilde{\tau}_r}|m_{\check{\tau}_r}$. The p-values associated with significant differences when using $d^i_{\mathrm{QT}}(n)$ decrease when using any modified instantaneous series, with this holding true for $\tau_{p,e}$ and $\Delta\tau_p$. Statistical significance of the differences in the pair of groups ECG-LR/COR-MR is not attained for either the exercise or the recovery delays.

The Laplacian-based estimator offers slightly greater discriminatory power for $\Delta\tau_1$. Therefore, these results, together with the better fit of a Laplacian probability density function to the QT histogram, support that the Laplacian assumption is advantageous as compared to the Gaussian one.

To show visual examples of the findings exposed previously, the estimated delays between $\check{d}^i_{\mathrm{QT}}(n)$ and $d_{\mathrm{QT}}(n)$ along the different groups are shown in Fig. 5.8(a-d). Moreover, the corresponding $d_{\mathrm{QT}}(n)$-$\check{d}^i_{\mathrm{QT}}(n)$ and QT-RR hysteresis curves can be seen in Fig. 5.8(e-h) and Fig. 5.8(i-l), respectively. Both representations serve to exemplify that the higher the risk, the higher the hysteresis area. Moreover, the observed QT values at baseline are larger while the observed RR values at peak exercise are lower in the COR-HR example than in the low-risk examples.

To better assess the capacity of the proposed markers to discriminate between low and high CAD risk groups, the analysis is repeated but grouping the two low-risk groups into a new ALL-LR group and using $\check{d}^i_{\mathrm{QT}}(n)$. This choice is motivated by the better performance obtained in simulated ECG, see Secs. 4.3.3. Results are shown in Fig. 5.9 and confirm that $\tau_{p,e}$, $\tau_{p,r}$ and $\Delta\tau_p$ can distinguish between low and high CAD risk patients. While $\tau_{1,e}$ shows a better discriminatory capacity than $\tau_{2,e}$, the reverted behavior is observed for $\tau_{p,r}$, although the significance of the differences between the ECG-LR and COR-MR

groups is borderline.

The QT time lags calculated for the combination of the two low-risk groups (ECG-LR and COR-LR) and those calculated for the combination of the two high-risk groups (COR-MR and COR-HR) are clustered to compute the ROC curve for $\tau_{1,e}$, $\tau_{1,r}$ and $\Delta\tau_1$ (or $\check{\tau}_{1,e}$, $\check{\tau}_{1,r}$, and $\Delta\check{\tau}_1$), as illustrated in Fig. 5.10(a), Fig. 5.10(b) and Fig. 5.10(c), respectively. The ROC curves are very similar for the delays calculated using any of the estimated QT series, although the results for $\check{d}^i_{\mathrm{QT}}(n)$ are slightly better. Also, the results point to the ability of the three QT adaptation time markers to discriminate between low and high CAD risk. The highest stratification value is attained by the marker $\Delta\check{\tau}_1$.

The values of the Spearman correlation coefficient between the defined degree of stenosis and the proposed QT rate adaptation markers, $\tau_{1,e}$, $\tau_{1,r}$ and $\Delta\tau_1$, are 0.25, -0.21, and -0.31, respectively, when calculating the delays from the $d^i_{\mathrm{QT}}(n)$ series, and 0.30, -0.22, and -0.31 when calculating the delays from the $\check{d}^i_{\mathrm{QT}}(n)$ series.

Finally, the results of the Pearson correlation coefficient between each proposed QT adaptation time lag marker and the three demographic variables are presented in Table 5.4. A modest linear relation between the confounding variables and the proposed markers can be observed, even when the p-values indicate statistical significance. The linear mixed model of the demographic variables reflects a variance of the random parameter of 7.6% (55 of 667), 0.7% (5 of 709) and 4.6% (93 of 1915) for $\check{\tau}_{1,e}$, $\check{\tau}_{1,r}$ and $\Delta\check{\tau}_1$, respectively, of the total variance of the model, which comprises the variance of the random parameter and the residual variance.

Table 5.4: Correlation results between the proposed markers and the demographic variables, being ρ the Pearson correlation coefficient using $\check{d}^i_{\mathrm{QT}}(n)$ series from FINCAVAS database.

	$\check{\tau}_{1,e}$		$\check{\tau}_{1,r}$		$\Delta\check{\tau}_1$	
	ρ	p-value	ρ	p-value	ρ	p-value
Age	0.24	< 0.01	-0.04	0.45	-0.17	< 0.01
BMI	0.16	< 0.01	-0.18	< 0.01	-0.20	< 0.01
Gender	-	0.12	-	< 0.01	-	< 0.01

Estimated time lags and regression models

Although $\tau_{p,e}$ shows worse performance than $\check{\tau}_{p,e}$, the former is necessary to estimate the latter. The QT adaptation time lag estimates are sometimes

negative when analyzing clinical ECGs, which is not feasible to interpret from a physiological perspective. Table 5.5 collects the number of $\tau_{p,e}$ and $\tau_{p,r}$ values that are less than 20 s, separately, for each regression model, termed as "nonusable" values in the FINCAVAS database.

The following rule is defined to reduce the number of nonusable values: in clinical ECGs where the estimated QT adaptation time lag $\tau_{p,e}$ is negative or less than 20 s, $\tau_{p,e}$ is set between 20 s and 70 s, selecting the first value within this range that allows obtaining a $\check{\tau}_{p,e}$ equal or higher than 20 s. The value of 20 s for $\tau_{p,e}$ corresponds to the lowest mean $\tau_{p,e}$, that is, the mean $\tau_{p,e}$ of the ECG-LR group. In cases in which the search does not provide any results, $\tau_{p,e}$ is set to 20 s. This implementation always enables the computation of $\check{\tau}_{p,e}$.

The percentage of nonusable estimates $\check{\tau}_{p,x}$ is represented in Table 5.5 for the FINCAVAS database. The results obtained with the hyperbolic regression model are the most influenced by this rule, where the number of rejected clinical ECGs is largely reduced after applying the rule described in the previous paragraph. The differences between the Gaussian and Laplacian estimators are not notable.

Table 5.5: Percent of nonusable $\tau_{p,x}$ estimates in each regression model using the instantaneous QT series $d^i_{\mathrm{QT}}(n)$ or $\check{d}^i_{\mathrm{QT}}(n)$ where $\tau_{p,x}, p = 1, 2; x \in \{e, r\}$ for Laplacian|Gaussian estimator and exercise|recovery phase, respectively, in FINCAVAS database.

			Parabolic	Linear	Hyperbolic	Logarithmic
$d^i_{\mathrm{QT}}(n)$	Nonusable $\tau_{p,x}$	$\tau_{1,e}$	7.9%	4.4%	59.2%	17.2%
		$\tau_{2,e}$	7.1%	3.3%	55.2%	14.8%
		$\tau_{1,r}$	47.9%	60.5%	17.4%	34.9%
		$\tau_{2,r}$	48.8%	61.8%	17.4%	35.1%
$\check{d}^i_{\mathrm{QT}}(n)$	Nonusable $\check{\tau}_{p,x}$	$\check{\tau}_{1,e}$	7.1%	3.3%	52.8%	13.9%
		$\check{\tau}_{2,e}$	6.6%	2.6%	49.7%	12.1%
		$\check{\tau}_{1,r}$	69.8%	80.8%	44.6%	52.5%
		$\check{\tau}_{2,r}$	72.0%	81.0%	45.7%	54.7%
$\check{d}^i_{\mathrm{QT}}(n)$	Nonusable $\check{\tau}_{p,e}$ after rule	$\check{\tau}_{1,e}$	1.8%	0.9%	24.9%	6.2%
		$\check{\tau}_{2,e}$	1.8%	0.7%	22.1%	5.1%
		$\check{\tau}_{1,r}$	69.5%	80.8%	28.9%	51.7%
		$\check{\tau}_{2,r}$	72.0%	80.6%	29.1%	53.9%

Therefore, the CAD discrimination capacity of the proposed markers is now studied in the FINCAVAS database after applying the above described rule and removing patients that present negative estimated delays. The results are shown in the box plots of Fig. 5.11, in which the corresponding groups ECG-LR, COR-LR, COR-MR and COR-HR are composed of 145, 41, 18 and

135 patients, respectively. The analysis is repeated by clustering the two low-risk groups into the ALL-LR group. The results improve in terms of statistical significance when compared to the results from Fig. 5.7 and Fig. 5.9. Significant differences can be observed between COR-LR/COR-MR with markers $\check{\tau}_{1,e}$ and $\Delta\check{\tau}_1$.

Estimated time lags using the observed $d^i_{\mathbf{RR}}(n)$ series

The results presented above have been calculated based on the model described in Fig. 2.3. Alternatively, this process is altered to propose to estimate the QT adaptation time as the delay between the observed RR intervals and a $d^i_{\mathrm{RR}}(n)$ series based on the observed QT intervals (see Fig. 2.4). The estimated delays using the $\check{d}^i_{\mathrm{RR}}(n)$ series and applying the rule described in Sec. 5.4.4 are shown in Fig. 5.12 using the FINCAVAS database. The trend of the results is the same as the ones shown in Fig. 5.11, with the Laplacian estimator also presenting better results than the Gaussian one. Table 5.6 shows that the number of nonusable delays is smaller than the ones presented in Table 5.5.

Estimated QT lags and hysteresis curves from the same patients as in Fig. 5.8 are calculated using the $d_{\mathrm{RR}}(n)$ and $\check{d}^i_{\mathrm{RR}}(n)$ series, and these are also presented in Fig. 5.13. The hysteresis curve shows the same behavior as a function of the analyzed CAD-risk group.

Table 5.6: Percent of nonusable $\tau_{p,x}$ estimates in each regression model using the instantaneous QT series $d^i_{\mathrm{RR}}(n)$ or $\check{d}^i_{\mathrm{RR}}(n)$ where $\tau_{p,x}, p = 1, 2; x \in \{e, r\}$.

			Parabolic	Linear	Hyperbolic	Logarithmic
$d^i_{\mathrm{RR}}(n)$	Nonusable $\tau_{p,x}$	$\tau_{1,e}$	7.3%	4.6%	36.2%	13.5%
		$\tau_{2,e}$	7.5%	3.3%	31.6%	11.7%
		$\tau_{1,r}$	48.1%	60.5%	19.6%	36.4%
		$\tau_{2,r}$	47.7%	60.9%	19.4%	35.3%
$\check{d}^i_{\mathrm{RR}}(n)$	Nonusable $\check{\tau}_{p,x}$	$\check{\tau}_{1,e}$	7.1%	3.8%	31.6%	10.4%
		$\check{\tau}_{2,e}$	7.1%	2.4%	28.0%	10.4%
		$\check{\tau}_{1,r}$	69.8%	79.7%	27.8%	52.1%
		$\check{\tau}_{2,r}$	71.3%	80.8%	28.5%	53.0%
$\check{d}^i_{\mathrm{RR}}(n)$	Nonusable $\check{\tau}_{p,e}$ after rule	$\check{\tau}_{1,e}$	3.3%	1.3%	17.4%	5.7%
		$\check{\tau}_{2,e}$	2.0%	0.9%	15.5%	5.5%
		$\check{\tau}_{1,r}$	69.8%	79.5%	29.1%	52.8%
		$\check{\tau}_{2,r}$	71.7%	80.6%	29.4%	53.9%

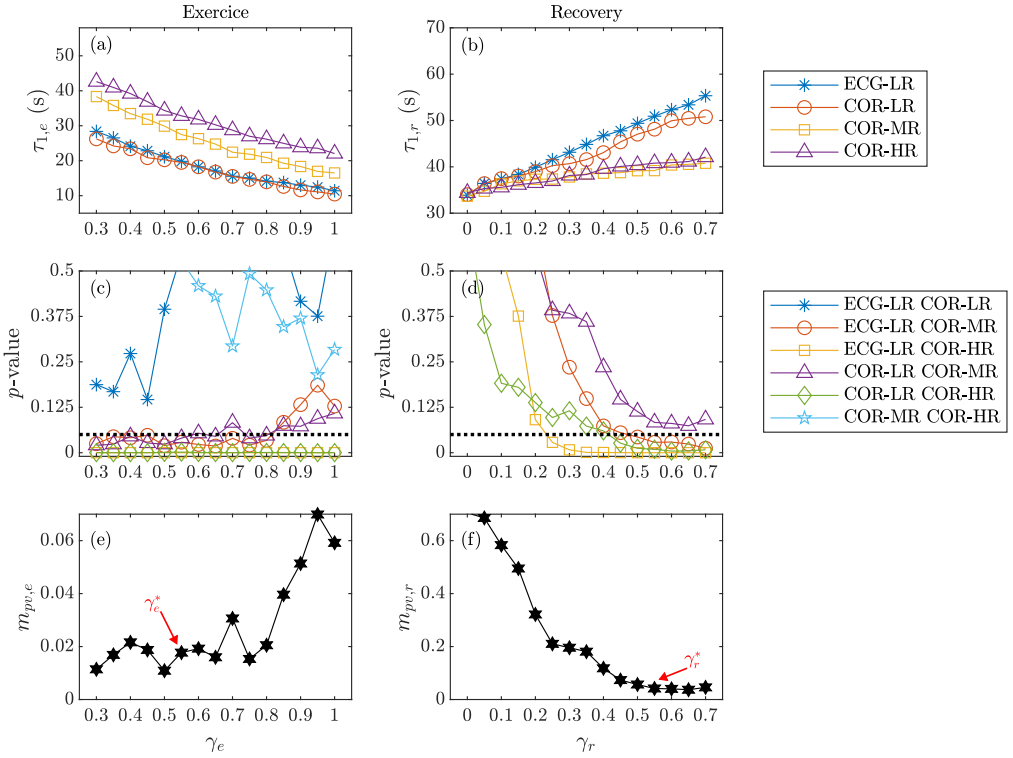

Figure 5.6: (a) $\tau_{1,e}$ and (b) $\tau_{1,r}$, values as a function of the position of $n_{e,e}$, and $n_{r,o}$, obtained by varying thresholds γ_e and γ_r, respectively. (c), and (d) corresponding p-values from (a) and (b), respectively, when comparing different pairs of patient groups. The dashed lines correspond to the significance level, $p = 0.05$. (e) Evolution of $m_{pv,e}$ obtained by varying the thresholds γ_e and (f) $m_{pv,r}$ by varying γ_r. For $m_{pv,e}$ and $m_{pv,r}$ calculation, the p-values corresponding to group pairs having at least half of the studied thresholds resulting in significant p-values, i.e., below dotted lines in panels (c) and (d), are taken into account. Selected thresholds γ_e^* and γ_r^* are marked with red arrows.

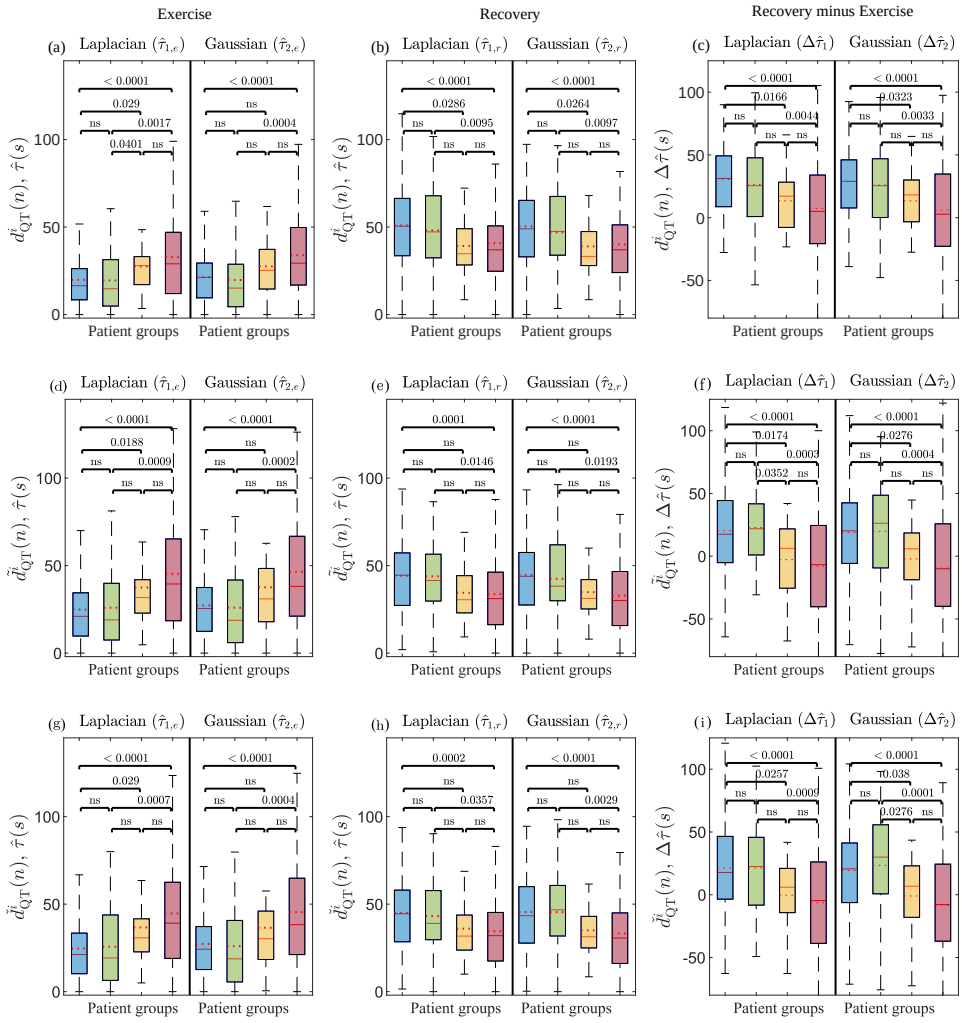

Figure 5.7: Box plots of the estimated time delay between $d^i_{\mathrm{QT}}(n)$ and $d_{\mathrm{QT}}(n)$ (top row), between $\tilde{d}^i_{\mathrm{QT}}(n)$ and $d_{\mathrm{QT}}(n)$ (middle row) and between $\ddot{d}^i_{\mathrm{QT}}(n)$ and $d_{\mathrm{QT}}(n)$ (bottom row) for the four patient groups of the FINCAVAS database, assuming either a Laplacian or a Gaussian noise model. The estimates are obtained for (a) exercise, resulting in $\hat{\tau}_{1,e}$ and $\hat{\tau}_{2,e}$, and (b) recovery, resulting in $\hat{\tau}_{1,r}$ and $\hat{\tau}_{2,r}$. (c) Box plots of the difference between recovery and exercise, resulting in $\Delta\hat{\tau}_1$ and $\Delta\hat{\tau}_2$. The dotted and continuous lines in red correspond to the mean and the median, respectively. Patient group color code is: ECG-LR (blue), COR-LR (green), COR-MR (yellow) and COR-HR (red). The p-values in separating patient groups are plotted on top of the box plot pairs.

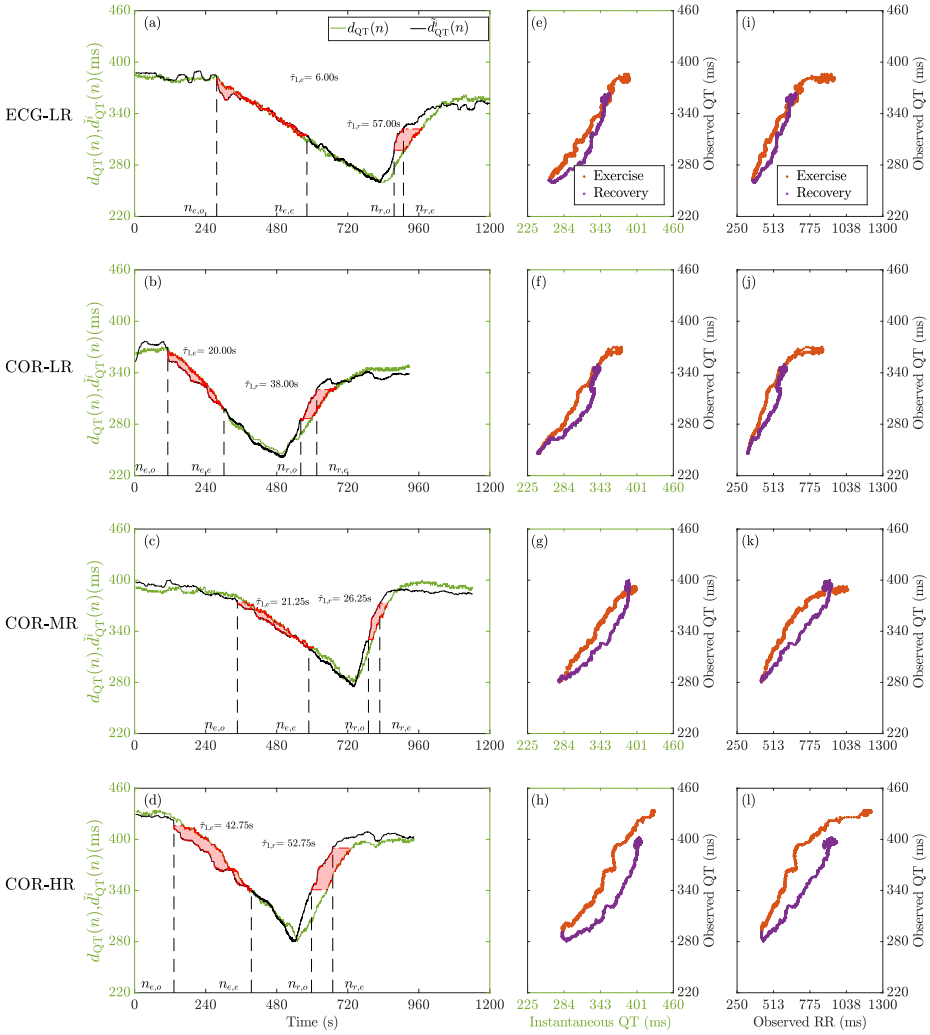

Figure 5.8: Panels (a-d) Examples of the QT series $\check{d}^{i}_{\mathrm{QT}}(n)$ and $d_{\mathrm{QT}}(n)$ and the estimated QT lags between them for each CAD-risk group (ECG-LR, COR-LR, COR-MR and COR-HR) from FINCAVAS database, respectively. Panels (e-h) show the associated $d_{\mathrm{QT}}(n)$-$\check{d}^{i}_{\mathrm{QT}}(n)$ hysteresis curves and panels (i-l) show the corresponding QT-RR hysteresis curves for each example, in which it can be seen that the higher the risk, the higher the hysteresis area.

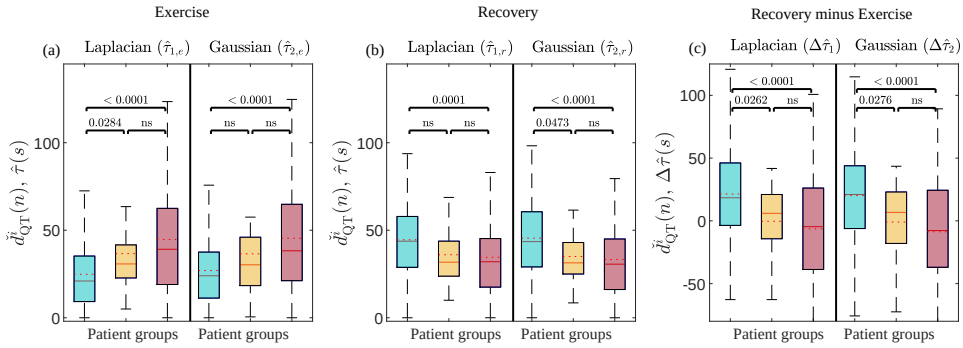

Figure 5.9: Results for the FINCAVAS database considering a new group, ALL-LR, that includes both low-risk groups. The figure shows box plots of the estimated time delay between $\check{d}^i_{\mathrm{QT}}(n)$ and $d_{\mathrm{QT}}(n)$ in (a) exercise, resulting in $\hat{\tau}_{1,e}$ and $\hat{\tau}_{2,e}$, and (b) recovery, resulting in $\hat{\tau}_{1,r}$ and $\hat{\tau}_{2,r}$. (c) Box plots of the difference between recovery and exercise, resulting in $\Delta\hat{\tau}_1$ and $\Delta\hat{\tau}_2$. The dotted and continuous lines in red correspond to the mean and the median, respectively. Patient group color code is: both low-risk groups (light blue), COR-MR (yellow) and COR-HR (red). The delay significance, p-values, in separating patient groups are plotted on top of the box plot pairs.

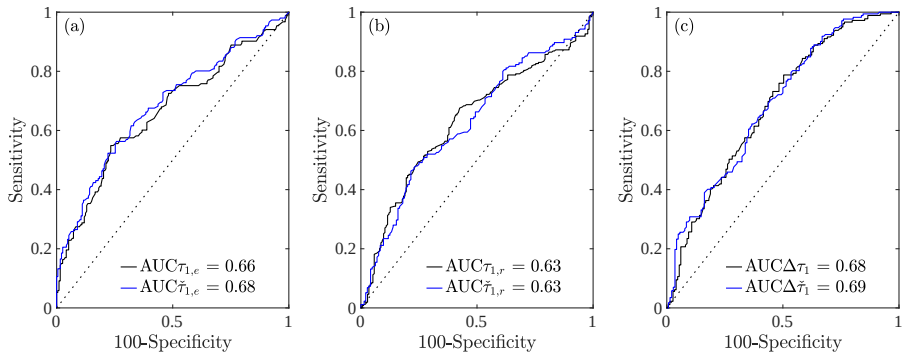

Figure 5.10: (a) (b) (c): ROC curves for $\check{\tau}_{1,e}$, $\check{\tau}_{1,r}$ and $\Delta\check{\tau}_1$, respectively, using for the classification the QT time lag calculated for the low-risk groups (ECG-LR and COR-LR) and the high-risk groups (COR-MR and COR-HR) of FINCAVAS database. The analyses are performed for both unmodified (black) and modified (blue) series.

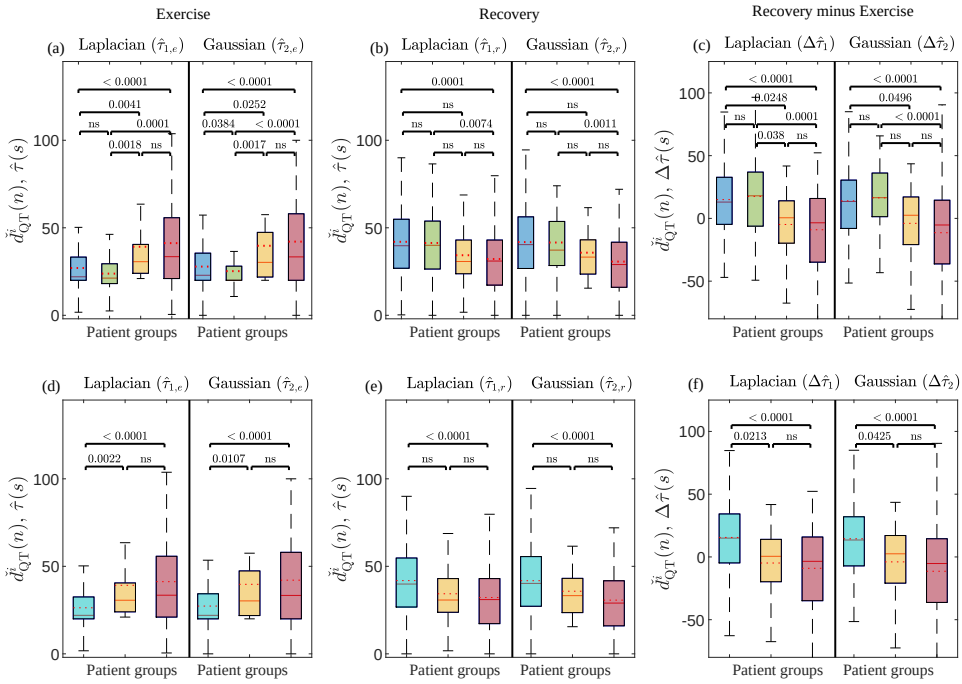

Figure 5.11: Box plots of the estimated time delay between $\check{d}^i_{\mathrm{QT}}(n)$ and $d_{\mathrm{QT}}(n)$ (top row) after applying the rule of excluding patients with no meaningful $\tau_{p,e}$ estimates, required to compute $\check{\tau}_{p,x}$, $p \in \{1,2\}$; $x \in \{e,r\}$. The estimates are obtained for (a) exercise, (b) recovery, and (c) the difference between recovery and exercise computed for the four patient groups of the FINCAVAS database, assuming either a Laplacian or a Gaussian noise model. The dotted and continuous lines in red correspond to the mean and the median, respectively. Patient group color code is: ECG-LR (blue), COR-LR (green), COR-MR (yellow), and COR-HR (red). The delay significance, p-values, in separating patient groups, are plotted above box plot pairs. (d), (e) and (f) show analogous results in the form of box plots after creating a new group, ALL-LR, that includes the two low-risk groups of the FINCAVAS database.

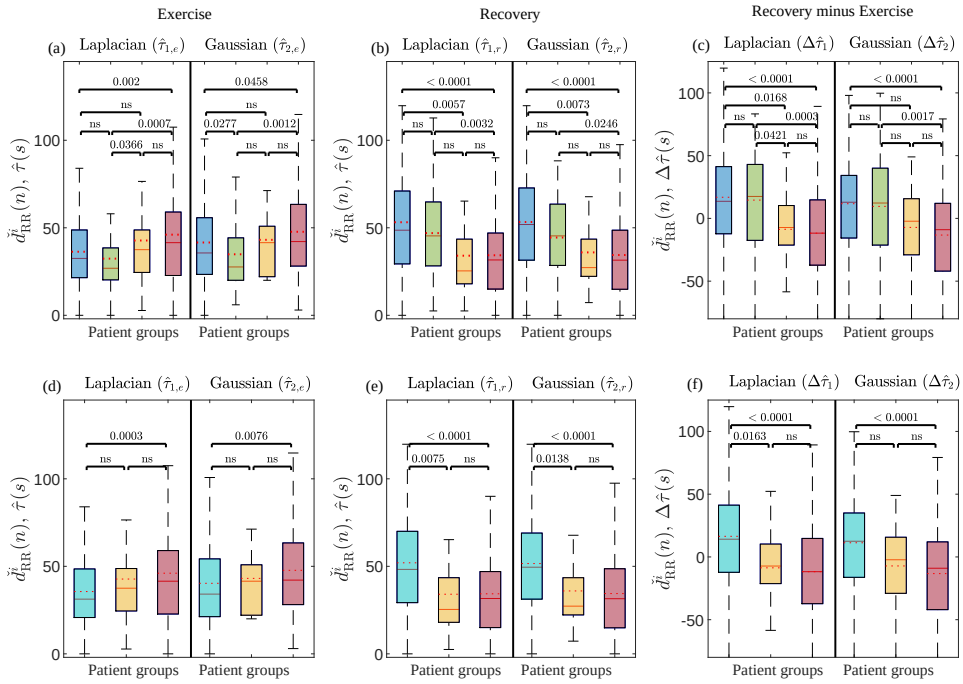

Figure 5.12: Box plots of the estimated time delay between $\check{d}^{i}_{\mathrm{RR}}(n)$ and $d_{\mathrm{RR}}(n)$ (top row) after applying a rule to reduce the number of nonusable $\tau_{p,e}$ estimates, required to compute $\check{\tau}_{p,x},\ p \in \{1,2\};\ x \in \{e,r\}$. The estimates are obtained for (a) exercise, (b) recovery, and (c) the difference between recovery and exercise computed for the four patient groups of the FINCAVAS database, assuming either a Laplacian or a Gaussian noise model. The dotted and continuous lines in red correspond to the mean and the median, respectively. Patient group color code is: ECG-LR (blue), COR-LR (green), COR-MR (yellow), and COR-HR (red). The delay significance, p-values, in separating patient groups, are plotted on top of the box plot pairs. (d), (e) and (f) show analogous results in the form of box plots after creating a new group that includes the two low-risk groups of the FINCAVAS database.

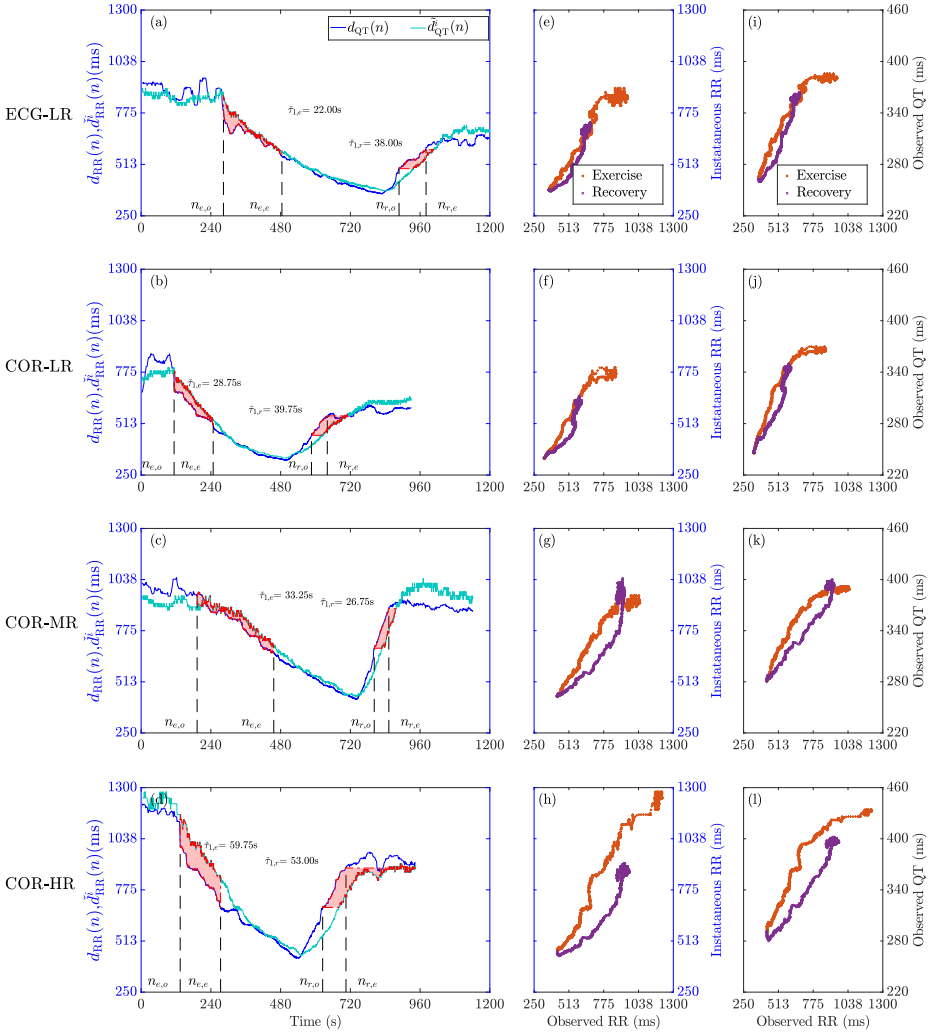

Figure 5.13: Panels (a-d) Examples of the RR series $d_{\mathrm{RR}}(n)$ and $\check{d}^{i}_{\mathrm{RR}}(n)$ and the estimated QT lags between them for each CAD-risk group (ECG-LR, COR-LR, COR-MR and COR-HR), respectively, from the same patients as in Fig. 5.8. Panels (e-h) show the associated $\check{d}^{i}_{\mathrm{RR}}(n)$-$d_{\mathrm{RR}}(n)$ hysteresis curves and panels (i-l) show the corresponding QT-RR hysteresis curves for each example, in which it can also be seen that the higher the risk, the higher the hysteresis area.

ARTEMIS database

Once the best suited method to estimate the QT adaptation time lag has been determined, the statistical power of the proposed markers to separate patients with different SXscore is also evaluated using the ARTEMIS database. First, the QT adaptation time lags are estimated between the observed series $d_{\mathrm{QT}}(n)$ and the instantaneous series $\check{d}^{i}_{\mathrm{QT}}(n)$, using only a Laplacian-based estimator due to the observed superior discriminatory results obtained with the FINCAVAS database. The results, calculated based on the rule described in Sec. 5.4.4, are presented in the first row of Fig. 5.14. The groups SXscore-LR, SXscore-MR and SXscore-HR are composed of 837, 109 and 75 patients, respectively. It can be seen in Fig. 5.14(a) that the tendency of $\check{\tau}_{1,e}$ observed in the FINCAVAS data is kept in this database: the higher the risk, the larger $\check{\tau}_{1,e}$; also, the higher the risk, the lower $\Delta\check{\tau}_1$ (see Fig. 5.14(c)). In addition, statistically significant differences, or p-values close to 0.05, are obtained in the pair of groups SXscore-LR/SXscore-HR and SXscore-MR/SXscore-HR for the two mentioned markers. The distribution of the estimated $\check{\tau}_{1,r}$ values is, however, similar along groups.

Next, the analysis was repeated using the observed series $d_{\mathrm{RR}}(n)$ and the instantaneous series $\check{d}^{i}_{\mathrm{RR}}(n)$, whose results are shown in the second row of Fig. 5.14. In this case, SXscore-LR, SXscore-MR and SXscore-HR groups are composed of 888, 112 and 75 patients, respectively. Statistical significant differences are observed by evaluating the delay between $\check{d}^{i}_{\mathrm{RR}}(n)$ and $d_{\mathrm{RR}}(n)$ in exercise, $\check{\tau}_{1,e}$, to stratify different SXscore groups. However, no statistical significance is observed using the other proposed markers.

It should be noted that the results for each risk group of the two databases, FINCAVAS and ARTEMIS, are not directly comparable since COR-MR and COR-HR groups from FINCAVAS would comprise all ARTEMIS patients, which, in turn, are divided into three different groups.

5.4.5 QT-RR adaptation and its power for SCD risk prediction

The ARTEMIS database was also used to study the capacity of the proposed markers to predict SCD or overall mortality. The estimated delay distributions for patients who suffer and do not suffer SCD or death by any cause are represented in the box plots of Fig. 5.15. Markers were calculated using either the instantaneous series $\check{d}^{i}_{\mathrm{QT}}$ or the instantaneous series $\check{d}^{i}_{\mathrm{RR}}$, the Laplacian-based estimator and the rule described in Sec. 5.4.4. Therefore, the number of victims and survivors of SCD were 1074 and 39 (1128 and 37 using $\check{d}^{i}_{\mathrm{RR}}$),

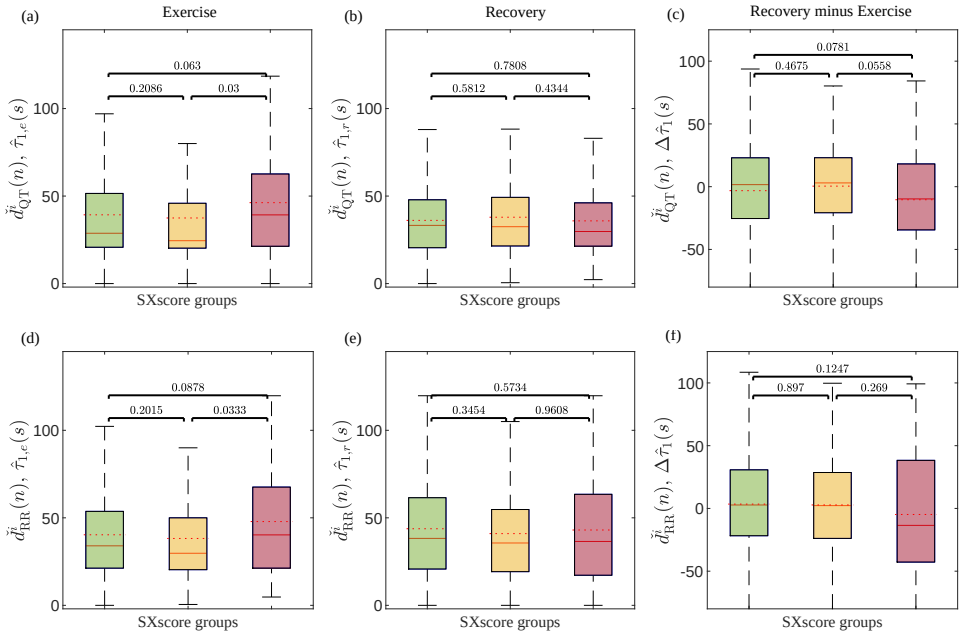

Figure 5.14: Box plots of the estimated time delay between $\check{d}^{i}_{\mathrm{QT}}(n)$ and $d_{\mathrm{QT}}(n)$ from ARTEMIS database after applying a rule to reduce the number of nonusable $\tau_{1,e}$ estimates, required to compute $\check{\tau}_{1,x},\ x \in \{e, r\}$. The estimates are obtained for (a) exercise, resulting in $\hat{\tau}_{1,e}$, and (b) recovery, resulting in $\hat{\tau}_{1,r}$. In (c) box plots of the difference between recovery and exercise, resulting in $\Delta\hat{\tau}_1$ are displayed. The dotted and continuous lines in red correspond to the mean and the median, respectively. Syntax Score group color code is: SXscore-LR (green), SXscore-MR (yellow) and SXscore-HR (red). The delay significance, p-values, in separating patient groups are plotted on top of the box plot pairs. The analysis is repeated using $\check{d}^{i}_{\mathrm{RR}}(n)$ and $d_{\mathrm{RR}}(n)$ series, whose $\hat{\tau}_{1,e}$, $\hat{\tau}_{1,r}$ and $\Delta\hat{\tau}_1$ are displayed in (d), (e) and (f) graphs, respectively.

respectively, while the number of victims and survivors of any cause-mortality were 1060 and 53 (1112 and 57 using $\check{d}^{i}_{\mathrm{RR}}$), respectively.

The $\check{\tau}_{1,r}$ marker was the one able to discriminate between victims and survivors of SCD when the delays were estimated using $\check{d}^{i}_{\mathrm{RR}}$ series (Fig. 5.15(e)). The marker $\check{\tau}_{1,r}$ was larger in patients who suffered SCD ($m_{\check{\tau}_{1,r}} = 53.17 \pm 27.28$ s) than in those who did not ($m_{\check{\tau}_{1,r}} = 42.96 \pm 28.02$ s), with the differences being statistically significant. These statistical differences were also observed using $\Delta\check{\tau}_1$ (Fig. 5.15(f)), with $m_{\Delta\check{\tau}_1} = 1.78 \pm 45.26$ s for SCD survivors and $m_{\Delta\check{\tau}_1} = 14.05 \pm 41.21$ s for SCD victims. However, $\check{\tau}_{1,r}$ marker rendered border-

line significant differences between patients victims and survivors of any-cause mortality ($m_{\check{\tau}_{1,r}} = 51.62 \pm 26.10$ s and $m_{\check{\tau}_{1,r}} = 42.89 \pm 28.08$ s, respectively). This last finding was also observed when $\check{\tau}_{1,r}$ marker was calculated using $\check{d}^{i}_{\mathrm{QT}}$ series (Fig. 5.15(b)).

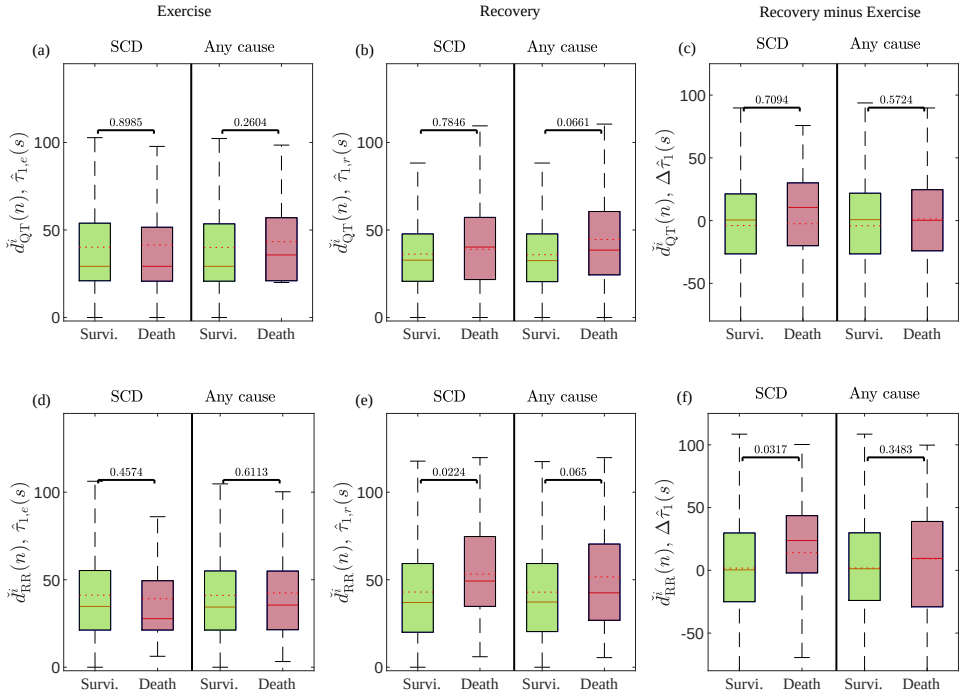

Figure 5.15: Box plots of the estimated time delay between $\check{d}^{i}_{\mathrm{QT}}(n)$ and $d_{\mathrm{QT}}(n)$ from ARTEMIS database after applying a rule to reduce the number of nonusable $\tau_{1,e}$ estimates, required to compute $\check{\tau}_{1,x},\ x \in \{e, r\}$. The estimates are obtained for (a) exercise, resulting in $\hat{\tau}_{1,e}$, and (b) recovery, resulting in $\hat{\tau}_{1,r}$. (c) Box plots of the difference between recovery and exercise, resulting in $\Delta\hat{\tau}_1$. The dotted and continuous lines in red correspond to the mean and the median, respectively. The outcome group color code is: survivor group (green) and death group (red) for both SCD and any cause-mortality outcomes. The delay significance, p-values, in separating patient groups are plotted on top of the box plot pairs. The analysis is repeated using $\check{d}^{i}_{\mathrm{RR}}(n)$ and $d_{\mathrm{RR}}(n)$ series, whose $\hat{\tau}_{1,e}$, $\hat{\tau}_{1,r}$ and $\Delta\hat{\tau}_1$ are displayed in (d), (e) and (f) graphs, respectively.

The univariable and multivariable Cox analyses for SCD and any cause-mortality predictions are summarized in Table 5.7 and Table 5.8, respectively. The median $\mathrm{QT_c}$ value for each learning window W_j, $j \in \{b, e, lr\}$ was computed using the Fridericia correction and was included in the predictive model evaluation.

The best univariable model for SCD was obtained with QT_{W_e} (C-index closed to 0.70) using either $\check{d}^i_{\mathrm{RR}}$ or $\check{d}^i_{\mathrm{QT}}$. In contrast, the best univariable model for any-cause mortality was obtained with HR_{W_e} (C-index = 0.73) using $\check{d}^i_{\mathrm{QT}}$ and with HR_{W_e} or QT_{W_e} (C-index = 0.73) using $\check{d}^i_{\mathrm{RR}}$.

The proposed $\check{\tau}_{1,r}$ marker was associated with both SCD and any-cause mortality when the delay was estimated using $\check{d}^i_{\mathrm{RR}}$, with a C-index equal to 0.62 and 0.57, respectively [$\mathcal{HZR}_{\mathrm{IQR}}$ of 1.55 (95%, CI 1.05-2.30) and 1.44 (95%, CI 1.03-2.01), respectively, resulting in $\mathcal{HZR}_{1\mathrm{s}} = 1.01$ in both cases]. However, when this index was calculated with $\check{d}^i_{\mathrm{QT}}$, it was only related to any cause-mortality, with a C-index equal to 0.58 [$\mathcal{HZR}_{\mathrm{IQR}}$ of 1.49 (95%, CI 1.13-1.96), resulting in $\mathcal{HZR}_{1\mathrm{s}} = 1.01$]. The markers $\check{\tau}_e$ and $\Delta_{\check{\tau}}$ did not yield statistically significant results.

Using $\check{d}^i_{\mathrm{QT}}$ series, the best multivariable model for SCD included the variables sex, HR_{W_b}, HR_{W_e} and QTc_{W_b}. The covariables with the greatest influence were sex, with the fact of being a man implying a 67% increase in the risk of SCD ($\mathcal{HZR}_{\mathrm{IQR}}$ of 0.33 (95%, CI 0.15-0.72)), and HR_{W_b}, with an increment of 1 bpm being associated with 7% increase in the risk of SCD ($\mathcal{HZR}_{1\mathrm{bpm}} = 1.07$). Using $\check{d}^i_{\mathrm{RR}}$ series, the best multivariable model for SCD included the variables HR_{W_b}, HR_{W_e}, QTc_{W_e} and $\check{\tau}_{1,r}$, with an increment of 1 bpm in HR_{W_b} being associated with 6% higher probability of suffering SCD ($\mathcal{HZR}_{1\mathrm{bpm}} = 1.06$), and an increment of 10 s in $\check{\tau}_{1,r}$ being associated with 17% higher likelihood of suffering SCD ($\mathcal{HZR}_{10\mathrm{s}} = 1.17$).

In the case of any-cause mortality, the best multivariable model included the variables sex, age, HR_{W_e}, $\mathrm{QT}_{W_{lr}}$, QTc_{W_b} and $\check{\tau}_{1,r}$, for all the possible series selected to calculate delays. An inverse relation was found between HR_{W_e} and any cause-mortality. Men and older patients were more likely to die of any cause-mortality.

All multivariable models had a C-index greater than 0.7, suggesting that these models can stratify individuals according to their risk of SCD or any-cause mortality. The values of the C-index were higher than those of the best univariable model in each case, thus showing that the predictive accuracy was enhanced with the inclusion of additional covariables.

Table 5.7: Univariable and multivariable association with SCD in ARTEMIS database.

Series	$\check{d}^i_{\mathrm{QT}}(n)$					$\check{d}^i_{\mathrm{RR}}(n)$				
Risk factor	**median ± IQR**	Univariable analysis		Multivariable analysis		**median ± IQR**	Univariable analysis		Multivariable analysis	
		$\mathcal{HZR}_{\mathrm{IQR}}$ (95% CI)	p-value	$\mathcal{HZR}_{\mathrm{IQR}}$ (95% CI)	p-value		$\mathcal{HZR}_{\mathrm{IQR}}$ (95% CI)	p-value	$\mathcal{HZR}_{\mathrm{IQR}}$ (95% CI)	p-value
Sex (male)	728 male	0.46 (0.21-1.00)	0.05*	0.33 (0.15-0.72)	0.01*	781 male	0.45 (0.20-1.03)	0.06	...	...
Age (years)	67.0 ± 11.0	1.52 (0.96-2.39)	0.07	...	...	67.0 ± 12.0	1.35 (0.83-2.20)	0.23	...	...
BMI (Kg/m^2)	28.0 ± 5.8	1.11 (0.75-1.66)	0.60	...	...	27.0 ± 5.0	1.19 (0.84-1.67)	0.33	...	...
HR_{W_b} (bpm)	59.5 ± 11.8	1.56 (1.10-2.20)	0.01*	2.24 (1.50-3.35)	<0.01*	59.3 ± 11.7	1.43 (0.99-2.07)	0.05*	1.99 (1.32-3.00)	<0.01*
HR_{W_e} (bpm)	119.51 ± 27.9	0.40 (0.25-0.65)	<0.01*	0.32 (0.19-0.56)	<0.01*	122.5 ± 29.3	0.43 (0.26-0.71)	<0.01*	0.46 (0.23-0.93)	0.03
$\mathrm{HR}_{W_{lr}}$ (bpm)	73.0 ± 14.0	0.90 (0.60-1.35)	0.62	...	...	73.6 ± 14.3	0.84 (0.55-1.28)	0.41	...	...
QT_{W_b} (ms)	418.0 ± 39.0	1.21 (0.81-1.78)	0.35	...	...	417.9 ± 38.4	1.27 (0.85-1.88)	0.24	...	...
QT_{W_e} (ms)	313.0 ± 42.0	2.20 (1.56-3.11)	<0.01*	...	...	308.0 ± 41.6	2.06 (1.46-2.90)	<0.01*	...	...
$\mathrm{QT}_{W_{lr}}$ (ms)	396.0 ± 38.0	1.34 (0.92-1.96)	0.13	...	...	394.0 ± 38.4	1.41 (0.96-2.07)	0.08	...	...
QTc_{W_b} (ms)	416.0 ± 28.0	1.69 (1.22-2.34)	<0.01*	1.66 (1.16-2.38)	0.01*	415.7 ± 27.0	1.69 (1.22-2.33)	<0.01*	...	..
QTc_{W_e} (ms)	392.6 ± 26.5	2.00 (1.46-2.72)	<0.01*	...	...	390.6 ± 27.1	2.01 (1.46-2.77)	<0.01*	1.50 (0.95-2.39)	0.08
$\mathrm{QTc}_{W_{lr}}$ (ms)	423.2 ± 25.8	1.34 (0.93-1.93)	0.11	...	...	423.0 ± 25.5	1.37 (0.95-1.99)	0.09	...	...
$\check{\tau}_e$ (s)	29.3 ± 32.5	1.08 (0.76-1.54)	0.67	...	...	34.5 ± 33.8	0.93 (0.62-1.40)	0.74	...	...
$\check{\tau}_r$ (s)	33.0 ± 27.3	1.18 (0.82-1.70)	0.37	...	...	37.5 ± 39.5	1.55 (1.05-2.30)	0.03*	1.85 (1.25-2.74)	<0.01*
$\Delta\check{\tau}$ (s)	0.75 ± 48.3	1.04 (0.71-1.52)	0.85	...	...	1.5 ± 54.5	1.39 (0.93-2.07)	0.11	...	...
C-index	0.69 (with QT_{W_e})			0.80		0.68 (with QT_{W_e})			0.75	

Table 5.8: Univariable and multivariable association with any cause-mortality in ARTEMIS database.

Series	$\check{d}^i_{\mathrm{QT}}(n)$					$\check{d}^i_{\mathrm{RR}}(n)$				
Risk factor	**median ± IQR**	Univariable analysis		Multivariable analysis		**median ± IQR**	Univariable analysis		Multivariable analysis	
		$\mathcal{HZR}_{\mathrm{IQR}}$ (95% CI)	p-value	$\mathcal{HZR}_{\mathrm{IQR}}$ (95% CI)	p-value		$\mathcal{HZR}_{\mathrm{IQR}}$ (95% CI)	p-value	$\mathcal{HZR}_{\mathrm{IQR}}$ (95% CI)	p-value
Sex (male)	728 male	0.37 (0.18-0.76)	0.01*	0.24 (0.11-0.50)	<0.01*	781 male	0.40 (0.20-0.82)	0.01*	0.26 (0.12-0.55)	<0.01*
Age (years)	67.0 ± 11.0	3.41 (2.19-5.30)	<0.01*	2.37 (1.49-3.77)	<0.01*	67.0 ± 12.0	3.46 (2.18-5.50)	<0.01*	2.23 (1.36-3.66)	<0.01*
BMI (Kg/m^2)	28.0 ± 5.8	0.92 (0.63-1.32)	0.64	...	...	27.0 ± 5.0	1.02 (0.75-1.39)	0.88	...	...
HR_{W_b} (bpm)	59.5 ± 11.8	1.05 (0.74-1.48)	0.80	...	...	59.3 ± 11.7	1.10 (0.78-1.54)	0.59	...	...
HR_{W_e} (bpm)	119.51 ± 27.9	0.27 (0.17-0.42)	<0.01*	0.22 (0.12-0.40)	<0.01*	122.5 ± 29.3	0.27 (0.17-0.42)	<0.01*	0.23 (0.13-0.42)	<0.01*
$\mathrm{HR}_{W_{lr}}$ (bpm)	73.0 ± 14.0	0.56 (0.39-0.81)	<0.01*	...	...	73.6 ± 14.3	0.52 (0.36-0.76)	<0.01*	...	...
QT_{W_b} (ms)	418.0 ± 39.0	1.33 (0.96-1.85)	0.09	...	...	417.9 ± 38.4	1.30 (0.93-1.80)	0.12	...	...
QT_{W_e} (ms)	313.0 ± 42.0	2.43 (1.83-3.24)	<0.01*	...	...	308.0 ± 41.6	2.38 (1.81-3.13)	<0.01*	...	...
$\mathrm{QT}_{W_{lr}}$ (ms)	396.0 ± 38.0	1.53 (1.12-2.10)	0.01*	0.42 (0.23-0.78)	<0.01*	394.0 ± 38.4	1.61 (1.18-2.21)	<0.01*	0.52 (0.29-0.95)	0.03*
QTc_{W_b} (ms)	416.0 ± 28.0	1.42 (1.05-1.92)	0.02*	2.10 (1.26-3.51)	<0.01*	415.7 ± 27.0	1.41 (1.06-1.89)	0.02*	1.68 (1.02-2.77)	0.04*
QTc_{W_e} (ms)	392.6 ± 26.5	1.93 (1.48-2.51)	<0.01*	...	...	390.6 ± 27.1	2.00 (1.54-2.61)	<0.01*	...	...
$\mathrm{QTc}_{W_{lr}}$ (ms)	423.2 ± 25.8	1.09 (0.78-1.52)	0.61	...	...	423.0 ± 25.5	1.12 (0.80-1.56)	0.51	...	...
$\check{\tau}_e$ (s)	29.3 ± 32.5	1.14 (0.85-1.52)	0.39	...	...	34.5 ± 33.8	1.20 (0.89-1.62)	0.23	...	...
$\check{\tau}_r$ (s)	33.0 ± 27.3	1.49 (1.13-1.96)	0.01*	1.47 (1.14-1.89)	<0.01*	37.5 ± 39.5	1.44 (1.03-2.01)	0.03*	1.59 (1.14-2.21)	<0.01*
$\Delta\check{\tau}$ (s)	0.75 ± 48.3	1.17 (0.84-1.64)	0.35	...	...	1.5 ± 54.5	1.21 (0.87-1.68)	0.25	...	...
C-index	0.73 (with HR_{W_e})			0.82		0.73 (with HR_{W_e} or QT_{W_e})			0.80	

5.5 Discussion

5.5.1 T wave end delineation

Computing the T wave end in ECG signals recorded during EST or high heart rate values is challenging. Here, we have evaluated different variants of spatial lead transformation methodologies to delineate the T wave end. The highest variance is observed when the MLeads methodology is used. Visual examples in Fig. 5.2 are in agreement with the numerical quantification of the QT variability power, $\mathcal{P}_{\mathrm{QTV}}$, shown in Fig. 5.4. From Fig. 5.2 it can be observed that a larger outlier contamination introduces a distortion in the median filtered trace which could affect the time lag estimation. Computing the T wave end in any TL1 is more stable than applying the multi-lead delineation. In particular, the best performing methods for ECG delineation during EST are those obtained with GπCA$_P$-based techniques rather than with PCA-based ones. Results show that all PCA-based techniques provide similar $\mathcal{P}_{\mathrm{QTV}}$ results and, analogously, all GπCA$_P$-based techniques render similar results.

These conclusions are also extracted by evaluating the T wave end delineation in simulated ECGs, quantified by a reference mark, cf. Sec. 4.3.1. Therefore, assessing the beat-to-beat variability of the observed QT series, assuming to be composed of natural variability and delineation errors, can be an alternative when a reference mark is not available.

Our results are in line with previous studies that used GπCA$_P$-based techniques to emphasize beat-to-beat periodic components in Holter ECG [90, 104] and found them to present superior performance than PCA or single-lead delineation strategies when high noise contamination is present. Other blind source separation methods, such as ICA, could have been considered. Still, the fact that GπCA$_P$-based incorporates a priori available knowledge of the beat-to-beat T wave periodicity structure, focusing on the transformation of the T wave enhancement, has led to restricting the analysis to GπCA$_P$ in this Ph.D. thesis and leave the evaluation of ICA methods for future works.

5.5.2 QT-RR adaptation time lag and its relation with coronary artery disease

According to the mean QT adaptation time lag estimated in this Ph.D. thesis, the higher CAD level, the higher the QT adaptation time lag during exercise. This is in agreement with results reported by Lauer *et al.* [80] where QT hysteresis is found to increase with the likelihood of any degree of ischemia or severe

ischemia. In addition, these values ranging from 20 to 50 s are of the same order of magnitude as those reported in [47], where the QT adaptation time constants are estimated from selected step-like heart rate changes and are reported to reach values ranging from 36 to 62 seconds, depending on the patients. A comparison of the results obtained in this Ph.D. thesis and those of other studies can be found in Table II. Taking the study published in [47], the adaptation time is measured at 50% of the complete QT adaptation time for abrupt RR changes and is denoted as L50. This percent (50%) is not far from 63%, which corresponds to the time constant in the exponential response of a first-order system when the input is a step. Thus, this range is compatible with the hypothesis that the QT adaptation time lag, measured as proposed here, during the exercise and recovery phases or in response to a sudden step-like heart rate change could provide equivalent information. Note that the patients in [47] are survivors of acute myocardial infarction, while the common situation in this study is that patients are at a certain risk of suffering CAD. Thus, the cardiac substrate in the patients of the two studies is different.

When comparing the results of the statistical analysis to separate the different patient groups using each of the three instantaneous QT series estimation (see Fig. 5.7), a small decrease in the p-values is generally observed using $\check{d}^{i}_{\mathrm{QT}}(n)$. Statistical significance is not reached when comparing the COR-LR and COR-MR groups using $\tau_{1,e}$ calculated with any modified instantaneous QT series. Nevertheless, the capacity for discriminating between the COR-LR and COR-MR groups is statistically significant for the proposed markers $\check{\tau}_{1,e}$ and $\Delta\check{\tau}_1$ when the delays are estimated using the $\check{d}^{i}_{\mathrm{QT}}(n)$ series and the rule defined in sec. 5.4.4 (see Fig. 5.11). Consequently, this rule helps to reject patients from the analysis and in the same way improves the discriminatory capacity of the proposed markers. The significance of the results remains unchanged after applying the Bonferroni correction if six comparisons are performed ($p < 0.008$ for statistical significance), except for the cases of ECG-LR/COR-MR and COR-LR/COR-MR with $\tau_{p,r}$ and $\Delta\tau_p$ for $p \in \{1, 2\}$. The nonuniform results in terms of statistical significance observed when including the COR-MR group in the comparisons could be a consequence of its reduced number of patients compared to other groups.

The trend of the results using $\check{d}^{i}_{\mathrm{RR}}(n)$ is the same as the ones estimated using $\check{d}^{i}_{\mathrm{QT}}(n)$ in the FINCAVAS database (see Fig. 5.12) and in the ARTEMIS database (see Fig. 5.14), although the delays are higher. Focusing on the FINCAVAS database, there are some changes in terms of the statistical significance when comparing all low-risk groups and the COR-MR group: statistical significance is not attained using $\check{\tau}_{1,e}$, but it is when using $\check{\tau}_{1,r}$, which leads to statistically

significant differences for $\Delta\check{\tau}_1$ marker. Moreover, Table 5.6 shows that the number of nonusable delays is smaller than the ones presented in Table 5.5. The correlation between the proposed markers computed with $\check{d}^i_{\mathrm{RR}}(n)$ and the degrees of stenosis, as well as the ROC curves, presents similar results. Thus, the methodology based on the $d^i_{\mathrm{RR}}(n)$ series could be an improved version of that based on $d^i_{\mathrm{QT}}(n)$.

The associated mean values for the ECG-LR group are $m_{\tau_{1,e}} = 19.82 \pm 14.62$ s and $m_{\tau_{1,r}} = 50.92 \pm 26.11$ s using $d^i_{\mathrm{QT}}(n)$ series. In [83], the mean time lag of QT interval adaptation for step-like heart rate changes is studied independently in response to heart rate acceleration and deceleration in healthy subjects performing postural changes. The values reported in [83] are $m_{\tau_e} = 34.8 \pm 13.6$ s and $m_{\tau_r} = 48.4 \pm 25.7$ s. The larger adaptation time lag in response to heart rate decelerations than to heart rate accelerations is consistent with the results in the present Ph.D. thesis. The computation of the delay using the modified $\check{d}^i_{\mathrm{QT}}(n)$ series (or $\check{d}^i_{\mathrm{RR}}(n)$ series) described in Sec. 2.7 and applying the rule described in Sec. 5.4.4, $m_{\check{\tau}_{1,e}} = 27.02 \pm 14.41$ s ($m_{\check{\tau}_{1,e}} = 36.32 \pm 21.57$ s) and $m_{\check{\tau}_{1,r}} = 41.99 \pm 23.32$ s ($m_{\check{\tau}_{1,r}} = 53.17 \pm 30.09$ s), agree better with the values reported in [83]. These results strengthen that the modification of the QT values at the peak exercise leads to a better representation of the QT-RR dynamics and, consequently, more accurate estimates of the QT adaptation time lag.

Axelsson *et al.* [75] studied the adaptation time of the QT interval following an abrupt heart rate change in patients with pacemakers. They concluded that the adaptation of ventricular repolarization duration is longer after the heart rate decreases than after it increases. This observation is supported by the results presented here, although the delays in the COR-HR group are practically the same in the exercise and recovery phases. A comparison of the method proposed in this Ph.D. thesis to measure the QT adaptation time with those reported in the literature, including the work reported in [75], is summarized in Table 5.9.

A modest linear correlation is found between the demographic variables and the proposed adaptation time markers in this work. Still, the sign of the small correlation indicates that patients with an elevated risk of suffering CAD are older, have a larger BMI, and $\check{\tau}_{1,e}$ is higher while both $\check{\tau}_{1,r}$ and $\Delta\check{\tau}_1$ are lower. The means of the adaptation markers are also different according to gender. A linear mixed model is calculated to express the QT time lag markers of the four CAD patient groups using a combination of the demographic variables. Statistically significant p-values are only obtained for variables BMI and gender (p-values equal to 0.04 and equal to 0.02, respectively) when they are used together in the linear mixed model to estimate the delay in the recovery phase.

Nevertheless, the low between-group variance (7.6%, 0.7% and 4.6%) for $\check{\tau}_{1,e}$, $\check{\tau}_{1,r}$ and $\Delta\check{\tau}_1$ markers, respectively, indicates that large delay differences are not observed between groups. Moreover, the residual variance is very high, which suggests that the proposed markers cannot be explained by the demographic variables.

To corroborate that the last conclusion is not contaminated by the similar values between the ECG-LR and COR-LR groups, the same linear mixed model is fitted but with the two low-risk groups merged into one (ALL-LR). Therefore, only three risk groups are distinguished: All-LR, COR-MR and COR-HR. The variance of the contributing variables explains 8.9%, 0.8% and 5.9% for $\check{\tau}_{1,e}$, $\check{\tau}_{1,r}$ and $\Delta\check{\tau}_1$ markers, respectively, observing that the values have increased slightly but they are still low. Therefore, it can be concluded that the combination of the three demographic parameters does not provide a linear model that represents the information of any QT adaptation delay marker. In the case that the QT time lag estimates were largely influenced by the confounding variables, a clear difference between intercepts of the different groups would be expected, together with a well-fitted linear model in which the explained variance would be high while the residual one would be low.

The correlation values between the degree of stenosis and the three proposed QT adaptation time lag markers confirm that there is a direct relation between $\tau_{p,e}$ and CAD, that is, the degree of stenosis. However, an inverse relation is found between $\tau_{p,r}$ and the degree of stenosis, or between $\Delta\tau_p$ and the degree of stenosis. As described in section 5.4, the Spearman correlation coefficient values do not present significant differences when computed from the $d^i_{\mathrm{QT}}(n)$ or the $\check{d}^i_{\mathrm{QT}}(n)$ series.

Therefore, computing the QT adaptation time lag in exercise ECG stress testing between the instantaneous $\check{d}^i_{\mathrm{QT}}(n)|\check{d}^i_{\mathrm{RR}}(n)$ and observed $d_{\mathrm{QT}}(n)|d_{\mathrm{RR}}(n)$ series using the Laplacian estimator provides the following information: low values of $\check{\tau}_{1,r}$ could be an indicator of a high risk of suffering CAD, while low $\check{\tau}_{1,e}$ values could be indicative of low risk of having CAD. According to $\check{\Delta}\tau_1$, its values decrease as the likelihood of suffering CAD increases, reaching values close to zero or even negative values. Thus, low $\check{\Delta}\tau_1$ values would be indicative of an elevated CAD risk. These findings are observed using the two clinical databases, i.e. FINCAVAS and ARTEMIS.

From a clinical perspective, patients in the ARTEMIS database would correspond to the ones of COR-MR and COR-HR groups from FINCAVAS database, who presented a stenosis greater than 50%. In the second row of Fig. 5.12, it can be observed that there are no statistically significant differences

Table 5.9: Comparison of presents results with published studies.

Authors	Subjects	Type of heart rate changes	QT adaptation time lag
Lau et al. [64]	7 patients with complete heart block diagnosis.	Abrupt heart rate changes from a temporary pacing electrode.	136s in heart rate acceleration, and 189s in heart rate deceleration for L_{90}.
Lauer et al. [80]	260 patients referred for treadmill exercise.	QT-RR hysteresis from gradual heart rate changes at stress test.	QT-RR hysteresis $\geqslant$ 313 s for CAD patients. QT-RR hysteresis $\geqslant$ 375 s for any ischemia. Higher QT-RR hysteresis is predictive of the presence and severity of myocardial ischemia.
Pueyo et al. [47]	866 patients survivors of acute myocardial infarction, of which 200 patients with the highest and lowest changes in heart rate were selected.	Abrupt heart rate changes from 24h-Holter recordings.	From 36 to 62 s for L_{50}.
Pueyo et al. [83]	33 healthy subjects.	Abrupt heart rate changes from controlled postural maneuvering.	35 s in heart rate acceleration, and 48 s in heart rate deceleration for L_{90}.
Axelsson et al. [75]	25 subjects with permanent pacemakers.	Abrupt heart rate changes controlled by a pacemaker.	Time constant for the exponential function of the low QT adaptation phase in ventricular pacing: 50 s in heart rate acceleration, and 62 s in heart rate deceleration. 110 s in heart rate acceleration, and 133 s in heart rate deceleration for L_{90} in ventricular pacing (this phase includes both the instantaneous and the low response of the QT adaptation when the heart rate change).
Martín-Yebra et al. [90]	171 patients with chronic heart failure with permanent AF.	1-h windows from ambulatory ECG recordings.	For nonSCD patients: τ = 50 s and L_{90} = 111 s. For SCD patients: τ = 67 s and L_{90} = 136 s.
Proposed	453 patients referred for a bicycle-ergometer exercise stress test.	Gradual heart rate changes at exercise stress testing.	For low-risk CAD patients: 27 s in heart rate acceleration and 42 s in heart rate deceleration. For high-risk CAD patients: 34 s in heart rate acceleration and 40 s in heart rate deceleration.

L_{50} and L_{90} represent the time required for QT to complete 50% and 90%, respectively, of the change in response to HR changes. τ is the delay of the first-order system with an impulse response that describing the relation between QT and RR intervals.

between these two groups for any proposed markers; in contrast to the results from Fig 5.14(d). Therefore, this observation could be valuable to support the importance of the SXscore index in the clinical decision.

It can be noted that other variables such as heart rate or QT (Table 5.1) also significantly discriminate between CAD groups. However, the time lags estimated from EST can provide complementary information to heart rate and QT intervals and can have value for arrhythmic risk prediction, as shown in [47, 65] in response to abrupt heart rate changes.

Lastly, related to the identification of the onset and end of the ramps for the delay computation, two considerations can be made. First, an automatic algorithm would not be necessary in cases where well-annotated exercise-phase onset and recovery-phase end were available, but this is not always the case and requires extra acquisition protocol requirements. This identification can be easily dealt with the proposed algorithm. Second, the final part of the exercise ramp and the onset of the recovery ramp coincide with the occurrence of a larger sympathetic activation. Consequently, the QT time lag might possibly not be constant and could even decrease with increasing sympathetic activation [92]. This phenomenon is observed between $d^{i}_{\mathrm{QT}}(n)$ and $d_{\mathrm{QT}}(n)$ series, which overlap, with no significant lag time, when approaching the peak exercise in the exercise phase, Fig. 2.5(b). Recent findings [92] show that the time lag for ventricular repolarization adaptation to sympathetic provocation becomes progressively reduced in response to increasingly higher levels of β-adrenergic stimulation, as occurs when approaching the peak exercise. Electrophysiological simulations including concurrent changes in ANS and in heart rate series such as those studied here can shed light on the basis of this observed behavior. This effect is also reflected in the selection of the optimal thresholds for patient classification $\gamma_e^* = \gamma_r^* = 0.55$, which are selected in areas far from the peak exercise where the lag can be considered to remain approximately constant. Defining the end of the exercise area, or the onset of the recovery area, far from the peak exercise also avoids estimating the delays in an area where the overlap of the P wave with the T wave could markedly influence the delineation of the T wave end.

5.5.3 QT-RR adaptation and its power for SCD risk prediction

A major finding of this study is the relevance of the proposed $\check{\tau}_{1,r}$ marker for (a) stratifying survivors and victims of either SCD or any cause-mortality, and (b) defining multivariable regression models to predict either SCD or any cause-mortality when the QT-RR time lag is estimated between $\check{d}^{i}_{\mathrm{RR}}(n)$ and the observed $d_{\mathrm{RR}}(n)$. In contrast to this capacity of the exercise time

lag, only significant results are obtained for prediction of any cause-mortality when the recovery time lag is estimated between $\check{d}^i_{\mathrm{QT}}(n)$ and the observed $d_{\mathrm{QT}}(n)$. Thus, using $\check{d}^i_{\mathrm{RR}}(n)$ is more advantageous from a clinical perspective for both separation of CAD groups and for prediction of either SCD or any-cause mortality.

The importance of $\check{\tau}_{1,r}$ marker estimated using $\check{d}^i_{\mathrm{RR}}(n)$ is observed not only in univariable but also in multivariable analysis, since this variable is part of the best model to predict SCD or any cause-mortality. An addition of 10 s in $\check{\tau}_{1,r}$ lead to 17% increase in the risk of SCD and 12% increase in the risk of dying of any cause.

Also, other demographic variables like gender and ECG-derived variables measured during peak exercise, such as HR_{W_e} and QT_{W_e}, show a strong correlation with the two investigated endpoints.

The multivariable Cox regression model for predicting any-cause mortality has also been studied using only sex, age, HR_{W_e}, $\mathrm{HR}_{W_{lr}}$ and $\check{\tau}_{1,r}$ variables, that is, removing any variable related to the QT interval. Using information from the $\check{d}^i_{\mathrm{RR}}(n)$ series, the final multivariable model after applying Akaike criterion is composed of HR_{W_e} and $\mathrm{HR}_{W_{lr}}$ variables, with their associated hazard ratios $\mathcal{HZR}_{\mathrm{IQR}}$ being 0.22 (95%, CI 0.12-0.42) and $\mathcal{HZR}_{\mathrm{IQR}}$ of 1.50 (95%, CI 0.90-2.50), respectively. In this multivariable model, a direct relation between $\mathrm{HR}_{W_{lr}}$ variable and any-cause mortality can be observed, with higher $\mathrm{HR}_{W_{lr}}$ values corresponding to higher mortality risk. However, the $\mathcal{HZR}$ value of this variable in the univariable model is lower than one ($\mathcal{HZR}_{\mathrm{IQR}}$ of 0.52 (95%, CI 0.36-0.76)), thus presenting an inverse relation with mortality risk (see Table 5.8). Taken together, our results should be interpreted in light of the changes in different variables. Particularly in the case of $\mathrm{HR}_{W_{lr}}$, they should be interpreted in light of the changes in HR_{W_e}. From the multivariable analysis, our results represent that, when $\mathrm{HR}_{W_{lr}}$ rises for a given HR_{W_e}, the risk of any-cause mortality increases. Clinically, it could mean that patients with a higher mortality risk achieve an elevated heart rate in the basal area after recovery, so either they cannot recover totally or have a high heart rate at rest condition. In terms of RR series, the risk of any-cause mortality increases when $\mathrm{RR}_{W_{lr}}$ decreases for a given RR_{W_e}. This analysis can also explain the opposite tendency of the $\mathcal{HZR}$ value of $\mathrm{QT}_{W_{lr}}$ obtained in the multivariable regression model in Table 5.8, as compared to the univariable model.

ECG predictors of SCD have been extensively studied in the literature [25, 135, 136] and their relevance due to their noninvasive nature has been pointed out [31, 60, 137]. In this Ph.D. thesis, longer QT-RR adaptation time

measured in the recovery phase of EST, $\check{\tau}_{1,r}$, is associated with SCD in patients from mild- to high-risk of CAD. The predictive capacity of both $\check{\tau}_{1,r}$ and $\Delta\check{\tau}_1$ derived from the ECG as noninvasive markers could be valuable from a clinical perspective.

Some considerations related to Cox analysis should be noted. First, the SXscore information is not included because a nonsignificant relation between this variable and any of the two investigated endpoints was found. Second, standardization of the variables based on their median and the IQR was performed after observing that not all variables follow a normal distribution. Dichotomizing the variables would have been another option. This would require setting a threshold on e.g. $\check{\tau}_{1,r}$, which has not been studied in the literature yet.

5.5.4 QT-RR modeling

Estimation of α and β

To calculate the instantaneous series $d^i_{\mathrm{QT}}(n)$, three windows are selected, W_b, W_e and W_{lr}, assumed to contain stationary RR and QT series from where to estimate the α and β parameters of the nonlinear function $g_f\left(d_{\mathrm{RR}}(n);\alpha,\beta\right)$. Stationary series guarantee that the dominant dependency between the RR and QT series is mostly driven by the nonlinear block in the model of Fig. 2.3 and, thus, well suited to estimate α and β. However, the stationarity of those segments is not ensured, even if they are the most likely available candidates for that during the EST. If the patients had complementary ECG recordings, with better stationary conditions and with large enough ranges of RR, the estimated values of α and β could be obtained from those recordings.

Interchangeability of QT-RR model blocks

Based on the estimated QT time lag values of this Ph.D. thesis, values of τ of about 25 s during exercise can be considered. The effective length of $h(n)$ is about 5τ, corresponding to about 125 s, which implies RR changes of as much as 100 ms ($\approx$ 5 bpm). During recovery, values of τ corresponding to about 50 s should rather be considered, implying RR changes as large as 200 ms ($\approx$ 10 bpm). Several definitions of regression models representing $g_f(d_{\mathrm{RR}}(n))$ were considered in [47] to cover a wide range of possible stationary QT-RR patterns. For any of those regression models, RR changes as small as 100 ms or 200 ms (in the time span of the QT memory) are well-approximated by a linear QT-RR dependence, thus supporting the derivation in Sec. 2.9

and the interchangeability of the model blocks in Fig. 2.3. The basis of this approximation can be observed in Fig. 2.5(a) for the hyperbolic transformation defined in (2.15).

5.5.5 Limitations

The robustness of the algorithm for computing the inflection point in (2.33) could be compromised by the EST protocol. If the ECG recording does not include a stage before starting the exercise phase or if the recovery period is not long enough, it would be difficult to calculate the points $n_{e,o}$ and $n_{r,e}$, respectively. In such cases, the objective function should be redefined to adapt it to the patterns of the recordings under analysis. Also, to have a proper estimation of the instantaneous parametric relation between the QT and RR intervals, heart rate stationary periods are required, which would suggest prolonging the pre-test and the recovery recording periods.

The use of biophysical modeling and simulation could help to assess the role of the sympathetic nervous system in the QT rate adaption measured from EST. Also, it could eventually help to refine the methodology here described.

5.6 Conclusion

This chapter shows that it is possible to quantify the QT memory in response to gradual heart rate changes from clinical exercise ECG stress testing. A prolongation in the QT adaptation time lag during exercise and a shortening during recovery are associated with an increased risk of CAD. A reduced difference between these two delays is also observed in high-risk CAD patients. The Laplacian-based estimator better discriminates patients with different CAD risk. The adaptation markers proposed in this Ph.D. thesis could be used to improve the accuracy of CAD diagnosis. Furthermore, the QT-RR adaptation time evaluated during the recovery phase, and calculated as the delay between the observed $d_{\mathrm{RR}}(n)$ and the instantaneous $\check{d}^{i}_{\mathrm{RR}}(n)$ series, has been identified as a predictor of SCD or any-cause mortality. In contrast, this estimated delay at recovery using $d_{\mathrm{QT}}(n)$ series is marginally significant to predict all-cause mortality and not significant for SCD, suggesting that estimators based on $d_{\mathrm{RR}}(n)$ are more suitable for stratification of patients according to their risk of SCD and overall mortality. In addition, the GπCA$_P$ method has been shown to be the best tested strategy to delineate the T wave end.

CHAPTER 6

THE ROLE OF β-ADRENERGIC STIMULATION IN QT-RR ADAPTATION TIME LAG DURING EXERCISE STRESS TESTING: AN ELECTROPHYSIOLOGICAL SIMULATION STUDY

6.1 Motivation

In previous chapters, the QT interval adaptation time lag to gradual heart rate changes during EST has been investigated, with this value estimated as the delay between the observed QT intervals and the QT intervals derived from the time series of the observed RR intervals. Although a constant time lag along the exercise phase of the EST is assumed, the ECG recordings from CAD patients undergoing EST show that close to the peak exercise, the two time series tended to overlap (see Fig. 2.5), suggesting a nonunique time lag but a time-varying time lag along the exercise. This led to hypothesize that other factors, in addition to heart rate, could influence the QT interval adaptation time lag, with the ANS possibly being a significant contributor [138–140]. The ANS modulates ventricular repolarization directly through its action on the ventricular myocardium and indirectly through its effects on the heart rate [141–145].

Previous studies in the literature have assessed the effects of sympathetic activation on the QT interval during exercise [146, 147], but the results are inconclusive. In other works, autonomic blockades are used to evaluate QT hysteresis during exercise and recovery, providing evidence of the important role of the ANS in the QT-RR relation [81]. However, subsequent reports suggest that these conclusions might be affected by factors such as the speed of heart rate change, also influenced by autonomic factors [85]. Despite the uncertainty on the ANS role in QT hysteresis, since the ANS can exert an influence not only on the QT interval duration but also on its adaptation to heart rate changes, it would be worth investigating its contribution to QT hysteresis modulation. If that contribution was corroborated, our observations regarding the gradual reduction in the QT interval adaptation lag when approaching the peak exercise might potentially be explained by the ANS influence.

In silico studies have investigated the dynamics of cellular repolarization duration in response to β-adrenergic stimulation [148, 149] and have reported that the APD time lag in response to β-adrenergic stimulation becomes reduced for higher pre-stimulation levels of β-adrenoceptors [92]. Based on these studies, we hypothesize that increased sympathetic activity approaching peak exercise, implying enhanced β-adrenergic stimulation, may play a role in the reduced QT adaptation time lag observed at the end of the exercise phase. More broadly, we hypothesize that a time-varying β-adrenergic stimulation pattern during

EST could help to better explain the QT rate adaptation profiles measured from CAD patients in response to exercise.

This chapter aims to clarify the role of β-adrenergic stimulation on APD and QT adaptation time lag following heart rate changes during exercise and recovery from EST. Importantly, we seek to propose a possible description of the β-adrenergic stimulation pattern that could explain the repolarization adaptation after heart rate changes during exercise ECG stress testing. To the best of our knowledge, no study has yet proposed individualized, time-varying β-adrenergic stimulation patterns to describe the QT adaptation time lag during exercise and recovery in CAD patients.

6.2 Methods

6.2.1 In silico ventricular cell models

To investigate the mechanisms underlying the QT interval adaptation to heart rate changes during EST, an *in silico* modeling and simulation study covering multiple scales, from cell to ECG, is conducted. The APD is evaluated in simulated cells and the QT interval is evaluated in pseudo-ECGs (pECGs) in response to changes in heart rate as those measured from the clinical ECGs.

At the cellular level, the electrophysiology of human ventricular cardiomyocytes is represented by the O'Hara *et al.* AP model [150]. In particular, the three models proposed by O'Hara *et al.* are used here to describe the electrical activity of subendocardial, midmyocardial and subepicardial cells across the ventricular wall. These models include descriptions of the main ionic currents and fluxes involved in the generation of the AP in the three cell types. The relation between the ionic currents and fluxes and the transmembrane potential are obtained by solving the following equation:

$$C_m \frac{dV(t)}{dt} + \sum_s g_s(V(t) - E_s) + \sum_b I_b(t) + \sum_i I_i(t) + I_{st}(t) = 0 \qquad (6.1)$$

where C_m is the membrane capacitance per unit of area, V is the transmembrane potential, g_s is the conductance of the ionic current for ion species s, E_s is the equilibrium potential of ion s, I_b is the current through pump b, I_i is the current through exchanger i and I_{st} is the stimulus current. The formulation of the fast sodium current in the O'Hara *et al.* models is replaced with the formulation by ten Tusscher *et al.* following the comment by O'Hara and coworkers [150, 151] (comment on article [150] from 05 October 2012).

The described electrophysiological models for the three types of ventricular cells are coupled to the Gong *et al.* model of β-adrenergic receptor signaling [152]. The Gong *et al.* model represents an adaptation of the Heijman *et al.* model originally developed for the canine myocyte [153]. The model describes the AP response to different concentrations of the β-adrenergic agonist isoproterenol (Iso) by computing each ionic current or flux as a weighted average of the phosphorylated and nonphosphorylated fractions of each cellular substrate. Based on the Heijman *et al.* model, the Iso -induced changes in individual substrates like the L-type Ca^{2+} channels, slow delayed rectifier K^+ channels and ryanodine receptors were calibrated according to experimental data [152]. Gong *et al.* made further adjustments in the model to reproduce healthy whole-cell human ventricular AP data at maximal β-adrenergic stimulation under a range of pacing frequencies.

To evaluate the cellular APD response to gradual heart rate changes, the cells are paced according to real RR intervals taken from twelve ECGs from the FINCAVAS database introduced in Sec. 5.2. These records are randomly selected and correspond to four patients of each of the three groups clustered according to their likelihood of suffering CAD: COR-LR, COR-MR and COR-HR groups. For each simulated beat, the APD in response to each given RR interval is computed as the APD at 90% repolarization. The APD time series sampled at 4 Hz is denoted as $d_{\mathrm{APD}}(n)$.

6.2.2 In silico ventricular tissue models and simulation of ECG signals

Based on the human ventricular cell models described in section 6.2.1, the response to changes in heart rate of a human ventricular tissue is evaluated. A ventricular transmural tissue fiber of length $L = 1.5$ cm composed of subendocardial, midmyocardial and subepicardial cells is considered. Electrical propagation in the tissue is represented by the monodomain model, which is a simplified version of the bidomain model [154, 155]. The monodomain model is described by a reaction-diffusion partial differential equation (PDE) for the transmembrane potential, with the extracellular potential calculated from another PDE once the transmembrane potential has been solved. The propagation of the transmembrane potential in the tissue is described by the following equation:

$$\frac{\partial V(x,t)}{\partial t} = \frac{-I_{ion}(V(x,t))}{C_m} + D\frac{\partial^2 V(x,t)}{\partial x^2} \tag{6.2}$$

where $\frac{\partial V(x,t)}{\partial t}$ is the partial time derivative of the transmembrane potential at a point x in the tissue fiber and a time t, $\frac{\partial^2 V(x,t)}{\partial x^2}$ is the second partial space derivative of the transmembrane potential at a point x in the tissue fiber and a time t, I_{ion} is the total ionic current (calculated as the sum of all the terms except for the first one in equation (6.1), with the stimulus current corresponding to the one in the fiber) and D is the diffusion coefficient. Zero-flux Neumann boundary conditions are imposed.

Cellular heterogeneities are defined according to the following transmural distribution across the tissue fiber: 45% of subendocardial cells, 25% of mid-myocardial cells and 30% of subepicardial cells, according to previous studies based on experimentally reported values [65, 156, 157].

The value of the diffusion coefficient D is set to have a conduction velocity value close to 70 cm/s in the fiber, which is within the physiological ranges reported in experimental studies [158, 159].

The reaction-diffusion PDE of the monodomain model is solved by using the operator splitting method [160] to decouple the reaction term, which describes the generation of the cellular AP, and the diffusion term, which describes the AP propagation in the tissue. The decoupled PDE is solved by the Finite Element Method (FEM) using the ELECTRA solver [161, 162] with a spatial resolution of 0.015 cm. Numerical time integration is performed using a dual adaptive explicit time integration algorithm [163].

Taking the simulated transmembrane potentials from the cardiac tissue fiber, a pECG signal is computed to represent the extracellular potential recorded by an electrode placed 2 cm away from the subepicardial end of the fiber in the direction of the fiber axis, as in previous studies investigating ventricular repolarization from simulated one-dimensional transmural tissues [164]. The pECG signal $\psi(t)$ is calculated at each time instant t, with a frequency of 1000 Hz, using the following equation and subsequently normalized to have unit amplitude:

$$\psi(x',t) = -\int_{x=0}^{x=L} \sigma \, \nabla_x V(x,t) \cdot \nabla_x \left(\frac{1}{r(x,x')} \right) dx, \tag{6.3}$$

where σ is the diffusion coefficient of the electrical medium surrounding the tissue, L is the fiber length, and $r(x,x')$ is the distance between a point x within the fiber and the recording electrode located at a point x' outside the fiber but in the fiber axis direction. Figure 6.1 shows the pECG waveforms (restricted to the ventricular activity) calculated at two-time instants along EST after pacing

the tissue fiber following the time series of the observed RR intervals $d_{\mathrm{RR}}(n)$ from a selected patient.

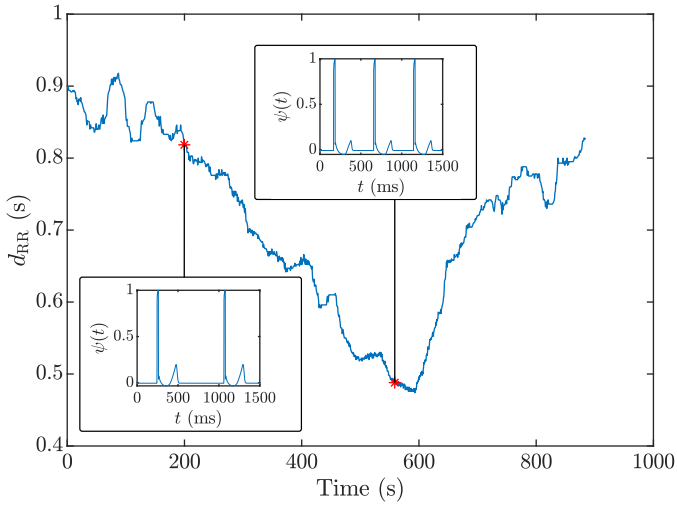

Figure 6.1: Main panel: $d_{\mathrm{RR}}(n)$ time series, in seconds, from the analyzed ECG recording of a CAD patient. Insets: normalized pECG $\psi(t)$ computed from the simulated transmembrane potentials of the tissue fiber at two time instants.

The QT interval is measured on the pECG by applying the wavelet-based delineation method [100] in a single lead. The simulated QT time series at 4 Hz is denoted as $d_{\mathrm{QT}}(n)$.

6.2.3 Simulated β-adrenergic stimulation patterns

The simulated APD responses to heart rate changes are analyzed for four different patterns of β-adrenergic stimulation.

The first pattern Iso-c is defined by a constant level of β-adrenergic stimulation that corresponds to a fixed Iso concentration of 0.005 μM, considered as a baseline level.

The second pattern Iso-tv is defined by a time-varying level of β -adrenergic stimulation that comprises an increase in stimulation when approaching the peak exercise during the exercise phase and a reduction in stimulation shortly after starting the recovery phase. In particular, this pattern departs from the baseline Iso concentration of 0.005 μM and, at a time point n_1 during exercise, the Iso concentration starts to linearly increase until reaching a concentration of 0.01 μM at peak exercise ($n_2 = n_{pe}$). This concentration value is kept constant at the

start of the recovery until the time point n_3. From the n_3 point onwards, Iso linearly drops until the time point n_4, when it reaches the baseline concentration. The points n_1, n_2, n_3 and n_4 are derived from the ECG data of each CAD patient, as described below.

Two other patterns of β-adrenergic stimulation are investigated departing from the Iso-tv pattern. For the linearly increasing pattern called Iso-li, the Iso concentration is initially equal to 0.005 μM and varies linearly from the exercise onset to peak exercise, where it reaches a value of 0.01 μM. The rest of the Iso curve is the same as for Iso-tv. For the last proposed pattern, the abruptly changing pattern called Iso-ab, the Iso concentration rises abruptly at the exercise onset from 0.005 to 0.01 μM and remains at this value until the peak exercise. The rest of the Iso curve is the same as Iso-tv. The four β-adrenergic stimulation patterns are illustrated in Fig. 6.2.

To determine the four time points that define the time-varying β-adrenergic stimulation pattern, the time series $d_{\mathrm{QT}}(n)$ and $d^i_{\mathrm{QT}}(n)$ of each patient are required, with the time series $d_{\mathrm{QT}}(n)$ corresponding to the observed QT intervals and the time series $d^i_{\mathrm{QT}}(n)$ corresponding to the QT intervals derived from the observed RR intervals. The four time points are obtained according to the following criteria, which are based on the examination of the QT and RR time series of all analyzed patients:

- n_1: time point closest to the peak exercise, and prior to it, for which the slopes of $d_{\mathrm{QT}}(n)$ and $d^i_{\mathrm{QT}}(n)$ are equal.
- n_2: time point corresponding to peak exercise n_{pe}.
- n_3: first time point during recovery for which the difference between $d_{\mathrm{QT}}(n)$ and $d^i_{\mathrm{QT}}(n)$ slopes presents a local maximum.
- n_4: $n_3 + 1$, representing an abrupt reduction in the Iso concentration soon after the start of the recovery phase.

6.3 Results

6.3.1 QT-RR adaptation time in patients

Linear (2.14) and hyperbolic (2.15) regression functions are used to model the dependence of the instantaneous APD $d^i_{\mathrm{APD}}(n)$ and the instantaneous series $d^i_{\mathrm{QT}}(n)$ with the RR interval time series. These models have been reported to

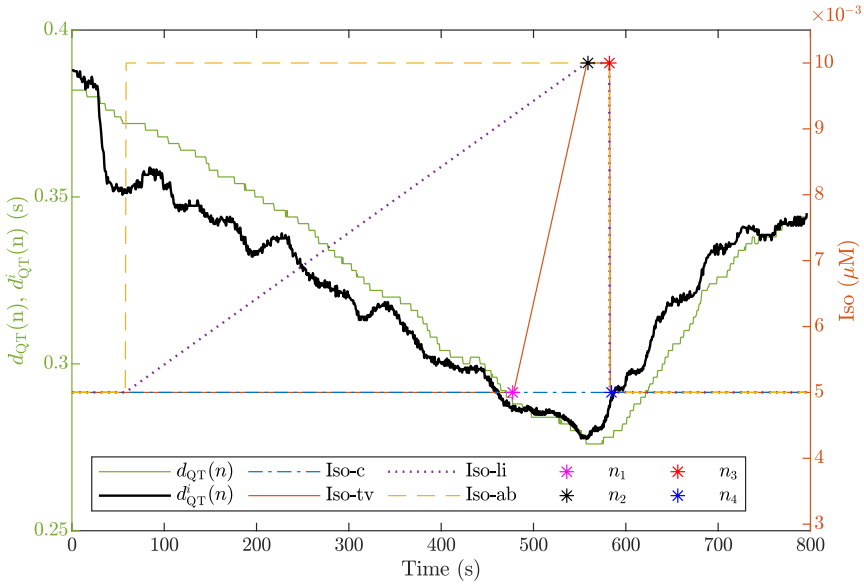

Figure 6.2: Simulated patterns of Iso concentrations during exercise and recovery. The constant pattern (Iso-c) is defined by a constant, baseline level of Iso equal to 0.005 μM. The time-varying pattern (Iso-tv) is defined by time points n1, n2, n3 and n4 determined from the $d^i_{QT}(n)$ and $d_{QT}(n)$ series of the analyzed ECG recording from each CAD patient. The linearly increasing pattern (Iso-li) is defined as the Iso-tv pattern but with an Iso concentration varying linearly along exercise from the baseline level of 0.005 to 0.01 μM. The abruptly changing pattern (Iso-ab) is defined as the Iso-tv pattern but with an abrupt change in Iso at the beginning of exercise from 0.005 to 0.01 μM, which remains at this value until peak exercise.

represent the most common patterns of the QT-RR relation [47]. The model that generates the lowest residual ε_{rms} in the three concatenated windows $W_b \cup W_e \cup W_{lr}$ is selected individually for each patient.

An example of [QT RR] datapairs in the three windows W_b, W_e and W_{lr} of a patient and the fitting of the two regression models are presented in Fig. 6.3. In general, the hyperbolic model allows the best fit according to the quantitative results presented in Table 6.1.

The QT adaptation time lag estimated separately in the exercise and recovery phases of the exercise ECG stress testing from the selected CAD patients is shown in Table 6.1. The middle columns contain the RMS error ε_{rms} calculated for each of the two regression models tested, used to individually select the optimal model for each patient. The other columns show the estimated QT adaptation time lag values in the exercise and recovery phases, separately,

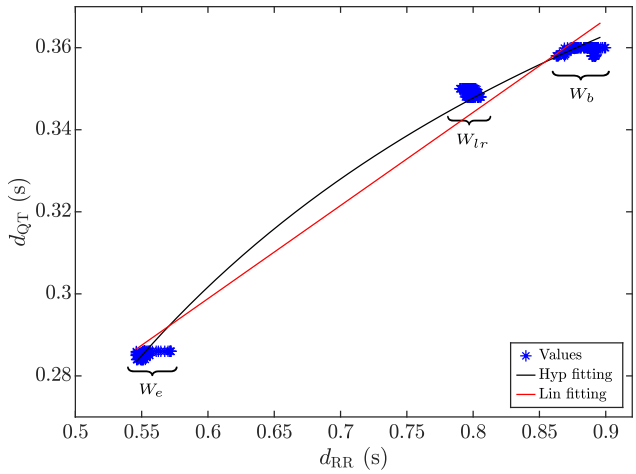

Figure 6.3: Fitting of linear (red) and hyperbolic (black) regression models to [QT, RR] datapairs from a patient's ECG. The data clusters correspond to the different windows W_j, $j \in b, e, lr$.

for each clinical ECG, using $d^i_{\mathrm{QT}}(n)$ series or $\check{d}^i_{\mathrm{QT}}(n)$ series, denoted by $\tau_{1,e}$ and $\tau_{1,r}$, or $\check{\tau}_{1,e}$ and $\check{\tau}_{1,r}$. All results are computed using the Laplacian estimator. The rule introduced in Sec. 5.4.4 is also applied to compute the time series $\check{d}^i_{\mathrm{APD}}(n)|\check{d}^i_{\mathrm{QT}}$.

The methods described in Sec. 2.5 and Sec. 2.7 are used to calculate instantaneous series $d^i_{\mathrm{APD}}(n)|d^i_{\mathrm{QT}}(n)$ and $\check{d}^i_{\mathrm{APD}}(n)|\check{d}^i_{\mathrm{QT}}$ for both the analyzed ECGs of the CAD patients and the simulated cells and pECGs. The procedure to estimate the QT adaptation is the one introduced in Sec. 2.6. Moreover, the rule introduced in Sec. 5.4.4 is applied to compute $\check{d}^i_{\mathrm{APD}}(n)|\check{d}^i_{\mathrm{QT}}$ series.

6.3.2 APD-RR adaptation time in simulated cells

Table 6.2 presents the mean and standard deviation values of the QT adaptation time $\tau_{1,e}|\check{\tau}_{1,e}$ and $\tau_{1,r}|\check{\tau}_{1,r}$ in each of the three CAD groups estimated from clinical ECGs, using the time series $d^i_{\mathrm{QT}}(n)$ and $\check{d}^i_{\mathrm{QT}}(n)$. In addition, the mean and standard deviation values of the APD adaptation time lag calculated in a single endocardial cell are included in the table for the four Iso patterns. As can be observed, the individual time-varying β-adrenergic stimulation pattern Iso-tv pattern leads to adaptation delays that are in better agreement with those measured from the patients than the two other time-varying patterns, Iso-li and Iso-ab, and the constant pattern Iso-c. These effects on the estimated time

Table 6.1: Left column: codes used to identify the analyzed patients according to the risk group and the patient order number # within the group. Middle columns: mean square error ε_{rms} for the linear and hyperbolic regression models. Right columns: estimated QT adaptation time lag values in the exercise and recovery phases for each clinical ECG, using $d^i_{\mathrm{QT}}(n)$ series or $\check{d}^i_{\mathrm{QT}}(n)$ series, denoted by $\tau_{1,e}$ and $\tau_{1,r}$, or $\check{\tau}_{1,e}$ and $\check{\tau}_{1,r}$. All the results are computed using the Laplacian estimator.

	ε_{rms} (ms)		Delays (s)			
	Lin	Hyp	$\tau_{1,e}$	$\tau_{1,r}$	$\check{\tau}_{1,e}$	$\check{\tau}_{1,r}$
COR-LR1	13.24	3.34	0	92.00	5.25	87.75
COR-LR2	6.16	3.23	17.50	43.50	22.75	39.00
COR-LR3	15.10	5.95	11.75	52.00	20.00	28.25
COR-LR4	8.91	8.28	62.00	7.75	80.50	−0.50
COR-MR1	13.87	8.06	29.00	32.50	40.00	22.50
COR-MR2	2.72	1.57	7.00	51.75	21.75	49.25
COR-MR3	3.51	2.34	9.00	27.75	20.00	24.25
COR-MR4	4.26	3.89	62.25	34.00	101.25	30.75
COR-HR1	5.57	2.92	33.75	26.75	39.25	26.00
COR-HR2	2.79	3.47	69.00	38.00	88.00	17.75
COR-HR3	7.46	9.96	47.25	38.50	57.00	28.75
COR-HR4	2.34	4.71	74.75	121.50	90.75	113.25

lags are better appreciated during the exercise than during the recovery and applied to the calculation with either the $d^i_{\mathrm{APD}}(n)$ or $\check{d}^i_{\mathrm{APD}}(n)$ time series. The obtained results support the conclusion that the Iso-tv pattern more accurately represents the repolarization time adaptation to heart rate changes observed in clinical data than the other tested patterns, including the constant one.

The APD adaptation time lag evaluated in an endocardial cell in response to the heart rate changes corresponding to the RR interval time series computed from a patient is shown in Fig. 6.4. Panel (a) illustrates the observed time series $d_{\mathrm{QT}}(n)$ and $d^i_{\mathrm{QT}}(n)$ of a patient, whose estimated delays $\tau_{1,e}$ and $\tau_{1,r}$ are also indicated. Panels (b) and (c) show the cellular time series $d_{\mathrm{APD}}(n)$ and $d^i_{\mathrm{APD}}(n)$ in response to the same changes in the heart rate of the patient and using constant Iso-c or time-varying Iso-tv Iso concentrations, respectively. The estimated delay values are also indicated. All top panels of Fig. 6.4 represent results using $d^i_{\mathrm{QT}}(n)|d^i_{\mathrm{APD}}(n)$ time series, while the bottom ones show results from $\check{d}^i_{\mathrm{QT}}(n)|\check{d}^i_{\mathrm{APD}}(n)$ time series.

The time series $d_{\mathrm{APD}}(n)$ simulated for the constant and the time-varying Iso concentrations take the same values before n_1 and after n_3, since the Iso concentration is identical in these time segments (see Fig. 6.2). However, since

the Iso concentrations are different between these points, that is, around the peak exercise, the [QT,RR] data pairs in the window $W_e|\check{W}_e$ are different for the constant and the time-varying Iso concentrations, thus generating different instantaneous APD series.

Table 6.2: Mean and standard deviation values of estimated QT adaptation time τ in the exercise and recovery phases computed for the patients in each of the CAD groups and in asimulated endocardial cell with a constant β-adrenergic stimulation (Iso-c), with the proposed time-varying β-adrenergic stimulation (Iso-tv) and with other two β-adrenergic patterns, Iso-li and Iso-ab. These values are computed using either $d^i_{\mathrm{QT}}(n)|d^i_{\mathrm{APD}}(n)$ or $\check{d}^i_{\mathrm{QT}}(n)|\check{d}^i_{\mathrm{APD}}(n)$ time series.

τ in Exercise

Estimation method	Iso pattern	COR-LR	COR-MR	COR-HR
$d^i_{\mathrm{APD}}(n)$	Iso-c	7.19 ± 13.00	-0.31 ± 1.71	37.50 ± 18.28
	Iso-tv	16.69 ± 17.93	15.31 ± 22.65	47.50 ± 23.75
	Iso-li	-3.31 ± 22.34	22.00 ± 31.37	7.88 ± 18.56
	Iso-ab	-32.13 ± 24.91	-20.94 ± 22.61	-38.50 ± 31.98
$d^i_{\mathrm{QT}}(n)$	QT adaptation time in patients	22.81 ± 27.12	26.81 ± 25.63	56.19 ± 19.05
$\check{d}^i_{\mathrm{APD}}(n)$	Iso-c	19.19 ± 13.00	21.13 ± 1.11	53.94 ± 24.64
	Iso-tv	32.19 ± 24.38	36.50 ± 30.52	66.94 ± 33.58
	Iso-li	3.31 ± 24.39	44.69 ± 35.25	23.94 ± 21.21
	Iso-ab	-27.13 ± 34.02	-27.69 ± 24.57	-3.13 ± 29.00
$\check{d}^i_{\mathrm{QT}}(n)$	QT adaptation time in patients	32.13 ± 33.15	45.75 ± 38.09	70.25 ± 26.79

τ in Recovery

Estimation method	Iso pattern	COR-LR	COR-MR	COR-HR
$d^i_{\mathrm{APD}}(n)$	Iso-c	37.50 ± 17.94	35.25 ± 11.62	15.12 ± 14.20
	Iso-tv	38.94 ± 22.21	37.19 ± 14.40	19.50 ± 15.99
	Iso-li	32.94 ± 17.49	19.75 ± 7.33	33.50 ± 14.03
	Iso-ab	30.56 ± 17.22	15.94 ± 8.22	30.00 ± 12.81
$d^i_{\mathrm{QT}}(n)$	QT adaptation time in patients	48.81 ± 34.59	36.50 ± 10.51	56.19 ± 43.88
$\check{d}^i_{\mathrm{APD}}(n)$	Iso-c	23.50 ± 20.34	22.75 ± 15.84	8.81 ± 16.76
	Iso-tv	24.69 ± 21.74	28.69 ± 18.55	10.38 ± 20.48
	Iso-li	26.44 ± 18.21	5.06 ± 18.13	23.81 ± 9.07
	Iso-ab	25.31 ± 11.08	25.88 ± 17.78	7.94 ± 6.10
$\check{d}^i_{\mathrm{QT}}(n)$	QT adaptation time in patients	38.63 ± 36.75	31.69 ± 12.23	46.44 ± 44.79

6.3.3 QT-RR adaptation time in pECGs

The QT adaptation time is also evaluated in simulated ECGs from a tissue fiber in response to heart rate changes from exercise ECGs stress testing of

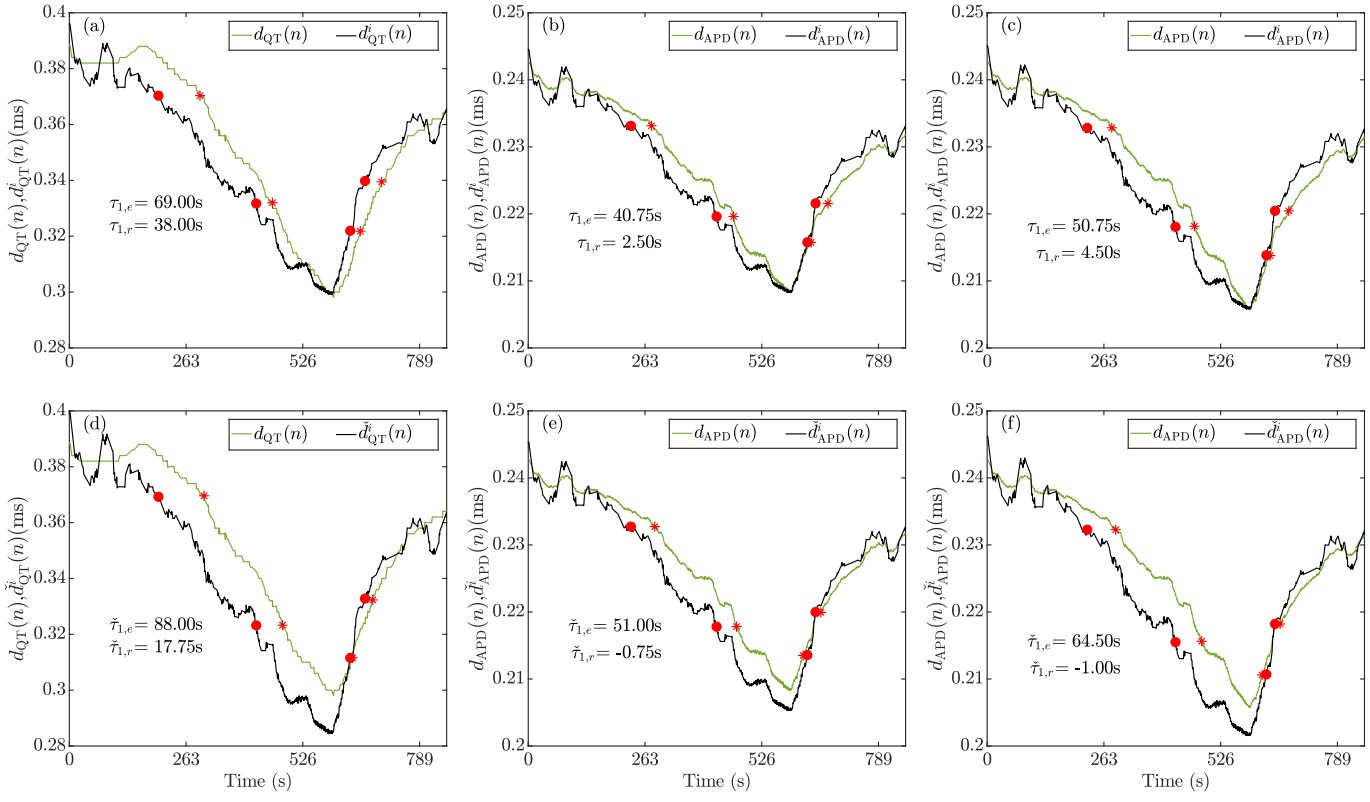

Figure 6.4: (a) QT adaptation time lag estimated between $d_{QT}(n)$ and $d^i_{QT}(n)$ during exercise and recovery for a CAD patient. APD adaptation time lag between $d_{APD}(n)$ and $d^i_{APD}(n)$ during exercise and recovery in a simulated endocardial cell (b) for constant β -adrenergic stimulation and (c) for the proposed time-varying β-adrenergic stimulation using in both cases the same heart rate as for the patient on the left. Panels (d)-(f) show the estimated delays after modifying and aligning the exercise learning window $\check{W}_e$, that is, using $\check{d}^i_{QT}(n)|\check{d}^i_{APD}(n)$. Red markers delimit areas where the delays are calculated.

CAD patients. An example can be seen in Fig. 6.7. Based on the results at the cellular level, the simulated QT responses to heart rate changes are analyzed only for the Iso-c and Iso-tv patterns.

Following the same representation as for the APD series results, panel (a) from Fig. 6.7 illustrates the observed $d_{\mathrm{QT}}(n)$ and $d^i_{\mathrm{QT}}(n)$ time series of a patient. Figures 6.7 (b)-(c) show the QT series from the tissue fiber pECG under constant Iso-c and time-varying Iso-tv Iso concentration patterns, respectively. The estimated delay values are indicated in all cases. The top panels of Fig. 6.7 show results using the time series $d^i_{\mathrm{QT}}(n)$, while the bottom ones show results using the time series $\check{d}^i_{\mathrm{QT}}(n)$.

Table 6.3 presents the mean and standard deviation values of the estimated QT adaptation time lags across patients in each of the three CAD groups during the exercise and recovery phases, separately. These values are also calculated from the simulated tissue fiber paced according to the RR interval time series of the same set of patients, using either an Iso-c or Iso-tv β-adrenergic stimulation pattern. The estimated delay values calculated for the Iso-tv pattern offer results closer to the clinical ones, with better estimated values in COR-LR patients for both exercise and recovery delays.

The relation between the QT adaptation time measured in patients and the QT adaptation time computed from pECGs using either the Iso-c or the Iso-tv β-adrenergic stimulation is shown in Fig. 6.5(a)-(b) for exercise and recovery, separately, using $d^i_{\mathrm{QT}}(n)$ series. The results obtained using the $\check{d}^i_{\mathrm{QT}}(n)$ series can be seen in Fig. 6.5(c)-(d). The fitted lines for the Iso-tv pattern in the exercise phase are closer to the diagonal, thus indicating improved results with respect to those obtained with the Iso-ct pattern.

Finally, the error between the QT adaptation time lag estimated from the patients' ECGs and the corresponding estimated values for the simulated APD|pECG in all cases is presented in Fig. 6.6. The differences between using the Iso-ct and the Iso-tv pattern are noticeable, particularly during the exercise phase.

6.4 Discussion

6.4.1 Role of β-adrenergic stimulation in APD-RR and QT-RR adaptation time

An individual time-varying pattern of β-adrenergic stimulation explains the repolarization adaptation to changes in heart rate better than a constant

Table 6.3: Mean and standard deviation values of the estimated QT adaptation time τ in the exercise and recovery phases computed for the patients in each of the CAD groups and in a simulated tissue fiber with the constant Iso-c and the time-varying Iso-tv β-adrenergic stimulation patterns. The values are computed using either $d^i_{\mathrm{QT}}(n)$ or $\check{d}^i_{\mathrm{QT}}(n)$.

τ in Exercise

Estimation method	Iso pattern	COR-LR	COR-MR	COR-HR
$d^i_{\mathrm{QT}}(n)$	Iso-c	-0.94 ± 21.96	4.63 ± 8.76	34.63 ± 8.70
	Iso-tv	5.69 ± 24.09	22.56 ± 38.36	39.44 ± 20.00
$d^i_{\mathrm{QT}}(n)$	QT adaptation time in patients	22.81 ± 27.12	26.81 ± 25.63	56.19 ± 19.05
$\check{d}^i_{\mathrm{QT}}(n)$	Iso-c	8.25 ± 20.17	26.31 ± 5.86	48.19 ± 16.68
	Iso-tv	28.56 ± 14.98	36.00 ± 24.54	55.88 ± 25.77
$\check{d}^i_{\mathrm{QT}}(n)$	QT adaptation time in patients	32.13 ± 33.15	45.75 ± 38.09	70.25 ± 26.79

τ in Recovery

Estimation method	Iso pattern	COR-LR	COR-MR	COR-HR
$d^i_{\mathrm{QT}}(n)$	Iso-c	58.64 ± 22.57	36.69 ± 8.84	17.56 ± 9.64
	Iso-tv	36.88 ± 13.52	25.81 ± 17.94	15.13 ± 12.15
$d^i_{\mathrm{QT}}(n)$	QT adaptation time in patients	48.81 ± 34.59	36.50 ± 10.51	56.19 ± 43.88
$\check{d}^i_{\mathrm{QT}}(n)$	Iso-c	34.63 ± 8.24	14.81 ± 30.98	11.69 ± 13.17
	Iso-tv	20.06 ± 18.51	2.63 ± 26.75	7.94 ± 15.21
$\check{d}^i_{\mathrm{QT}}(n)$	QT adaptation time in patients	38.63 ± 36.75	31.69 ± 12.23	46.44 ± 44.79

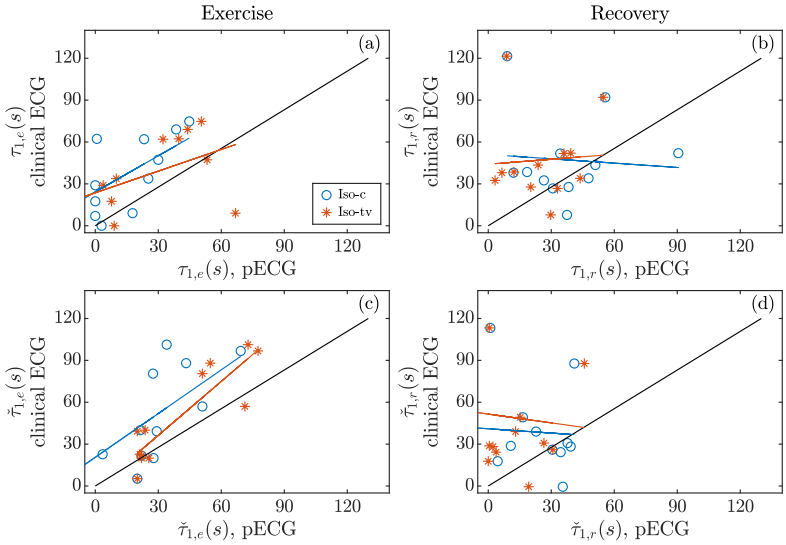

Figure 6.5: Relation between the QT adaptation time lags calculated from patients (vertical axis) and from pECGs (horizontal axis) for the constant Iso-c (blue) and the time-varying Iso-tv (red) patterns, in (a) exercise and (b) recovery phases. Fitted lines are shown in the corresponding colors, while black lines show the diagonal. The $d^i_{\mathrm{QT}}(n)$ series is used to obtain the results in the two panels. The same representation is repeated using the $d_{\mathrm{QT}}(n)$ series windowed with $\check{W}_e$, i.e., $\check{d}^i_{\mathrm{QT}}(n)$ series, and the results are shown in (c) for the exercise and (d) for the recovery phases.

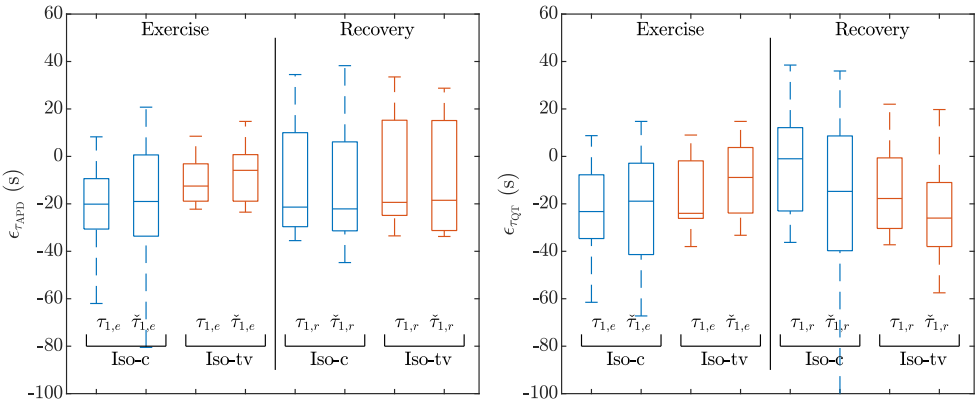

Figure 6.6: Distributions of the differences between the estimated APD|QT adaptation time lag calculated from simulated cell|tissue and the corresponding QT adaptation delays from the patients, both under constant (Iso-c) and time-varying (Iso-tv) β-adrenegic stimulation, for exercise and recovery, separately, using the Laplacian estimator and using $d^i_{\mathrm{QT}}(n)$ or $\check{d}^i_{\mathrm{QT}}(n)$ series to calculate the associated $\tau_{1,x}$ or $\check{\tau}_{1,x}$, $x \in \{e, r\}$.

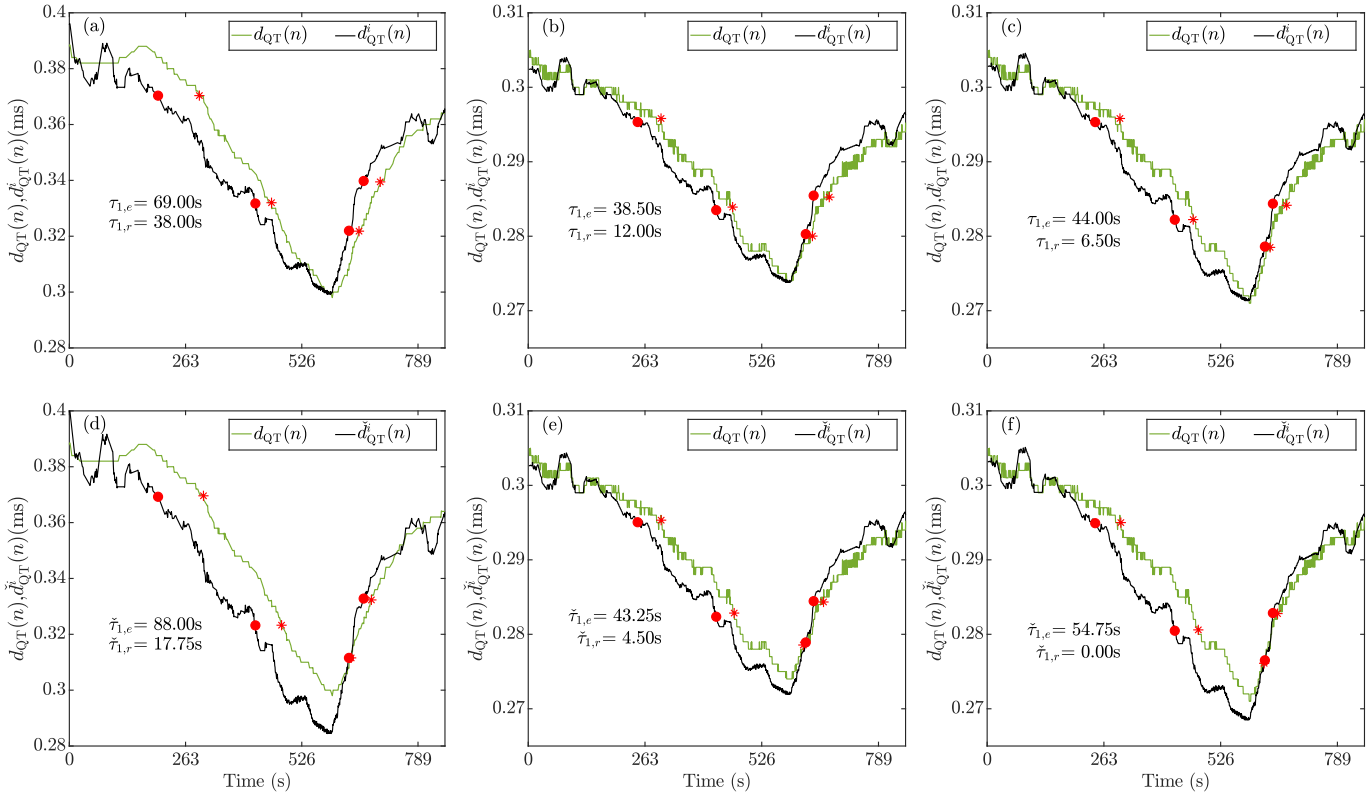

Figure 6.7: (a) QT adaptation time lag estimated between $d_{QT}(n)$ and $d^i_{QT}(n)$ during exercise and recovery for a CAD patient. QT adaptation time lag between $d_{QT}(n)$ and $d^i_{QT}(n)$ during exercise and recovery in a simulated ECG pECG (b) for constant β -adrenergic stimulation or (c) for the proposed time-varying β-adrenergic stimulation using in both cases the same heart rate as for the patient on the left. Panels (d)-(f) show the estimated delays after modifying and aligning the exercise learning window $\check{W}_e$, that is, using $\check{d}^i_{QT}(n)$. Red markers delimit areas where the delays are calculated.

baseline β-adrenergic stimulation level in *in silico* cell and tissue models of human ventricular electrophysiology. Simulated delays using the time-varying pattern are in agreement with the delays estimated from clinical ECGs. Other β-adrenergic stimulation patterns defined by a constant, high Iso concentration along exercise or by a linearly increasing Iso concentration all along the exercise phase represent adaptation delays that are not in such good agreement with those of patients. Thus, a β-adrenergic stimulation pattern with high Iso levels around the peak shows the best results in terms of replicating the repolarization adaptation measured from the patients.

The APD|QT interval delays are, in general, lower in the simulated cells and pECGs than the ones estimated from clinical ECGs. It is important to note that the APD|QT adaptation time lags estimated during exercise with the time series $d^{i}_{\mathrm{QT}}(n)$ and $\check{d}^{i}_{\mathrm{QT}}(n)$ and using a time-varying β-adrenergic stimulation pattern are closer to the QT delays measured from the patients. This is illustrated in Fig. 6.6, where the distributions of the delay differences between cells and clinical ECGs (left panel) and between pECGs and clinical ECGs (right panel) are closer to zero, and in Fig. 6.5(a)|(c), where the fitted line is nearer to the diagonal in the case of the time-varying pattern, thus pointing to a closer agreement. During recovery, the differences in the estimated APD|QT adaptation time lags between the constant and time-varying β-adrenergic stimulation patterns are not as evident as during exercise. In addition, the variance of the estimated delays is higher in the recovery than in the exercise phase. All these results on the relevant role of β-adrenergic stimulation in the adaptation of repolarization duration agree with previous studies in the literature [68, 92, 140, 165]. Furthermore, the fact that the QT adaptation time becomes progressively reduced when approaching the peak exercise is consistent with *in silico* cell studies reporting that the higher the pre-stimulation level of β-adrenoceptors, the shorter the APD adaptation time [92].

The effects of the ANS on the QT interval, and consequently on its adaptation, have been investigated in some studies of the literature and no clear consensus has been reached. Some studies have postulated that heart rate is the foremost determinant of the QT interval, whereas heart rate-independent differences in autonomic tone play a small role [81, 166]. According to these studies, no major role of the autonomic tone on the rate adaptation of the QT interval would be expected. Other studies have compared the QT adaptation after blocking the parasympathetic activity with atropine [81, 140], which can have both indirect effects on the QT interval due to its dependence on the RR interval and direct effects on the QT interval associated with the autonomic innervation of the ventricular myocardium. In some of these studies, the QT-RR

hysteresis has been reported not to be caused by the different directional changes in the RR interval during exercise and recovery but by differential ANS effects [81]. It should be noted, however, that these investigations assess the autonomic effects only in a restricted range of RR intervals corresponding to high heart rates and disregard the impact of a longer time for the heart rate to return to basal levels. In this thesis, a different approach is adopted in which the RR interval time series are taken from those measured in patients, thus accounting for both sympathetic and parasympathetic effects on the SA node. On top of that, the effect of β-adrenergic stimulation on the ventricular myocardium is accounted for by simulating increases and decreases during the exercise and recovery, respectively, and evaluating its impact on the QT interval and its rate adaptation.

6.4.2 Differential role of β-adrenergic stimulation as a function of the extent of disease

Analyzing the results for the three CAD groups separately, the role of time-varying β-adrenergic stimulation appears to be more relevant in the COR-LR group than in the COR-MR and COR-HR groups, although further analysis with a larger number of patients is required. This observation is confirmed by the results in Table 6.3, which show that the differences between the estimated QT delays in simulations under constant and time-varying β-adrenergic stimulation are larger in the low-risk group than in the high-risk groups.

The estimated exercise delays from simulations using time-varying β-adrenergic stimulation are closer to the delays computed from clinical ECGs, but the opposite behavior is observed in the estimated recovery delays. Further investigations could account for remodeling in ventricular electrophysiology and/or β-adrenergic signaling as a function of the extent of the disease to uncover the differential role of β-adrenergic stimulation in the three analyzed groups [148, 167–169]. Moreover, the use of cell and tissue models of diseased ventricles could lead to larger QT adaptation time lags in the simulations, as previous studies have reported protracted QT adaptation in diseases associated with impairment of sodium-potassium pump activity, such as heart failure, ischemic heart disease, or hypertension [65, 69, 170–172]. This would be expected to render QT adaptation time lags from pECGs in better accordance with the QT adaptation time lags quantified in clinical ECGs (dots in Fig. 6.5 closer to the diagonal).

Although the inter-patient variability in the QT adaptation lags is very high, which is in line with prior works on adaptation rate of repolarization

[47, 64, 68, 83, 89, 173], the QT interval time lag estimated in the exercise phase between $d_{\mathrm{APD}}(n)|d_{\mathrm{QT}}(n)$ and $\check{d}^{i}_{\mathrm{APD}}(n)|\check{d}^{i}_{\mathrm{QT}}(n)$ from cell|pECG increases according to the risk of suffering CAD, being in agreement with the results from clinical ECGs (see Sec. 5.4).

The significance of our findings can be appreciated in the context of the increased risk of SCD during or shortly after exercise. Among the potential causes for this elevated risk, changes in cardiac autonomic modulation associated with exercise have been cited as important factors [174]. Autonomic alterations significantly impact ventricular repolarization in general and the QT interval specifically, due to their effects on the ventricular myocardium as well as on the heart rate through autonomic control of the SA node activity. As these changes may be related to the generation of ventricular arrhythmias, assessing the relation between the QT interval and heart rate in stress test recordings, especially regarding the QT interval adaptation rate and its mechanisms, becomes crucial. In particular, the identification of the individual time-varying β-adrenergic stimulation pattern driving QT rate adaptation during and just after exercise may elucidate why certain patients are at higher arrhythmic risk than others and could represent a basis for future research aimed at designing risk reduction strategies.

6.4.3 QT rate adaptation can be explained by cellular rate adaptation dynamics

The simulation results presented in this Ph.D. thesis show that the rate adaptation dynamics of the QT interval and the cellular APD are similar, in agreement with previous studies investigating repolarization adaptation to other types of heart rate changes, such as abrupt heart rate changes, at different ventricular scales [65]. Simulated APD delays in single subendocardial cells are even closer to the QT delays measured from the patients than the QT delays from pECGs, as can be observed in Fig. 6.6. This could be partially explained by the fact that the simulated tissue fiber is composed of subendocardial, midmyocardial, and subepicardial cells, with quantitative differences in the APD adaptation delay of the three cell types.

6.5 Limitations

In this modeling and simulation study, a transmural fiber with a unique transmural composition and without a specific CAD characterization is used.

Future studies could assess the extent to which the transmural composition and the degree of CAD-induced remodeling in ventricular electrophysiology and β-adrenergic signaling impact the simulated QT adaptation time lag. Also, when modeling the transmural heterogeneities, more advanced methods like those proposed by Rivolta *et.al* [175] could be applied in future works. In those proposed methods, a gradient surface of cells was included to model the heterogeneities from endocardium to epicardium and was shown to render repolarization patterns more closely mimicking those observed experimentally than when fixed layers of endocardial, midmyocardial and epicardial cells were considered.

Furthermore, this modeling presents limitations in terms of explaining the QT adaptation time lags during recovery from exercise. Different time-varying patterns of β-adrenergic stimulation also during the EST recovery phase could be investigated to improve the results and reproduce the adaptation times measured from clinical ECGs more closely.

Finally, future works could take the estimated time lag and the parameters of the optimally fitted regression model and use them to correct the QT interval for the effects of heart rate, following an approach similar to that proposed in previous studies [47, 48].

6.6 Conclusions

In silico modeling and simulation of cell and tissue ventricular electrophysiology show that β-adrenergic stimulation modulates the QT interval adaptation time to gradual heart rate changes produced during EST. Specifically, a time-varying pattern of β-adrenergic stimulation with higher stimulation levels around the peak exercise helps to better reproduce the QT adaptation time lags quantified from CAD patients, particularly during the exercise phase of the test. The role of β-adrenergic stimulation in the adaptation of the QT interval seems to be more relevant in patients with low than in those with mild or high risk of coronary occlusion, and it is well described by the cellular dynamics of APD rate adaptation.

CHAPTER 7

CONCLUSIONS AND FUTURE WORK

In this Ph.D. thesis, novel methods for characterization of the QT adaptation time lag after gradual heart rate changes have been proposed. These methods have been evaluated in the exercise and recovery phases of exercise ECGs stress testing from CAD patients as well as in simulated ECG signals. Also, an *in silico* study has been conducted to assess the role of the sympathetic activity in modulating such QT adaptation characteristics. This chapter provides a summary of the analyses performed and the results obtained in the Ph.D. thesis and outlines potential directions for future research.

7.1 Discussion of main findings

Enhanced heterogeneity in ventricular myocardial repolarization can cause ventricular fibrillation and SCD. The intrinsic spatial dispersion of repolarization can be emphasized in response to heart rate changes by varied patterns of repolarization adaptation in different ventricular cells. Most studies have investigated this repolarization time lag in response to abrupt heart rate changes from noninvasive recordings as Holter ECGs or following invasive pacing. However, these types of changes are not always present in ambulatory

recordings. In this thesis, and for the first time to the best of our knowledge, the QT adaptation time lag is estimated from gradual changes in heart rate observed in EST, as a more feasible alternative to the investigation of sudden heart rate changes.

Estimation of QT Adaptation Time Lag. The QT adaptation time lag is characterized as the delay between the observed time series of QT intervals from the ECG and an estimated memoryless QT time series derived using an instantaneous transformation of the RR intervals also computed from the ECG. This delay is estimated and evaluated independently during the exercise and recovery phases of the EST. To obtain the estimated memoryless QT interval series based on the observed RR intervals, a hyperbolic regression model is selected, whose parameters are individually estimated for each patient. For this purpose, the QT and RR series in three learning windows are extracted, corresponding to periods where the heart rate remains approximately constant: one in each basal (pre- and post-exercise) phase and one around the peak exercise. To account for the questionable signal stationarity at this last window, different data modification approaches are considered. The best approach modifies the data in this window based on a first estimate of the QT adaptation time lag and shifts it to include only values from the exercise phase. The Laplacian estimator shows more precise estimates than the Gaussian one, as assessed from simulated ECGs. To determine the limits of the exercise and recovery phases from which the QT delay is estimated, basal phases are required to be present and are considered both at the onset and at the end of the test. Additionally, a reduction in the QT delay, possibly associated with sympathetic activation, is observed close to the peak exercise, which suggests avoiding this time segment for the estimation of the exercise delay.

Improvement of T wave end point delineation. An overlap between the T wave and the P wave may occur at high heart rates, which can often be present in ECGs recorded during EST. This issue, along with the augmented noise levels due to physical activity, makes the delineation of the QT interval series more challenging throughout the EST recording. To deal with it, various methods using principal component analysis and periodic component analysis are evaluated here to enhance the delineation of the T wave. Periodic component analysis demonstrates the highest accuracy in this task and is superior to the use of multi-lead delineation techniques. The T wave is delineated in the TL1, emphasizing the beat periodicity of the T wave. This approach exhibits the best performance in both simulated and clinical ECGs. The transformation matrix is learned at the beginning of the EST, avoiding relearning, since the signal morphology changes along EST introduce undesirable discontinuities in

the QT series estimation when relearning is implemented.

Clinical validation. The clinical impact of the QT adaptation time lag estimation is assessed by evaluating the delay in the exercise phase, the recovery phase, and the difference between these two metrics to stratify patients with varying risks of developing CAD. The findings of this Ph.D. thesis indicate that the delay during the exercise phase rises with the increasing risk for CAD. Conversely, the delay during the recovery phase shortens with higher CAD risk. Moreover, the delay values estimated with the proposed methodology are in the same range as those reported in the literature when estimated from abrupt heart rate changes. The predictive capacity of the proposed markers is also assessed. The delay calculated in the recovery phase is significantly higher in patients that died from SCD or from any cause-mortality than in survivors.

Electrophysiological model. The delay between the observed and memoryless estimated QT series during the exercise phase decreases as EST approaches the peak exercise. This phenomenon and its potential underlying mechanisms are investigated by assessing the impact of various β-adrenergic stimulation patterns on ventricular repolarization adaptation using *in silico* cell and tissue models. The estimated delays in these simulated scenarios are compared with those obtained in clinical exercise ECGs stress testing, revealing that a time-varying β-adrenergic pattern yields results that better align with those obtained clinically. The observed time-varying QT lag should be accounted for when interpreting the results from QT adaptation studies conducted over EST recordings.

7.2 Overall conclusion

New estimators of the QT adaptation time lag derived from exercise ECGs stress testing are proposed, which quantify the QT adaptation time lag behind gradual heart rate changes present at the test. The QT adaptation time marker is computed as the delay between the observed QT intervals series and an estimated memoryless QT series derived from the observed RR intervals, in the exercise and recovery phases, separately. A hyperbolic regression model is used to describe the memoryless QT-RR relation, and different learning windows are defined to estimate the model parameters. The most accurate estimates are obtained using a data-dependent adjustment of the peak exercise window and using a Laplacian estimator. The effect of the overlap between the T wave and the P wave at high heart rates on the delineation of the T wave end point is mitigated using a spatial lead transformation based on periodic component analysis. All the proposed methods are tested in simulated ECGs.

Clinical validation shows that the QT adaptation time lag can stratify patients by their CAD level and the adaptation estimated during the recovery phase is helpful to risk stratify patients for SCD or any cause-mortality. Specifically, a prolonged delay during exercise and a shorter delay during recovery indicate higher CAD risk. *In silico* cell and tissue models are used to assess the role of the ANS, showing that time-varying β-adrenergic stimulation patterns, rather than constant stimulation, lead to QT adaptation time measures that are more closely aligned to the QT adaptation time lags measured clinically, suggesting that this should be taken into account when interpreting any repolarization adaptation results.

7.3 Future work

The findings and methodologies introduced in this Ph.D. thesis set the basis for additional studies. Some potential research directions are described below that could further improve the presented work:

1. **Enhancing the QT interval delineation.** Delineating the TL1 after applying periodic component analysis is shown to improve the delineation performance in signals with a low SNR. In the present work, only the ST-T complex is used to learn the transformation matrix. It would be interesting to select a wider part of the ECG to gather more information and assess the delineation of the R point, the QRS onset and the T wave end from the same transformed lead. In that way, the computational cost would be reduced. Moreover, the method could be more cost-efficient if only the ECG leads with the highest SNR values are selected before performing the periodic component analysis. Lastly, more elaborate relearning strategies along time in the exercise ECG stress testing could further improve the delineation by accounting for the observed T wave morphology variations over time. Different window lengths for learning could also be tested, although we hypothesize that the influence would be minor.

2. **QT-RR modeling.** Reducing the quantity of nonphysiological, negative estimated delays is advisable to achieve a more clinically relevant impact of the proposed markers. Moreover, it would be interesting to test different regression models to fit the exercise and the recovery phases separately, thus ensuring to select the best model for each phase. Although the physiological bases supporting the separate fitting in the exercise and the

recovery phases are not clear, the results that could be thus obtained could generate new hypotheses.

3. **Simulator improvements.** An important aspect of the exercise ECG stress testing is the time-varying ST-segment morphology. Including its time-varying behavior and its possible pathology-related morphology patterns in the ECG simulator would not only be useful to assess the methods presented in this dissertation, but would also allow to extend the representation of other heart diseases and obtain larger datasets for application of machine learning techniques. Moreover, the inclusion of time-varying QT time lags in the ECG simulator, resembling the behavior observed at the peak exercise, could help to evaluate the performance of the proposed estimation methods in a more realistic scenario.

4. **Clinical practice.** Exercise ECG stress testing is often recorded in other research fields like sports cardiology or in the evaluation of the effects of microgravity. Assessing the capacity of the proposed markers in these research areas, or even studying the evolution of the estimated delays in longitudinal studies, could demonstrate the capacity of these markers to detect alterations in the ventricular repolarization or the possible development of arrhythmias. Besides, a protocol could be designed to estimate the delays due to abrupt or gradual heart rate changes from the same Holter recording, and compare with the results from EST to quantify the comparability of the QT adaptation marker measured in different scenarios. Finally, the clinical relevance of the markers proposed in this Ph.D. thesis could be compared with other characteristics, or markers, extracted from exercise ECGs stress testing such as the area of the QT-RR hysteresis curve and T wave morphology variations respected to a normal T wave morphologic reference.

5. **Electrophysiological models.** In the modeling and simulation study of this Ph.D. thesis, a transmural ventricular fiber with a unique transmural composition and with no specific CAD characterization is used. Future studies could assess the extent to which the transmural composition and the degree of CAD-induced remodeling in ventricular electrophysiology and β-adrenergic signaling impact the simulated QT delay. A procedure could be developed to define the tissue models so that they more closely reproduce the clinically measured QT delays in different patient groups. These type of studies, along with others using more personalized *in silico* models, possibly based on QT adaptation delays quantified in larger study populations, could help to confirm the outcomes of our present research

regarding autonomic modulation of QT adaptation. Moreover, different time-varying patterns of β-adrenergic stimulation, particularly during the EST recovery phase, could be identified to more closely replicate the adaptation times measured from clinical ECGs and establish the underlying mechanisms more accurately.

BIBLIOGRAPHY

[1] R. Gordan, J. K. Gwathmey, and L.-H. Xie, "Autonomic and endocrine control of cardiovascular function," *World Journal of Cardiology*, vol. 7, p. 204, 4 2015.

[2] D. P. Zipes, J. Jalife, and W. G. W. G. Stevenson, "Cardiac electrophysiology: from cell to bedside,"

[3] L. Sörnmo and P. Laguna, "Bioelectrical signal processing in cardiac and neurological applications," pp. 392–415, 2005.

[4] D. D. Bernardo and A. Murray, "Origin on the electrocardiogram of U-waves and abnormal U-wave inversion," *Cardiovascular Research*, vol. 53, pp. 202–208, 1 2002.

[5] M. Kihlgren, C. Almqvist, F. Amankhani, L. Jonasson, C. Norman, M. Perez, A. Ebrahimi, and C. Gottfridsson, "The U-wave: A remaining enigma of the electrocardiogram," *Journal of Electrocardiology*, vol. 79, pp. 13–20, 7 2023.

[6] I. Andršová, K. Hnatkova, M. Šišáková, O. Toman, P. Smetana, K. M. Huster, P. Barthel, T. Novotný', G. Schmidt, and M. Malik, "Influence of heart rate correction formulas on QTc interval stability," *Scientific Reports 2021 11:1*, vol. 11, pp. 1–21, 7 2021.

[7] E. Bertrand, M. Caru, A. Harvey, G. Andelfinger, C. Laverdiere, M. Krajinovic, D. Sinnett, V. Jacquemet, and D. Curnier, "QTc intervals at rest and during exercise assessed by group correction formulas in survivors of

childhood acute lymphoblastic leukemia," *Journal of Electrocardiology*, vol. 83, pp. 80–94, 3 2024.

[8] E. Frank, "An accurate, clinically practical system for spatial vectorcardiography," *Circulation*, vol. 13, pp. 737–749, 1956.

[9] G. E. Dower, "A lead synthesizer for the Frank system to simulate the standard 12-lead electrocardiogram," *Journal of Electrocardiology*, vol. 1, pp. 101–116, 1 1968.

[10] J. A. Kors, G. V. Herpen, A. C. Sittig, and J. H. V. Bemmel, "Reconstruction of the Frank vectorcardiogram from standard electrocardiographic leads: diagnostic comparison of different methods," *European Heart Journal*, vol. 11, pp. 1083–1092, 12 1990.

[11] G. Bortolan, I. Christov, I. Simova, and I. Dotsinsky, "Noise processing in exercise ECG stress test for the analysis and the clinical characterization of QRS and T wave alternans," *Biomedical Signal Processing and Control*, vol. 18, pp. 378–385, 4 2015.

[12] J. DeMaso and C. Sellers, "Progress in Holter technology," *Cardiac Electrophysiology Review*, vol. 3, pp. 239–242, 1999.

[13] G. F. Fletcher, G. Balady, V. F. Froelicher, L. H. Hartley, W. L. Haskell, and M. L. Pollock, "Exercise standards," *Circulation*, vol. 91, pp. 580–615, 1 1995.

[14] R. J. Gibbons, G. J. Balady, J. T. Bricker, B. R. Chaitman, G. F. Fletcher, V. F. Froelicher, D. B. Mark, B. D. McCallister, A. N. Mooss, M. G. O'Reilly, W. L. Winters, R. J. Gibbons, E. M. Antman, J. S. Alpert, D. P. Faxon, V. Fuster, G. Gregoratos, L. F. Hiratzka, A. K. Jacobs, R. O. Russell, and S. C. Smith, "ACC/AHA 2002 guideline update for exercise testing: summary article: A report of the american college of cardiology/american heart association task force on practice guidelines (committee to update the 1997 exercise testing guidelines)," *Journal of the American College of Cardiology*, vol. 40, pp. 1531–1540, 10 2002.

[15] M. J. Janse and A. L. Wit, "Electrophysiological mechanisms of ventricular arrhythmias resulting from myocardial ischemia and infarction," *Physiological reviews*, vol. 69, pp. 1049–1169, 1989.

[16] E. Carmeliet, "Cardiac ionic currents and acute ischemia: From channels to arrhythmias," *Physiological Reviews*, vol. 79, pp. 917–1017, 1999.

[17] N. Luqman, R. J. Sung, C. L. Wang, and C. T. Kuo, "Myocardial ischemia and ventricular fibrillation: Pathophysiology and clinical implications," *International Journal of Cardiology*, vol. 119, pp. 283–290, 7 2007.

[18] M. Gheorghiade and R. O. Bonow, "Chronic heart failure in the United States," *Circulation*, vol. 97, pp. 282–289, 1 1998.

[19] M. Gheorghiade, G. Sopko, L. D. Luca, E. J. Velazquez, J. D. Parker, P. F. Binkley, Z. Sadowski, K. S. Golba, D. L. Prior, J. L. Rouleau, and R. O. Bonow, "Navigating the crossroads of coronary artery disease and heart failure," *Circulation*, vol. 114, pp. 1202–1213, 9 2006.

[20] G. L. Sumner, V. P. Kuriachan, and L. B. Mitchell, "Sudden cardiac death," *Encyclopedia of Cardiovascular Research and Medicine*, vol. 1-4, pp. 511–520, 1 2018.

[21] M. W. Deyell, A. D. Krahn, and J. J. Goldberger, "Sudden cardiac death risk stratification," *Circulation Research*, vol. 116, pp. 1907–1918, 6 2015.

[22] A. Leiherer, A. Muendlein, C. H. Saely, K. Geiger, E. M. Brandtner, C. Heinzle, S. Gaenger, S. Mink, R. Laaksonen, P. Fraunberger, and H. Drexel, "Coronary event risk test (CERT) as a risk predictor for the 10-year clinical outcome of patients with peripheral artery disease," *Journal of Clinical Medicine*, vol. 12, p. 6151, 10 2023.

[23] S. Greulich, A. Seitz, D. Herter, F. Günther, S. Probst, R. Bekeredjian, M. Gawaz, U. Sechtem, and H. Mahrholdt, "Long-term risk of sudden cardiac death in hypertrophic cardiomyopathy: a cardiac magnetic resonance outcome study," *European Heart Journal - Cardiovascular Imaging*, vol. 22, pp. 732–741, 6 2021.

[24] J. D. Sara, M. F. Eleid, R. Gulati, and D. R. Holmes, "Sudden cardiac death from the perspective of coronary artery disease," *Mayo Clinic Proceedings*, vol. 89, pp. 1685–1698, 12 2014.

[25] N. V. Arteyeva, "Dispersion of ventricular repolarization: Temporal and spatial," *World Journal of Cardiology*, vol. 12, p. 437, 9 2020.

[26] C. X. Wong, A. Brown, D. H. Lau, S. S. Chugh, C. M. Albert, J. M. Kalman, and P. Sanders, "Epidemiology of sudden cardiac death: Global and regional perspectives," *Heart Lung and Circulation*, vol. 28, pp. 6–14, 1 2019.

[27] F. J. Neumann, U. Sechtem, A. P. Banning, N. Bonaros, H. Bueno, and et al., "2019 ESC guidelines for the diagnosis and management of chronic coronary syndromes," *European Heart Journal*, vol. 41, pp. 407–477, 1 2020.

[28] M. Esmaeilzadeh, M. Parsaee, and M. Maleki, "The role of echocardiography in coronary artery disease and acute myocardial infarction," *The Journal of Tehran University Heart Center*, vol. 8, p. 1, 2013.

[29] N. A. Chatterjee, M. V. Moorthy, J. Pester, A. Schaecter, G. K. Panicker, D. Narula, and D. C. L. et al., "Sudden death in patients with coronary heart disease without severe systolic dysfunction," *JAMA Cardiology*, vol. 3, pp. 591–600, 7 2018.

[30] K. Zeppenfeld, J. Tfelt-Hansen, M. D. Riva, B. G. Winkel, E. R. Behr, and et.al, "2022 ESC guidelines for the management of patients with ventricular arrhythmias and the prevention of sudden cardiac death: Developed by the task force for the management of patients with ventricular arrhythmias and the prevention of sudden cardiac death of the european society of cardiology (ESC) endorsed by the association for european paediatric and congenital cardiology (AEPC)," *European Heart Journal*, vol. 43, pp. 3997–4126, 10 2022.

[31] P. Laguna, J. P. M. Cortes, and E. Pueyo, "Techniques for ventricular repolarization instability assessment from the ECG," *Proceedings of the IEEE*, vol. 104, pp. 392–415, 2 2016.

[32] Y. Birnbaum, J. M. Wilson, and K. Nikus, "The electrocardiogram in coronary artery disease," *Coronary Artery Disease*, pp. 205–216, 2015.

[33] E. Hiltner, A. A. Akshar, P. Thanawala, A. Hakeem, J. Coromilas, and J. Kassotis, "Is isolated ST segment elevation in lead avr associated with high grade coronary artery disease?," *Journal of Electrocardiology*, vol. 62, pp. 170–177, 9 2020.

[34] J. J. Goldberger, A. E. Buxton, M. Cain, O. Costantini, D. V. Exner, B. P. Knight, D. Lloyd-Jones, A. H. Kadish, B. Lee, A. Moss, R. Myerburg, J. Olgin, R. Passman, D. Rosenbaum, W. Stevenson, W. Zareba, and D. P. Zipes, "Risk stratification for arrhythmic sudden cardiac death," *Circulation*, vol. 123, pp. 2423–2430, 5 2011.

[35] R. J. Myerburg and M. J. Junttila, "Sudden cardiac death caused by coronary heart disease," *Circulation*, vol. 125, pp. 1043–1052, 2 2012.

[36] M. N. Niemeijer, M. E. V. D. Berg, M. Eijgelsheim, G. V. Herpen, B. H. Stricker, J. A. Kors, and P. R. Rijnbeek, "Short-term QT variability markers for the prediction of ventricular arrhythmias and sudden cardiac death: a systematic review," *Heart*, vol. 100, pp. 1831–1836, 12 2014.

[37] H. Gravel, V. Jacquemet, N. Dahdah, and D. Curnier, "Clinical applications of QT/RR hysteresis assessment: Asystematic review," *Annals of Noninvasive Electrocardiology*, vol. 23, pp. 1–9, 2018.

[38] P. J. Schwartz and S. Wolf, "QT interval prolongation as predictor of sudden death in patients with myocardial infarction.," *Circulation*, vol. 57, pp. 1074–1077, 1978.

[39] M. Malik, "Problems of heart rate correction in assessment of drug-induced QT interval prolongation," *Journal of Cardiovascular Electrophysiology*, vol. 12, pp. 411–420, 4 2001.

[40] D. H. Cho, J. Choi, M. N. Kim, H. D. Kim, S. J. Hong, and et al., "Incremental value of QT interval for the prediction of obstructive coronary artery disease in patients with chest pain," *Scientific Reports*, vol. 11, p. 10513, 12 2021.

[41] E. Homs, V. Martí, J. Guindo, P. Laguna, X. Viñolas, P. Caminal, R. Elosua, and A. B. de Luna, "Automatic measurement of corrected QT interval in holter recordings: Comparison of its dynamic behavior in patients after myocardial infarction with and without life-threatening arrhythmias," *American Heart Journal*, vol. 134, pp. 181–187, 8 1997.

[42] S. S. Chugh, K. Reinier, T. Singh, A. Uy-Evanado, C. Socoteanu, D. Peters, R. Mariani, K. Gunson, and J. Jui, "Determinants of prolonged QT interval and their contribution to sudden death risk in coronary artery disease: The Oregon sudden unexpected death study," *Circulation*, vol. 119, pp. 663–670, 2 2009.

[43] M. Baumert, A. Porta, M. A. Vos, M. Malik, J. P. Couderc, P. Laguna, G. Piccirillo, G. L. Smith, L. G. Tereshchenko, and P. G. Volders, "QT interval variability in body surface ECG: Measurement, physiological basis, and clinical value: Position statement and consensus guidance endorsed by the European heart rhythm association jointly with the ESC working group on cardiac cellular electrophysiology," *Europace*, vol. 18, pp. 925–944, 6 2016.

[44] G. Kudaiberdieva, B. Gorenek, O. Goktekin, Y. Cavusoglu, A. Birdane, A. Unalir, N. Ata, and B. Timuralp, "Combination of QT variability and signal-averaged electrocardiography in association with ventricular tachycardia in postinfarction patients," *Journal of Electrocardiology*, vol. 36, pp. 17–24, 1 2003.

[45] G. Piccirillo, D. Magrí, S. Matera, M. Magnanti, A. Torrini, E. Pasquazzi, E. Schifano, S. Velitti, V. Marigliano, R. Quaglione, and F. Barillà, "QT variability strongly predicts sudden cardiac death in asymptomatic subjects with mild or moderate left ventricular systolic dysfunction: a prospective study," *European Heart Journal*, vol. 28, pp. 1344–1350, 6 2007.

[46] X. Chen and N. A. Trayanova, "A novel methodology for assessing the bounded-input bounded-output instability in QT interval dynamics: application to clinical ECG with ventricular tachycardia," *IEEE Transactions on Biomedical Engineering*, vol. 59, no. 8, pp. 2111–2117, 2011.

[47] E. Pueyo, P. Smetana, P. Caminal, A. Bayes de Luna, M. Malik, and P. Laguna, "Characterization of QT interval adaptation to RR interval changes and its use as a risk-stratifier of arrhythmic mortality in amiodarone-treated survivors of acute myocardial infarction," *IEEE Transactions on Biomedical Engineering*, vol. 51, no. 9, 2004.

[48] P. Smetana, E. Pueyo, K. Hnatkova, V. Batchvarov, P. Laguna, and M. Malik, "Individual patterns of dynamic QT/RR relationship in survivors of acute myocardial infarction and their relationship to antiarrhythmic efficacy of amiodarone," *Journal of Cardiovascular Electrophysiology*, vol. 15, pp. 1147–1154, 10 2004.

[49] W. Zareba and I. Cygankiewicz, *The QT Interval*, pp. 833–862. Springer, London, 2010.

[50] A. Pathak, D. Curnier, J. Fourcade, J. Roncalli, P. K. Stein, P. Hermant, M. Bousquet, P. Massabuau, J.-M. Sénard, J.-L. Montastruc, *et al.*, "QT dynamicity: a prognostic factor for sudden cardiac death in chronic heart failure," *European journal of heart failure*, vol. 7, no. 2, pp. 269–275, 2005.

[51] N. P. Johnson, T. A. Holly, and J. J. Goldberger, "QT dynamics early after exercise as a predictor of mortality," *Heart Rhythm*, vol. 7, no. 8, pp. 1077–1084, 2010.

[52] N. J. Verouden, K. T. Koch, R. J. Peters, J. P. Henriques, J. Baan, R. J. V. D. Schaaf, M. M. Vis, J. G. Tijssen, J. J. Piek, H. J. Wellens, A. A. Wilde, and R. J. D. Winter, "Persistent precordial "hyperacute" T-waves signify proximal left anterior descending artery occlusion," *Heart*, vol. 95, pp. 1701–1706, 10 2009.

[53] M. A. Pessah, H. Huhtala, P. Kosonen, M. Eskola, A. R. Pérez-Riera, K. Nikus, and J. Rankinen, "Early ischemic ST-segment and T-wave changes during balloon angioplasty," *Journal of Electrocardiology*, vol. 73, pp. 87–95, 7 2022.

[54] P. D. Arini, G. C. Bertrán, E. R. Valverde, and P. Laguna, "T-wave width as an index for quantification of ventricular repolarization dispersion: Evaluation in an isolated rabbit heart model," *Biomedical Signal Processing and Control*, vol. 3, pp. 67–77, 1 2008.

[55] A. Mincholé, E. Pueyo, J. F. Rodrguez, E. Zacur, M. Doblaré, and P. Laguna, "Quantification of restitution dispersion from the dynamic changes of the T-wave peak to end, measured at the surface ECG," *IEEE Transactions on Biomedical Engineering*, vol. 58, pp. 1172–1182, 5 2011.

[56] A. Mincholé, A. Bueno-Orovio, P. Laguna, E. Pueyo, and B. Rodríguez, "ECG-based estimation of dispersion of APD restitution as a tool to stratify sotalol-induced arrhythmic risk," *Journal of Electrocardiology*, vol. 48, pp. 867–873, 9 2015.

[57] R. L. Verrier, T. Klingenheben, M. Malik, N. El-Sherif, D. V. Exner, S. H. Hohnloser, T. Ikeda, J. P. Martínez, S. M. Narayan, T. Nieminen, and D. S. Rosenbaum, "Microvolt T-wave alternans: Physiological basis, methods of measurement, and clinical utility-consensus guideline by international society for Holter and noninvasive electrocardiology," *Journal of the American College of Cardiology*, vol. 58, pp. 1309–1324, 9 2011.

[58] V. Monasterio, P. Laguna, I. Cygankiewicz, R. Vázquez, A. Bayés-Genís, A. B. D. Luna, and J. P. Martínez, "Average T-wave alternans activity in ambulatory ECG records predicts sudden cardiac death in patients with chronic heart failure," *Heart Rhythm*, vol. 9, pp. 383–389, 3 2012.

[59] J. Ramírez, M. Orini, A. Mincholé, V. Monasterio, I. Cygankiewicz, A. B. de Luna, J. P. Martínez, P. Laguna, and E. Pueyo, "Sudden cardiac death and pump failure death prediction in chronic heart failure by combining ECG and clinical markers in an integrated risk model," *PLoS ONE*, vol. 12, 10 2017.

[60] J. Ramírez, A. Kiviniemi, S. van Duijvenboden, A. Tinker, P. D. Lambiase, J. Junttila, J. S. Perkiömäki, H. V. Huikuri, M. Orini, and P. B. Munroe, "ECG T-wave morphologic variations predict ventricular arrhythmic risk in low- and moderate-risk populations," *Journal of the American Heart Association*, vol. 11, p. e025897, 2022.

[61] H. D. Huang and Y. Birnbaum, "ST elevation: differentiation between ST elevation myocardial infarction and nonischemic ST elevation," *Journal of Electrocardiology*, vol. 44, pp. 494.e1–494.e12, 9 2011.

[62] G. Russo, S. E. Ravenna, A. D. Vita, C. Aurigemma, P. Lamendola, G. A. Lanza, and F. Crea, "Exercise test predictors of severe coronary artery disease: Role of ST-segment elevation in lead aVR," *Clinical Cardiology*, vol. 40, pp. 102–108, 2 2017.

[63] M. R. Franz, C. D. Swerdlow, L. B. Liem, and J. Schaefer, "Cycle length dependence of human action potential duration in vivo. effects of single extrastimuli, sudden sustained rate acceleration and deceleration, and different steady-state frequencies.," *The Journal of Clinical Investigation*, vol. 82, pp. 972–979, 9 1988.

[64] C. P. Lau, A. R. Freedman, S. Fleming, M. Malik, A. J. Camm, and D. E. Ward, "Hysteresis of the ventricular paced QT interval in response to abrupt changes in pacing rate," *Cardiovascular Research*, vol. 22, pp. 67–72, 1.

[65] E. Pueyo, Z. Husti, T. Hornyik, I. Baczkó, P. Laguna, A. Varró, and B. Rodríguez, "Mechanisms of ventricular rate adaptation as a predictor of arrhythmic risk," *Am. J. Physiol.-Heart and Circulatory Physiology*, vol. 298, no. 5, pp. H1577–H1587, 2010.

[66] J. M. Morgan, A. D. Cunningham, and E. Rowland, "Relationship of the effective refractory period and monophasic action potential duration after a step increase in pacing frequency," *Pacing and Clinical Electrophysiology*, vol. 13, pp. 1002–1008, 8 1990.

[67] A. Zaza, G. Malfatto, and P. J. Schwartz, "Sympathetic modulation of the relation between ventricular repolarization and cycle length," *Circulation research*, vol. 68, pp. 1191–1203, 1991.

[68] S. Seethala, V. Shusterman, S. Saba, S. Mularski, and J. Němec, "Effect of β-adrenergic stimulation on QT interval accommodation," *Heart Rhythm*, vol. 8, pp. 263–270, 2 2011.

[69] A. Bueno-Orovio, B. M. Hanson, J. S. Gill, P. Taggart, and B. Rodriguez, "Slow adaptation of ventricular repolarization as a cause of arrhythmia?," *Methods of Information in Medicine*, vol. 53, pp. 320–323, 2014.

[70] O. E. Osadchii, "Flecainide attenuates rate adaptation of ventricular repolarization in guinea-pig heart," *Scandinavian Cardiovascular Journal*, vol. 50, pp. 28–35, 1 2016.

[71] O. E. Osadchii, "Effects of antiarrhythmics and hypokalemia on the rate adaptation of cardiac repolarization," *Scandinavian Cardiovascular Journal*, vol. 52, pp. 218–226, 7 2018.

[72] A. Cabasson, O. Meste, and J. M. Vesin, "Estimation and modeling of QT-interval adaptation to heart rate changes," *IEEE Transactions on Biomedical Engineering*, vol. 59, pp. 956–965, 4 2012.

[73] H. Gravel, D. Curnier, N. Dahdah, and V. Jacquemet, "Categorization and theoretical comparison of quantitative methods for assessing QT/RR hysteresis," *Annals of Noninvasive Electrocardiology*, vol. 22, pp. 1–12, 2017.

[74] K. J. Axelsson, A. Bränn lund, L. Gransberg, G. Lundahl, F. Vahedi, and L. Bergfeldt, "Adaptation of ventricular repolarization duration and dispersion during changes in heart rate induced by atrial stimulation," *Annals of Noninvasive Electrocardiology*, vol. 25, 5 2020.

[75] K. J. Axelsson, L. Gransberg, G. Lundahl, F. Vahedi, and L. Bergfeldt, "Adaptation of ventricular repolarization time following abrupt changes in heart rate: Comparisons and reproducibility of repeated atrial and ventricular pacing," *American Journal of Physiology - Heart and Circulatory Physiology*, vol. 320, pp. H381–H392, 1 2021.

[76] N. Mantri, M. Lu, J. G. Zaroff, N. Risch, T. Hoffmann, A. Oni-Orisan, C. Lee, E. Jorgenson, and C. Iribarren, "QT interval dynamics and cardiovascular outcomes: A cohort study in an integrated health care delivery system," *Journal of the American Heart Association*, vol. 10, p. 18513, 10 2021.

[77] H. H. Draisma, B. H. V. Huysduynen, C. A. Swenne, A. C. Maan, E. E. V. D. Wall, and M. J. Schalij, "Increased dispersion of ventricular repolarization during recovery from exercise," *Computers in Cardiology*, vol. 32, pp. 85–88, 2005.

[78] C. A. Swenne, "Mechanisms of exercise-recovery hysteresis in the ECG: ISCE 2015 paper," *Journal of Electrocardiology*, vol. 48, pp. 1006–1009, 11 2015.

[79] A. O. Demirtas and O. D. Urgun, "Can QT interval prolongation or dispersion detected in a positive exercise ECG test predict critical coronary artery disease?," *Archives of Medical Science - Atherosclerotic Diseases*, vol. 4, pp. 7–12, 3 2019.

[80] M. S. Lauer, C. E. Pothier, Y. B. Chernyak, R. Brunken, M. Lieber, C. Apperson-Hansen, and J. M. Starobin, "Exercise-induced QT/RR-interval hysteresis as a predictor of myocardial ischemia," *Journal of Electrocardiology*, vol. 39, pp. 315–323, 7 2006.

[81] D. J. Pelchovitz, J. Ng, A. B. Chicos, D. W. Bergner, and J. J. Goldberger, "QT-RR hysteresis is caused by differential autonomic states during exercise and recovery," *American Journal of Physiology - Heart and Circulatory Physiology*, vol. 302, pp. 2567–2573, 6 2012.

[82] Y. Zhang, M. Bao, M. Dai, H. Zhong, Y. Li, and T. Tan, "QT hysteresis index improves the power of treadmill exercise test in the screening of coronary artery disease," *Circulation Journal*, vol. 78, pp. 2942–2949, 2014.

[83] E. Pueyo, M. Malik, and P. Laguna, "A dynamic model to characterize beat-to-beat adaptation of repolarization to heart rate changes," *Biomedical Signal Processing and Control*, vol. 3, no. 1, pp. 29–43, 2008.

[84] V. Jacquemet, H. Gravel, D. Curnier, and A. Vinet, "Theoretical and experimental comparison of lag-based and time-based exponential moving average models of QT hysteresis," *Physiological Measurement*, vol. 38, pp. 1885–1905, 9 2017.

[85] I. Andršová, K. Hnatkova, M. Šišáková, O. Toman, P. Smetana, K. M. Huster, P. Barthel, T. Novotný', G. Schmidt, and M. Malik, "Sex and rate change differences in QT/RR hysteresis in healthy subjects," *Frontiers in Physiology*, vol. 12, p. 2473, 2 2022.

[86] P. J. Schwartz, L. Crotti, and R. Insolia, "Long-QT syndrome," *Circulation: Arrhythmia and Electrophysiology*, vol. 5, pp. 868–877, 2012.

[87] J. A. Wong, L. J. Gula, G. J. Klein, R. Yee, A. C. Skanes, and A. D. Krahn, "Utility of treadmill testing in identification and genotype prediction

in long-QT syndrome," *Circulation: Arrhythmia and Electrophysiology*, vol. 3, pp. 120–125, 4 2010.

[88] P. Kligfield, K. G. Lax, and P. M. Okin, "QT interval-heart rate relation during exercise in normal men and women: definition by linear regression analysis," *J. Am. Coll. Cardiol.*, vol. 28, no. 6, 1996.

[89] A. Grom, T. S. Faber, M. Brunner, C. Bode, and M. Zehender, "Delayed adaptation of ventricular repolarization after sudden changes in heart rate due to conversion of atrial fibrillation. a potential risk factor for proarrhythmia?," *Europace*, vol. 7, pp. 113–121, 1 2005.

[90] A. Martín-Yebra, L. Sörnmo, and P. Laguna, "QT interval adaptation to heart rate changes in atrial fibrillation as a predictor of sudden cardiac death," *IEEE Transactions on Biomedical Engineering*, vol. 69, pp. 3109–3118, 10 2022.

[91] D. C. Trost, "A method for constructing and estimating the RR-memory of the QT-interval and its inclusion in a multivariate biomarker for torsades de pointes risk," *Journal of biopharmaceutical statistics*, vol. 18, no. 4, pp. 773–796, 2008.

[92] D. A. Sampedro-Puente, J. Fernandez-Bes, N. Szentandrássy, P. Nánási, P. Taggart, and E. Pueyo, "Time course of low-frequency oscillatory behavior in human ventricular repolarization following enhanced sympathetic activity and relation to arrhythmogenesis," *Frontiers in Physiology*, vol. 10, 1 2020.

[93] A. Petrenas, V. Marozas, A. Sološenko, R. Kubilius, J. Skibarkiene, J. Oster, and L. Sörnmo, "Electrocardiogram modeling during paroxysmal atrial fibrillation: Application to the detection of brief episodes," *Physiological Measurement*, vol. 38, pp. 2058–2080, 11 2017.

[94] A. Porta, E. Tobaldini, T. Gnecchi-Ruscone, and N. Montano, "RT variability unrelated to heart period and respiration progressively increases during graded head-up tilt," *American Journal of Physiology - Heart and Circulatory Physiology*, vol. 298, 5 2010.

[95] K. Ogata, *Ogata, Modern Control Engineering, 5th Edition | Pearson.* 2010.

[96] D. Charisopoulou, G. Koulaouzidis, L. F. Law, A. Rydberg, and M. Y. Henein, "Exercise induced worsening of mechanical heterogeneity and

diastolic impairment in long QT syndrome," *Journal of Clinical Medicine 2021, Vol. 10, Page 37*, vol. 10, p. 37, 12 2020.

[97] T. M. Roston, A. M. D. Souza, H. V. Romans, S. Franciosi, K. R. Armstrong, and S. Sanatani, "Potential overdiagnosis of long QT syndrome using exercise stress and QT stand testing in children and adolescents with a low probability of disease," *Journal of Cardiovascular Electrophysiology*, vol. 32, pp. 500–506, 2 2021.

[98] C. R. Meyer and H. N. Keiser, "Electrocardiogram baseline noise estimation and removal using cubic splines and state-space computation techniques," *Computers and Biomedical Research*, vol. 10, pp. 459–470, 10 1977.

[99] J. Mateo and P. Laguna, "Analysis of heart rate variability in the presence of ectopic beats using the heart timing signal," *IEEE Transactions on Biomedical Engineering*, vol. 50, pp. 334–343, 3 2003.

[100] J. P. Martínez, R. Almeida, S. Olmos, A. P. Rocha, and P. Laguna, "A wavelet-based ECG delineator evaluation on standard databases," *IEEE Transactions on Biomedical Engineering*, vol. 51, pp. 570–581, 4 2004.

[101] F. Castells, P. Laguna, L. Sörnmo, A. Bollmann, and J. M. Roig, "Principal component analysis in ECG signal processing," *Eurasip Journal on Advances in Signal Processing*, vol. 2007, p. 074580, 12 2007.

[102] R. Sameni, C. Jutten, and M. B. Shamsollahi, "Multichannel electrocardiogram decomposition using periodic component analysis," *IEEE Transactions on Biomedical Engineering*, vol. 55, pp. 1935–1940, 8 2008.

[103] R. Bailón, J. Mateo, S. Olmos, P. Serrano, J. García, A. del Río, I. J. Ferreira, and P. Laguna, "Coronary artery disease diagnosis based on exercise electrocardiogram indexes from repolarisation, depolarisation and heart rate variability," *Medical and Biological Engineering and Computing*, vol. 41, pp. 561–571, 9 2003.

[104] F. Palmieri, P. Gomis, D. Ferreira, J. E. Ruiz, B. Bergasa, A. Martín-Yebra, H. A. Bukhari, E. Pueyo, J. P. Martínez, J. Ramírez, and P. Laguna, "Monitoring blood potassium concentration in hemodialysis patients by quantifying T-wave morphology dynamics," *Scientific Reports*, vol. 11, p. 3883, 12 2021.

[105] S. Romagnoli, C. Peréz, L. Burattini, E. Pueyo, M. Morettini, A. Sbrollini, J. P. Martínez, and P. Laguna, "Model-based estimators of QT series

time delay in following heart-rate changes," *45th Annual International Conference of the IEEE Engineering in Medicine and Biology Society (EMBC)*, pp. 1–4, 2023.

[106] S. Romagnoli, A. Sbrollini, L. Burattini, J. P. Martínez, and P. Laguna, "Characterization of QT-interval adaptation time lag in response to sport-induced heart rate changes measured from wearable ECG recordings," *IEEE Transactions on Biomedical Engineering*, pp. 1–13, 2024.

[107] D. Romero, J. P. Martínez, P. Laguna, and E. Pueyo, "Ischemia detection from morphological QRS angle changes," *Physiological Measurement*, vol. 37, pp. 1004–1023, 5 2016.

[108] A. Mincholé, L. Sörnmo, and P. Laguna, "Detection of body position changes from the ECG using a laplacian noise model," *Biomedical Signal Processing and Control*, vol. 14, pp. 189–196, 11 2014.

[109] R. Killick, P. Fearnhead, and I. A. Eckley, "Optimal detection of change-points with a linear computational cost," *Journal of the American Statistical Association*, vol. 107, pp. 1590–1598, 2012.

[110] R. Sameni, G. D. Clifford, C. Jutten, and M. B. Shamsollahi, "Multichannel ECG and noise modeling: Application to maternal and fetal ECG signals," *Eurasip Journal on Advances in Signal Processing*, vol. 2007, pp. 1–14, 12 2007.

[111] J. Behar, F. Andreotti, S. Zaunseder, Q. Li, J. Oster, and G. D. Clifford, "An ECG simulator for generating maternal-foetal activity mixtures on abdominal ECG recordings," *Physiological Measurement*, vol. 35, pp. 1537–1550, 2014.

[112] E. Keenan, C. K. Karmakar, and M. Palaniswami, "The effects of asymmetric volume conductor modeling on non-invasive fetal ECG extraction," *Physiological Measurement*, vol. 39, p. 105013, 10 2018.

[113] G. D. Clifford, S. Nemati, and R. Sameni, "An artificial vector model for generating abnormal electrocardiographic rhythms," *Physiological Measurement*, vol. 31, pp. 595–609, 2010.

[114] A. Mincholé, J. Camps, A. Lyon, and B. Rodríguez, "Machine learning in the electrocardiogram," *Journal of Electrocardiology*, vol. 57, pp. S61–S64, 11 2019.

[115] P. E. McSharry, G. D. Clifford, L. Tarassenko, and L. A. Smith, "A dynamical model for generating synthetic electrocardiogram signals," *IEEE Transactions on Biomedical Engineering*, vol. 50, pp. 289–294, 3 2003.

[116] O. Sayadi, M. B. Shamsollahi, and G. D. Clifford, "Synthetic ECG generation and bayesian filtering using a gaussian wave-based dynamical model," *Physiological Measurement*, vol. 31, pp. 1309–1329, 8 2010.

[117] J.-C. Edelmann, D. Mair, D. Ziesel, M. Burtscher, and T. Ussmueller, "An ECG simulator with a novel ECG profile for physiological signals," *Journal of medical engineering & technology*, vol. 42, no. 7, pp. 501–509, 2018.

[118] J. H. Atterhög and E. Loogna, "P-R interval in relation to heart rate during exercise and the influence of posture and autonomic tone," *Journal of Electrocardiology*, vol. 10, pp. 331–336, 1 1977.

[119] A. Cabasson, O. Meste, G. Blain, and S. Bermon, "Quantifying the PR interval pattern during dynamic exercise and recovery," *IEEE Transactions on Biomedical Engineering*, vol. 56, pp. 2675–2683, 11 2009.

[120] L. Bachi, H. Halvaei, C. Pérez, A. Martin-Yebra, A. Petrenas, A. Solosenko, L. Johnson, V. Marozas, J. P. Martínez, E. Pueyo, M. Stridh, P. Laguna, and L. Sörnmo, "ECG modeling for simulation of arrhythmias in time-varying conditions," *IEEE Transactions on Biomedical Engineering*, vol. 70, pp. 3449–3460, 12 2023.

[121] H. Riekkinen and P. Rautaharju, "Body position, electrode level, and respiration effects on the frank lead electrocardiogram.," *Circulation*, vol. 53, pp. 40–45, 1976.

[122] R. Pallás-Areny, J. Colominas-Balagué', and F. J. Rosell, "The effect of respiration-induced heart movents on the ECG," *IEEE Transactions on Biomedical Engineering*, vol. 36, pp. 585–590, 1989.

[123] R. Bailón, L. Sörnmo, and P. Laguna, "A robust method for ECG-based estimation of the respiratory frequency during stress testing.," *IEEE transactions on bio-medical engineering*, vol. 53, pp. 1273–85, 7 2006.

[124] M. Aström, E. C. Santos, L. Sörnmo, P. Laguna, and B. Wohlfart, "Vectorcardiographic loop alignment and the measurement of morphologic

beat-to-beat variability in noisy signals," *IEEE Transactions on Biomedical Engineering*, vol. 47, pp. 497–506, 2000.

[125] D. Hernando, A. Hernando, J. A. Casajús, P. Laguna, N. Garatachea, and R. Bailón, "Methodological framework for heart rate variability analysis during exercise: application to running and cycling stress testing," *Medical and Biological Engineering and Computing*, vol. 56, pp. 781–794, 2018.

[126] M. Pilhall, M. Riha, and S. Jern, "Changes in the QRS segment during exercise: effects of acute β-blockade with propranolol," *Clinical Physiology*, vol. 13, pp. 113–131, 3 1993.

[127] M. Virtanen, M. Kähönen, T. Nieminen, P. Karjalainen, M. Tarvainen, T. Lehtimäki, R. Lehtinen, K. Nikus, T. Kööbi, M. Niemi, K. Niemelä, V. Turjanmaa, J. Malmivuo, and J. Viik, "Heart rate variability derived from exercise ECG in the detection of coronary artery disease," *Physiological Measurement*, vol. 28, p. 1189, 9 2007.

[128] A. Cabasson and O. Meste, "Time delay estimation: A new insight into the woody's method," *IEEE Signal Processing Letters*, vol. 15, pp. 573–576, 2008.

[129] G. Jimenez-Perez, A. Alcaine, and O. Camara, "Delineation of the electrocardiogram with a mixed-quality-annotations dataset using convolutional neural networks," *Scientific reports*, vol. 11, 12 2021.

[130] M. S. Haleem and L. Pecchia, "A deep learning based ECG segmentation tool for detection of ECG beat parameters," *Proceedings - IEEE Symposium on Computers and Communications*, vol. 2022-June, 2022.

[131] M. D. Diaw, S. Papelier, A. Durand-Salmon, J. Felblinger, and J. Oster, "Ai-assisted QT measurements for highly automated drug safety studies," *IEEE Transactions on Biomedical Engineering*, vol. 70, pp. 1504–1515, 5 2023.

[132] M. G. D. Castillo, D. Hernando, M. Orini, P. Laguna, J. Viik, R. Bailón, and E. Pueyo, "QT variability unrelated to RR variability during stress testing for identification of coronary artery disease," *Philosophical Transactions of the Royal Society A: Mathematical, Physical and Engineering Sciences*, vol. 379, 12 2021.

[133] M. J. Junttila, A. M. Kiviniemi, E. S. Lepojärvi, M. Tulppo, O. P. Piira, T. Kenttä, J. S. Perkiömäki, O. H. Ukkola, R. J. Myerburg, and H. V.

Huikuri, "Type 2 diabetes and coronary artery disease: Preserved ejection fraction and sudden cardiac death," *Heart Rhythm*, vol. 15, pp. 1450–1456, 2018.

[134] P. W. Serruys, M.-C. Morice, A. P. Kappetein, A. Colombo, D. R. Holmes, M. J. Mack, E. Ståhle, T. E. Feldman, M. van den Brand, E. J. Bass, N. V. Dyck, K. Leadley, K. D. Dawkins, and F. W. Mohr, "Percutaneous coronary intervention versus coronary-artery bypass grafting for severe coronary artery disease," *New England Journal of Medicine*, vol. 360, pp. 961–972, 3 2009.

[135] G.-S. Fu, A. Meissner, and R. Simon, "Repolarization dispersion and sudden cardiac death in patients with impaired left ventricular function," *European Heart Journal*, vol. 18, pp. 281–289, 1997.

[136] K. M. Leong, F. S. Ng, C. Roney, C. Cantwell, M. J. Shun-Shin, N. W. Linton, Z. I. Whinnett, D. C. Lefroy, D. W. Davies, S. E. Harding, P. B. Lim, D. Francis, N. S. Peters, A. M. Varnava, and P. Kanagaratnam, "Repolarization abnormalities unmasked with exercise in sudden cardiac death survivors with structurally normal hearts," *Journal of Cardiovascular Electrophysiology*, vol. 29, pp. 115–126, 1 2018.

[137] G. Tse and B. P. Yan, "Traditional and novel electrocardiographic conduction and repolarization markers of sudden cardiac death," *EP Europace*, vol. 19, pp. 712–721, 5 2017.

[138] K. F. Browne, D. P. Zipes, J. J. Heger, and E. N. Prystowsky, "Influence of the autonomic nervous system on the Q-T interval in man," *The American Journal of Cardiology*, vol. 50, pp. 1099–1103, 11 1982.

[139] R. Bexton, H. Vallin, and A. Camm, "Diurnal variation of the QT interval–influence of the autonomic nervous system.," *Heart*, vol. 55, pp. 253–258, 3 1986.

[140] A. R. Magnano, S. Holleran, R. Ramakrishnan, J. A. Reiffel, and D. M. Bloomfield, "Autonomic nervous system influences on QT interval in normal subjects," *Journal of the American College of Cardiology*, vol. 39, pp. 1820–1826, 6 2002.

[141] J. Bolea, E. Pueyo, P. Laguna, and R. Bailón, "Non-linear HRV indices under autonomic nervous system blockade," *2014 36th Annual International Conference of the IEEE Engineering in Medicine and Biology Society, EMBC 2014*, pp. 3252–3255, 11 2014.

[142] R. Mantravadi, B. Gabris, T. Liu, B. R. Choi, W. C. de Groat, G. A. Ng, and G. Salama, "Autonomic nerve stimulation reverses ventricular repolarization sequence in rabbit hearts," *Circulation Research*, vol. 100, 4 2007.

[143] S. Nayyar, K. C. Roberts-Thomson, M. A. Hasan, T. Sullivan, J. Harrington, P. Sanders, and M. Baumert, "Autonomic modulation of repolarization instability in patients with heart failure prone to ventricular tachycardia," *American Journal of Physiology - Heart and Circulatory Physiology*, vol. 305, pp. 1181–1188, 10 2013.

[144] M. T. L. Rovere, A. Gorini, and P. J. Schwartz, "Stress, the autonomic nervous system, and sudden death," *Autonomic Neuroscience*, vol. 237, p. 102921, 1 2022.

[145] P. Kowallik, C. Braun, and M. Meesmann, "Independent autonomic modulation of sinus node and ventricular myocardium in healthy young men during sleep," *Journal of Cardiovascular Electrophysiology*, vol. 11, pp. 1063–1070, 10 2000.

[146] K. Rajappan, C. O'Connell, and D. J. Sheridan, "Changes in QT interval with exercise in elite male rowers and controls," *International Journal of Cardiology*, vol. 87, pp. 217–222, 2 2003.

[147] J. S. Sarma, S. K. Venkataraman, D. R. Samant, and G. U, "Hysteresis in the human RR-QT relationship during exercise and recovery," *Pacing and Clinical Electrophysiology*, vol. 10, pp. 485–491, 5 1987.

[148] E. Pueyo, M. Orini, J. F. Rodríguez, and P. Taggart, "Interactive effect of beta-adrenergic stimulation and mechanical stretch on low-frequency oscillations of ventricular action potential duration in humans," *Journal of Molecular and Cellular Cardiology*, vol. 97, pp. 93–105, 8 2016.

[149] D. A. Sampedro-Puente, F. Raphel, J. Fernandez-Bes, P. Laguna, D. Lombardi, and E. Pueyo, "Characterization of spatio-temporal cardiac action potential variability at baseline and under β-adrenergic stimulation by combined unscented Kalman filter and double greedy dimension reduction," *IEEE Journal of Biomedical and Health Informatics*, vol. 25, pp. 276–288, 1 2021.

[150] T. O'Hara, L. Virág, A. Varró, and Y. Rudy, "Simulation of the undiseased human cardiac ventricular action potential: model formulation and exper-

imental validation," *PLOS Computational Biology*, vol. 7, p. e1002061, 2011.

[151] K. H. T. Tusscher and A. V. Panfilov, "Alternans and spiral breakup in a human ventricular tissue model," *American Journal of Physiology - Heart and Circulatory Physiology*, vol. 291, pp. H1088–H100, 2006.

[152] J. Q. Gong, M. E. Susilo, A. Sher, C. J. Musante, and E. A. Sobie, "Quantitative analysis of variability in an integrated model of human ventricular electrophysiology and β-adrenergic signaling," *Journal of Molecular and Cellular Cardiology*, vol. 143, pp. 96–106, 6 2020.

[153] J. Heijman, P. G. Volders, R. L. Westra, and Y. Rudy, "Local control of β-adrenergic stimulation: Effects on ventricular myocyte electrophysiology and Ca^{2+}-transient," *Journal of molecular and cellular cardiology*, vol. 50, pp. 863–871, 5 2011.

[154] L. Tung, "A bi-domain model for describing ischemic myocardial dc potentials," 1978.

[155] M. Potse, B. Dubé, J. Richer, A. Vinet, and R. Gulrajani, "A comparison of monodomain and bidomain reaction-diffusion models for action potential propagation in the human heart," *IEEE Transactions on Biomedical Engineering*, vol. 53, pp. 2425–2435, 2006.

[156] E. Pueyo, A. Corrias, L. Virág, N. Jost, T. Szél, A. Varró, N. Szentandrássy, P. P. Nánási, K. Burrage, and B. Rodríguez, "A multiscale investigation of repolarization variability and its role in cardiac arrhythmogenesis," *Biophys J*, vol. 101, no. 12, pp. 2892–2902, 2011.

[157] E. Drouin, F. Charpentier, C. Gauthier, K. Laurent, and H. L. Marec, "Electrophysiologic characteristics of cells spanning the left ventricular wall of human heart: Evidence for presence of M cells," *Journal of the American College of Cardiology*, vol. 26, pp. 185–192, 7 1995.

[158] P. Taggart, P. M. Sutton, T. Opthof, R. Coronel, R. Trimlett, W. Pugsley, and P. Kallis, "Inhomogeneous transmural conduction during early ischaemia in patients with coronary artery disease," *Journal of Molecular and Cellular Cardiology*, vol. 32, pp. 621–630, 4 2000.

[159] K. Nanthakumar, J. Jalife, S. Massé, E. Downar, M. Pop, J. Asta, H. Ross, V. Rao, S. Mironov, E. Sevaptsidis, J. Rogers, G. Wright, and R. Dhopeshwarkar, "Optical mapping of langendorff-perfused human

hearts: establishing a model for the study of ventricular fibrillation in humans," *American Journal of Physiology - Heart and Circulatory Physiology*, vol. 293, pp. 875–880, 7 2007.

[160] Z. Qu and A. Garfinkel, "An advanced algorithm for solving partial differential equation in cardiac conduction," *IEEE Transactions on Biomedical Engineering*, vol. 46, pp. 1166–1168, 1999.

[161] K. A. Mountris and E. Pueyo, "The radial point interpolation mixed collocation (RPIMC) method for the solution of the reaction-diffusion equation in cardiac electrophysiology," *Mechanisms and Machine Science*, vol. 98, pp. 39–44, 2021.

[162] K. A. Mountris and E. Pueyo, "Next-generation in silico cardiac electrophysiology through immersed grid meshfree modeling: Application to simulation of myocardial infarction," *Computing in Cardiology*, vol. 2020-September, 9 2020.

[163] K. A. Mountris and E. Pueyo, "A dual adaptive explicit time integration algorithm for efficiently solving the cardiac monodomain equation," *International Journal for Numerical Methods in Biomedical Engineering*, vol. 37, p. e3461, 7 2021.

[164] K. Gima and Y. Rudy, "Ionic current basis of electrocardiographic waveforms," *Circulation Research*, vol. 90, pp. 889–896, 5 2002.

[165] F. Ruzsnavszky, B. Hegyi, K. Kistamás, K. Váczi, B. Horváth, N. Szentandrássy, T. Bányász, P. P. Nánási, and J. Magyar, "Asynchronous activation of calcium and potassium currents by isoproterenol in canine ventricular myocytes," *Naunyn-Schmiedeberg's Archives of Pharmacology*, vol. 387, pp. 457–467, 2 2014.

[166] M. Malik, K. Hnatkova, A. Schmidt, and P. Smetana, "Accurately measured and properly heart-rate corrected QTc intervals show little daytime variability," *Heart Rhythm*, vol. 5, pp. 1424–1431, 10 2008.

[167] D. A. Sampedro-Puente, J. Fernandez-Bes, B. Porter, S. V. Duijvenboden, P. Taggart, and E. Pueyo, "Mechanisms underlying interactions between low-frequency oscillations and beat-to-beat variability of celullar ventricular repolarization in response to sympathetic stimulation: Implications for arrhythmogenesis," *Frontiers in Physiology*, vol. 10, p. 443488, 8 2019.

[168] I. Planinc, P. Garcia-Canadilla, H. Dejea, I. Ilic, E. Guasch, M. Zamora, F. Crispi, M. Stampanoni, D. Milicic, B. Bijnens, A. Bonnin, and M. Cikes, "Comprehensive assessment of myocardial remodeling in ischemic heart disease by synchrotron propagation based X-ray phase contrast imaging," *Scientific Reports 2021 11:1*, vol. 11, pp. 1–13, 7 2021.

[169] N. S. Dhalla, H. K. Saini, P. S. Tappia, R. Sethi, S. A. Mengi, and S. K. Gupta, "Potential role and mechanisms of subcellular remodeling in cardiac dysfunction due to ischemic heart disease," *Journal of Cardiovascular Medicine*, vol. 8, pp. 238–250, 4 2007.

[170] H. Bundgaard and K. Kjeldsen, "Human myocardial Na,K-ATPase concentration in heart failure," *Molecular and Cellular Biochemistry*, vol. 163-164, pp. 277–283, 1996.

[171] J. Müller-Ehmsen, A. A. McDonough, R. A. Farley, and R. H. Schwinger, "Sodium pump isoform expression in heart failure: Implication for treatment," *Basic Research in Cardiology, Supplement*, vol. 97, pp. 25–30, 2002.

[172] W. Fuller, V. Parmar, P. Eaton, J. R. Bell, and M. J. Shattock, "Cardiac ischemia causes inhibition of the Na/K ATPase by a labile cytosolic compound whose production is linked to oxidant stress," *Cardiovascular Research*, vol. 57, pp. 1044–1051, 4 2003.

[173] E. Nosakhare, G. C. Verghese, R. C. Tasker, and T. Heldt, "QT interval adaptation to changes in autonomic balance," *Computing in Cardiology*, vol. 41, pp. 605–608, 2014.

[174] S. Sundaram, M. Carnethon, K. Polito, A. H. Kadish, and J. J. Goldberger, "Autonomic effects on QT-RR interval dynamics after exercise," *American Journal of Physiology - Heart and Circulatory Physiology*, vol. 294, pp. 490–497, 1 2008.

[175] M. W. Rivolta, G. H. Bevan, V. Gurev, J. J. Rice, C. M. Lopes, and J. P. Couderc, "T-wave morphology depends on transmural heterogeneity in a high-resolution human left-ventricular wedge model," *Computing in Cardiology*, vol. 42, pp. 433–436, 2 2015.

LIST OF PUBLICATIONS

Journal Publications

- **C. Pérez**, E. Pueyo, J. P. Martínez, J. Viik and P. Laguna, "QT interval time lag in response to heart rate changes during stress test for coronary artery disease diagnosis," Biomedical Signal Processing and Control, 2023, vol. 86, p. 105056, doi: 10.1016/j.bspc.2023.10505.

- **C. Pérez**, R. Cebollada, K.A. Mountris, J.P. Martínez, P. Laguna, E. Pueyo, "The role of β-adrenergic stimulation in QT interval adaptation to heart rate during stress test," PLoS One, 2023, vol. 18, no 1, p. e0280901, doi: 10.1371/journal.pone.0280901.

- L. Bachi, H. Halvaei, **C. Pérez** et al., "ECG Modeling for Simulation of Arrhythmias in Time-Varying Conditions," in IEEE Transactions on Biomedical Engineering, vol. 70, no. 12, pp. 3449-3460, 2023, doi: 10.1109/TBME.2023.3288701.

- **C. Pérez**, E. Pueyo, J. P. Martínez, J. Viik, L. Sörnmo and P. Laguna, "Performance Evaluation of QT-RR Adaptation Time Lag Estimation in Exercise Stress Testing ," in IEEE Transactions on Biomedical Engineering, vol. 71, no. 11, pp. 3170-3180, 2024, 2024, doi:10.1109/TBME.2024.3410008.

Conference Publications

- **C. Pérez**, E. Pueyo, J. P. Martínez, J. Viik and P. Laguna, "Characterization of impaired repolarization by quantification of the QT delay in response to heart rate changes from stress test recordings," 2020 11th Conference

of the European Study Group on Cardiovascular Oscillations (ESGCO), Pisa, Italy, 2020, pp. 1-2, doi: 10.1109/ESGCO49734.2020.9158186.

- **C. Pérez**, E. Pueyo, J. P. Martínez, J. Viik and P. Laguna, "Characterization of Impaired Ventricular Repolarization by Quantification of QT Delayed Response to Heart Rate Changes in Stress Test," 2020 Computing in Cardiology, Rimini, Italy, 2020, pp. 1-4, doi: 10.22489/CinC.2020.194.

- **C. Pérez**, E. Pueyo, J. P. Martínez, J. Viik and P. Laguna, "Retardo entre QT y RR en registros de prueba de esfuerzo como indicador de la heterogeneidad de la repolarización ventricular," XXXVIII Congreso Anual de la Sociedad Española de Ingeniería Biomédica (CASEIB), Virtual, 2020, pp. 6-9.

- **C. Pérez**, E. Pueyo, J. P. Martínez, J. Viik and P. Laguna, "Characterization of impaired repolarization by quantification of the QT delay in response to heart rate changes from stress test recordings," 45th Annual Conference of International Society for Computerized Electrocardiology (ISCE), Virtual, 2021.

- Young Investigator Award for the best oral presentation. "Characterization of Impaired Ventricular Repolarization by Quantification of QT Delay after Heart Rate Changes in Stress Test," 17th STAFF/MALT Symposium, Sirolo, Italy, 2021.

- **C. Pérez**, A. Martín-Yebra, J. Viik, J. P. Martínez, E. Pueyo and P. Laguna, "Eigenvector-based spatial ECG filtering improves QT delineation in stress test recordings," 2021 55th Asilomar Conference on Signals, Systems, and Computers, Pacific Grove, CA, USA, 2021, pp. 261-264, doi: 10.1109/IEEECONF53345.2021.9723261.

- R. Cebollada, **C. Pérez**, K. A. Mountris, J. P. Martínez, P. Laguna and E. Pueyo, "Mechanisms Underlying QT Interval Adaptation Behind Heart Rate During Stress Test," 2021 Computing in Cardiology (CinC), Brno, Czech Republic, 2021, pp. 1-4, doi: 10.23919/CinC53138.2021.9662880

- **C. Pérez**, E. Pueyo, J. P. Martínez, L. Sörnmo and P. Laguna, "Simulación de señales ECG incluyendo dinámica del intervalo PQ con el ritmo cardiaco y ruido muscular variante en el tiempo," XLI Congreso Anual de la Sociedad Española de Ingeniería Biomédica (CASEIB), Valladolid, Spain, 2022, pp. 436-439.

- S. Romagnoli, **C. Pérez**, L. Burattini, E. Pueyo, M. Morettini, A. Sbrollini, J.P. Martínez, P. Laguna, "Model-based Estimators of QT Series Time Delay in Following Heart-Rate Changes," Annu Int Conf IEEE Eng Med Biol Soc., Sidney, Astralia, 2023, pp. 1-4, doi: 10.1109/EMBC40787.2023.10340130.

- **C. Pérez**, E. Pueyo, J. P. Martínez, L. Sörnmo and P. Laguna, "Evaluation of a QT Adaptation Time Estimator for ECG Exercise Stress Test in Controlled Simulation," 2023 Computing in Cardiology (CinC), Atlanta, GA, USA, 2023, pp. 1-4, doi: 10.22489/CinC.2023.235.

- **C. Pérez**, E. Pueyo, J. P. Martínez, L. Sörnmo and P. Laguna, "Estimadores del retardo entre las series de QT y RR en registros ECG de prueba de esfuerzo: evaluación en simulación," XLI Congreso Anual de la Sociedad Española de Ingeniería Biomédica (CASEIB), Cartagena, Spain, 2023, pp. 606-609.

LIST OF FIGURES

LIST OF TABLES